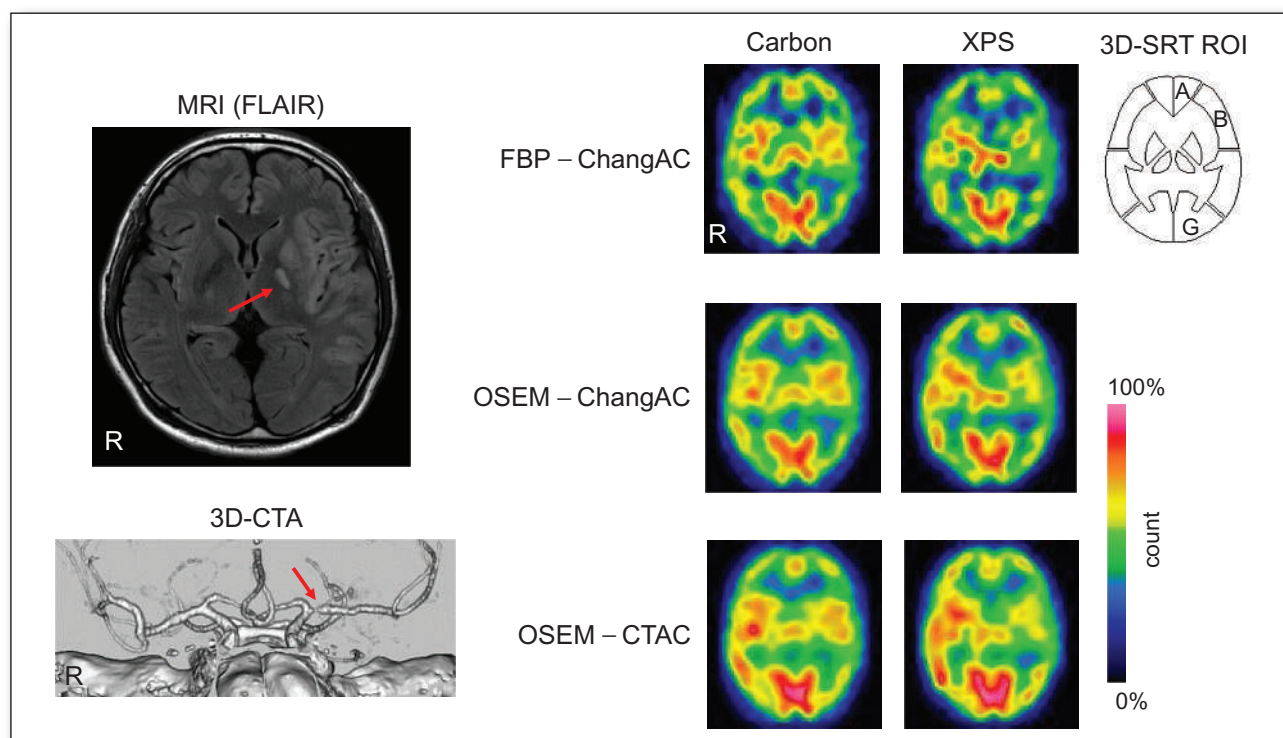


JNM

Journal of Nuclear Medicine Technology

FEATURED IMAGE

A Headrest Made of Extruded Polystyrene Reduces the Influence of Attenuation Correction on Human Brain SPECT Images. Makoto Ohba et al. See page 44.



VERITON-CT[®]

DIGITAL SPECT/CT



Optimization of Every Step

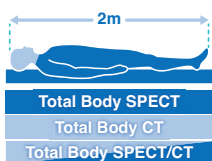
Spectrum Dynamics has integrated its ground-breaking BroadView Technology design into the VERITON-CT system, providing a digital platform enabling routine 3D imaging in Nuclear Medicine. The result is optimization of every step, from image acquisition to interpretation.

VERITON-CT digital SPECT/CT combines the best-in-class CZT detectors, novel system design, high resolution CT, and advanced software technology to elevate the performance of 360° digital SPECT/CT.



BroadView Technology

Proprietary swiveling detector design provides increased sensitivity for faster scans



Total Body 3D Imaging

200cm continuous coverage vertex to feet
SPECT | CT | SPECT/CT



80cm NM and CT bore

Wide Bore SPECT/CT
80cm NM and CT bore



Choice of 16/64 slice

Choice of high-resolution CT for diagnostic applications and low dose total body CTAC



TruView Console

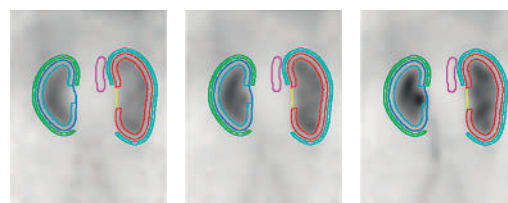
One platform, one location for clinical care decision-making:

1. Acquisition
2. Advanced quantitative reconstruction
3. Both 3D and 4D data analysis and review

VERITON-CT Feature Application: 3D Dynamic Imaging

TruFlow for VERITON-CT offers real-time 3D in-vivo fast dynamic imaging to capture the radiopharmaceutical distribution, uptake, or clearance over time in 3D SPECT/CT parametric imaging.

TruFlow



Pass the NMTCB CT Exam. We GUARANTEE it!

Because MIC is all about outcomes.

Over
30
Years!

We guarantee you'll pass the NMTCB CT Exam or your money back!

- Technologists must complete 35 hours of didactic education related to CT during the 3 year period prior to applying for the CT Exam.
- NMTCB has approved MIC's **CT Registry Review Program** along with **Sectional Anatomy & Imaging Strategies** to **completely satisfy that 35-hour CT didactic requirement!**
- Excellent companion for technologists in hybrid imaging.

There's no better time
to participate in

MIC's Self-Study CE

- Prepare for **CT certification**
- Satisfy NMTCB's **prerequisite**
- Ensure the **highest standards**

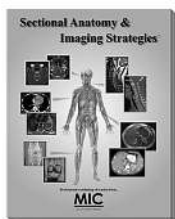
Ask for the CNMT discount when you enroll in both courses!

Technologists and their managers agree:

"MIC's courses really work!"

Sectional Anatomy & Imaging Strategies

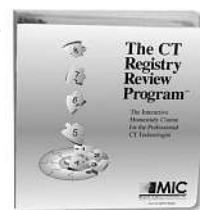
**Learn the essentials
of sectional imaging in
a convenient self-study
format!**



- Patient positioning, artifact reduction, image orientation, slice thickness, etc., for each clinical area.
- Explains sectional imaging with over 1,000 images and figures. The perfect companion to **The CT Registry Review Program**.
- 26 Credits • 6 StudyModules

The CT Registry Review Program™

**Pass the CT Exam after
completing this course
or we will refund your
entire tuition!**



- Learn **essential** and **advanced** topics on the NMTCB and ARRT CT Exam.
- Prior training in CT is recommended.
- Pass the NMTCB or ARRT Exam in CT or your money back!
- 25 Credits • 8 StudyModules

5th
Ed!

"Over 30 years of helping technologists achieve their educational goals!"

A Proud Member of...

SNMMI

Call today for your
Free Info Kit
800-589-5685
or visit www.MICinfo.com



Medical Imaging Consultants, Inc.
1037 US Highway 46, Suite G2 • Clifton, NJ 07013 • 800-589-5685

...for your perfect image.

EDITOR'S PAGE

- 1** 2023—Looking Forward to a New Normal
Kathy S. Thomas

CONTINUING EDUCATION

- 2** SNMMI Clinical Trial Network Research Series for Technologists: Application of Good Clinical Practice to Clinical Research in Medical Imaging
LisaAnn Trembath, Sarah A. Frye, Peter J.H. Scott, and John M. Hoffman
- 9** V/Q SPECT and SPECT/CT in Pulmonary Embolism
Geoffrey M. Currie and Dale L. Bailey
- 16** Clinical Trials of Prostate-Specific Membrane Antigen Radiopharmaceutical Therapy
Hossein Jadvar and Patrick M. Colletti

BRIEF COMMUNICATION

- 22** Peptide Receptor Radionuclide Therapy in Merkel Cell Carcinoma: A Comprehensive Review
Emran Askari, Soroush Zarehparvar Moghadam, Damian Wild, Ebrahim Delpassand, Sergio Baldari, Bernhard Nilica, Philipp E. Hartrampf, Grace Kong, Chiara Maria Grana, Martin Alexander Walter, Francesca Capocchetti, Pashtoon Murtaza Kasi, and Jonathan Strosberg

IMAGING

- 26** Improving ^{90}Y PET Scan Image Quality Through Optimized Reconstruction Algorithms
Pei Ing Ngam, Eelin Tan, Gabriel Lim, and Sean Xuexian Yan
- 32** Evaluation of Data-Driven Respiration Gating in Continuous Bed Motion in Lung Lesions
Takeshi Nii, Shota Hosokawa, Tomoya Kotani, Hiroshi Domoto, Yasunori Nakamura, Yasutomo Tanada, Ryotaro Kondo, and Yasuyuki Takahashi
- 38** Abnormal Biologic Distribution Related to Normal Saline Among $^{99\text{m}}\text{Tc}$ -Dimercaptosuccinic Acid Scans
Turkiya Mahmood Al Bulushi, Khalsa Zahran Al-Nabhani, Deeksha Shetty, Marwa Hamed Al Sabahi, and Abdulhakeem Al-Rawahi
- 44** A Headrest Made of Extruded Polystyrene Reduces the Influence of Attenuation Correction on Human Brain SPECT Images
Makoto Ohba, Yasuaki Kokubo, Koji Suzuki, Masafumi Kanoto, and Yukihiko Sonoda

- 49** Optimization of the Attenuation Coefficient for Chang Attenuation Correction in ^{123}I Brain Perfusion SPECT

Taisuke Murata, Yuri Hayashi, Masahisa Onoguchi, Takayuki Shibutani, Takashi Iimori, Koichi Sawada, Tetsuro Umezawa, Yoshitada Masuda, and Takashi Uno

QUALITY & PRACTICE MANAGEMENT

- 57** Technologist-Based Implementation of Total Metabolic Tumor Volume into Clinical Practice
Erina Quinn, Claire Olson, Manoj K. Jain, Jaiden Sullivan, Matthew P. Thorpe, Geoffrey B. Johnson, and Jason R. Young
- 60** Posttreatment Exposure Rates for ^{90}Y -Microsphere Patients: A Comparison of Products
Steven Blum, Eugenio Silvestrini, Jonathan Weinstein, and Craig Greben

RADIATION SAFETY

- 63** National Diagnostic Reference Levels for Nuclear Medicine in Qatar
Hadi Fayad, Sultan Ahmed, Alaa El khatib, Amer Ghujeh, Antar Aly, Mohammad Hassan Kharita, and Huda Al-Naemi

TEACHING CASE STUDIES

- 68** Radioactive Iodine Uptake in Postoperative Seroma: A Cause for False Positivity
Piyush Aggarwal, Rajkumar K. Seenivasagam, Ashwani Sood, Sarika Prashar, Piyush Pathak, Naresh Sachdeva, and Parikshaa Gupta
- 70** Confirmation of Intracranial Neuroendocrine Metastasis Using ^{68}Ga -DOTATATE PET/CT
Rahim Ismail, Mark Manganaro, and James Bai
- 73** False-Positive ^{68}Ga -DOTATATE PET/CT Findings in Hereditary Hypophosphatemia–Osteomalacia Mimicking Culprit Lesions of Tumor-Induced Osteomalacia
Rahul V. Parghane and Sandip Basu
- 75** Metachronous Adenocarcinoma of the Lung in the Setting of Metastatic Gastric Neuroendocrine Tumor: Value of Elucidating Discordance on Dual-Tracer PET/CT with Ki-67 Index
Sarvesh Loharkar and Sandip Basu
- 78** Femoral Neck Fracture with Avascular Necrosis
Elissa R. Ballas, Vincent T. Nguyen, and Ely A. Wolin

DEPARTMENTS

- 5A** Message from the President
- 80** Letters to the Editor
- 7A** The 2022 Year in Review

JNMT Journal of NUCLEAR MEDICINE TECHNOLOGY

The Official Publication of **SNMMI-TS**

Publications Committee

Chairperson

JESSICA WILLIAMS, CNMT, RT(N), FSNMMI-TS

Ex-Officio Member

KRYSTLE W. GLASGOW, CNMT, NMTCB(CT),
NMAA

DANNY A. BASSO, MS, CNMT, NCT,
FSNMMI-TS

ERIN B. BELOIN, CNMT, RT(CT)

JACQUELYN BROGLEY, CNMT

AMANDA COFFEY, CNMT

GEOFFREY M. CURRIE, PHD BPHARM
MMRS CNMT

MARY BETH FARRELL, EdD, CNMT,
FSNMMI-TS

SARAH A. FRYE, MBA, CNMT, PET, CCRP

JANET L. GELBACH, BA, BS, RT(N), MBA

SARAH R. GIBBONS, MBA, CNMT, NMTCB(CT)

TOMMY LIEU, RTNM, CNMT

FRANCES L. NEAGLEY, BA, CNMT, FSNMMI-TS

CYBIL J. NIELSEN, MBA, CNMT, FSNMMI-TS

ELIZABETH C. ROMERO, RT(N)(CT), FSNMMI-TS

KATHY S. THOMAS, MHA, CNMT, PET,
FSNMMI-TS

Associate Director of Communications

SUSAN ALEXANDER

Senior Publications & Marketing Service Manager

STEVE KLEIN

Senior Copyeditor

SUSAN NATH

Editorial Production Manager

PAULETTE MCGEE

Editorial Project Manager

MARK SUMIMOTO

Director of Communications

REBECCA MAXEY

CEO

VIRGINIA PAPPAS

The *JOURNAL OF NUCLEAR MEDICINE TECHNOLOGY* (ISSN 0091-4916 [print]; ISSN 1535-5675 [online]) is published quarterly by the SNMMI, 1850 Samuel Morse Dr., Reston, VA 20190-5316; phone: (703) 708-9000; fax: (703) 708-9018. Periodicals postage paid at Reston, VA, and at additional mailing offices.

POSTMASTER: Send address changes to the *Journal of Nuclear Medicine Technology*, 1850 Samuel Morse Dr., Reston, VA 20190-5316.

EDITORIAL COMMUNICATIONS should be sent to the editor, Kathy S. Thomas, MHA, CNMT, PET, FSNMMI-TS, JNMT Office, SNMMI, 1850 Samuel Morse Dr., Reston, VA 20190-5316; phone: (703) 326-1185; fax: (703) 708-9018. To submit a manuscript, go to <http://submit-tech.snmjournals.org>.

BUSINESS COMMUNICATIONS concerning permission requests should be sent to the publisher, SNMMI, 1850 Samuel Morse Dr., Reston, VA 20190-5316; phone: (703) 708-9000; home page address: <http://tech.snmjournals.org>. Subscription requests, address changes, and missed issue claims should be sent to Membership Department, SNMMI, at the address above. Notify the Society of change of address and telephone number at least 30 days before date of issue by sending both the old and new addresses. Claims for copies lost in the mail are allowed within 90 days of the date of issue. Claims are not allowed for issues lost as a result of insufficient notice of change of address. For information on advertising, contact Team SNMMI (Kevin Dunn, Rich Devanna, and Charlie Meitner; (201) 767-4170; fax: (201) 767-8065; TeamSNMMI@cunnasso.com). Advertisements are subject to editorial approval and are restricted to products or services pertinent to nuclear medicine. Closing date is the 25th of the second month preceding the date of issue.

INDIVIDUAL SUBSCRIPTION RATES for the 2023 calendar year are \$261 within the United States and Canada; \$278 elsewhere. CPC IPM Sales Agreement No. 1415131. Sales of individual back copies are available for \$60 at <http://www.snmmt.org/subscribe> (subscriptions@snmmi.org; fax: (703) 667-5134). Individual articles are available for sale online at <http://tech.snmjournals.org>.

MISSION: SNMMI-TS is dedicated to the advancement of molecular and nuclear medicine technologists by providing education, advocating for the profession, and supporting research to achieve clinical excellence and optimal patient outcomes. **VISION:** To be recognized as the leader in molecular imaging and therapy. To be dedicated to the advancement of the profession through adoption of emerging technologies.

COPYRIGHT © 2023 by the Society of Nuclear Medicine and Molecular Imaging, Inc. All rights reserved. No part of this work may be reproduced or translated without permission from the copyright owner. Individuals are asked to fill out a permission-request form at <http://tech.snmjournals.org/misc/permission.dtl>. Because the copyright on articles published in the *Journal of Nuclear Medicine Technology* is held by the Society, each author of accepted manuscripts must sign a statement transferring copyright (available for downloading at <http://tech.snmjournals.org/site/misc/ifafora.xhtml>).

The ideas and opinions expressed in *JNMT* do not necessarily reflect those of the SNMMI or the Editors of *JNMT* unless so stated. Publication of an advertisement or other product mentioned in *JNMT* should not be construed as an endorsement of the product or the manufacturer's claims. Readers are encouraged to contact the manufacturer with any questions about the features or limitations of the products mentioned. The SNMMI does not assume any responsibility for any injury or damage to persons or property arising from or related to any use of the material contained in this journal. The reader is advised to check the appropriate medical literature and the product information currently provided by the manufacturer of each drug to be administered to verify the dosage, the method and duration of administration, and contraindications.

JNM^T Journal of NUCLEAR MEDICINE TECHNOLOGY

Editor

Kathy S. Thomas, MHA, CNMT, PET, FSNMMI-TS

Battle Ground, Washington

Associate Editors

Sarah A. Frye, MBA, CNMT, PET, NCT, CCRP
*St. Louis University
St. Louis, Missouri*

Sara G. Johnson, MBA, CNMT, NCT,
FSNMMI-TS
*VA Hospital San Diego
San Diego, California*

Sara L. Johnson, MEd, CNMT, NMTCB (RS),
ARRT(N)(CT)
*Hillsborough Community College
Tampa, Florida*

April Mann, MBA, CNMT, NCT, RT(N),
FSNMMI-TS
*Hartford Healthcare Corporation
Hartford, Connecticut*

Jennifer Prekeges, MS, CNMT, FSNMMI-TS
*Bellevue College
Bellevue, Washington*

Jessica Williams, CNMT, RT(N), FSNMMI-TS
*HCA Healthcare
London, England*

Associate Editor, Continuing Education

Mary Beth Farrell, MS, CNMT, NCT,
FSNMMI-TS
*Intersocietal Accreditation Commission
Langhorne, Pennsylvania*

Associate Editor, Book Reviews

Frances L. Neagley, BA, CNMT, FSNMMI-TS
San Francisco, California

Consulting Editors

Jon A. Baldwin, DO, MBS
*University of Alabama
Birmingham, Alabama*

Twyla Bartel, DO, MBA, FACNM, FSNMMI
*Global Advanced Imaging PLLC
Little Rock, Arkansas*

Norman Bolus, MSPH, MPH, CNMT,
FSNMMI-TS
*University of Alabama
Birmingham, Alabama*

Patrick M. Colletti, MD
*University of Southern California
Los Angeles, California*

George H. Hinkle, RPh, MS, BCNP
*The Ohio State University
Columbus, Ohio*

Alexander W. Scott, II, PhD, DABR,
DABSNM
*Cedars-Sinai Medical Center
Los Angeles, California*

Michael E. Spieth, MD
*Rochester General Hospital
Rochester, New York*

Jennifer R. Stickel, PhD
*Colorado Associates in Medical Physics
Golden, Colorado*

Consulting Editors (International)

Geoffrey M. Currie, BPharm,
MMedRadSc (NucMed),
MAppMngt (Hlth), MBA, PhD
*Charles Sturt University
Wagga Wagga, Australia*

John D. Thompson, PhD, MSc, BSc (HONS)
*University Hospitals of Morecambe Bay
NHS Foundation Trust
Barrow-in-Furness, United Kingdom*

Reimagining the Future

Krystle W. Glasgow, MIS, CNMT, NMTCB(CT), NMAA, FSNMMI-TS

During the 2023 Mid-Winter Meeting, the SNMMI-TS National Council of Representatives and Executive Board reviewed and approved the new SNMMI-TS Strategic Plan. Given the drastic changes in the field and within the Technologist Section over the past 3 years, the new strategic plan was an emergent need, and through efforts begun last year, it truly embraces the future.

The SNMMI-TS Executive Board agreed that it is important to have one cohesive mission/vision for the SNMMI and the Technologist Section:

Vision: SNMMI is the leading global organization transforming the science and practice of diagnostic and therapeutic nuclear medicine.

Mission: Empowering our members to transform the science and practice of precision nuclear medicine for diagnosis and therapy to advance patient care.

The “SNMMI-TS Future, Imagined” statement in the plan adds further context: The SNMMI-TS will be able to drive change within hospitals, institutions, and academia to better educate and advocate for the field of nuclear medicine and molecular imaging. Therapy will be practiced in all hospitals around the country, and as key members of the care team, nuclear medicine technologists (NMTs) will use their enhanced expertise in precision medicine to collaboratively improve patient outcomes.

Workforce Pipeline

In 2022, the SNMMI-TS created a Workforce Pipeline Task Force to investigate and better understand the current challenges involved in entering the field and how students are exposed to nuclear medicine as a career pathway during high school and undergraduate education. Through outreach, education, and the exchange of knowledge, the SNMMI-TS hoped to create communication bridges for NMT programs to work collaboratively with institutions around the country who need to hire qualified NMTs.

In January 2023, under the vision of Immediate Past President Dusty York, the SNMMI-TS launched a new video titled “Careers in Nuclear Medicine Technology” that showcases the many different opportunities available to NMTs. The video, which can be found on the new career website at nmcareers.snmmi.org, serves as the first resource for recruitment into the field. The social media response to the video launch has been incredible, including 172 views on YouTube and many views of the teaser video: 3,071 on Instagram

(which makes this SNMMI’s most watched Instagram reel), 1,805 on LinkedIn, 269 on Facebook, and 380 on Twitter.

The Workforce Pipeline group is now organizing a recruitment event for the 2023 Annual Meeting in Chicago. The half-day session would bring in high school students and their parents to learn about nuclear medicine, take special tours of the exhibit hall showcasing imaging equipment and cutting-edge therapies, and meet program directors. The event will close with a guest speaker focusing on college admissions counseling and student success coaching. The task force is connecting with individuals in the Chicago area to help with recruiting students and marketing the event.



Krystle W. Glasgow, MIS, CNMT, NMTCB(CT), NMAA, FSNMMI-TS

Welcome and Congratulations to the SNMMI-TS Leadership Academy Class of 2023!

For the first time since 2020, SNMMI-TS is pleased to announce the graduates for the SNMMI-TS Leadership Academy. The Academy, which took place during the SNMMI Mid-Winter Meeting, accepts only a limited number of applicants each year and is considered to be the cornerstone of SNMMI’s governance training for committee chairs, council and center leadership, and the SNMMI/SNMMI-TS boards of directors. Participants included Ejda Bajric (Missouri Valley), Emily Brooks (Central), Sarah Clements (New England); Michael Dillard (Pacific Northwest), Jose “Freddy” Gonzalez (Southwestern), Jason Joson (Pacific Southwest), David Kelkis (Mid-Eastern), Jessica Long (Southeastern), Martha Mar (Southwestern), Elad Nevo (Greater New York), Erika Padilla-Morales (Northern California), Alexia Romano (New England), Melissa Snody (Central), Angela Weiler (Central), and Caitlin Woltering (Missouri Valley).

With the 2023 graduating class, the SNMMI-TS Leadership Academy has trained more than 200 graduates since its inception in 2007. We look forward to seeing what leadership positions these future graduates will strive to hold!

Through the efforts of the Professional Development Task Force, the first Student Leadership Academy will be held during the 2023 SNMMI Annual Meeting. The one-day event, scheduled for Saturday, June 24, will mimic the SNMMI-TS Leadership Academy but will focus on NMT

students entering the workforce for the first time. Students will have the opportunity to participate in emotional intelligence assessment before the event and will learn key leadership skills to make their NMT transition successful. The Academy will be open to all NMT students (free to members) but will require registration.

Training in Radiopharmaceutical Therapy

A pressing issue for the SNMMI-TS is ensuring NMTs are appropriately trained in radiopharmaceutical therapy procedures. While the administration of therapies is part of the scope of practice for NMTs, the continuous approval of new therapies makes it necessary to ensure they stay up to date with the most current and cutting-edge information. The September 2022 issue of the *Journal of Nuclear Medicine Technology* focused entirely on radiopharmaceutical

therapies—in particular, I-131, Xofigo, Lu-DOTA, Lu-PSMA, and Azedra—and provided information on patient selection; clinical, technical, and regulatory considerations; protocols; radiation safety; dosimetry; imaging; billing; coding; and how to make the therapy a success.

In January, the SNMMI-TS debuted “Therapy Thursdays” to provide you with resources and updates from around the world in radiopharmaceutical therapy. Watch for additional information, and be sure to visit “Tools for Technologists” at www.snmmti.org/therapy. The Molecular Therapy Task Force is planning a Townhall Meeting in March, where technologists will be able to ask questions and share information on how their sites are performing therapies (pitfalls, successes, best practices, etc.). Short videos are also being created at several universities to serve as resources for technologists.

2023—Looking Forward to a New Normal

Kathy S. Thomas, MHA, CNMT, PET, FSNMMI-TS

Editor, *JNMT*

By the time this editorial is published, the phrase “Happy New Year!” will be more than a little stale; however, with any luck, the new year will be happy as the world tentatively returns to something approaching a new “normal.” For the nuclear medicine community, the new normal includes an opportunity to gather once again, either in person or virtually, to share the latest advances in molecular imaging and therapeutic procedures at the Mid-Winter Meeting in San Francisco, California. I hope you had the opportunity to kick off the new year in a positive way by attending the conference and catching up with friends and colleagues.

Once again, the continuing education (CE) articles in this issue offer a diverse selection of topics. The SNMMI Clinical Trials Network continues its series discussing good clinical practices required in clinical research (1). The next CE offering discusses how V/Q lung imaging, a tried-and-true procedure in nuclear medicine for decades, can be enhanced using SPECT or SPECT/CT imaging (2). Finally, an overview of many PSMA-directed radiopharmaceutical therapy clinical trials using α - or β -emitters in prostate cancer is discussed (3).

The Quality and Practice Management section introduces a potential role nuclear medicine technologists may have to assist the radiologist in calculating total metabolic tumor volume for patients with diffuse large B-cell lymphoma (DLBCL) (4). Additionally, Blum et al. provide quantitative data analysis of 2 ^{90}Y -microsphere products comparing exposure rates and special safety considerations (5).

In the United States, radiation safety and protection guidelines are commonplace; however, critical data are required in developing countries to optimize diagnostic reference levels (DRLs) and radiation protection guidelines in nuclear medicine imaging, including SPECT, SPECT/CT, and PET/CT. Fayad et al. discuss Qatar’s work establishing DRLs for administered activity optimization for nuclear medicine procedures (6).

The scientific manuscripts offer an assortment of topics, including optimized image quality for ^{90}Y PET imaging, respiratory gating for lung lesions, a $^{99\text{m}}\text{Tc}$ -DMSA biodistribution issue associated with the quality of saline used in preparing the radiopharmaceutical, and an improved headrest for PET brain imaging.

The teaching case studies offer a variety of examples where key facts or concepts are demonstrated and were helpful in a specific diagnosis.

As always, I will conclude with my plea for your ideas, suggestions, or comments to improve *JNMT* content. But most importantly, I would also encourage you to consider sharing your expertise by writing up a research study from your institution, an interesting case study, or a brief communication discussing a project that resulted in a positive outcome in your work environment. Don’t know where to start? Help is available! Contact me at ksthenomas0412@msn.com.



Kathy S. Thomas, MHA,
CNMT, PET, FSNMMI-TS

REFERENCES

1. Trembath L, Frye SA, Scott PJH, Hoffman JM. SNMMI Clinical Trial Network research series for technologists: application of good clinical practice to clinical research in medical imaging. *J Nucl Med Technol.* 2023;51:2–8.
2. Currie GM, Bailey DL. V/Q SPECT and SPECT/CT in pulmonary embolism. *J Nucl Med Technol.* 2023;51:9–15.
3. Jadvar H, Colletti PM. Clinical trials of prostate-specific membrane antigen radiopharmaceutical therapy. *J Nucl Med Technol.* 2023;51:16–21.
4. Quinn E, Olson C, Jain MK, et al. Technologist-based implementation of total metabolic tumor volume into clinical practice. *J Nucl Med Technol.* 2023;51:57–59.
5. Blum S, Silvestrini E, Weinstein J, Greben C. Posttreatment exposure rates for ^{90}Y -microsphere patients: a comparison of products. *J Nucl Med Technol.* 2023;51:60–62.
6. Fayad H, Ahmed S, El khatib A, et al. National diagnostic reference levels for nuclear medicine in Qatar. *J Nucl Med Technol.* 2023;51:63–67.

SNMMI Clinical Trial Network Research Series for Technologists: Application of Good Clinical Practice to Clinical Research in Medical Imaging

LisaAnn Trembath¹, Sarah A. Frye², Peter J.H. Scott³, and John M. Hoffman⁴

¹Avid Radiopharmaceuticals, Philadelphia, Pennsylvania; ²Department of Clinical Health Sciences, Saint Louis University, St. Louis, Missouri; ³Department of Radiology, University of Michigan, Ann Arbor, Michigan; and ⁴Huntsman Cancer Institute and Department of Radiology and Imaging Sciences, University of Utah School of Medicine, Salt Lake City, Utah

CE credit: For CE credit, you can access the test for this article, as well as additional JNMT CE tests, online at <https://www.snmmilearningcenter.org>. Complete the test online no later than March 2026. Your online test will be scored immediately. You may make 3 attempts to pass the test and must answer 80% of the questions correctly to receive 1.0 CEH (Continuing Education Hour) credit. SNMMI members will have their CEH credit added to their VOICE transcript automatically; nonmembers will be able to print out a CE certificate upon successfully completing the test. The online test is free to SNMMI members; nonmembers must pay \$15.00 by credit card when logging onto the website to take the test.

This article is part of a series developed by the Clinical Trials Network of the Society of Nuclear Medicine and Molecular Imaging to offer training and information for molecular imaging technologists and researchers about various aspects of clinical research. This article covers the topic of good clinical practice and how that relates to those portions of the *Code of Federal Regulations* that govern clinical research in the United States, such as title 21, part 312, and the Common Rule. The purpose of this article is to inform technologists and researchers about standard roles, documents, guidance, and processes that are elemental to the conduct of clinical trials and to offer additional resources for learning about these processes.

Key Words: good clinical practice; ICH E6; clinical research

J Nucl Med Technol 2023; 51:2–8

DOI: 10.2967/jnmt.122.264778

Participating in sponsored research trials is an exciting part of being a nuclear medicine or PET imaging technologist today. As described in an earlier article in this series, by Jeffers et al. (1), molecular imaging is a key part of the new-drug discovery paradigm that uses biomarkers and radiopharmaceutical products to answer critical questions on the pathway to development and approval of a new therapeutic drug. Nuclear medicine and PET technologists play a critical role in collecting research data in the form of patient scans, as well as safety data such as vital signs or pharmacokinetic data with blood sampling. This article will highlight aspects of good clinical practice (GCP) and federal research regulations that molecular imaging researchers and

technologists should be aware of when planning and conducting research involving human subjects. The paper's focus is on drug development and use of molecular imaging as biomarkers, although the principles discussed are applicable to any clinical trial setting.

GCP

GCP refers to a prescribed set of quality and ethical standards for how to plan, conduct, and document research involving human subjects. Compliance with the standards described in the GCP framework ensures that the rights, safety, and well-being of human subjects involved in research are protected and that the resulting research data are rigorous and have reliability and integrity.

A document on GCP is published by an organization called the International Council for Harmonisation of Technical Requirements for Pharmaceuticals for Human Use (ICH). The ICH publishes standards that cover topics in the categories of quality, safety, and efficacy in clinical trials. The collection of guidelines in the efficacy category contains 20 subjects, including topics such as pharmacovigilance, clinical study reports, dose–response studies, statistical principles, and GCP. The GCP publication, coded as E6 (an abbreviation for the sixth report in the efficacy section) in the ICH guidelines, was revised in 2016 and is officially entitled “Integrated Addendum to ICH E6(R1): Guideline for Good Clinical Practice—E6(R2).” At the time of this writing, the ICH has drafted version R3, which is targeted for adoption in August 2023. The GCP publication and other ICH publications are easily found online with an internet search and are recommended reading for anyone interested in learning more about clinical research (2).

The ICH is an international consensus organization in which the U.S. Food and Drug Administration (FDA), European Medicines Agency, Japan Pharmaceuticals and Medical Devices Agency, and other drug regulatory authorities

Received Aug. 8, 2022; revision accepted Oct. 27, 2022.
For correspondence or reprints, contact LisaAnn Trembath (latrembath@gmail.com).

Published online Nov. 9, 2022.

COPYRIGHT © 2023 by the Society of Nuclear Medicine and Molecular Imaging.

such as the Departments of Health of Australia, Brazil, China, Taipei, India, Russia, Singapore, and South Korea all have permanent representatives (3).

In addition to the international GCP standard, there are several sections in the *Code of Federal Regulations* (CFR) that govern human subject research in the United States and are aligned with GCP (4). The testing of investigational new drugs on human subjects is governed by title 21 of the CFR, part 312 (referred to as 21CFR§312) (5). Radiopharmaceuticals can also be used without an investigational-new-drug application in certain cases, such as when they meet the provisions for use under approval of an institutional radioactive drug research committee as defined in 21CFR§361 (6). Regulations for testing medical devices on human subjects are found in 21CFR§812 (7). Other types of research that do not involve an investigational drug or device, such as behavioral research or clinical trials with U.S. military personnel, are governed by 45CFR§46 under the Department of Health and Human Services (8). Protection of human subjects by the creation of institutional review boards (IRBs) and the informed consent process is found in 21CFR§50 and §56, respectively (9,10). An overview of the investigational-new-drug process and regulations can be found in a previous paper in this series (11).

GCP and federal regulations governing clinical research are applicable to all human subject research, including studies that use investigational radiopharmaceuticals for diagnosis or treatment, or approved radiopharmaceuticals used for screening, for monitoring therapy, or as biomarkers of a disease process. More information about various types of studies that use radiopharmaceuticals can be found in a previous paper in this series (1). Data resulting from the use of a molecular imaging biomarker in a study to investigate a new therapeutic are subject to levels of scrutiny similar to those for any other clinical trial data. GCP and federal research regulations are designed not only to protect patient privacy and safety but also to ensure that data are collected, documented, and reported with scientific rigor and quality.

COMMON RULE

Human subject research that is not for registration of a new drug or device is regulated by federal policy 45CFR§46, subpart A, which is known as the Common Rule (12). Subpart B of the federal policy includes additional protections for pregnant women, human fetuses, and neonates; additional protections are included in subpart C for prisoners and subpart D for children, both of whom are considered vulnerable populations (13,14).

More than 15 separate federal agencies have linked 45CFR§46 to their regulations, binding any of their research efforts in humans to the same regulatory statute. For all participating departments and agencies, the Common Rule outlines the basic provisions for IRBs, informed consent, and assurances of compliance (15).

The Department of Health and Human Services website provides educational videos, frequently asked questions, and other information about how recent changes in the Common Rule, effective in 2019, impact academic research centers (16). As with 21CFR§312, GCP is aligned with the Common Rule, and regulators expect researchers and staff to be compliant with both the current regulations and GCP principles.

KEY ROLES IN CLINICAL RESEARCH

Drug development research that uses molecular imaging for screening, diagnosis, monitoring of therapy, or as a biomarker is subject to the rules found in both 21CFR§312 and the GCP framework, as are the key roles and responsibilities.

Sponsor

The sponsor of a clinical trial is the person or entity that holds regulatory accountability for conduct of the trial. This is often, but not always, the same entity as the one that financially supports the research (e.g., a pharmaceutical company). Sponsors can be an individual person, pharmaceutical company, academic institution, government agency, or other organization. A sponsor initiates and is responsible for a clinical investigation but does not conduct trial activities unless the sponsor is a sponsor-investigator. Pharmaceutical sponsors typically contract with investigators (medical experts on the disease or condition under study) to conduct the trial. Sponsors have clearly defined responsibilities cited in GCP and 21CFR312§50. These responsibilities include selecting qualified investigators and providing them with all the information they need to conduct the investigation safely and properly; ensuring that the investigation is properly monitored; ensuring that the investigation is conducted in accordance with the investigational plan in the investigational-new-drug application, as well as with all protocols therein; maintaining an effective investigational-new-drug application with respect to all clinical trials; and promptly informing the FDA and all participating investigators of significant new adverse effects or risks (17,18).

Contract Research Organization (CRO)

A CRO is an entity that can be hired by the sponsor to conduct various aspects of the trial on the sponsor's behalf (17). A sponsor is allowed to transfer, in writing, any or all obligations described in 21CFR§312. Once the CRO assumes these obligations, the CRO is subject to the same regulatory oversight and action as the sponsor (19). In molecular imaging trials, it is common for a sponsor to engage an imaging CRO to work with nuclear medicine departments to obtain protocol-required scan data. An imaging CRO has personnel with specialized experience and knowledge in medical imaging, as well as in how to obtain, transfer, analyze, and archive image data used in clinical trials. CROs exist that can perform many functions in a clinical trial, such as laboratory testing, safety monitoring, statistics, cardiac monitoring, protocol development, and study monitoring.

Investigator

An investigator is an individual who conducts the clinical trial, or under whose direct supervision the trial activities are performed, and who is qualified by training and experience to perform the protocol procedures and ensure the safety of subjects. The investigator, often referred to as the principal investigator (PI), is the responsible team leader in a group of people who are conducting a trial. The PI is most commonly a medical doctor, but can also be a PhD, dentist, psychologist, osteopath, or another licensed professional such as a radiochemist or medical physicist, who is qualified by training and experience to conduct the research (17). Other individuals who work on the clinical trial team are referred to as subinvestigators per 21CFR§312.3 (20).

Although the sponsor holds responsibility for choosing qualified and trained investigators, the PI is responsible for ensuring that the clinical trial is conducted according to the protocol. The PI is also responsible for protecting the rights, safety, and welfare of patients in the trial; for obtaining informed consent from each person who receives the investigational drug; and for ensuring that any protected health information is handled in a compliant fashion. The PI is responsible for control of the investigational drug by keeping adequate records and by administering the investigational product only to subjects who are under the PI's personal supervision (or under the supervision of a subinvestigator) and who have consented to participate in the study (17,21). When a nuclear medicine technologist is responsible for injecting an investigational radiopharmaceutical, the technologist's name should be listed on the delegation-of-authority log, which is described later in this paper.

Investigators are responsible for preparing and maintaining accurate case histories (17,22) for all subjects in a clinical trial, whether the subject is receiving the investigational drug or serving as a control subject. This case history includes case report forms (CRFs) (often provided by the sponsor), hospital and progress notes, source documents, follow-up reports, and other records. The case history for every individual in the trial must document that informed consent had been obtained before any research procedures were performed, including but not limited to scans or lab tests. If molecular imaging is being used as a screening procedure for a trial involving an investigational drug, it is imperative that the informed consent be signed and on file before injection of any radiopharmaceutical (17,23).

Study Coordinator

The study coordinator, or clinical research coordinator, works under the direct supervision of the PI at the investigational site. This role is sometimes referred to as a clinical coordinator or as a study nurse when applicable. The study coordinator must be knowledgeable about GCP and research regulations and typically has some form of health-care training such as in nursing, radiology, or medical assistance. The study coordinator can assist with a myriad of administrative, clinical, regulatory, and documentation duties (24).

There are 2 major professional organizations that support, educate, and certify clinical research coordinators: the Association of Clinical Research Professionals (<https://acrpnet.org/>) and the Society of Clinical Research Associates (<https://www.socra.org/>). Certification by 1 of these 2 organizations indicates to an investigator and potential sponsor that an individual is trained in GCP and research regulations and has experience in the conduct of clinical trials.

Clinical Research Associate

A clinical research associate, or monitor, is hired by the sponsor or CRO to ensure that a clinical study is conducted according to the protocol and that the PI fulfills all responsibilities to the IRB, trial, and patients. Clinical research associates perform the work of monitoring, but they also may be involved in protocol writing, site selection, recruitment strategies, medical writing, and more. To monitor a clinical trial means to work directly with a research site and PI to oversee the conduct of the trial, ensuring that protocols are followed and that subjects' safety and privacy rights are protected. Monitors compare case report forms against source documents, ensure that written informed consent is documented for each subject before any study procedures take place, enquires about discrepant data points, and reviews the drug accountability log for omissions or errors, as well as performing other tasks. Monitors also conduct the study-initiation and close-out visits; provide protocol-specific training for the PI, subinvestigators, and other staff involved in research; and confirm that all participants in research activities are trained in GCP. Remote monitoring, or review of documentation electronically without travel to the research site, is more common now because of the impact that the coronavirus disease 2019 pandemic has had on in-person site visits. In a guidance document published by the FDA in March 2020 about the impact of the pandemic on clinical trials, the FDA encouraged sponsors to "consider optimizing use of central and remote monitoring programs to maintain oversight of clinical sites" (25).

IRB

The IRB is a requisite component for research involving FDA-regulated clinical studies. The IRB, whose purpose and makeup are described in 21CFR§50 and §56, is formally designated to review and monitor biomedical research involving human subjects (9,10). Additional information about the IRB can be found in an earlier paper in this series (26).

KEY DOCUMENTS IN CLINICAL TRIALS

Participation in clinical research activities requires knowledge of the key documents used to verify adherence to protocol procedures and regulations and to ensure the safety of subjects. The following documents are discussed in this article: protocol, form FDA 1572, imaging charter/manual, investigator's brochure (IB), CRF, source document, informed-consent form, drug accountability log, and delegation-of-authority log. Recording of adverse events is also discussed, and additional resources are provided.

Protocol

A protocol is a document that describes the objectives, design, methodology, statistical considerations, and organization of the trial (1). According to 21CFR§312, a protocol document must contain the following elements: a statement of the objectives (often referred to as endpoints) and purpose of the study, and the observations and measurements to be made to fulfill the objectives of the study; the name and address and a statement of the qualifications of each investigator; the name of each subinvestigator working under the supervision of the PI; the name and address of the research facilities to be used; the name and address of each reviewing IRB (in practice, this information is often not included in the protocol document per se but is part of form FDA 1572, “Statement of Investigator”); the criteria for patient inclusion and exclusion and an estimate of the number of patients to be studied; a description of the design of the study, including the kind of control group to be used, if any; a description of methods to be used to minimize bias on the part of subjects, investigators, and analysts; the method for determining the doses to be administered, the planned maximum dosage, and the duration of individual patient exposure to the drug; and a description of the clinical procedures, laboratory tests, or other measures to be taken to monitor the effects of the drug on human subjects and to minimize risk.

The term *protocol* is commonly used in imaging departments to describe the dose, injection, scanning, and processing protocols for an imaging procedure. In clinical research, especially pharmaceutical research, scanning details are typically not in the study protocol but are in a separate document referred to as an imaging charter or imaging manual.

Form FDA 1572

Form FDA 1572 is a statement that includes a commitment that the investigator will conduct the study in accordance with the relevant, current protocols and will make changes to a protocol only after notifying the sponsor, except when necessary to protect the safety, rights, or welfare of subjects; will comply with all clinical investigator obligations and other pertinent requirements; will personally conduct or supervise the investigations; will inform any potential subjects that the drugs are being used for investigational purposes and ensure that the requirements on informed consent (21CFR§50) and IRB approval (21CFR§56) are being met; will report to the sponsor any adverse experiences that occur (21CFR§312.64); has read and understands the information in the IB, including the potential risks and side effects of the drug; and will ensure that all associates, colleagues, and employees assisting with the study are informed about their obligations in helping the investigator meet this commitment (27,28).

All nuclear medicine physicians who participate in the trial by reading images, administering investigational products, or analyzing data should be listed on form FDA 1572 as subinvestigators. Because nuclear medicine technologists can be such an integral part of collecting research data, some sponsors require that any technologist who participates in the study be

listed on form FDA 1572 and that training and licensure be documented and submitted to the sponsor for regulatory filing. Some sponsors or institutions also require listing of research nurses or physician assistants who obtain the informed consent.

Additional information about protocol amendments, deviations, and variations; form FDA 1572; and practical advice on how to maximize compliance with the protocol can be found in a previous publication (29).

Imaging Charter

An important document for molecular imaging researchers and technologists to be aware of is the imaging charter (sometimes referred to as an imaging manual or technical manual). This document contains detailed instructions, usually not provided in the study protocol, that describe how, when, and with what parameters research subjects should be imaged to ensure standardization and harmonization of imaging results. The FDA published a guidance document in 2018, “Clinical Trial Imaging Endpoint Process Standards Guidance for Industry,” that suggests what a sponsor should include in an imaging charter or manual (30). This guidance document, although written for sponsors of clinical trials, helps molecular imaging researchers and technologists understand the broad scope of considerations that go into designing an imaging protocol to test a drug.

Several standards are recommended for inclusion in an imaging charter. One standard is equipment standardization and optimization, including vendor-specific equipment and platforms; equipment technical settings to be used at each site; the role of technologists in the imaging process; phantoms to be used for site qualification and monitoring of quality; subject preparation, positioning, and comfort measures; schedules for imaging, off-protocol imaging; imaging risks; the site qualification process; acquisition quality control and monitoring; and data storage and transfer. Another standard is for the imaging drug, such as preparative drugs, contrast agents, and radiopharmaceutical agents, and a third standard is for image interpretation, including image display, selection of images for interpretation, randomization for the central read process, imaging CRFs, and quality control of display and interpretation, among others.

For study protocols that implement a central read process (vs. an interpretation by the nuclear medicine physician at the research site), the guidance document offers advice on identifying readers and their background qualifications, training readers for the protocol, timing reads, and determining the read process or methodology to be used (30).

IB

The IB, or investigator’s drug brochure, is critical for any investigator in a clinical trial to read and understand. Per the GCP guidelines, “The Investigator’s Brochure (IB) is a compilation of the clinical and nonclinical data on investigational product(s) that are relevant to the study of the product(s) in human subjects. Its purpose is to provide the

investigators and others involved in the trial with the information to facilitate their understanding of the rationale for, and their compliance with, many key features of the protocol, such as the dose, dose frequency/interval, methods of administration[,] and safety monitoring procedures. The IB also provides insight to support the clinical management of the study subjects during the course of the clinical trial.” (17). The IB is updated annually by the sponsor and reissued to all investigators. It is critical to review the IB for any changes in the safety profile of the drug. For example, if there has been a significant increase in side effects or adverse events, the consent language may require revision (31).

CRF

CRFs and *source documents* are terms that are often mistakenly used interchangeably, but each has a specific purpose, and both are needed. A CRF is a physical document or an electronic document or repository that contains the records and results from all observations and clinical procedures that are performed to monitor the effects of the investigational drug in humans and to fulfill the objectives of the study. The investigator records all study data onto subject-specific CRFs and submits them to the sponsor for analysis of data across subjects and investigational sites. Per GCP, “data reported on the CRF, that are derived from source documents, should be consistent with the source documents or the discrepancies should be explained” (17).

Source Documents

Source documents are the original location of data that is subsequently recorded into a CRF. The first place that data are generated is considered the source. Source documents can be medical records, forms that are filled out by the trial personnel, or pieces of paper on which data are recorded. GCP requires that all information on a CRF be verified from a source document (17). Digital data can be a source document if they are the first output of data from a test, such as an electrocardiogram recording or DICOM (Digital Imaging and Communications in Medicine) headers in a PET scan (32). One key role of a monitor is to compare data entries in the CRF with the original data from the source. When there is a discrepancy, the monitor asks the investigator to clarify which data are correct. For example, if a CRF states that the scan start time is 12:07 but the PET scan DICOM header says the scan started at 12:12, a monitor will flag that discrepancy. The monitor writes to the investigator to ask which was the correct start time. In another example, if a blood pressure measurement was entered into a CRF as 120/80 but the hospital chart notes that it was 122/80, a monitor will ask the investigator for clarification and correction. This clarification is required even if the discrepancy results in a measurement that is considered within normal limits and might not be clinically meaningful to patient care.

Trials using radiopharmaceuticals will often take advantage of the ability to measure radioactivity in samples of blood or urine. Analog data from a well counter that prints

out a strip of numbers should be annotated with the date, time, subject identification number, and what sample is represented by the number (e.g., 5-min plasma). Because ink from analog printouts is prone to fading over time, it is recommended that the technologist make a certified copy of the source document for clarity and accessibility in any future regulatory inspection.

Informed-Consent Form

The informed-consent form is a protocol-specific document that describes to a patient what the study entails, what procedures will take place, and what the risks of study participation are. This document, the required content of which is defined in 21CFR§50.25, must be signed by patients before they undergo any study procedures and indicates that they understand the study and have consented to participate. An appropriate translation must be provided to nonnative English speakers if needed, and accommodations must be made for subjects incapable of giving consent themselves (e.g., medical power of attorney for dementia patients). The informed-consent document is reviewed by the IRB to ensure an adequate explanation of risks (including any anticipated radiation dose or exposure from the diagnostic or therapeutic procedures) and potential benefits. For clinical trials in which molecular imaging is part of a therapeutic study, the informed-consent process is conducted by PIs or their representatives, and the imaging department will probably not see it or be involved. For studies in which a radiopharmaceutical is the investigational agent, the imaging staff may be involved in the consent process or be responsible for ensuring that no study procedures are performed before the patient signs the informed-consent form. More information about the importance of the informed-consent process can be found on the FDA website, which has helpful information for patients and a guidance document for sponsors and researchers (33).

Drug Accountability Log

The investigator is responsible for the control of all investigational drugs in a study per GCP and 21CFR§312.62. To facilitate that control, and document how and when each dose of an investigational product is administered, a drug accountability log should be used. This log is typically provided by the sponsor and maintained by the department or entity that administers the investigational product (e.g., the dispensing nuclear pharmacy). For therapeutic investigational drugs, often this is a hospital pharmacy. For studies in which the radiopharmaceutical is investigational, the imaging department may be responsible for tracking receipt, administration, decay, and disposal each time a subject is administered a dose. Even though administration of radioactive materials is carefully documented via dose-ordering systems in a nuclear medicine department, a drug accountability log for investigational radiopharmaceuticals is required above and beyond departmental dose records. At the completion of a clinical trial or if the investigation is terminated for any reason, the

investigational product must be either returned to the sponsor or destroyed. For radiopharmaceuticals, the typical disposition consists of allowing decay to background levels, discarding or destroying the nonradioactive vial, and documenting that disposal. Sometimes a sponsor will request that disposal of the nonradioactive vial be done in the presence of a clinical research associate or monitor, in which case vials should be stored for the length of the trial (17,21).

Delegation-of-Authority Log

Although the PI is ultimately responsible for everything that happens in a clinical trial, for practical reasons many of the protocol tasks are delegated to qualified and trained individuals. GCP advises in section 4.6.2 of the guidance, “If the investigator/institution retains the services of any individual or party to perform trial-related duties and functions, the investigator/institution should ensure this individual or party is qualified to perform those trial-related duties and functions and should implement procedures to ensure the integrity of the trial-related duties and functions performed and any data generated” (17). To document that the PI has ensured that only qualified personnel are performing protocol-required tasks, a delegation-of-authority log is often used even though it is not specifically required in 21CFR§312. A delegation-of-authority log maintains a record of which specific tasks and procedures are delegated by the PI and to whom they are delegated. For example, the log may state that a named study coordinator is delegated the responsibility for initiating the informed-consent process, that a named nurse is delegated the responsibility for taking vital signs per the protocol, or that a named nuclear medicine technologist is delegated the responsibility for injecting an investigational radiopharmaceutical. Delegation logs typically require an individual’s full name in legible print, signature and initials, job title or role in the study, and dates of study involvement. The PI’s signature on the delegation log is an attestation that the PI approves authorization of these individuals to perform the stated tasks. Updates to the delegation-of-authority log due to staff departure from or entrance into the study should be documented and a new signature from the PI obtained. A good example of a delegation-of-authority log can be found on the National Center for Complementary and Integrative Health website (34).

Adverse-Event Reporting

Imaging departments contribute key data to the developing picture of an investigational drug’s side effects, especially when the drug is a radiopharmaceutical. Not every adverse event must be reported, but every adverse event must be recorded in a source document and CRF for review and subsequent determination of causality by the sponsor in conjunction with the PI. Although a detailed discussion of adverse-reporting definitions and procedures is beyond the scope of this article, it is recommended that imaging technologists and researchers have a clear understanding of their role in monitoring patients for adverse effects, how to document them, and when to report them to the sponsor or IRB.

Individuals who are unsure of their role in recording adverse events in a sponsored trial should reach out to the sponsor or the sponsor’s representative for clarity. More information on adverse event reporting in a clinical trial can be found in the FDA’s draft guidance document “Investigator Responsibilities: Safety Reporting for Investigational Drugs and Devices—Guidance for Industry” (35).

CONCLUSION

This article has reviewed GCP definitions and application of its principles to clinical trials that use molecular imaging, as well as presenting key roles, documents, and procedures essential for clinical trial work. Relevant references to the CFR and additional sources of information have been provided when applicable.

DISCLOSURE

No potential conflict of interest relevant to this article was reported.

REFERENCES

1. Jeffers CD, Lawhn-Heath C, Butterfield RI, Hoffman JM, Scott PJH. SNMMI clinical trials network research series for technologists: clinical research primer—use of imaging agents in therapeutic drug development and approval. *J Nucl Med Technol.* 2022;50:291–300.
2. Efficacy guidelines. ICH website. <https://www.ich.org/page/efficacy-guidelines>. Accessed November 30, 2022.
3. Members and observers. ICH website. <https://www.ich.org/page/members-observers>. Accessed November 30, 2022.
4. Good clinical practice. Food and Drug Administration website. <https://www.fda.gov/about-fda/center-drug-evaluation-and-research-cder/good-clinical-practice>. Updated December 11, 2019. Accessed November 30, 2022.
5. Part 312: investigational new drug application. Code of Federal Regulations website. <https://www.ecfr.gov/current/title-21/chapter-I/subchapter-D/part-312>. Updated November 28, 2022. Accessed November 30, 2022.
6. Part 361: prescription drugs for human use generally recognized as safe and effective and not misbranded—drugs used in research. Code of Federal Regulations website. <https://www.ecfr.gov/current/title-21/chapter-I/subchapter-D/part-361>. Updated November 28, 2022. Accessed November 30, 2022.
7. Part 812: investigational device exemptions. Code of Federal Regulations website. <https://www.ecfr.gov/current/title-21/chapter-I/subchapter-H/part-812>. Updated November 28, 2022. Accessed November 30, 2022.
8. Part 46: protection of human subjects. Code of Federal Regulations website. <https://www.ecfr.gov/current/title-45/subtitle-A/subchapter-A/part-46>. Updated November 28, 2022. Accessed November 30, 2022.
9. Part 50: protection of human subjects. Code of Federal Regulations website. <https://www.ecfr.gov/current/title-21/chapter-I/subchapter-A/part-50>. Updated November 28, 2022. Accessed November 30, 2022.
10. Part 56: institutional review boards. Code of Federal Regulations website. <https://www.ecfr.gov/current/title-21/chapter-I/subchapter-A/part-56>. Updated November 28, 2022. Accessed November 30, 2022.
11. Jeffers CD, Frye SA, Hoffman JM. SNMMI Clinical Trials Network research series for technologists: clinical research primer—regulatory process, part I: how and when radiopharmaceuticals can be used. *J Nucl Med Technol.* 2022;50:2–9.
12. Subpart A: basic HHS policy for protection of human research subjects. Code of Federal Regulations website. <https://www.ecfr.gov/current/title-45/part-46/subpart-A>. Updated November 28, 2022. Accessed November 30, 2022.
13. Subpart B: additional protections for pregnant women, human fetuses and neonates involved in research. Code of Federal Regulations website. <https://www.ecfr.gov/current/title-45/subtitle-A/subchapter-A/part-46/subpart-B>. Updated November 28, 2022. Accessed November 30, 2022.
14. Subpart C: additional protections pertaining to biomedical and behavioral research involving prisoners as subjects. Code of Federal Regulations website. <https://www.ecfr.gov/current/title-45/subtitle-A/subchapter-A/part-46/subpart-C>. Updated November 28, 2022. Accessed November 30, 2022.

15. Federal policy for the protection of human subjects ('common rule'). Department of Health and Human Services website. <https://www.hhs.gov/ohrp/regulations-and-policy/regulations/common-rule/index.html>. Updated November 28, 2022. Accessed November 30, 2022.
16. Revised common rule educational materials. Department of Health and Human Services website. <https://www.hhs.gov/ohrp/education-and-outreach/revised-common-rule/index.html>. Updated December 1, 2021. Accessed November 30, 2022.
17. Integrated addendum to ICH E6(R1): guideline for good clinical practice—E6(R2). ICH website. https://database.ich.org/sites/default/files/E6_R2_Addendum.pdf. Published November 9, 2016. Accessed November 30, 2022.
18. Part 312.50: general responsibilities of sponsors. Code of Federal Regulations website. <https://www.ecfr.gov/current/title-21/chapter-I/subchapter-D/part-312/subpart-D/section-312.50>. Updated November 28, 2022. Accessed November 30, 2022.
19. Part 312.52: transfer of obligations to a contract research organization. Code of Federal Regulations website. <https://www.ecfr.gov/current/title-21/chapter-I/subchapter-D/part-312/subpart-D/section-312.52>. Updated November 28, 2022. Accessed November 30, 2022.
20. Part 312.3: definitions and interpretations. Code of Federal Regulations website. <https://www.ecfr.gov/current/title-21/chapter-I/subchapter-D/part-312/subpart-A/section-312.3>. Updated November 28, 2022. Accessed November 30, 2022.
21. Part 312.61: control of investigational drug. Code of Federal Regulations website. <https://www.ecfr.gov/current/title-21/chapter-I/subchapter-D/part-312/subpart-D/section-312.61>. Updated November 28, 2022. Accessed November 30, 2022.
22. Part 312.62: investigator recordkeeping and record retention. Code of Federal Regulations website. <https://www.ecfr.gov/current/title-21/chapter-I/subchapter-D/part-312/subpart-D/section-312.62>. Updated November 28, 2022. Accessed November 30, 2022.
23. Part 50.20: general requirements for informed consent. Code of Federal Regulations website. <https://www.ecfr.gov/current/title-21/chapter-I/subchapter-A/part-50/subpart-B/section-50.20>. Updated November 28, 2022. Accessed November 30, 2022.
24. Clinical research coordinator roles and responsibilities. Washington University in St. Louis website. <https://research.wustl.edu/about/roles-responsibilities/clinical-research-coordinator/>. Published 2007. Updated January 2009. Accessed November 30, 2022.
25. Conduct of clinical trials of medical products during the COVID-19 public health emergency: guidance for industry, investigators, and institutional review boards. Food and Drug Administration website. <https://www.fda.gov/media/136238/download>. Published March 2020. Updated August 2021. Accessed November 30, 2022.
26. Jeffers CD, Hoffman JM. SNMMI Clinical Trials Network research series for technologists: clinical research primer—regulatory process, part II: the role of the Institutional Review Board in Food and Drug Administration-regulated radiopharmaceutical research. *J Nucl Med Technol*. 2022;50:97–102.
27. Statement of investigator [form FDA 1572]. Food and Drug Administration website. <https://www.fda.gov/media/71816/download>. Accessed November 30, 2022.
28. Part 312.53: selecting investigators and monitors. Code of Federal Regulations website. <https://www.ecfr.gov/current/title-21/chapter-I/subchapter-D/part-312/subpart-D/section-312.53>. Updated November 28, 2022. Accessed November 30, 2022.
29. Trembath L, Opanowski A. Clinical trials in molecular imaging: the importance of following the protocol. *J Nucl Med Technol*. 2011;39:63–69.
30. Clinical trial imaging endpoint process standards guidance for industry. Food and Drug Administration website. <https://www.fda.gov/regulatory-information/search-fda-guidance-documents/clinical-trial-imaging-endpoint-process-standards-guidance-industry>. Published April 2018. Updated May 6, 2020. Accessed November 30, 2022.
31. Part 312.55: informing investigators. Code of Federal Regulations website. <https://www.ecfr.gov/current/title-21/chapter-I/subchapter-D/part-312/subpart-D/section-312.55>. Updated November 28, 2022. Accessed November 30, 2022.
32. Trembath L. Clinical research. In: Waterstram-Rich K, Gilmore D, eds. *Nuclear Medicine and PET/CT Technology and Techniques*. Elsevier; 2017:201–206.
33. Informed consent for clinical trials. Food and Drug Administration website. <https://www.fda.gov/patients/clinical-trials-what-patients-need-know/informed-consent-clinical-trials>. Updated January 4, 2018. Accessed November 30, 2022.
34. Tool summary sheet. National Center for Complementary and Integrative Health website. https://view.officeapps.live.com/op/view.aspx?src=https%3A%2F%2Ffiles.nccih.nih.gov%2Fs3fs-public%2FCR-Toolbox%2FDelegation_of_Authority_Log_ver2_07-17-2015.docx&wdOrigin=BROWSELINK. Published April 24, 2013. Accessed November 30, 2022.
35. Investigator responsibilities: safety reporting for investigational drugs and devices—guidance for industry. Food and Drug Administration website. <https://www.fda.gov/media/152530/download>. Published September 2021. Accessed November 30, 2022.

V/Q SPECT and SPECT/CT in Pulmonary Embolism

Geoffrey M. Currie¹ and Dale L. Bailey²

¹Charles Sturt University, Wagga Wagga, New South Wales, Australia, and Baylor College of Medicine, Houston, Texas; and ²Royal North Shore Hospital and University of Sydney, Sydney, New South Wales, Australia

CE credit: For CE credit, you can access the test for this article, as well as additional JNMT CE tests, online at <https://www.snmlearningcenter.org>. Complete the test online no later than March 2026. Your online test will be scored immediately. You may make 3 attempts to pass the test and must answer 80% of the questions correctly to receive 1.0 CEH (Continuing Education Hour) credit. SNMMI members will have their CEH credit added to their VOICE transcript automatically; nonmembers will be able to print out a CE certificate upon successfully completing the test. The online test is free to SNMMI members; nonmembers must pay \$15.00 by credit card when logging onto the website to take the test.

Ventilation and perfusion (V/Q) lung scintigraphy has been used in the assessment of patients with suspected pulmonary embolism for more than 50 y. Advances in imaging technology make SPECT and SPECT/CT feasible. This article will examine the application and technical considerations associated with performing 3-dimensional V/Q SPECT and the contribution of a coacquired CT scan. The literature tends to be mixed and contradictory in terms of appropriate investigation algorithms for pulmonary embolism. V/Q SPECT and SPECT/CT offer significant advantages over planar V/Q, with or without the advantages of Technegas ventilation, and if available should be the preferred option in the evaluation of patients with suspected pulmonary embolism.

Key Words: lung imaging; V/Q; SPECT; SPECT/CT; CTPA

J Nucl Med Technol 2023; 51:9–15

DOI: 10.2967/jnmt.122.264880

Although ventilation and perfusion (V/Q) lung scintigraphy has been used in the assessment of patients with suspected pulmonary embolism for more than 50 y, there have been advances in imaging technology to provide superior resolution and sensitivity, SPECT techniques, and SPECT/CT hybrid imaging. Advances in ventilation agents, Technegas (Cyclomedica) in particular, have contributed to assimilation to SPECT and SPECT/CT protocols. Technegas was developed in Australia in 1984 (1), and Chris McLaren, an Australian pioneer nuclear medicine technologist, was part of the team evaluating its original clinical application. Unlike radioaerosols, Technegas does not redistribute after administration, a requirement for any prolonged tomographic acquisition (such as SPECT). McLaren appears to be the first (in 1987) to recognize the potential not only for performing SPECT V/Q lung scanning but also for computerized subtraction of SPECT data to map and quantify potential perfusion defects (2).

His approach highlighted the major issue associated with the fact that both phases use ^{99m}Tc in a single-day protocol and provided a solution: “A useful spin-off from the subtraction technique is that ‘true’ perfusion images are obtainable” (2).

This discussion will not examine the broader debate on the role and application of V/Q imaging or the merits of Technegas; these have been detailed widely elsewhere. The discussion will explore the application and technical considerations associated with performing the entire V/Q protocol as 3-dimensional SPECT imaging and the addition of a coacquired CT scan.

This article aims to both challenge and inform readers on the role of SPECT and SPECT/CT. The original perspective for the article focused on the added value of technologic innovation that not only makes planar imaging redundant but also makes SPECT a requisite. Drawing a comparison to the omission of SPECT from the armamentarium of myocardial perfusion, skeletal or cerebral perfusion imaging was thought to highlight the importance of SPECT in lung scanning. Challenging readers to consider the appropriateness of a clinical department that performs planar cerebral perfusion imaging, myocardial perfusion or spine imaging was initially thought analogous to a department performing only planar lung scanning. Although provocative, the challenge was not intended to be critical or insulting. Nonetheless, the optics changed with the realization that there are additional factors that might influence the decision to use SPECT or SPECT/CT in lung scanning. Not the least of these factors is the excellent positive and negative predictive value for planar V/Q. This feature of V/Q is challenged when single-day, ^{99m}Tc-based ventilation and perfusion imaging is undertaken, especially when the ratio of count rate differences is not met. To further clarify, an informal poll was posted for 24 h by 2 separate nuclear medicine technologist groups: one comprising predominantly members from the United States and another comprising predominantly Australian members (Table 1). Although not expected to be quantitatively representative of either population, the insights did provide a snapshot with generalizability of findings. The stark contrast in results, with 67% of respondents from the United States indicating they performed planar-only studies, compared with just 3% of Australian sites, is thought to reflect, in part, the greater suitability of

Received Sep. 2, 2022; revision accepted Dec. 21, 2022.
For correspondence or reprints, contact Geoffrey M. Currie (gcurrie@csu.edu.au).

Published online Jan. 4, 2023.

COPYRIGHT © 2023 by the Society of Nuclear Medicine and Molecular Imaging.

TABLE 1
Summary of Results of 24-Hour Social Media Poll
Conducted August 22, 2022

Imaging type	United States (%) (n = 222)	Australia (%) (n = 154)
Planar only	66.7	3.2
Planar and SPECT	2.7	1.9
SPECT only with planar generated from SPECT	11.3	27.3
Planar and SPECT/CT	12.6	3.9
SPECT/CT only with planar generated from SPECT	5.4	61.1
SPECT/CT only	1.4	2.6

Technegas for SPECT than ^{81m}Kr , ^{133}Xe , or ^{99m}Tc aerosol ventilation studies. As previously outlined (3), Technegas is considered the preferred ventilation method in more than 60 countries, including Australia, yet has limited adoption in the United States. Indeed, several additional comments by U.S. respondents indicated that poor ventilation SPECT is a barrier whereas omission of the ventilation scan in favor of CT for patients during the COVID era is a driver for SPECT/CT. Conversely, the principal discussion among the Australian respondents was related to advanced SPECT/CT techniques using breath-hold approaches and justification of base to apex against radiographer-preferred apex to base protocols. The impending approval of Technegas by the Food and Drug Administration in the United States may change that landscape and, therefore, demands a detailed discussion of the advances that allow the entire V/Q protocol to move to 3-dimensional SPECT or SPECT/CT imaging.

THE V/Q TEST

Although pulmonary embolism is the principal pathology of interest in V/Q lung scanning, it is not the only application investigated with the V/Q scan. The basic premise in pulmonary embolism is the mismatch scan, in which a perfusion deficit is accompanied by normal ventilation. The V/Q mismatch, however, can be caused by pathology other than pulmonary embolism, and not all pulmonary emboli produce a mismatch (4). Acute pulmonary embolism may partially resolve (diminishing the perfusion defect) or may progress to infarction, which produces a matching V/Q defect (4). Traditionally, the chest radiograph was used to improve the accuracy of the V/Q scan and to identify those patients more suited to CT pulmonary angiography (CTPA). The use of SPECT V/Q independently improves V/Q accuracy and, when combined with CT, produces coregistration with anatomic detail superior to that of chest radiographs. The possibility of combining SPECT with CTPA creates an additional layer of insight that demands attention. The potential redundancy of the chest radiograph and the ventilation scan warrant consideration with the emergence of lung V/Q SPECT/CT and V/Q SPECT/CTPA.

Planar V/Q has several challenges. First, perfusion defects are segmental or subsegmental, often with overlap of segments

using 2-dimensional planar imaging. As a result, identification of specific defect localization or segments is difficult (5). Second, the overlap of tissues using 2-dimensional images means that a perfusion defect may have events superimposed from over- or underlying normally perfused lung tissue. This shine-through can confound perfusion defect detection and interpretation (5). For example, a small subsegmental defect may have sufficient superimposed counts to go undetected or the perfusion deficit may be underestimated for a larger defect. Third, the shine-through of ventilation data in the perfusion data can also confound perfusion defect detection and interpretation. The count rate difference between ^{99m}Tc -based ventilation and the subsequent ^{99m}Tc -based perfusion study is ideally a minimum of 7 times higher perfusion counts, with 4 times being an absolute minimum. This is seldom actually confirmed before imaging or reporting and has the same implications as anatomic shine-through either globally or, particularly for aerosol studies that can produce airway deposition at the branching of the airways, focally. Next, there are variable approaches to ventilation that directly impact the interpretability of the studies and the proportion of indeterminate studies. Availability of Technegas as the preferred method is not universal, which also influences the lack of universality of interpretation criteria. Adoption of Technegas could use a same-day protocol with ventilation followed by perfusion and this protocol comes with the potential “shine-through” (Fig. 1) issues discussed above. Alternatively, a two-day protocol with perfusion first and the ventilation only performed on abnormal perfusion studies could be adopted. The latter approach has been revisited during the 2019 coronavirus disease pandemic because of concerns about aerosols and disease transmission. It may also reduce the radiation dose for some patients (normal perfusion) and eliminate ventilation shine-through on the perfusion study but delays confirmatory diagnosis by 24 h in an emergency.

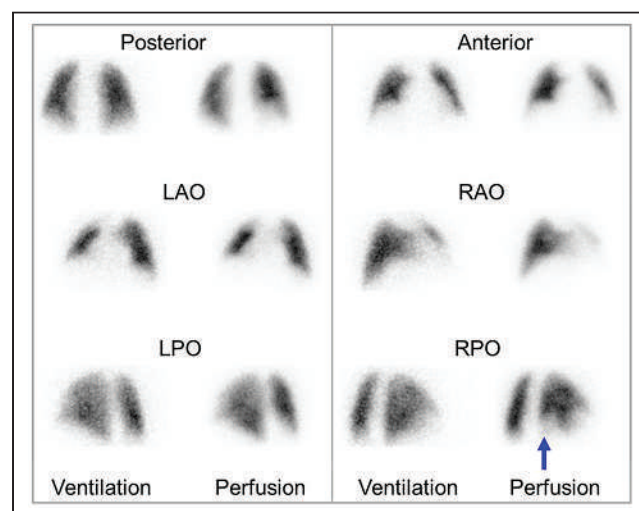


FIGURE 1. Planar V/Q scan with single mismatched perfusion defect (arrow) suggestive of intermediate probability of pulmonary embolism. LAO = left anterior oblique; LPO = left posterior oblique; RAP = right anterior oblique; RPO = right posterior oblique. (Reprinted from (5).)

Finally, the interpretation criteria generally used are not fit for the purpose and have largely migrated from probabilistic approaches to categoric classification.

Despite significant advances in the technology associated with nuclear medicine imaging, planar V/Q imaging has not evolved since the mid-1980s despite the application of advanced technology and associated protocol modifications to most other long-standing procedures. The arguments against SPECT V/Q adoption are largely the same confronting the transition to SPECT and gated SPECT myocardial perfusion. Transitioning to Technegas might be analogous to displacement of ^{201}Tl by $^{99\text{m}}\text{Tc}$ -based agents for myocardial perfusion. The additional time required for acquisition of both planar and SPECT acquisitions during the learning phase of SPECT adoption is shared between V/Q and myocardial perfusion, although several authors have shown how to produce adequate pseudo-planar images from the SPECT data. The invested experience in planar interpretation and associated new learning are common reasons to avoid the transition to SPECT previously cited for the myocardial perfusion SPECT transition. Although transition to Technegas confronts regulatory hurdles in the United States, perhaps the only barrier elsewhere to the adoption of SPECT V/Q is the net benefit given that planar V/Q has high accuracy and that the incremental benefit of SPECT is much smaller than that of myocardial perfusion imaging.

Regardless of the $^{99\text{m}}\text{Tc}$ ventilation method adopted (radio-aerosol or Technegas) or the imaging approach used (planar or SPECT), both the ventilation and the administration of the perfusion radiopharmaceutical should be performed with the patient supine to minimize the effects of gravitational gradients. The ventilation count rate should not exceed 1,000–1,500 per second; otherwise, the residual ventilation counts may reduce the detectability of perfusion defects. The Rose model associated with image contrast and object detection determined, mathematically, that human perception requires a signal-to-noise ratio of at least 5–7 (6). This conflicts with advice from the Society of Nuclear Medicine and Molecular Imaging guidelines (7) suggesting that a count rate of 3–4 times is adequate and that decreased contrast may lead to increased false-negative studies. With 100 MBq of $^{99\text{m}}\text{Tc}$ -macroaggregated albumin producing count rates of 2.3–5.0 per second (decreasing with increasing body mass index), a patient dose of 200–250 MBq of $^{99\text{m}}\text{Tc}$ -macroaggregated albumin is generally required. When ventilation has been efficient and produced higher count rates, a delay before the perfusion administration and acquisition should be used until count rates reduce to 1,000–1,500 per second. Increasing the administered dose beyond 250 MBq imposes not only a higher radiation dose to the patient but also a greater risk due to increased capillary blockade.

SPECT V/Q

SPECT and the associated 3-dimensional imaging overcomes many of the challenges of planar imaging. First, SPECT allows more accurate localization of segmental and

subsegmental perfusion defects. Second, SPECT eliminates over- and underlying tissues and the associated shine-through, which enhances defect detection and interpretation. Third, the ventilation study shine-through can be normalized and subtracted, and parametric approaches can be used (e.g., the V/Q ratio). All 3 of these factors enhance V/Q contrast and the ability to detect perfusion defects. Importantly, SPECT can improve the sensitivity, specificity, accuracy, and reproducibility of the V/Q study compared with planar imaging and can reduce the proportion of indeterminate studies (Table 2) (5). SPECT has been reported to increase detection of segmental perfusion defects by more than 10% and subsegmental perfusion defects by as much as 80% (Fig. 2) (8). Indeed, the advantages of SPECT V/Q over planar V/Q are so well established in the literature that SPECT V/Q is standard practice in many European and Latin American countries, Canada, and Australia. SPECT V/Q is also the preferred approach of the European Association of Nuclear Medicine (9), whereas the Society of Nuclear Medicine and Molecular Imaging guidelines indicate that, except in patients with complex comorbidities, planar V/Q remains preferred in the United States (10). This view reflects lack of access to a suitable ventilation agent at present and may change in the future. One should keep in mind, however, that simultaneous V/Q imaging with continuous tidal breathing using $^{81\text{m}}\text{Kr}$ for ventilation has been widely reported as providing high-quality V/Q SPECT studies.

SPECT acquisition protocols should include 120–128 projections using a dual-detector γ -camera over 360° with a 128×128 matrix and high-resolution collimation. The ventilation study is typically 10–12 s per projection (but can be 15–20 s), whereas the higher-count perfusion study is typically 8–10 s per projection (but can be 12–15 s). For a single-day V/Q scan, the patient should be positioned supine with arms hyperextended above the head and an injection line in place in either arm. On completion of the ventilation SPECT, without the patient moving, the $^{99\text{m}}\text{Tc}$ -macroaggregated albumin should be administered and perfusion SPECT commenced. For convenience, protocols can be established to perform dual SPECT studies using the same orbit parameters, with the ventilation rotating clockwise and then the perfusion simply rotating back counter-clockwise. The SPECT images should be reconstructed using an iterative algorithm, typically ordered-subset expectation maximization. The images can be used to produce planar imaging-equivalent images from the dataset. One approach is to sum several projections from either side of the required view (anterior, for example, would be projection 1 summed with projections 2, 3, 119, and 120) (11). A better approach is to reproject the SPECT data with an associated attenuation map (12). More commonly, however, the SPECT data provides the insights required and the extracted planar data are not required or produced. The ordered-subset expectation maximization parameters depend on the acquisition parameters and total counts per pixel; however, 8 subsets and 4 iterations with a low-pass filter are typical, with a 3- to

TABLE 2
Characteristics Enhanced by SPECT over Planar Imaging for V/Q Scan

Parameter	Planar	V/Q SPECT	V/Q SPECT/CT	CTPA	Q/CT	Source
Sensitivity	85%	100%	—	—	—	20
	76%	97%	—	—	—	8
	—	97%	97%	68%	93%	21
	—	97%	—	86%	—	22
	—	—	—	83%	—	23
Specificity	87%	91%	100%	—	100%	13
	High	Very high	High	Moderate	Very high	5,24
	100%	95%	—	—	—	20
	78%	96%	—	—	—	25
	85%	91%	—	—	—	8
	—	88%	100%	100%	51%	21
	—	91%	—	98%	—	22
	—	—	—	96%	—	23
	40%	56%	98%	—	52%	13
	Moderate	High	Very high	Very high	Low	5,24
Other findings	Uncommon	Uncommon	Often	Often	Often	5,24
Radiation dose	Low	Low	High	Very high	High	5,24
Technical issues	Rare	Rare	Uncommon	Often	Uncommon	5,24
Availability	During hours*	During hours*	During hours*	During and after hours	—	5,24
Adverse effects	No	No	No	Yes	No	5,24

*Availability after hours is possible in some nuclear medicine departments.

4-mm slice thickness. SPECT V/Q data should be displayed after simultaneous reconstruction as V/Q pairs sequentially for each projection (Fig. 3). Representative slices can be extracted to correlate with parametric images (Fig. 4).

SPECT/CT V/Q

The low-dose CT scan acquired with SPECT reduces the radiation dose to the patient compared with a diagnostic

CT scan. When used in conjunction with V/Q, SPECT provides attenuation correction, localization, and additional insight into vascular, parenchymal, and pleural abnormalities (4). For example, low-dose CT provides richer detail than chest radiography in identifying hypoperfused lung (Westermarck sign), pulmonary artery enlargement (Palla sign and Fleishner sign), or pulmonary artery tapering (knuckle sign) that may support a diagnosis of pulmonary embolism (Fig. 5). Conversely, opacities more consistent with pathologies that cause a matched V/Q defect (Fig. 6) and, thus, less likely to represent pulmonary embolism can also be identified on low-dose CT (e.g., consolidation, bullae, atelectasis, interstitial disease, or space-occupying lesions). The combination of SPECT/CT in the evaluation of pulmonary emboli may reduce the false-positive rate, improving specificity (4). Although it seems intuitive that CT may make the ventilation study redundant, evidence suggests that the ventilation study substantially improves test specificity over perfusion SPECT/CT alone (13).

For simple attenuation correction, low-dose CT parameters might include 120 kV_p, 10 mAs per slice, and a pitch of 1.0–1.5 to produce an additional radiation dose of less than 1 mSv. More typically and of greater value is a low-dose CT scan for coregistration and

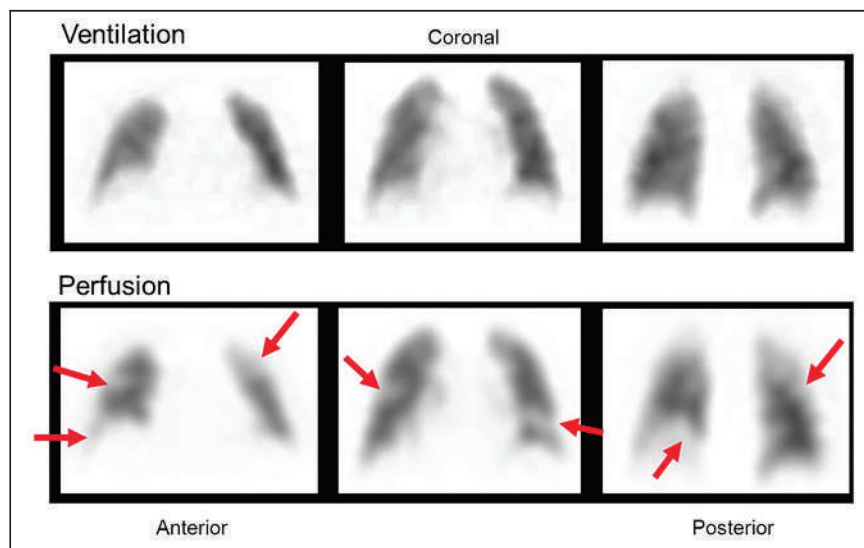


FIGURE 2. For same patient study as outlined in Figure 1, planar V/Q scan after SPECT with representative slices demonstrating multiple defects (arrows), indicating more widespread pulmonary emboli. (Reprinted from (5).)



FIGURE 3. Slice-by-slice V/Q pairs for SPECT data with arrows highlighting mismatch defect typical of pulmonary embolism. (Reprinted from (26).)

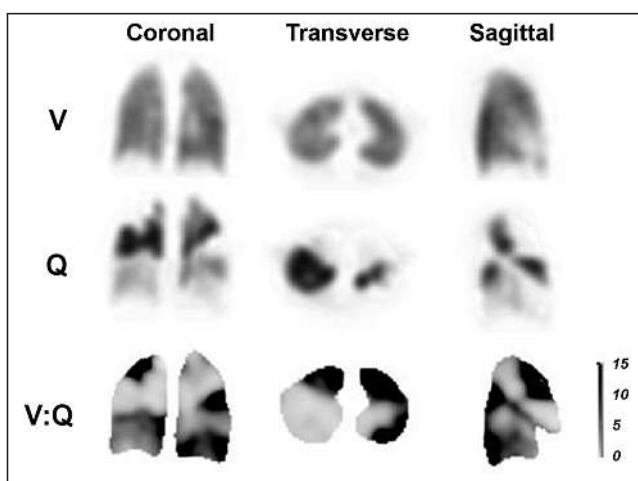


FIGURE 4. Representative slices for ventilation (top), perfusion (middle), and parametric V:Q ratio images (bottom), with positive segments for pulmonary embolism denoted by darker shading on parametric images. (Reprinted with permission of (27).)

mapping of anatomic information. This low-dose CT scan produces a higher dose of 2–3 mSv using 80–120 kV_p, 20 mAs per slice, a 512 × 512 matrix, and a pitch of 0.8 (14). Specific parameters and doses will vary depending on the CT system used. The V/Q SPECT scan alone is typically 2 mSv (4). A full diagnostic CT scan without contrast medium may also be performed using 100–140 kV_p, 130–200 mAs per slice, a 512 × 512 matrix, and a pitch of 0.9, producing a dose of 3–8 mSv (15). Although not feasible for the SPECT phases, a mid-inspiration breath-hold should be used for the CT, with imaging adjusted to base to apex rather than the traditional apex to base to minimize coregistration artifacts. In the absence of a mid-inspiration breath-hold for the CT scan, shallow, continuous breathing can be used (4).

SPECT/CT V/Q AND CTPA

It is possible to combine SPECT and CTPA studies using software fusion, and although this adds insight, it also adds

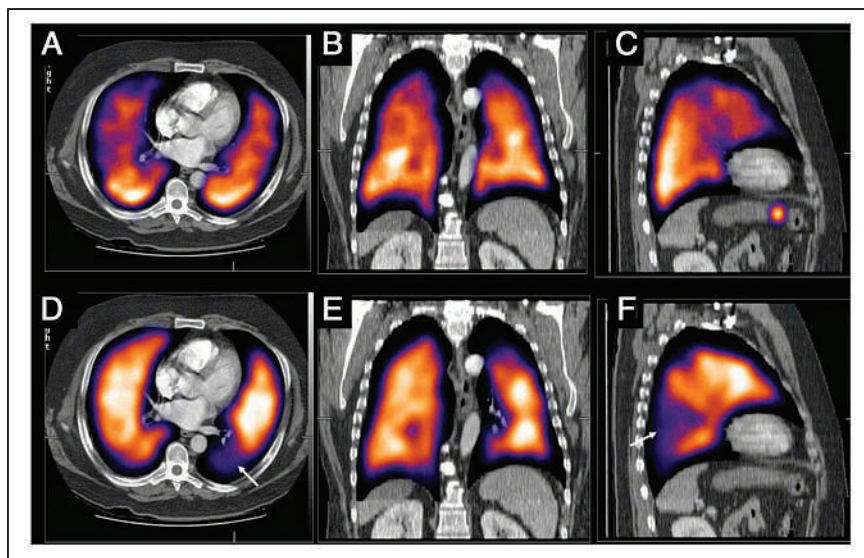


FIGURE 5. Representative SPECT/CT images of lung ventilation (top) and perfusion (bottom) demonstrating segmental perfusion defect (arrow in D and F) in left lower lobe with no CT opacity or matched ventilation defect consistent with pulmonary embolism. (Reprinted from (3).)

radiation exposure and confronts registration errors. Hybrid technology allows SPECT/CT and SPECT/CTPA to be performed with hardware fusion that overcomes the registration errors of software fusion (Fig. 7). The value of SPECT/CTPA is the combination of the highly sensitive perfusion map with the highly specific angiographic map to enhance

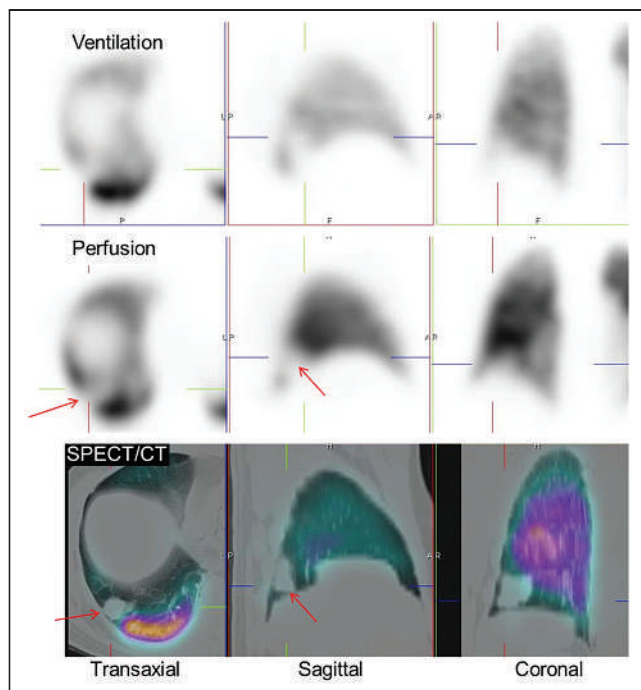


FIGURE 6. Fusion of SPECT and low-dose CT showing opacity (arrows) on CT corresponding to perfusion defect producing matching defect consistent with lung metastases. (Reprinted from (5).)

diagnostic efficacy. In most patients, despite the feasibility of SPECT/CTPA in a single session, both procedures are usually neither required nor justified.

CTPA might be performed using 80–120 kV_p, 150–200 mAs per slice, a 512 × 512 matrix, and a pitch of 0.9 with 80 mL of iodine contrast medium using bolus tracking and a deep-inspiration breath hold producing a dose upward of 8–20 mSv (14,16). A key concern for CTPA is the adverse effects from the contrast medium, the risk of nephropathy, and the high radiation dose. These factors preclude justification of CTPA in premenopausal women, pregnant women, patients with renal dysfunction or diabetes, and patients taking some types of medications. The breast radiation dose during CTPA is a significant issue that perhaps does not get enough attention.

The breast dose from CTPA ranges from 10 to 70 mSv—equivalent to as many as 25 mammograms or 400 chest radiographs, which substantially increases the lifetime risk of developing breast cancer (16).

Although adverse reactions to iodinated contrast medium have been reduced with the introduction of nonionic, low-osmolality contrast media, there remains a 3% adverse reaction rate with a 1 in 170,000 fatality rate (17). Acute kidney injury and contrast-induced nephropathy are of particular concern, with as many of 3% of contrast administrations resulting in contrast-induced nephropathy (16). Generally, contrast-induced nephropathy is evidenced by increased serum creatinine; however, these effects may not be noted until 2 d after contrast

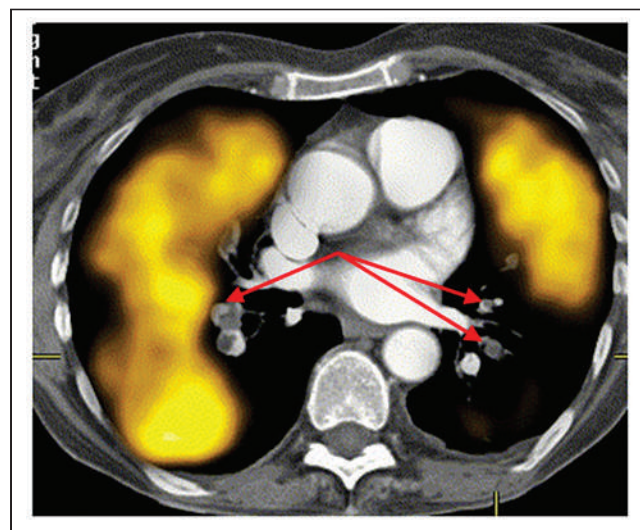


FIGURE 7. Fused perfusion SPECT and CTPA showing pulmonary emboli (arrows) bilaterally in arteries with associated perfusion defects on SPECT. (Reprinted with permission of (4).)

administration, peaking at 4 d after the scan and returning to baseline after 1–3 wk later (18). It is likely that in many patients with contrast-induced nephropathy, it goes undetected, and consequently, the incidence is probably underestimated. Although the risk factors for contrast-induced nephrotoxicity are well documented (e.g., renal dysfunction, diabetes, and congestive heart failure), there is a paucity of literature outlining the longer-term effects of contrast media on renal function or on the confounding effects of contrast media on medications that increase the risk of renal toxicity (e.g., the triple whammy of a concurrent diuretic, angiotensin-converting enzyme inhibitor, or angiotensin receptor blocker and a nonsteroidal antiinflammatory drug added to the risk of the contrast medium). As a general rule, an effective glomerular filtration rate below 30 mL/min/1.73 m² estimated from serum creatinine levels is a relative contraindication to contrast medium (17,19). Contrast-induced nephropathy increases in incidence from 3% in normal renal function (>60 mL/min/1.73 m²) to 12%–27% in renal dysfunction to 50% in diabetic nephropathy (17). Indeed, concurrent use of metformin with chronic renal insufficiency and intravenous iodinated contrast medium is associated with a 50% mortality rate (17,19).

CONCLUSION

The literature tends to be mixed and contradictory in terms of appropriate investigation algorithms for pulmonary embolism. This may reflect political, health, economic, or professional preference-based factors. The European Association of Nuclear Medicine provides an evidence-based diagnostic algorithm that serves as an excellent resource (9). The Society of Nuclear Medicine and Molecular Imaging guidelines (7) require updating to reflect the advances discussed. For the patient presenting with suspected acute pulmonary embolism, if V/Q SPECT is available, that is the preferred approach. A positive scan result should direct treatment for pulmonary embolism, a negative scan result excludes pulmonary embolism, and a nondiagnostic SPECT result should be followed up with CTPA. When V/Q SPECT is not available, CTPA or planar V/Q should be used (9). V/Q SPECT and SPECT/CT offer significant advantages over planar V/Q with or without the advantages of Technegas ventilation.

DISCLOSURE

No potential conflict of interest relevant to this article was reported.

REFERENCES

- Burch WM, Sullivan PJ, McLaren C. Technegas: a new ventilation agent for lung scanning. *Nucl Med Commun*. 1986;7:865–871.
- McLaren CJ. Ventilation and perfusion lung tomography [abstract]. *Aust N Z J Med*. 1987;17(suppl 2):459.
- Currie GM, Bailey D. A technical overview of Technegas as a lung ventilation agent. *J Nucl Med Technol*. 2021;49:313–319.
- Roach PJ, Gradinscak DJ, Schembri GP, Bailey EA, Willowson KP, Bailey DL. SPECT/CT in V/Q scanning. *Semin Nucl Med*. 2010;40:455–466.
- Roach PJ, Schembri G, Bailey DL. V/Q scanning using SPECT and SPECT/CT. *J Nucl Med*. 2013;54:1588–1596.
- Rzeszutowski MS. Counting statistics. *Radiographics*. 1999;19:765–782.
- Parker JA, Coleman RE, Grady E, et al. SNM practice guideline for lung scintigraphy 4.0. *J Nucl Med Technol*. 2012;40:57–65.
- Reinartz P, Wildberger JE, Schaefer W, Nowak B, Mahnken AH, Buell U. Tomographic imaging in the diagnosis of pulmonary embolism: a comparison between V/Q lung scintigraphy in SPECT technique and multislice spiral CT. *J Nucl Med*. 2004;45:1501–1508.
- Bajc M, Schümichen C, Grüning T, et al. EANM guideline for ventilation/perfusion single-photon emission computed tomography (SPECT) for diagnosis of pulmonary embolism and beyond. *Eur J Nucl Med Mol Imaging*. 2019;46:2429–2451.
- Waxman AD, Bajc M, Brown M, et al. Appropriate use criteria for ventilation-perfusion imaging in pulmonary embolism: summary and excerpts. *J Nucl Med*. 2017;58(5):13N–15N.
- Reinartz P, Schirp U, Zimmy M, et al. Optimizing ventilation-perfusion lung scintigraphy: parting with planar imaging. *Nuklearmedizin*. 2001;40:38–43.
- Bailey DL, Schembri GP, Cooper RA, Bailey EA, Roach PJ. Reprojection of reconstructed V/Q SPECT scans to provide high count planar images [abstract]. *J Nucl Med*. 2005;46(suppl):337P.
- Thanuja M, Maimanah M, Sara U. Diagnosis of pulmonary embolism: a comparison between ventilation/perfusion SPECT/CT and perfusion-only SPECT/CT. *Med J Malaysia*. 2020;75:490–493.
- Bajc M. Potential of hybrid V/P SPECT: low dose CT in lung diagnostics. *Breathe (Sheff)*. 2012;9:49–60.
- Mortensen J, Gutte H. SPECT/CT and pulmonary embolism. *Eur J Nucl Med Mol Imaging*. 2014;41(suppl 1):S81–S90.
- Schembri GP, Miller A, Smart RC. Radiation dosimetry and safety issues in the investigation of pulmonary embolism. *Semin Nucl Med*. 2010;40:442–454.
- Currie G. *Pharmacology Primer for Nuclear Medicine and Medical imaging*. Society of Nuclear Medicine and Molecular Imaging; 2020:121–134.
- Kim IY, Lee SB, Lee DW, Song SH, Seong EY, Kwak IS. Long-term effect of radiocontrast-enhanced computed tomography on the renal function of chronic kidney disease patients. *Clin Exp Nephrol*. 2012;16:755–759.
- Currie GM. Pharmacology, part 5: CT and MRI contrast. *J Nucl Med Technol*. 2019;47:189–202.
- Bajc M, Olsson CG, Olsson B, Palmer J, Jonson B. Diagnostic evaluation of planar and tomographic ventilation/perfusion lung images in patients with suspected pulmonary emboli. *Clin Physiol Funct Imaging*. 2004;24:249–256.
- Gutte H, Mortensen J, Jensen CV, et al. Detection of pulmonary embolism with combined ventilation-perfusion SPECT and low-dose CT: head-to-head comparison with multidetector CT angiography. *J Nucl Med*. 2009;50:1987–1992.
- Reinartz P, Wildberger JE, Schaefer W, Nowak B, Mahnken AH, Buell U. Tomographic imaging in the diagnosis of pulmonary embolism: a comparison between V/Q lung scintigraphy in SPECT technique and multislice spiral CT. *J Nucl Med*. 2004;45:1501–1508.
- Stein PD, Fowler SE, Goodman LR, et al. Multidetector computed tomography for acute pulmonary embolism. *N Engl J Med*. 2006;354:2317–2327.
- Leblanc M, Paul N. V/Q SPECT and computed tomography pulmonary angiography. *Semin Nucl Med*. 2010;40:426–441.
- Collart JP, Roelants V, Vanpee D, et al. Is a lung perfusion scan obtained by using single photon emission computed tomography able to improve the radionuclide diagnosis of pulmonary embolism? *Nucl Med Commun*. 2002;23:1107–1113.
- Schaefer WM, Knollmann D, Meyer PT. V/Q SPECT/CT in the time of COVID-19: changing the order to improve safety without sacrificing accuracy. *J Nucl Med*. 2021;62:1022–1024.
- Roach PJ, Bailey DL, Harris BE. Enhancing lung scintigraphy with single-photon emission computed tomography. *Semin Nucl Med*. 2008;38:441–449.

Clinical Trials of Prostate-Specific Membrane Antigen Radiopharmaceutical Therapy

Hossein Jadvar and Patrick M. Colletti

Division of Nuclear Medicine, Department of Radiology, Keck School of Medicine, University of Southern California, Los Angeles, California

CE credit: For CE credit, you can access the test for this article, as well as additional *JNMT* CE tests, online at <https://www.snmlearningcenter.org>. Complete the test online no later than March 2026. Your online test will be scored immediately. You may make 3 attempts to pass the test and must answer 80% of the questions correctly to receive 1.0 CEH (Continuing Education Hour) credit. SNMMI members will have their CEH credit added to their VOICE transcript automatically; nonmembers will be able to print out a CE certificate upon successfully completing the test. The online test is free to SNMMI members; nonmembers must pay \$15.00 by credit card when logging onto the website to take the test.

Prostate-specific membrane antigen (PSMA) theranostics has been a momentous triumph for nuclear medicine. The recent approvals of PSMA-targeted imaging agents (^{68}Ga -PSMA-11, ^{18}F -DCFPyL) and radiopharmaceutical therapy (^{177}Lu -PSMA-617) have paved the way for theranostics as a viable care strategy for men with metastatic castration-resistant prostate cancer. The imaging clinical trials OSPREY, CONDOR, and those conducted at the University of California (Los Angeles and San Francisco), as well as the randomized phase 3 therapy trial VISION, have been the fruitful beginnings for PSMA theranostics. There are currently several ongoing clinical trials to expand the reach of PSMA theranostics to the earlier phases of prostate cancer and to optimize its utility in combination therapeutic regimens. We provide a brief narrative review of the many PSMA-directed radiopharmaceutical therapy clinical trials with the β -emitter ^{177}Lu -PSMA-617 and the α -emitter ^{225}Ac -PSMA-617 in prostate cancer.

Key Words: prostate; cancer; PET; radiopharmaceutical; therapy; VISION

J Nucl Med Technol 2023; 51:16–21

DOI: 10.2967/jnmt.122.264928

Radiopharmaceutical therapy (RPT) with radiolabeled agents targeted to the prostate-specific membrane antigen (PSMA) has provided an effective treatment strategy with manageable adverse events in men with metastatic castration-resistant prostate cancer (mCRPC). PSMA RPT is the therapeutic arm of the theranostics algorithm in which sufficient PSMA expression is first documented with imaging in accordance with the concept of precision oncology. The U.S. Food and Drug Administration approval of ^{68}Ga -PSMA-11 on December 1, 2020, was based on 2 comparable new-drug applications submitted by the University of California, Los Angeles, and the University of California, San Francisco.

The first commercial ^{18}F -labeled PSMA radiotracer, 2-(3-{1-carboxy-5-[(6- ^{18}F -fluoro-pyridine 3-carbonyl)-amino]-pentyl}-ureido)-pentanedioic acid (^{18}F -DCFPyL, also known as ^{18}F -piflufolastat or Pylarify [Lantheus]) was approved on May 27, 2021. Two kits (Ilucix [Telix Pharmaceuticals] and Locametz [Novartis]) for the preparation of ^{68}Ga -gozetotide (^{68}Ga -PSMA-11) were also approved—on December 20, 2021, and March 23, 2022, respectively. The approved indications are, first, for the imaging evaluation of men with suspected metastasis who are candidates for initial definitive therapy and, second, for suspected recurrence based on elevated serum prostate-specific antigen (PSA) levels. The Locametz kit is also approved for the selection of patients with mCRPC for whom the recently approved ^{177}Lu -vipivotide tetraxetan (Pluvicto [Novartis]) PSMA RPT is indicated. Moreover, the recent National Comprehensive Cancer Network guidelines for prostate cancer, version 4-2022, indicated that both ^{68}Ga -PSMA-11 and ^{18}F -piflufolastat PSMA PET imaging can be used to determine whether patients are eligible to receive ^{177}Lu -PSMA-617 RPT (1). Similar opinions have been expressed in a joint consensus statement by the European Association of Urology and the European Association of Nuclear Medicine (2). Over the past several years, the growing interest in PSMA RPT has ensured an increasing number of clinical trials in this clinical space using the β -emitting radiolabels ^{177}Lu -PSMA-617 and ^{177}Lu -PSMA-I&T (I&T stands for imaging and therapy) and, more recently, the α -emitting ^{225}Ac -PSMA-617 (3–6). The aim of this narrative review is to summarize some of the major PSMA-directed RPT clinical trials.

LUPPSMA

LuPSMA was a prospective single-center, single-arm, phase 2 clinical trial conducted in Australia that enrolled 30 men with mCRPC and progressive disease, of whom 28 had received chemotherapy (80% docetaxel, 47% cabazitaxel) and 25 had received second-generation antiandrogens (enzalutamide, abiraterone acetate, or both) (7). The men

Received Sep. 15, 2022; revision accepted Dec. 6, 2022.
For correspondence or reprints, contact Hossein Jadvar (jadvar@med.usc.edu).

Published online Jan. 4, 2023.

COPYRIGHT © 2023 by the Society of Nuclear Medicine and Molecular Imaging.

were screened with ^{68}Ga -PSMA-11 PET/CT to confirm high PSMA expression (a lesion SUV_{max} of at least 1.5 times the hepatic SUV_{mean}), and no ^{18}F -FDG-positive disease without sufficient PSMA expression. With these dual imaging criteria, 16% of the patients were excluded. The patients were also required to have sufficient renal (glomerular filtration rate > 40 mL/min), hepatic (albumin > 25 g/L), and bone marrow (hemoglobin > 90 g/L, neutrophils $> 1.5 \times 10^9/\text{L}$, platelets $> 75 \times 10^9/\text{L}$) function. The primary endpoint of the trial was PSA response rate according to the Prostate Cancer Clinical Trials Working Group (PCWG) 2 criteria, defined as a 50% or more PSA decline from baseline (PSA50) with confirmation 3–4 wk apart. Treatment toxicity was assessed according to the Common Terminology Criteria for Adverse Events, version 4.03. A mean ^{177}Lu -PSMA-617 dose of 7.5 GBq was administered per cycle (range, 4.4–8.7 GBq) for up to 4 cycles at 6-week intervals. The men received 1 (100%), 2 (93%), 3 (80%), or 4 (47%) therapy cycles. PSA50 was achieved in 57% of patients. The most common adverse event was grade 1 xerostomia, in 87% of patients, and grade 3–4 thrombocytopenia, in 13% of patients. There were no treatment-related deaths. The encouraging results of the LuPSMA trial paved the way for subsequent randomized controlled trials.

THERAP

TheraP was the first randomized study of ^{177}Lu -PSMA-617 RPT. It was an Australian multicenter, unmasked, randomized, phase 2 trial in the clinical setting of progressive mCRPC (prior docetaxel therapy with a rising serum PSA level according to the PCWG 3 criteria) that compared the safety and efficacy of Lu-PSMA-617 therapy in 98 men with the safety and efficacy of cabazitaxel chemotherapy in 85 men (NCT03392428) (8). The eligibility criteria for PET imaging were PSMA-positive disease with an SUV_{max} of at least 20 at a site of disease, an SUV_{max} of greater than 10 at all other measurable sites of metastatic disease, and no sites of metastatic disease with discordant ^{18}F -FDG-positive and PSMA-negative findings. On the basis of these imaging criteria, 10% and 18% of men were ineligible because of low metastasis PSMA uptake and discordant ^{18}F -FDG-positive disease, respectively. The primary endpoint was PSA50. The secondary endpoints were progression-free survival (interval from randomization to first evidence of PSA progression per the PCWG 3 criteria) and radiographic progression (RECIST 1.1 for CT and PCWG 3 criteria for bone lesions). ^{177}Lu -PSMA-617 RPT was more effective than cabazitaxel in terms of PSA50, which was observed in 66% of men in the ^{177}Lu -PSMA-617 group versus 44% in the cabazitaxel group. There was also less grade 3–4 toxicity in the ^{177}Lu -PSMA-617 group than in the cabazitaxel group (33% vs. 53%, respectively). Grade 1 or 2 xerostomia was observed in 61% of the patients in the ^{177}Lu -PSMA-617 RPT group only. No deaths were attributable to ^{177}Lu -PSMA-617 RPT. The trial concluded that ^{177}Lu -PSMA-617

may be a viable alternative to cabazitaxel in view of the enhanced efficacy and decreased toxicity of ^{177}Lu -PSMA-617 compared with cabazitaxel.

VISION

The multinational, randomized, phase 3 VISION trial was a pivotal milestone for nuclear medicine. The study design was similar to that of the ALSYMPCA randomized, phase 3 trial that led to the approval of ^{223}Ra -dichloride (Xofigo [Bayer]) for men with bone-dominant mCRPC. Men with mCRPC were randomized 2:1 to receive either ^{177}Lu -PSMA-11 (7.4 GBq [200 mCi] every 6 wk for 4 cycles, with an additional 2 cycles for total of 6 cycles at the discretion of treating physicians in responding patients, plus the best supportive care or the best standard of care [SOC]) or SOC only (NCT03511664) (9). The primary outcome measure was overall survival (OS). The secondary outcome measures were radiographic progression-free survival (rPFS) and time to first skeleton-related events. Eligible patients were those who had progressed on at least one taxane-based chemotherapy (41% were previously treated with 2 taxane regimens) and one or more androgen pathway inhibitors (abiraterone acetate, enzalutamide, darolutamide, or apalutamide). The best SOC did not permit additional chemotherapy (e.g., cabazitaxel), immunotherapy (e.g., pembrolizumab), or use of investigational drugs (e.g., olaparib). This decision was reasoned in view of lack of safety data on combination therapies and potential imbalance that may occur with variable additional treatments between the 2 study arms. However, additional androgen deprivation therapy, bone-health-directed therapy, or palliative radiation therapy were allowed at the discretion of the treating physician. The screening included imaging with contrast-enhanced diagnostic CT of the chest, abdomen, and pelvis; total-body bone scintigraphy; and ^{68}Ga -PSMA-11 PET/CT to confirm sufficient PSMA expression of at least 1 metastatic lesion (defined as uptake greater than that of liver parenchyma in lesions of any size in any organ system; no SUV cutoff threshold) and no PSMA-negative lesions (defined as uptake no higher than that of liver parenchyma in any lymph node with a short axis of at least 2.5 cm, in any solid-organ lesion with a short axis of at least 1.0 cm, or in any bone lesion with a soft-tissue component of at least 1.0 cm in the short axis). Patients with a superscan pattern on bone scintigraphy were excluded. With these imaging selection criteria, 12.6% of patients were excluded after PSMA PET/CT imaging. ^{18}F -FDG PET/CT was not performed. The imaging eligibility criteria that excluded ^{18}F -FDG PET/CT were an operational decision to reduce complexity, meet the basic needs for regulatory approval, avoid potential issues with reimbursement of 2 PET/CT scans, meet the requirement for devising a scheme for combined scan interpretation, and provide reasonable accommodations for patient and physician acceptance. The trial showed a 4.0-mo OS benefit, a 5.3-mo rPFS benefit, and a 4.3-mo benefit regarding the time to the first skeleton-related event with the experimental arm of

¹⁷⁷Lu-PSMA-617 plus best SOC over the best-SOC-only arm. The incidence of grade 3 or higher adverse events was higher in the experimental arm than in the control arm (52.7% vs. 38%, respectively), but quality of life was not adversely affected. No grade 3 or higher xerostomia was observed in the experimental arm. The OS benefit with ¹⁷⁷Lu-PSMA-617 plus SOC was at par with those previously reported with other nonradioactive drug regimens in the mCRPC clinical space. The favorable results of the VISION trial led to the Food and Drug Administration approval of Pluvicto on March 23, 2022. Despite the approval, the debate on the most optimal imaging selection criteria continues, as does the issue of the potential need for individualized dosimetry for improved outcome (10–16). Nevertheless, reports indicate a poor outcome in patients with low PSMA expression or discordant ¹⁸F-FDG-avid disease who are considered ineligible for ¹⁷⁷Lu-PSMA-617 treatment (17–19).

ENZAP

The goal of the ongoing open-label, randomized, stratified, 2-arm, multicenter, phase 2 EnzaP clinical trial is to investigate the safety and activity of adding ¹⁷⁷Lu-PSMA-617 RPT to enzalutamide (an androgen receptor antagonist) in patients with mCRPC not previously treated with chemotherapy (NCT04419402) (20). The trial is recruiting 160 participants over 12 mo and following them until 150 events occur (approximately another 18 mo). The randomization is 1:1 to either enzalutamide alone or enzalutamide plus ¹⁷⁷Lu-PSMA-617 RPT. The enzalutamide dose will be 160 mg per day orally (until there is no benefit or there is unacceptable toxicity). The ¹⁷⁷Lu-PSMA-617 will be given as an intravenous dose of 7.5 GBq ($\pm 10\%$) each for 4 doses on days 15, 57, 113, and 169. ⁶⁸Ga-PSMA-11 PET/CT is performed at mid cycle on day 92. Stratification factors will be study site, volume of disease (>20 vs. <20 disease sites on ⁶⁸Ga-PSMA-11 PET/CT), prior treatment with early docetaxel for castration-sensitive disease, and prior treatment with early abiraterone acetate (an androgen biosynthesis inhibitor) for castration-sensitive disease. Imaging exclusion criteria entail measurable metastatic lesions (>10 mm) that display an SUV_{max} of less than 10 on ⁶⁸Ga-PSMA-11 PET/CT. The primary outcome measure is PSA PFS. PSA progression is defined as a rise in PSA by at least 25% and at least 2 ng/mL above the nadir, which needs to be confirmed by a repeat PSA measurement 3 wk later. There are also several secondary outcome measures, including rPFS, PSA response rate, and others.

PSMAFORE

The purpose of the ongoing open-label, multicenter, 1:1 randomized, phase 3 PSMAFore clinical trial (NCT04689828) is to compare ¹⁷⁷Lu-PSMA-617 (7.4 GBq intravenously every 6 wk for 6 cycles) versus a change in androgen receptor-directed therapy in taxane-naïve patients with progressive mCRPC (21). The best supportive care is allowed in both study arms. The primary outcome measure is rPFS according

to the PCWG 3–modified RECIST 1.1. OS is a key secondary endpoint. PSMA expression is confirmed with ⁶⁸Ga-PSMA-11 PET/CT. The estimated enrollment is 450 participants.

PSMADDITION

PSMAddition (NCT04720157) is an ongoing international, prospective, open-label, 1:1 randomized, phase 3 trial comparing the safety and efficacy of ¹⁷⁷Lu-PSMA-617 (7.4 GBq intravenously every 6 wk for up to 6 cycles) plus SOC versus SOC alone in men with metastatic castration-sensitive prostate cancer (22). SOC is defined as androgen receptor pathway inhibitors and androgen deprivation therapy. Docetaxel is not allowed. Eligible patients are treatment-naïve or minimally treated hormonal therapy candidates with PSMA-positive disease on ⁶⁸Ga-PSMA-11 PET/CT. Patients with rapidly progressing tumors who require chemotherapy are excluded. The approximate cohort will be 1,126 patients. rPFS is the primary endpoint.

UPFRONTPSMA

UPFrontPSMA is an ongoing open-label, multicenter Australian, 1:1 randomized, phase 2 clinical trial comparing the efficacy of ¹⁷⁷Lu-PSMA-617 (7.5 GBq intravenously every 6 wk for 2 cycles) followed 6 wk later by docetaxel chemotherapy (75 mg/m² every 3 wk for 6 cycles) versus docetaxel chemotherapy in patients with newly diagnosed high-volume (4 or more bone metastases with 1 or more bone lesion outside the axial skeleton, or visceral metastases) metastatic castration-sensitive prostate cancer (NCT04343885) (23). All patients also receive continuous androgen-deprivation therapy, and up to 4 wk of androgen-deprivation therapy are permitted before commencement of screening. PSMA expression is confirmed with ⁶⁸Ga-PSMA-11 PET/CT with no major discordance on ¹⁸F-FDG PET/CT (defined as ¹⁸F-FDG-positive disease with minimal PSMA expression in more than 5 sites or more than 50% of total disease volume). The primary endpoint is undetectable PSA (<0.2 ng/mL) at 12 mo. There are also several secondary and exploratory endpoints. The planned cohort is 140 participants.

SPLASH

SPLASH is an ongoing multicenter, open-label, phase 3 clinical trial evaluating the efficacy of ¹⁷⁷Lu-PNT2002 (¹⁷⁷Lu-PSMA I&T) in men with progressive mCRPC after androgen receptor pathway inhibitor therapy (NCT04647526) (24). In the dosimetry phase, 25 patients will receive up to 4 cycles of ¹⁷⁷Lu-PNT2002, 6.8 GBq intravenously, every 8 wk. In the randomization phase, about 390 patients will be randomized 2:1 to receive either ¹⁷⁷Lu-PNT2002 ($n = 260$) or androgen receptor pathway inhibitor therapy (enzalutamide or abiraterone acetate, with prednisone or dexamethasone; $n = 130$). The primary endpoint is rPFS as assessed by RECIST 1.1. and PCWG 3 criteria. Crossover of patients progressing on the androgen receptor pathway inhibitor therapy arm to the ¹⁷⁷Lu-PNT2002 therapy arm is allowed. Sufficient

TABLE 1
Clinical Trials of PSMA RPT

Trial	Year	Subjects (n)	Location	Description	Diagnostic agent	Therapeutic agent	Clinical phase	Outcome	Comments
LuPSMA (7)	2018	30	Australia	Prospective phase 2, single-center, single-arm trial	⁶⁸ Ga, no ¹⁸ F-FDG+	¹⁷⁷ Lu	mCRPC	PSA50 achieved by 57%	Grade 1 xerostomia in 87% and grade 3–4 thrombocytopenia in 13%
TheraP (8), NCT03392428	2021	35	Australia	Randomized phase 2 trial	⁶⁸ Ga, no ¹⁸ F-FDG+	¹⁷⁷ Lu	mCRPC	¹⁷⁷ Lu-PSMA more effective than cabazitaxel	RPT with less grade 3–4 toxicity (33%) than cabazitaxel (53%); RPT with 61% grade 1–2 xerostomia
VISION (9), NCT03511664	2022	831	International	Open-label, 2:1 randomized, phase 3 trial of ¹⁷⁷ Lu-PSMA + SOC vs. SOC; previously treated with at least 1 ARPI and taxane	⁶⁸ Ga	¹⁷⁷ Lu	mCRPC	PFS (median, 8.7 vs. 3.4 mo); OS (median, 15.3 vs. 11.3 mo)	Adverse events of grade ≥ 3 higher with ¹⁷⁷ Lu-PSMA than without (52.7% vs. 38.0%)
EnzaP (20), NCT04419402	2020	160	Australia	Open-label, 1:1 randomized, phase 2 trial of ENZ alone or ENZ + ¹⁷⁷ Lu-PSMA	⁶⁸ Ga	¹⁷⁷ Lu	mCRPC	PSA PFS	Ongoing prospective trial
PSMAFore (21), NCT04689828	2022	Estimation: 450	International	Open-label, phase 3, multicenter trial	⁶⁸ Ga	¹⁷⁷ Lu	mCRPC	rPFS	Ongoing prospective trial
PSMAAddition (22), NCT04720157	2022	Estimation: 1,126	International	Open-label, phase 3, 1:1 randomized trial of RPT + SOC vs. SOC	⁶⁸ Ga	¹⁷⁷ Lu	mCSPC	rPFS	Ongoing prospective trial
UPFrontPSMA (23), NCT04343885	2021	Estimation: 140	Australia	Open-label, multicenter, phase 2, 1:1 randomized trial of RPT + DTX vs. DTX	⁶⁸ Ga	¹⁷⁷ Lu	mCSPC	Undetectable PSA at 1 y	Ongoing prospective trial
SPLASH (24), NCT04647526	2021	Estimation: 260	International	Open-label, multicenter, phase 3 trial	⁶⁸ Ga or ¹⁸ F	¹⁷⁷ Lu	mCRPC	rPFS	Ongoing prospective trial
ECLIPSE (25), NCT05204927	2022	Estimation: 400	United States	Open-label, multicenter, phase 3 trial	⁶⁸ Ga or ¹⁸ F	¹⁷⁷ Lu	mCRPC	rPFS	Ongoing prospective trial
LuTectomy (26), NCT04430192	2021	20	Australia	Open-label, phase 1/2, nonrandomized trial of dosimetry, efficacy, safety of ¹⁷⁷ Lu-PSMA	⁶⁸ Ga	¹⁷⁷ Lu	High-risk prostate cancer	Absorbed radiation dose of prostate and metastatic lymph nodes	Ongoing prospective trial
PRINCE (27), NCT03658447	2022	37	Australia	Phase 1/2, safety and efficacy trial of RPT and programmed death 1 inhibitor	⁶⁸ Ga	¹⁷⁷ Lu	mCRPC	PSA50	Ongoing prospective trial
LuPARP (28), NCT03874884	2022	52	Australia	Phase 1 dose-escalation and dose-expansion trial	⁶⁸ Ga	¹⁷⁷ Lu	mCRPC	Primary outcomes: DLT, MTD, and RP2D	Ongoing prospective trial
TATCIIST (29), NCT05219500	2022	Estimation: 100	Texas	²²⁵ Ac-PSMA I&T	⁶⁸ Ga	²²⁵ Ac	mCRPC	PSA50	Ongoing prospective trial

¹⁷⁷Lu-PSMA = ¹⁷⁷Lu-PSMA-617; ARPI = androgen receptor pathway inhibitor; PFS = progression-free survival; ENZ = enzalutamide; DTX = docetaxel; DLT = dose-limiting toxicity; MTD = maximum tolerated dose; RP2D = recommended phase 2 dose.

PSMA expression is confirmed with PSMA PET/CT. Exclusion criteria include patients with prior cytotoxic chemotherapy for mCRPC, hepatic metastases 1 cm or larger, central nervous system metastases, and a superscan on bone scintigraphy.

ECLIPSE

ECLIPSE is an ongoing prospective, multicenter, open-label, randomized, phase 3 study to compare the safety and efficacy of ^{177}Lu -PSMA I&T versus hormone therapy in mCRPC patients (NCT05204927) (25). Approximately 400 patients will be randomized at a 2:1 ratio to receive either ^{177}Lu -PSMA I&T or SOC hormone therapy (abiraterone acetate with prednisone, or enzalutamide). PSMA expression is confirmed with either ^{68}Ga -PSMA 11 PET/CT or ^{18}F -DCFPyL PET/CT as determined by central readers. Exclusion criteria include prior treatment with radioligand therapy, ^{223}Ra -dichloride therapy within the past 12 wk, prior chemotherapy, or any other concurrent therapy. The primary outcome measure is rPFS as assessed by RECIST 1.1 and PCWG 3 criteria. There are also several secondary outcomes, including OS and PSA50 response rate, among others.

LUTECTOMY

LuTectomy is an ongoing Australian open-label, nonrandomized, phase 1/2 trial to assess the dosimetry, efficacy, and safety of ^{177}Lu -PSMA-617 in men with high-risk (defined as PSA > 20 ng/mL, International Society of Urological Pathology grade group 3–5, clinical stage T2c or higher) localized or locoregional (N1) prostate cancer before undergoing radical prostatectomy and pelvic lymph node dissection (NCT04430192) (26). The first 10 patients will receive 5 GBq of ^{177}Lu -PSMA-617 intravenously for the dosimetry study. The subsequent 10 patients will receive 2 cycles of 5 GBq of ^{177}Lu -PSMA-617 intravenously, separated by 6 wk. The primary outcome measure is to determine the absorbed radiation dose in the prostate and metastatic lymph nodes. PSMA PET/CT will be performed to confirm high PSMA expression defined as an SUV_{max} of more than 20. Patients with prior prostate radiotherapy or androgen-deprivation therapy, and evidence of metastatic disease involving the bone, viscera, and lymph nodes above the common iliac bifurcation, are excluded.

PRINCE

PRINCE is an ongoing Australian phase 1/2 study assessing the safety and efficacy of the combination of ^{177}Lu -PSMA-617 (up to 6-week cycles with an initial intravenous dose of 8.5 GBq reduced by 0.5 GBq for each of the subsequent 5 cycles) and the programmed death 1 protein inhibitor pembrolizumab (200 mg every 3 wk for up to 35 doses) in 37 mCRPC patients (NCT03658447) (27). Major exclusion criteria include any prior exposure to immunotherapy drug regimens, cabazitaxel chemotherapy, and ^{177}Lu -PSMA-617 RPT. The primary outcome measures are PSA50, incidence of adverse events, and tolerability (defined as time from

treatment commencement to treatment discontinuation due to toxicity).

LUPARP

LuPARP is an Australian dose-escalation and dose-expansion phase 1 trial evaluating the safety and tolerability of the poly(adenosine diphosphate ribose) polymerase (PARP) inhibitor olaparib in combination with ^{177}Lu -PSMA-617 in 52 mCRPC patients (NCT03874884) (28). Patients will be administered ^{177}Lu -PSMA-617 (7.4 GBq intravenously every 6 wk) together with olaparib on days 2–15 of each cycle for total of 4 cycles; a cycle is 42 d. The recommended phase 2 dose of olaparib will be used during the dose expansion part of the trial. Exclusion criteria include patients with a superscan pattern on bone scintigraphy, ^{18}F -FDG-positive disease with low PSMA expression ($\text{SUV}_{\text{max}} < 10$), a history of brain or leptomeningeal metastases, and prior exposure to ^{177}Lu -PSMA-617, cabazitaxel, platinum, PARP inhibitors, mitoxantrone, or cyclophosphamide. The primary outcome measures are determination of the dose-limiting toxicity, maximum tolerated dose, and recommended phase 2 dose. PSA50 and rPFS are among several secondary outcome measures.

TATCIST

TATCIST is an oncoming prospective, open-label, single-arm study to assess the efficacy of PSMA-targeted α -particle therapy with ^{225}Ac -PSMA I&T in approximately 100 patients with mCRPC (NCT05219500) (29). Eligible patients include those with progressive disease on taxane chemotherapy or those who are naïve to or have been treated previously and progressed with ^{177}Lu -PSMA-617 or ^{177}Lu -PSMA I&T. All patients will receive ^{225}Ac -PSMA I&T at an interval of 8 ± 1 wk, with the initial activity of 100 kBq/kg ($\pm 10\%$), followed by deescalation to 87 kBq/kg ($\pm 10\%$), 75 kBq/kg ($\pm 10\%$), or 50 kBq/kg ($\pm 10\%$) in cases of good response at the discretion of the investigator. The primary outcome measure is PSA50.

SUMMARY

We have reviewed several major clinical trials that use PSMA-directed RPT (Table 1). The VISION trial established PSMA-directed therapy as a viable treatment strategy option in men with mCRPC. The other ongoing trials will hopefully expand the applicability of PSMA-targeted RPT to earlier phases of prostate cancer and shed light on the proper sequencing and combination with other treatments to optimize overall therapeutic efficacy and patient outcome at acceptable biologic and financial toxicities.

DISCLOSURE

This work was supported in part by grant P30-CA014089 from the U.S. National Institutes of Health. Hossein Jadvar is on the advisory boards of Radiomedix and PharmaLogic, is on the speakers' bureau for Lantheus, and is a consultant

to Bayer and Blue Earth Diagnostics. No other potential conflict of interest relevant to this article was reported.

REFERENCES

1. NCCN clinical practice guidelines in oncology (NCCN Guidelines®): prostate cancer—version 1.2023. National Comprehensive Cancer Network website. https://www.nccn.org/professionals/physician_gls/pdf/prostate.pdf. Published September 16, 2022. Accessed January 17, 2023.
2. Fanti S, Brigatti A, Emmett L, et al. EAU-EANM consensus statements on the role of the prostate-specific membrane antigen positron emission tomography/computed tomography in patients with prostate cancer and with respect to [¹⁷⁷Lu]Lu-PSMA radioligand therapy. *Eur Urol Oncol*. 2022;5:530–536.
3. Sadaghiani MS, Sheikhabahaei S, Werner RA, et al. ¹⁷⁷Lu-PSMA radioligand therapy in metastatic castration-resistant prostate cancer: an updated systematic review and meta-analysis. *Prostate*. 2022;82:826–835.
4. Kim YJ, Kim YI. Therapeutic responses and survival effects of ¹⁷⁷Lu-PSMA-617 radioligand therapy in metastatic castrate-resistant prostate cancer: a meta-analysis. *Clin Nucl Med*. 2018;43:728–734.
5. Satapathy S, Sood A, Das CK, Mittal BR. Evolving role of ²²⁵Ac-PSMA radioligand therapy in metastatic castration-resistant prostate cancer—a systematic review and meta-analysis. *Prostate Cancer Prostatic Dis*. 2021;24:880–890.
6. Ballal S, Yadav MP, Sahoo RK, et al. ²²⁵Ac-PSMA-617-targeted alpha therapy for the treatment of metastatic castration-resistant prostate cancer: a systematic review and meta-analysis. *Prostate*. 2021;81:580–591.
7. Hofman MS, Violet J, Hicks RJ, et al. [¹⁷⁷Lu]-PSMA-617 radionuclide treatment in patients with metastatic castration resistant prostate cancer (LuPSMA trial): a single-center, single-arm, phase 2 study. *Lancet Oncol*. 2018;19:825–833.
8. Hofman MS, Emmett L, Sandhu S, et al. [¹⁷⁷Lu]Lu-PSMA-167 versus cabazitaxel in patients with metastatic castration-resistant prostate cancer (TheraP): a randomized, open-label, phase 2 trial. *Lancet*. 2021;397:797–804.
9. Sartor O, de Bono J, Chi KN, et al. Lutetium-177-PSMA-617 for metastatic castration-resistant prostate cancer. *N Engl J Med*. 2021;385:1091–1103.
10. Calais J, Czernin J. PSMA expression assessed by PET imaging is a required biomarker for selecting patients for any PSMA-targeted therapy. *J Nucl Med*. 2021;62:1489–1491.
11. Srinivas S, Iagaru A. To scan or not to scan: an unnecessary dilemma for PSMA radioligand therapy. *J Nucl Med*. 2021;62:1487–1488.
12. Jadvar H. The VISION forward: recognition and implication of PSMA—/¹⁸F-FDG+ mCRPC. *J Nucl Med*. 2022;63:812–815.
13. Jackson P, Hofman M, McIntosh L, et al. Radiation dosimetry in ¹⁷⁷LuPSMA-617 therapy. *Semin Nucl Med*. 2022;52:243–254.
14. Kuo PH, Benson T, Messmann R, Groaning M. Why we did what we did: PSMA PET/CT selection criteria for the VISION trial. *J Nucl Med*. 2022;63:816–818.
15. Eshghi A, Covington MF, Eshgi N, Kuo PH. Utility of PET to appropriately select patients for PSMA-targeted theranostics. *Clin Nucl Med*. 2022;47:488–495.
16. Chandran E, Figg WD, Madan R. Lutetium-177-PSMA-617: a vision of the future. *Cancer Biol Ther*. 2022;23:186–190.
17. Thang SP, Violet J, Sandhu S, et al. Poor outcomes for patients with metastatic castration-resistant prostate cancer with low prostate-specific membrane antigen (PSMA) expression deemed ineligible for ¹⁷⁷Lu-labelled PSMA radioligand therapy. *Eur Urol Oncol*. 2019;2:670–676.
18. Sartor O, Hermann K. Prostate cancer treatment: ¹⁷⁷Lu-PSMA-617 considerations, concepts, and limitations. *J Nucl Med*. 2022;63:823–829.
19. Hotta M, Gafita A, Czernin J, Calais J. Outcome of patients with PSMA PET/CT screen failure by VISION criteria and treated with ¹⁷⁷Lu-PSMA therapy: a multicenter retrospective analysis. *J Nucl Med*. 2022;63:1484–1488.
20. Enzalutamide with Lu PSMA-617 versus enzalutamide alone in men with metastatic castration-resistant prostate cancer (ENZA-p). ClinicalTrials.gov website. <https://clinicaltrials.gov/ct2/show/NCT04419402>. Published June 5, 2020. Updated February 16, 2022. Accessed January 17, 2023.
21. Sartor O, Morris MJ, Chi KN, et al. PSMAFore: a phase 3 study to compare ¹⁷⁷Lu-PSMA-617 treatment with a change in androgen receptor pathway inhibitor in taxane-naïve patients with metastatic castration-resistant prostate cancer [abstract]. *J Clin Oncol*. 2022;40(suppl):TPS211.
22. Sartor O, Tagawa ST, Saad F, et al. PSMAAddition: a phase 3 trial to compare treatment with ¹⁷⁷Lu-PSMA-617 plus standard of care (SOC) versus SOC alone in patients with metastatic hormone-sensitive prostate cancer [abstract]. *J Clin Oncol*. 2022;40(suppl):TP210.
23. Azad A, Dhantravan N, Emmett L, et al. UpfrontPSMA: a randomized phase II study of sequential ¹⁷⁷Lu-PSMA-617 and docetaxel in metastatic hormone-naïve prostate cancer (mHNPC) [abstract]. *J Clin Oncol*. 2021;39(suppl):TPS180.
24. Chi KN, Metser U, Czernin J, et al. Study evaluating metastatic castrate resistant prostate cancer (mCRPC) treatment using ¹⁷⁷Lu-PNT2002 PSMA therapy after second-line hormonal treatment (SPLASH) [abstract]. *J Clin Oncol*. 2021;39(suppl):TPS5087.
25. Lu-177-PSMA-I&T for metastatic castration-resistant prostate cancer. ClinicalTrials.gov website. <https://clinicaltrials.gov/ct2/show/NCT05204927?term=eclipse&cond=Prostate+Cancer&draw=2&rank=3>. Published January 24, 2022. Updated December 20, 2022. Accessed January 17, 2023.
26. Dhantravan N, Violet J, Eapen R, et al. Clinical trial protocol for LuTectomy: a single-arm study of the dosimetry, safety, and potential benefit of ¹⁷⁷Lu-PSMA-617 prior to prostatectomy. *Eur Urol Focus*. 2021;7:234–237.
27. PRINCE (PSMA-lutetium radionuclide therapy and immunotherapy in prostate cancer). ClinicalTrials.gov website. <https://clinicaltrials.gov/ct2/show/NCT03658447?term=prince&cond=prostate+cancer&draw=2&rank=1>. Published September 5, 2018. Updated May 25, 2022. Accessed January 17, 2023.
28. ¹⁷⁷Lu-PSMA-617 therapy and olaparib in patients with metastatic castration resistant prostate cancer (LuPARP). ClinicalTrials.gov website. <https://clinicaltrials.gov/ct2/show/NCT03874884>. Published March 14, 2019. Updated November 17, 2022. Accessed January 17, 2023.
29. Targeted alpha therapy with ²²⁵actinium-PSMA-I&T of castration-resistant prostate cancer (TATCIST). ClinicalTrials.gov website. <https://clinicaltrials.gov/ct2/show/NCT05219500?term=225ac-psma&cond=Prostate+Cancer&draw=2&rank=1>. Published February 2, 2022. Accessed January 17, 2023.

Peptide Receptor Radionuclide Therapy in Merkel Cell Carcinoma: A Comprehensive Review

Emran Askari^{*1}, Soroush Zarehparvar Moghadam^{*1}, Damian Wild², Ebrahim Delpassand³, Sergio Baldari⁴, Bernhard Nilica⁵, Philipp E. Hartrampf⁶, Grace Kong⁷, Chiara Maria Grana⁸, Martin Alexander Walter⁹, Francesca Capocchetti¹⁰, Pashtoon Murtaza Kasi¹¹, and Jonathan Strosberg¹²

¹Nuclear Medicine Research Center, Mashhad University of Medical Sciences, Mashhad, Iran; ²ENETS Center of Excellence, Radiology and Nuclear Medicine, University Hospital Basel, Basel, Switzerland; ³Department of Clinical Nuclear Medicine, Excel Diagnostics Imaging Clinic, Houston, Texas; ⁴Nuclear Medicine Unit, Department of Biomedical and Dental Sciences and of Morpho-Functional Imaging, University of Messina, Messina, Italy; ⁵Department of Nuclear Medicine, Medical University Innsbruck, Innsbruck, Austria; ⁶Department of Nuclear Medicine, University Hospital Würzburg, Würzburg, Germany; ⁷Sir Peter MacCallum Department of Oncology and Molecular Imaging and Therapeutic Nuclear Medicine, Peter MacCallum Cancer Centre, Melbourne, Victoria, Australia; ⁸Division of Nuclear Medicine, European Institute of Oncology, IRCCS, Milan, Italy; ⁹Nuclear Medicine and Molecular Division, Geneva Medical Hospital, Geneva, Switzerland; ¹⁰UOC Nuclear Medicine–PET Center–Single Regional Center for Radiometabolic Therapy, Department of Radiological Diagnosis and Services, ASUR Marche Area Vasta 3, Macerata, Italy; ¹¹Meyer Cancer Center and Englander Institute of Precision Medicine, Weill Cornell Medicine, New York Presbyterian Hospital, New York, New York; and ¹²Neuroendocrine Tumor Division, Gastrointestinal Department, Moffitt Cancer Center, Tampa, Florida

Merkel cell carcinoma is a rare, aggressive skin malignancy, also known as neuroendocrine carcinoma of the skin, with high rates of recurrence and distant metastasis. In refractory metastatic Merkel cell carcinoma (mMCC), besides immunotherapy, chemotherapy, and radiation, peptide receptor radionuclide therapy (PRRT) may be a viable option since this type of tumor can express somatostatin receptors. **Methods:** We performed a comprehensive review of the literature to evaluate the efficacy of PRRT in mMCC patients. **Results:** Thirty-seven patients with mMCC received PRRT (1–5 cycles) with ¹⁷⁷Lu- or ⁹⁰Y-labeled somatostatin analogs (cumulative activity, 1.5–30 GBq). Radiographic response was available for 19 of 28 patients who received PRRT alone. Six (31.6%) of 19 patients showed objective responses, from partial to complete, and no severe adverse events were reported. **Conclusion:** Our analysis supports the use of PRRT in mMCC with sufficient somatostatin receptor uptake, although the quality of the available evidence is low. Prospective clinical trials are already in development and have started accruing in some parts of the world.

Key Words: PRRT; SSTR; Merkel cell carcinoma; theranostics; Lu-177

J Nucl Med Technol 2023; 51:22–25

DOI: 10.2967/jnmt.122.264904

Merkel cell carcinoma (MCC) is a rare, aggressive skin malignancy. The known risk factors for MCC are immunosuppression and extensive exposure to ultraviolet light. It usually

occurs in elderly patients (median age, 70 y); typically arises in the head, neck, or extremities; and is slightly more common in men. Treatments for MCC vary depending on the stage of the disease, from complete surgical resection with or without radiation therapy for localized disease to systemic therapies (immunotherapy or chemotherapy) for metastatic disease. The 5-y survival rates for patients with metastatic disease have been approximately 18% (1,2). Although the introduction of immune checkpoint inhibitors has shown promising results, with an approximately 50% objective response, about half of patients with metastatic MCC (mMCC) experience disease progression or resistance.

At least one third of MCC cases express high levels of somatostatin receptors (SSTRs) (3,4). In some studies, SSTR expression has been reported in as many as 80%–100% of MCC cases (5). There have even been reports of using SSAs for the treatment of MCC (4). A recent trial of a novel second-generation SSA (pasireotide) allowed MCC patients to participate given the SSTR expression (NCT01652547). All this sets the stage for a new therapeutic option of theranostics/peptide receptor radionuclide therapy (PRRT) in MCC.

MATERIALS AND METHODS

Data on PRRT in MCC exist only in the form of case reports or series. A search for articles or abstracts pertaining to “PRRT” and “MCC” on PubMed, Scopus, and Google Scholar was systematically performed. Articles or abstracts published up to January 2022 were retrieved. The references of all relevant studies were evaluated as well. We also contacted centers that had previously reported experience with SSTR imaging or therapy in mMCC patients (the search strategy and PRISMA flow diagram can be found in Supplemental Figs. 1 and 2; supplemental materials are available at <http://jnmt.snmjournals.org>) (6–26). Overall, 37 patients with mMCC have received PRRT with ¹⁷⁷Lu- or ⁹⁰Y-labeled somatostatin analogs

Received Sep. 10, 2022; revision accepted Sep. 14, 2022.

For correspondence or reprints, contact Jonathan Strosberg (jonathan.strosberg@moffitt.org).

*Contributed equally to this work.

Published online Oct. 4, 2022.

COPYRIGHT © 2023 by the Society of Nuclear Medicine and Molecular Imaging.

TABLE 1
Review of Studies Evaluating Treatment Response to PRRT Monotherapy in mMCC (n = 10)

Study	Age (y)	Sex	Primary location	Other sites of involvement	Type of radiotracer, cumulative dose, and no. of cycles	Treatments before PRRT					Survival from start of PRRT (mo)	Response to PRRT
						Surgery	EBRT	Chemo.	SSA	ICI		
Meier (7)	83	F	Facial (left cheek) (3 cm)	Cervical LNs	⁹⁰ Y-DOTATOC, 15.72 GBq, 4 cycles	Yes	Yes	Yes	No	No	27	CR
Bodei (8)	78*	F*	Leg (left)*	Pelvic LNs*	⁹⁰ Y-DOTATOC, 9.6 GBq, 3 cycles*	Yes*	Yes*	No*	No*	No*	7*	PD*
Maecke (9)	43	F	Head	NA	⁹⁰ Y-DOTATOC, 5.4 GBq/m ² , 4 cycles	NA	NA	NA	NA	NA	>19*	CR
Imhof (10)	70*	M*	NA*	NA*	⁹⁰ Y-DOTATOC, 8.14 GBq, 1 cycle*	Yes*	No*	Yes*	No*	No*	6.1*	PD*
	77*	M*	NA*	Liver, bone*	⁹⁰ Y-DOTATOC, 6.66 GBq, 1 cycle*	Yes*	Yes*	No*	No*	No*	1*	PD*
	69*	F*	NA*	NA*	⁹⁰ Y-DOTATOC, 5.37 GBq, 1 cycle*	No*	Yes*	Yes*	No*	No*	1.2*	PD*
	55*	M*	NA*	Liver*	⁹⁰ Y-DOTATOC, 8.14 GBq, 1 cycle*	Yes*	No*	Yes*	No*	No*	1.7*	PD*
	54*	F*	NA*	NA*	⁹⁰ Y-DOTATOC, 12.96 GBq, 2 cycles*	Yes*	No*	No*	No*	No*	13.9*	PR*
	66*	M*	NA*	Liver*	⁹⁰ Y-DOTATOC, 14.06 GBq, 2 cycles*	Yes*	Yes*	No*	No*	No*	4.5*	SD*
	83*	F*	NA*	NA*	⁹⁰ Y-DOTATOC, 15.73 GBq, 4 cycles*	Yes*	Yes*	No*	No*	No*	9.1*	SD*
	69*	F*	NA*	Liver*	⁹⁰ Y-DOTATOC, 11.1 GBq, 2 cycles*	Yes*	No*	No*	No*	No*	9.7*	PR*
Villard (11)	76*	F*	NA*	NA*	¹⁷⁷ Lu-DOTATOC, 12.95 GBq, 2 cycles; ⁹⁰ Y-DOTATOC, 13.88 GBq, 2 cycles*	Yes*	No*	No*	No*	No*	15.1*	SD*
	73*	F*	NA*	NA*	¹⁷⁷ Lu-DOTATOC, 14.43 GBq, 2 cycles; ⁹⁰ Y-DOTATOC, 14.43 GBq, 2 cycles*	Yes*	Yes*	Yes*	No*	No*	9.8*	SD*
Romer (12)	76*	F*	NA*	Bone*	¹⁷⁷ Lu-DOTATOC, 7.4 GBq, 1 cycle*	No*	Yes*	Yes*	No*	No*	0.7*	PD*
	53*	M*	NA*	NA*	¹⁷⁷ Lu-DOTATOC, 7.4 GBq, 1 cycle*	No*	No*	Yes*	No*	No*	1.3*	PD*
Basu (2)	54	M	Facial (right malar)	Cervical LNs, liver	¹⁷⁷ Lu-DOTATATE, 13.14 GBq, 2 cycles	Yes	No	Yes	Yes	Yes*	>3	PR
Nilica (13)	65*	M*	Arm (right forearm)*	Widespread (LNs, liver, bone, peritoneum, heart)*	¹⁷⁷ Lu-DOTATATE, 14.2 GBq, 2 cycles; ⁹⁰ Y-DOTATOC, 2.4 GBq, 1 cycle*	Yes*	Yes*	Yes*†	No*	No*	5*	PD*
Noorelahi (14)	59	M	Axilla (right) (9 cm)	Subpectoral and axillary LNs	¹⁷⁷ Lu-DOTATOC, 10.62 GBq, 2 cycles	Yes	Yes	Yes	NA	NA	NA	PD
Moghadam (3)	77	M	Facial (right malar)	Extensive LNs (cervical, supraclavicular, mediastinal, axillary, abdominal)	¹⁷⁷ Lu-DOTATATE, 5.5 GBq, 1 cycle	Yes	Yes	Yes	Yes	No	2*‡	PR

*Data were obtained after personal communication with corresponding authors of that article/unpublished data.

†Intracardiac instillation of chemotherapeutic drugs due to cardiac involvement.

‡Death due to other cause (acute respiratory distress syndrome).

EBRT = external-beam radiation therapy; chemo. = chemotherapy; SSA = somatostatin analogue; ICI = immune checkpoint inhibitor; LN = lymph node; CR = complete response;

PD = progressive disease; NA = not available; PR = partial response; SD = stable disease.

(DOTATATE/DOTATOC) (Table 1; Supplemental Tables 1 and 2). Fifteen and 18 patients received ^{177}Lu -DOTATATE and ^{90}Y -DOTATOC, respectively. Four patients underwent tandem PRRT with ^{177}Lu and ^{90}Y . The number of PRRT cycles ranged from 1 to 5, with the cumulative activity ranging from 1.5 to 30 GBq. Three patients received PRRT in combination with chemotherapy, and 4 patients received PRRT with immune checkpoint inhibitors.

RESULTS

Of the 37 patients who received PRRT, 18 were excluded because response data were unavailable (Supplemental Tables 1 and 2) or because PRRT had been used in combination with other active treatments (Supplemental Table 1). Consequently, radiographic response was available for 19 of 28 patients who received PRRT alone (not in combination with immunotherapy or chemotherapy). Six (31.6%) of 19 patients showed objective responses, from partial to complete, and no severe adverse events were reported (Table 1).

The median overall survival from the start of PRRT was 5 and 8 mo in patients receiving PRRT alone and in combination with other active treatments, respectively (Table 1; Supplemental Table 1). Median overall survival from diagnosis was 22 mo (Supplemental Table 3; methods for statistical analyses are described in the supplemental materials). Few studies addressed the Merkel cell polyomavirus status or ^{18}F -FDG PET findings, whereas most reported the Krenning score (Supplemental Table 4). No significant difference was noted between Krenning scores in terms of objective response to PRRT ($P = 0.86$).

DISCUSSION

Because of the small sample size, retrospective nature of the studies, selection bias, and low quality of the evidence, we cannot recommend PRRT for mMCC patients. However, the promising results from the available data lay the foundation for clinical trials in this space. Despite approval of immune checkpoint inhibitors, treatment resistance can occur and a fair proportion do not respond. Five of 7 patients who received PRRT in combination with immune checkpoint inhibitors or chemotherapy showed partial to complete responses, indicating better objective responses in this category than in the PRRT-alone group. Novel therapies or combinations are needed to further improve patient outcome. The ongoing GoTHAM trial (NCT04261855) is one example of a clinical trial evaluating the immunotherapy avelumab with ^{177}Lu -DOTATATE in patients with mMCC. The results of this and other ongoing trials using theranostics might change the management of mMCC patients soon.

CONCLUSION

Our analysis supports the use of PRRT in mMCC with sufficient SSTR uptake, although the quality of the available evidence is low. Prospective studies in terms of clinical trials are already in development and have started accruing in some parts of the world.

DISCLOSURE

Jonathan Strosberg has consulted for Novartis and is on the speakers' bureau for Ipsen. Damian Wild reports personal fees from Ipsen. Pashtoon Murtaza Kasi reports having a consultancy or advisory board role with Natera, Foundation Medicine, Merck/MSD Oncology, Tempus, Bayer, Lilly, Delcath Systems, QED Therapeutics, Servier, Taiho Oncology, Exact Sciences, and Ipsen and has received grant or research funding from Advanced Accelerator Applications, Boston Scientific, and Tersera. No other potential conflict of interest relevant to this article was reported.

ACKNOWLEDGMENTS

We thank Soheil Yazdani for the patient data of Hamiditabar et al. (17), Sandip Basu for the patient data of Basu et al. (2), and Riccardo Laudicella and Ludovica Crocè for the patient data of Herberg et al. (15). We also thank Paul Nghiem for useful links for collaboration between centers, Tomoko Akaike for thoughtful comments on the manuscript, Lindsay Gunnell for an MCC skin lesion, and Owen Prall for SSTR-staining slides.

KEY POINTS

QUESTION: Is radioligand therapy with ^{177}Lu -DOTATATE effective and safe in mMCC patients?

PERTINENT FINDINGS: Because of the small sample size and low-quality evidence, we cannot recommend PRRT for mMCC patients; however, the available data show promising results, laying the foundation for clinical trials in this space.

IMPLICATIONS FOR PATIENT CARE: ^{177}Lu -DOTATATE may be effective in some mMCC patients with high SSTR expression.

REFERENCES

1. Becker JC, Eigentler T, Frerich B, et al. S2k guidelines for Merkel cell carcinoma (MCC, neuroendocrine carcinoma of the skin): update 2018. *J Dtsch Dermatol Ges*. 2019;17:562–576.
2. Basu S, Ranade R. Favorable response of metastatic Merkel cell carcinoma to targeted ^{177}Lu -DOTATATE therapy: will PRRT evolve to become an important approach in receptor-positive cases? *J Nucl Med Technol*. 2016;44:85–87.
3. Moghadam SZ, Divband G, Shakeri S, Aryana K. Favorable response after only one cycle of peptide receptor radionuclide therapy with ^{177}Lu -DOTATATE in a patient with metastatic Merkel cell carcinoma. *Clin Nucl Med*. 2019;44:650–652.
4. Akaike T, Qazi J, Anderson A, et al. High somatostatin receptor expression and efficacy of somatostatin analogues in patients with metastatic Merkel cell carcinoma. *Br J Dermatol*. 2021;184:319–327.
5. Gardair C, Samimi M, Touze A, et al. Somatostatin receptors 2A and 5 are expressed in Merkel cell carcinoma with no association with disease severity. *Neuroendocrinology*. 2015;101:223–235.
6. Page MJ, McKenzie JE, Bossuyt PM, et al. The PRISMA 2020 statement: an updated guideline for reporting systematic reviews. *Syst Rev*. 2021;10:89.
7. Meier G, Waldherr C, Herrmann R, Maecke H, Mueller-Brand J, Pless M. Successful targeted radiotherapy with ^{90}Y -DOTATOC in a patient with Merkel cell carcinoma. *Oncology*. 2004;66:160–163.
8. Bodei L, Cremonesi M, Grana C, et al. Receptor radionuclide therapy with ^{90}Y -[DOTA] 0 -Tyr 3 -octreotide (^{90}Y -DOTATOC) in neuroendocrine tumors. *Eur J Nucl Med Mol Imaging*. 2004;31:1038–1046.

9. Maecke HR. Radiolabeled peptides in nuclear oncology: influence of peptide structure and labeling strategy on pharmacology. In: Bogdanov A, Licha K, eds. *Molecular Imaging: An Essential Tool in Preclinical Research, Diagnostic Imaging, and Therapy*. Springer; 2005:43–72.
10. Imhof A, Brunner P, Marincek N, et al. Response, survival, and long-term toxicity after therapy with the radiolabeled somatostatin analogue [⁹⁰Y-DOTA]-TOC in metastasized neuroendocrine cancers. *J Clin Oncol*. 2011;29:2416–2423.
11. Villard L, Romer A, Marincek N, et al. Cohort study of somatostatin-based radiopeptide therapy with [⁹⁰Y-DOTA]-TOC versus [⁹⁰Y-DOTA]-TOC plus [¹⁷⁷Lu-DOTA]-TOC in neuroendocrine cancers. *J Clin Oncol*. 2012;30:1100–1106.
12. Romer A, Seiler D, Marincek N, et al. Somatostatin-based radiopeptide therapy with [¹⁷⁷Lu-DOTA]-TOC versus [⁹⁰Y-DOTA]-TOC in neuroendocrine tumors. *Eur J Nucl Med Mol Imaging*. 2014;41:214–222.
13. Nilica B. Peptide receptor radionuclide therapy in non-neuroendocrine tumors: a field report [abstract]. *Eur J Nucl Med Mol Imaging*. 2016;43(suppl):S223.
14. Noorelahi M, Mahmood R. Multiple enlarged lymph nodes in axilla: a case report of Merkel cell carcinoma. *Ann Ital Chir*. 2017;6:S2239253X17026378.
15. Herberg A, Murè G, Militano V, Lo Gullo R, Paratore R, Baldari S. ⁹⁰Y-DOTA-TOC and/or ¹¹¹In-pentetreotide in the treatment of the somatostatin expressing tumors (SSTR): personal experience [abstract]. *Eur J Nucl Med Mol Imaging*. 2009;36(suppl):S418.
16. Cirillo F, Vismarra M, Cafaro I, Martinotti M. Merkel cell carcinoma: a retrospective study on 48 cases and review of literature. *J Oncol*. 2012;2012:749030.
17. Hamiditabar M, Ali M, Roys J, et al. Peptide receptor radionuclide therapy with ¹⁷⁷Lu-octreotate in patients with somatostatin receptor expressing neuroendocrine tumors: six years' assessment. *Clin Nucl Med*. 2017;42:436–443.
18. Schmidt MC, Uhrhan K, Markiefka B, et al. ⁶⁸Ga-DotaTATE PET-CT followed by peptide receptor radiotherapy in combination with capecitabine in two patients with Merkel cell carcinoma. *Int J Clin Exp Med*. 2012;5:363–366.
19. Salavati A, Prasad V, Schneider CP, Herbst R, Baum RP. Peptide receptor radionuclide therapy of Merkel cell carcinoma using ¹⁷⁷lutetium-labeled somatostatin analogs in combination with radiosensitizing chemotherapy: a potential novel treatment based on molecular pathology. *Ann Nucl Med*. 2012;26:365–369.
20. Kasi PM, Sharma A, Jain MK. Expanding the indication for novel theranostic ¹⁷⁷Lu-dotatate peptide receptor radionuclide therapy: proof-of-concept of PRRT in Merkel cell cancer. *Case Rep Oncol*. 2019;12:98–103.
21. Ferdinandus J, Fendler WP, Lueckerath K, et al. Response to combined peptide receptor radionuclide therapy and checkpoint immunotherapy with ipilimumab plus nivolumab in metastatic Merkel cell carcinoma. *J Nucl Med*. 2022;63:396–398.
22. Sindrilaru A, Aicher A, Crisan D, Prasad V. Use of the low-dose hyperfractionated ¹⁷⁷Lu-HA-DOTATATE peptide receptor radionuclide therapy in patients with immunotherapy-refractory Merkel cell carcinoma: testing of the therapeutic concept in two patients with metastatic Merkel cell carcinoma [abstract]. *J Dtsch Dermatol Ges*. 2021;19:20–21.
23. Barucca S, Berbellini A, Ancidei C, et al. Radionuclide dosimetry in ⁹⁰Y-DOTA-TOC therapy: preliminary report [abstract]. *Eur J Nucl Med Mol Imaging*. 2006;33(suppl):S180.
24. Stefanova M, Kratochwil C, Schwartz L, Haberkorn U, Giesel F. Impact of normal tissue uptake using ⁶⁸Ga DOTATOC-PET/CT in patients with neuroendocrine tumor: a follow-up study [abstract]. *Insights Imaging*. 2012;3(suppl):S160–S161.
25. Koukouraki S, Strauss LG, Georgoulas V, et al. Evaluation of the pharmacokinetics of ⁶⁸Ga-DOTATOC in patients with metastatic neuroendocrine tumors scheduled for ⁹⁰Y-DOTATOC therapy. *Eur J Nucl Med Mol Imaging*. 2006;33:460–466.
26. Epstude M, Tornquist K, Riklin C, et al. Comparison of ¹⁸F-FDG PET/CT and ⁶⁸Ga-DOTATATE PET/CT imaging in metastasized Merkel cell carcinoma. *Clin Nucl Med*. 2013;38:283–284.

Improving ^{90}Y PET Scan Image Quality Through Optimized Reconstruction Algorithms

Pei Ing Ngam^{1,2}, Eelin Tan³, Gabriel Lim¹, and Sean Xuexian Yan¹

¹Department of Nuclear Medicine and Molecular Imaging, Singapore General Hospital, Singapore; ²Department of Diagnostic Imaging, National University Hospital, Singapore; and ³SingHealth Radiological Sciences Academic Clinical Programme, Singapore General Hospital, Singapore

This study aimed to improve the quality of ^{90}Y PET imaging by optimizing the reconstruction algorithm. **Methods:** We recruited 10 patients with neuroendocrine tumor metastatic to the liver or primary hepatocellular carcinoma who were qualified for ^{90}Y -labeled selective internal radiation therapy or peptide receptor radionuclide therapy. They underwent posttherapeutic PET/CT imaging using 3 different reconstruction parameters: VUE Point HD with a 6.4-mm filter cutoff, 24 subsets, and 2 iterations (algorithm A); VUE Point FX with a 6.0-mm filter cutoff, 18 subsets, and 3 iterations using time of flight (algorithm B); and VUE Point HD (LKYG) with a 5-mm filter cutoff, 32 subsets, and 1 iteration (algorithm C). The reconstructed PET/CT images were assessed by 10 nuclear medicine physicians using 4-point semiquantitative scoring criteria. A P value of less than 0.05 was considered significant. **Results:** The median quality assessment scores for algorithm C were consistently scored the highest, with algorithms A, B, and C, scoring 3, 2, and 4, respectively. The ^{90}Y PET scans using algorithm C were deemed diagnostic 91% of the time. There was a statistically significant difference in quality assessment scores among the algorithms by the Kruskal-Wallis rank sum test ($\chi^2_2 = 86.5$, $P < 0.001$), with a mean rank quality score of 130.03 for algorithm A, 109.76 for algorithm B, and 211.71 for algorithm C. Subgroup analysis for quality assessment scoring of post-peptide receptor radionuclide therapy imaging alone showed a statistically significant difference between different scanning algorithms ($\chi^2_2 = 35.35$, $P < 0.001$), with mean rank quality scores of 45.85 for algorithm A, 50.05 for algorithm B, and 85.6 for algorithm C. Similar results were observed for quality assessment scoring of imaging after selective internal radiation therapy ($\chi^2_2 = 79.90$, $P < 0.001$), with mean ranks of 82.33 for algorithm A, 55.79 for algorithm B, and 133.38 for algorithm C. **Conclusion:** The new LKYG algorithm that was featured by decreasing the number of iterations, decreasing the cutoff of the filter thickness, and increasing the number of subsets successfully improved image quality.

Key Words: reconstruction algorithms; image quality; ^{90}Y PET; SIRT; PRRT

J Nucl Med Technol 2023; 51:26–31

DOI: 10.2967/jnmt.122.264439

Received May 26, 2022; revision accepted Oct. 20, 2022.
For correspondence or reprints, contact Sean Xuexian Yan (sean.yan.x.x@singhealth.com.sg).
Published online Nov. 9, 2022.
COPYRIGHT © 2023 by the Society of Nuclear Medicine and Molecular Imaging.

Because of its outstanding physical and chemical features, ^{90}Y is one of the most commonly used radionuclides in contemporary nuclear medicine as both a diagnostic and a therapeutic agent, giving rise to the lauded concept of theranostics (1). ^{90}Y -based radiopharmaceuticals have been used in various oncologic therapies, which include but are not limited to ^{90}Y -labeled anti-CD20 monoclonal antibody (ibritumomab tiuxetan [Zevalin; Acrotech Biopharma, Inc.]) radioimmunotherapy for lymphoma, ^{90}Y -dotapeptide radionuclide therapy for neuroendocrine tumors, and ^{90}Y -microsphere selective internal radiation therapy (SIRT) for liver tumors (2). Posttherapy imaging is therefore essential in confirming successful delivery of ^{90}Y -labeled agents, dosimetry of the tumor and critical organs, and dose planning for the next treatment.

The conventional postimaging modality using ^{90}Y bremsstrahlung technique unfortunately bears the inherent drawbacks of poor spatial resolution and unsatisfactory readability. ^{90}Y PET/CT, on the other hand, has emerged as the modality of choice for better-quality posttherapeutic scans. Despite the advances in technology, the main challenge for ^{90}Y PET imaging is its extremely low abundance of positron emissions per decay, requiring a long scanning time for an adequate signal-to-noise ratio. Because of patients' general lack of toleration of prolonged scanning times, it is difficult to achieve adequate counts, and the quality of PET images using standard or modified reconstruction algorithms has been found unsatisfactory in many literature reports. There is also a lack of consensus guidelines for the technical acquisition, imaging reconstruction, and qualitative and quantitative interpretation of ^{90}Y planar, SPECT, and PET images. In addition, most nuclear medicine imaging systems are not currently designed or specifically optimized for ^{90}Y imaging applications (3).

In this article, we report our efforts to modify the reconstruction algorithm and consequently improve ^{90}Y PET imaging quality in order for our experience to serve as a reference for other practitioners.

MATERIALS AND METHODS

Study Cohort

In total, 10 consecutive patients qualified for ^{90}Y -labeled SIRT or peptide receptor radionuclide therapy (PRRT) were recruited. For ^{90}Y -PRRT, the ^{90}Y was purchased from Perkin Elmer, and the

^{90}Y -DOTATATE was then synthesized in our department's radio-pharmacy. ^{90}Y -DOTATATE, with a dose ranging from 3.0 to 5.0 GBq, was given intravenously to the patients in the dedicated isolation ward. For ^{90}Y -SIRT, ^{90}Y microspheres were purchased from SIRTEX Medical Singapore Pte. Ltd. ^{90}Y -microspheres, with a dose ranging from 0.5 to 3.0 GBq, were administered intraarterially to the targeted hepatic lesions in the interventional radiology suite at Singapore General Hospital.

The institutional review board approved this study, and the requirement to obtain informed consent was waived because most patients in the study had passed away or were overseas.

Scanning Protocol and Reconstruction Algorithm

All patients were scanned on a GE Healthcare Discovery PET/CT 690 scanner either on the same day as radiotracer injection or the next morning. A low-dose CT protocol at 120 kV, with an automated current ranging between 10 and 200 mA and a noise index of 18, was obtained for attenuation correction and anatomic localization followed by a PET acquisition for 30 min per bed position, covering the diaphragm to the iliac crest of the pelvis for SIRT patients and variable locations for PRRT patients, depending on where the disease burden was. PET images were corrected for motion and attenuation on the basis of the CT data. The reconstruction was performed using both a fully 3-dimensional ordered-subset expectation maximization algorithm either with or without time of flight (TOF) and a GE Healthcare Sharp IR point-spread function algorithm. Three different reconstruction parameters with variations in the full-width-at-half-maximum gaussian filter size and in the number of iterations and subsets were used: VUE Point HD (GE Healthcare) (non-TOF) with a 6.4-mm filter cutoff, 24 subsets, and 2 iterations (algorithm A); VUE Point FX (GE Healthcare) (with TOF) with a 6.0-mm filter cutoff, 18 subsets, and 3 iterations (algorithm B); and VUE Point HD (LKYG) (non-TOF) with a 5-mm filter cutoff, 32 subsets, and 1 iteration (algorithm C) (Table 1). The reconstructed matrix size was 192×192 , with a pixel dimension of 3.65 mm. Algorithms A and B were routinely used in our center and many other centers, whereas algorithm C was purposefully modified and named LKYG. Maximum-intensity-projection images were also generated. Both attenuation-corrected and uncorrected PET images, as well as PET/CT fusion images, were reviewed.

Quality Assessment

For each patient, the reconstructed PET/CT images using the 3 different algorithms were presented for quality assessment to 10 nuclear medicine physicians (readers) with work experience ranging

from 2 to 20 y. The quality of the images was graded according to semiquantitative scoring criteria as nondiagnostic, barely diagnostic, fairly diagnostic and diagnostically excellent (Table 2). All readers were masked to the reconstruction algorithms.

Statistical Analysis

Statistical quality assessment scores were compared among the algorithms by nonparametric Kruskal–Wallis rank sum testing and, in the event of a statistically significant difference in the Kruskal–Wallis test, by post hoc Wilcoxon rank sum testing. The potential confounding factors, including age, sex, body mass index, type of radioligand, and dose, were examined with multivariable ordered logistic regression analysis. The threshold for statistical significance (P value) was set at 0.05. Ordinal and continuous variables are reported as median values with interquartile range. The results from ordered logistic regression analysis are reported as odds ratios (ORs) with corresponding 95% CIs. Interrater reliability was assessed with the mixed-effects intraclass correlation coefficient (ICC), whereby an ICC of less than 0.5 constituted poor interrater agreement, an ICC of between 0.5 and 0.75 constituted moderate interrater agreement, an ICC of between 0.75 and 0.9 constituted good interrater agreement, and an ICC of more than 0.9 constituted excellent interrater agreement.

Statistical analysis was conducted on RStudio (R, version 3.6.3; R Foundation for Statistical Computing).

RESULTS

Patient Demographics and PET Study Parameters

Eight men and 2 women with a mean age of 61.5 ± 17.3 y and a mean body mass index of 23.54 ± 3.49 kg/m² were recruited into our study (Table 3). Four of the patients (1 with rectal neuroendocrine tumor, 2 with midgut neuroendocrine tumor, and 1 with paraganglioma) received a mean ^{90}Y -PRRT dose of 3.66 GBq. The other 6 patients (5 with hepatocellular carcinoma and 1 with pancreatic neuroendocrine tumor metastatic to liver) received a mean ^{90}Y -SIRT dose of 1.85 GBq.

Interrater Reliability

Interrater reliability was moderate to good, with a κ of 0.82 ($P < 0.001$; 95% CI, 0.66–0.93) for algorithm A, 0.625 ($P < 0.005$; 95% CI, 0.29–0.85) for algorithm B, and 0.502 ($P < 0.05$; 95% CI, 0.06–0.80) for algorithm C.

TABLE 1
Parameters of the 3 Tested Algorithms

Parameter	Algorithm A	Algorithm B	Algorithm C
VUE Point	VUE Point HD (OSEM)	VUE Point FX (OSEM + TOF)	VUE Point HD (OSEM)
Gaussian filter cutoff	6.4 mm	6.0 mm	5.0 mm
Number of subsets	24	18	32
Sharp IR (point-spread function)	On	On	On
z-axis filter	Standard	Heavy	Standard
Number of iterations	2	3	1
Matrix	192×192	192×192	192×192
Minutes per bed position	30	30	30

OSEM = ordered-subset expectation maximization.

TABLE 2
Scoring Criteria for Image Quality Assessment

QS	Rating	Description
1	Nondiagnostic	Excessive noise or artifacts; delineation of tumor and background uptake mostly impossible
2	Barely diagnostic	Substantial noise and artifacts; delineation of tumor and background uptake difficult but possible
3	Fairly diagnostic	Somewhat noisy and artifacts that interfere with reading; delineation of tumor and background uptake feasible but not satisfactory
4	Diagnostically excellent	No interfering noise or artifacts; delineation of tumor and background uptake satisfactory

Quality Assessment Scores

The median quality assessment scores for algorithms A, B, and C were 3 (interquartile range, 1), 2 (interquartile range, 1), and 4 (interquartile range, 1), respectively (Fig. 1). Algorithm C consistently scored the highest for each patient. Ninety-one percent of the time, the post-SIRT or post-PRRT scans using algorithm C were deemed diagnostic (quality score [QS]-3 or QS-4) by the 10 readers, achieving QS-4 53% of the time and QS-3 39% of the time. Only 1% of the time was algorithm C not diagnostic, compared with 10% of the time for algorithm A and 14% for algorithm B.

There was a statistically significant difference in quality assessment scores between algorithms by the Kruskal–Wallis rank sum test ($\chi^2 = 86.5$, $P < 0.001$) (Table 4), with a mean rank QS of 130.03 for algorithm A, 109.76 for algorithm B, and 211.71 for algorithm C. Post hoc Wilcoxon rank sum testing showed that algorithm C scored significantly higher than algorithm A or B (A vs. C, $P < 0.001$; B vs. C, $P < 0.001$), whereas there was no significant difference in quality assessment scores between algorithms A and B (A vs. B, $P = 0.064$).

Subgroup analysis for quality assessment scoring of post-PRRT imaging alone showed a statistically significant difference among scanning algorithms as well ($\chi^2 = 35.35$, $P < 0.001$), with a mean rank QS of 45.85 for algorithm A, 50.05 for algorithm B, and 85.6 for algorithm C. Similar results were observed for quality assessment scoring of post-

SIRT imaging ($\chi^2 = 79.90$, $P < 0.001$), with a mean rank QS of 82.33 for algorithm A, 55.79 for algorithm B, and 133.38 for algorithm C. Therefore, we concluded that algorithm C remained better than algorithm A or B for both post-SIRT therapy scans and post-PRRT scans. For post-SIRT therapy scans, algorithm C fared remarkably better, with a minimum score of QS-3, and achieved excellent scoring of QS-4 75% of the time. For post-PRRT PET scans, algorithm C again fared remarkably better, achieving a good score of either QS-3 or QS-4 77.5% of the time, compared with 15% for algorithm A and 32.5% for algorithm B.

The Wilcoxon signed-rank test showed that the quality of post-SIRT therapy images (mean rank of 65.3 for algorithm A, 58.26 for algorithm B, and 63.13 for algorithm C) was consistently better than that of post-PRRT images regardless of the type of algorithm used (mean rank of 28.3 for algorithm A, 38.86 for algorithm B, and 31.56 for algorithm C) ($z = -6.70$, $P < 0.001$, for algorithm A; $z = -3.54$, $P < 0.001$, for algorithm B; and $z = -5.96$, $P < 0.001$, for algorithm C).

We present a case example of rectal neuroendocrine tumor metastatic to the liver (Fig. 2). The SUV_{max} for the dominant lesion in the left hepatic lobe was 47.7, 34.0, and 33.7 for algorithms A, B, and C, respectively, whereas the SUV_{max} for the dominant lesion in the right hepatic lobe was 33.9, 35.2, and 22.8 for algorithms A, B, and C, respectively. Overall, algorithm C demonstrated outstanding diagnostic

TABLE 3
Patients' Demographic Data

Participant	Age (y)	Sex	BMI (kg/m ²)	Diagnosis	Therapy	Radiotracer dose (GBq)
1	52	M	20.6	Rectal NET	PRRT	3.70
2	58	M	24.9	Midgut NET	PRRT	3.70
3	39	M	19.2	Paraganglioma	PRRT	4.22
4	54	F	21.8	Midgut NET metastatic to liver	PRRT	3.03
5	41	M	19.7	Pancreatic NET metastatic to liver	SIRT	2.97
6	68	M	25.9	HCC	SIRT	1.30
7	69	M	26.1	HCC	SIRT	0.58
8	59	M	29.9	HCC	SIRT	2.50
9	96	M	25.9	HCC	SIRT	0.73
10	79	F	21.4	HCC	SIRT	3.00

BMI = body mass index; NET = neuroendocrine tumor; HCC = hepatocellular carcinoma.

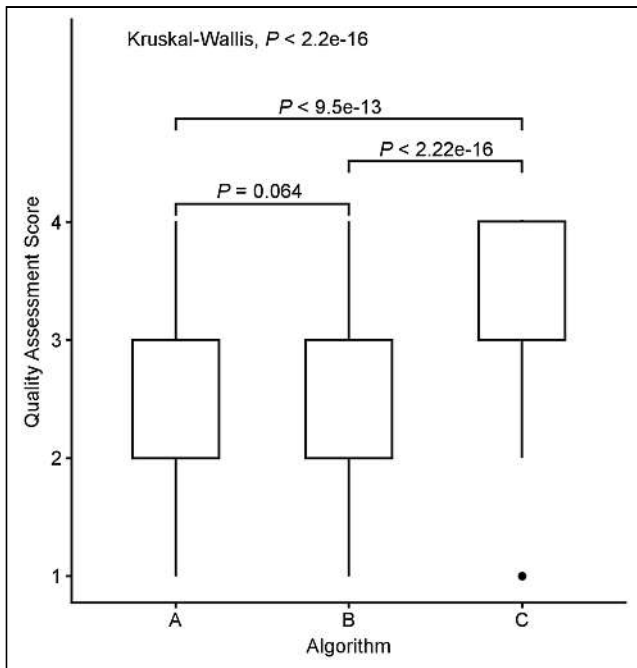


FIGURE 1. Box plots comparing median quality assessment scores among algorithms. Results from Kruskal–Wallis rank sum test and Wilcoxon rank sum test are included.

yield, with an excellent signal-to-noise ratio compared with that of algorithms A and B.

Confounding Factors

Results from multivariable ordered logistic regression analysis are summarized in Table 5. Age, body mass index, and type of radiotracer were found to be the confounding factors. Younger age (adjusted OR, 0.98; 95% CI, 0.95–0.997) and lower body mass index (adjusted OR, 0.90; 95% CI, 0.81–0.99) were associated with better quality assessment scores. SIRT was associated with significantly higher scores than PRRT (adjusted OR, 23.99; 95% CI, 11.87–50.35). Additionally, the multivariable model also confirmed that quality assessment scores for algorithm C were significantly higher (adjusted OR, 17.4; 95% CI, 9.16–34.15). On the multivariable model, algorithm B performed significantly worse than algorithm A (adjusted OR, 0.46; 95% CI, 0.26–0.80).

DISCUSSION

^{90}Y is the commonly used theranostics agent for personalized patient treatment because of its excellent physical and chemical features; its optimal half-life of 64.1 h, which is both long enough to allow relative ease in shipping and short enough to achieve a critical dosing rate in tumor tissue; its high specific activity with relatively longer soft-tissue penetration (mean, 2.5 mm), which allows effective treatment with high cross-fire effect; and its being a pure β -emitter, which results in low radiation exposure to the medical staff and family members and therefore allows outpatient application.

Absence of γ -photon emission for ^{90}Y , however, significantly limits its utility in posttherapeutic imaging and dosimetry. Bremsstrahlung imaging and PET scanning, on the other hand, are commonly used for posttherapeutic localization and dosimetry of ^{90}Y -labeled agents.

Generation of ^{90}Y bremsstrahlung photons from interaction between β^- particles and matter allows imaging of these photons using a γ -camera (4). This imaging technique is easily available but bears the inherent drawbacks of the poor resolution of scintigraphy and, thus, poor localization of biodistribution and inaccurate dosimetry of the tumor. These drawbacks are attributed to the wide range of photon energies produced, internal photon scattering, variable count rates, low spatial resolution, difficulty with collimator selection, and overlying tissue attenuation.

Although the branching ratio for internal-pair production is small, at approximately 32 per million decays, ^{90}Y PET/CT imaging has better spatial resolution and contrast and thus a higher detection rate than the traditionally used bremsstrahlung imaging in numerous phantoms and clinical studies (5,6). Interestingly, Kao et al. recently demonstrated the feasibility of using ^{90}Y PET for quantitative assessment of residual activity in the delivery apparatus instead of the conventional indirect method recommended by the manufacturer (7). The inherent problem is that the low percentage of internal-pair production requires an unrealistically long acquisition time for an adequate signal-to-noise ratio. In the real world, for the patient to remain still, 30 min per bed position would be the maximum achievable imaging time.

TABLE 4
Number and Percentage of Discrete Scores Rated by 10 Readers on 10 Patients' Scans Reconstructed Using Algorithms A–C

Algorithm	Therapy	Score 1	Score 2	Score 3	Score 4	P
A	SIRT	0 (0.0%)	11 (18.3%)	38 (63.3%)	11 (18.3%)	<0.001
	PRRT	10 (25.0%)	24 (60.0%)	6 (15.0%)	0 (0.0%)	
	SIRT + PRRT	10 (10.0%)	35 (35.0%)	44 (44.0%)	11 (11.0%)	
B	SIRT	0 (0.0%)	28 (46.7%)	29 (48.3%)	3 (5.0%)	<0.001
	PRRT	14 (35.0%)	13 (32.5%)	13 (32.5%)	0 (0.0%)	
	SIRT + PRRT	14 (14.0%)	41 (41.0%)	42 (42.0%)	3 (3.0%)	
C	SIRT	0 (0.0%)	0 (0.0%)	15 (25.0%)	45 (75.0%)	<0.001
	PRRT	1 (2.5%)	8 (20.0%)	24 (60.0%)	7 (17.5%)	
	SIRT + PRRT	1 (1.0%)	8 (8.0%)	39 (39.0%)	52 (52.0%)	

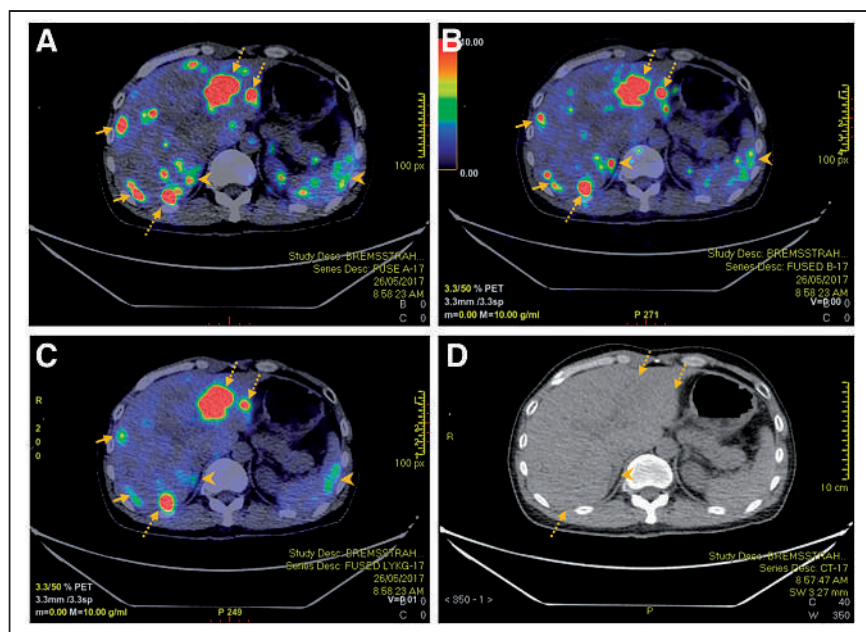


FIGURE 2. A 52-y-old man with rectal neuroendocrine cancer metastatic to liver underwent ^{90}Y -PRRT therapy. Reconstructed PET/CT using algorithms A (A), B (B), and C (C) managed to detect hepatic metastases (dotted arrows) seen on corresponding CT images (D). However, there was more visible noise within liver for PET using algorithms A and B than for PET using algorithm C (solid arrows). In addition, extrahepatic noise such as that in right adrenal gland and spleen (arrowheads) was less apparent using algorithm C. Right adrenal noise can potentially be mistaken as hepatic metastasis using algorithms A and B (arrowheads).

Any longer scan time is strongly discouraged, as movement by the patient will result in blurring of the image.

Various ^{90}Y PET imaging techniques with or without TOF and resolution recovery capabilities, as well as on semiconductor-based scanners, have shown potential resolution and contrast superior to bremsstrahlung SPECT (8,9). Despite multiple in vitro and in vivo studies using various PET imaging systems, acquisition times, and reconstruction algorithms, there

is no standardized imaging protocol thus far, although some manufacturers have provided technical support (10). Using our routinely applied algorithms, PET images are usually of poor quality despite increases in the acquisition time. The low signal-to-noise ratio makes tumor uptake quite often indistinguishable from background uptake.

Our team explored different reconstruction algorithms by formulating the filter dynamics for reconstruction in PET imaging. We noticed that the sharpness and resolution of the image improved with an increased number of iterations and subsets. This, however, also increases noise. Therefore, striking the right balance of signal-to-noise ratio is key to any filter algorithm. Our team subsequently pursued a sharp reduction in the number of iterations, thus resulting in considerable noise reduction. In addition, we reduced the filter cutoff to 5 mm, aiming for a more stringent signal bandwidth and an increased number of subsets to enhance sharpness. After multiple attempts to adjust the settings

and fine-tune the parameters, we finally settled on the LKYG algorithm, which has a significantly lower number of iterations, a thinner filter cutoff, and a larger number of subsets than our conventional algorithm. The strength of this combination is well demonstrated by the achieved significantly improved image quality.

Our study was limited by the small cohort; hence, analysis of the confounding factors was limited. Semiquantitative scoring allows room for variation, and hence, quantitative scoring will be preferred for a more objective assessment.

CONCLUSION

Optimization of image quality by improving the reconstruction algorithms for an inherently challenging PET radionuclide with low internal-pair production allows us to confirm tumoral deposition, detect nontarget radionuclide distribution, accurately calculate posttherapeutic dosimetry, and predict treatment efficacy, thus allowing advanced, personalized care planning. Aiming to increase signal-to-noise ratio, we developed a new algorithm, LKYG, for ^{90}Y PET image reconstruction, which features a decrease in the number of iterations, a decrease in the cutoff of filter thickness, and an increase in the number of subsets. This approach significantly enhanced image quality. This algorithm should be recommended for routine use of ^{90}Y PET imaging if the hypothesis is further confirmed in a multicenter prospective study.

TABLE 5

Multivariate Analysis Comparing Quality Assessment Scores

Variable	Multivariable model		
	Adjusted OR	95% CI	P
Age	0.98	0.95–0.997	0.024
Sex			
Male	Reference	—	—
Female	0.83	0.44–1.58	0.576
Body mass index	0.90	0.81–0.99	0.026
Radioligand			
PRRT	Reference	—	—
SIRT	23.99	11.87–50.35	<0.001
Dose	0.89	0.66–1.19	0.418
Algorithm			
A	Reference	—	—
B	0.46	0.26–0.80	0.007
C	17.4	9.16–34.15	<0.001

DISCLOSURE

No potential conflict of interest relevant to this article was reported.

KEY POINTS

QUESTIONS: Can the quality of ^{90}Y PET imaging be improved by optimizing the reconstruction algorithm?

PERTINENT FINDINGS: A new ^{90}Y PET image reconstruction algorithm that decreases the number of iterations, decreases the cutoff of the filter thickness, and increases the number of the subsets compared with the conventional reconstruction algorithm consistently achieved the highest-quality assessment score in both post-SIRT and post-PRRT ^{90}Y PET imaging.

IMPLICATIONS FOR PATIENT CARE: The new reconstruction algorithm significantly improved the signal-to-noise ratio and therefore enhanced the diagnostic yield of ^{90}Y PET by successfully localizing the pathologies and avoiding false-positive findings.

REFERENCES

1. Liu S. The role of coordination chemistry in the development of target-specific radiopharmaceuticals. *Chem Soc Rev*. 2004;33:445–461.
2. Sangro B, Bilbao JI, Iñarrairaegui M, Rodríguez M, Garrastachu P, Martínez-Cuesta A. Treatment of hepatocellular carcinoma by radioembolization using ^{90}Y microspheres. *Dig Dis*. 2009;27:164–169.
3. Wright CL, Zhang J, Tweedle MF, Knopp MV, Hall NC. Theranostic imaging of yttrium-90. *BioMed Res Int*. 2015;2015:481279.
4. Shen S, DeNardo GL, Yuan A, DeNardo DA, DeNardo SJ. Planar gamma camera imaging and quantitation of yttrium-90 bremsstrahlung. *J Nucl Med*. 1994;35:1381–1389.
5. Gates VL, Esmail AA, Marshall K, Spies S, Salem R. Internal pair production of ^{90}Y permits hepatic localization of microspheres using routine PET: proof of concept. *J Nucl Med*. 2011;52:72–76.
6. Bagni O, D'Arienzo M, Chiaramida P, et al. ^{90}Y -PET for the assessment of microsphere biodistribution after selective internal radiotherapy. *Nucl Med Commun*. 2012;33:198–204.
7. Kao YH, Corlett A, Jorna K, Rhodes A, Sivaratnam D. ^{90}Y PET for qualitative and quantitative assessment of residual activity in delivery apparatus after radioembolization. *J Nucl Med Technol*. 2021;49:178–179.
8. Pasciak AS, Bourgeois AC, McKinney JM, et al. Radioembolization and the dynamic role of ^{90}Y PET/CT. *Front Oncol*. 2014;4:38.
9. Mamawan MD, Ong SC, Senupe JM. Post- ^{90}Y radioembolization PET/CT scan with respiratory gating using time-of-flight reconstruction. *J Nucl Med Technol*. 2013;41:42.
10. Goedicke A, Berker Y, Verburg FA, Behrendt FF, Winz O, Mottaghy FM. Study-parameter impact in quantitative 90-yttrium PET imaging for radioembolization treatment monitoring and dosimetry. *IEEE Trans Med Imaging*. 2013;32:485–492.

Evaluation of Data-Driven Respiration Gating in Continuous Bed Motion in Lung Lesions

Takeshi Nii¹, Shota Hosokawa², Tomoya Kotani³, Hiroshi Domoto¹, Yasunori Nakamura^{1,4}, Yasutomo Tanada^{1,5}, Ryotaro Kondo¹, and Yasuyuki Takahashi²

¹Division of Radiological Technology, Department of Medical Technology, University Hospital, Kyoto Prefectural University of Medicine, Kyoto, Japan; ²Department of Radiation Science, Graduate School of Health Sciences, Hirosaki University, Hirosaki, Japan; ³Department of Radiology, Graduate School of Medical Science, Kyoto Prefectural University of Medicine, Kyoto, Japan; ⁴Department of Medical Physics, Graduate School of Medical Sciences, Kindai University, Osaka, Japan; and ⁵Department of Quantum Medical Technology, Graduate School of Medical Sciences, Kanazawa University, Ishikawa, Japan

Respiration gating is used in PET to prevent image quality degradation due to respiratory effects. In this study, we evaluated a type of data-driven respiration gating for continuous bed motion, OncoFreeze AI, which was implemented to improve image quality and the accuracy of semiquantitative uptake values affected by respiratory motion. **Methods:** ¹⁸F-FDG PET/CT was performed on 32 patients with lung lesions. Two types of respiration-gated images (OncoFreeze AI with data-driven respiration gating, device-based amplitude-based OncoFreeze with elastic motion compensation) and ungated images (static) were reconstructed. For each image, we calculated SUV and metabolic tumor volume (MTV). The improvement rate (IR) from respiration gating and the contrast-to-noise ratio (CNR), which indicates the improvement in image noise, were also calculated for these indices. IR was also calculated for the upper and lower lobes of the lung. As OncoFreeze AI assumes the presence of respiratory motion, we examined quantitative accuracy in regions where respiratory motion was not present using a ⁶⁸Ge cylinder phantom with known quantitative accuracy. **Results:** OncoFreeze and OncoFreeze AI showed similar values, with a significant increase in SUV and decrease in MTV compared with static reconstruction. OncoFreeze and OncoFreeze AI also showed similar values for IR and CNR. OncoFreeze AI increased SUV_{max} by an average of 18% and decreased MTV by an average of 25% compared with static reconstruction. From the IR results, both OncoFreeze and OncoFreeze AI showed a greater IR from static reconstruction in the lower lobe than in the upper lobe. OncoFreeze and OncoFreeze AI increased CNR by 17.9% and 18.0%, respectively, compared with static reconstruction. The quantitative accuracy of the ⁶⁸Ge phantom, assuming a region of no respiratory motion, was almost equal for the static reconstruction and OncoFreeze AI. **Conclusion:** OncoFreeze AI improved the influence of respiratory motion in the assessment of lung lesion uptake to a level comparable to that of the previously launched OncoFreeze. OncoFreeze AI provides more accurate imaging with significantly larger SUVs and smaller MTVs than static reconstruction.

Key Words: data-driven gating; lung lesions; FDG; PET/CT

J Nucl Med Technol 2023; 51:32–37

DOI: 10.2967/jnmt.122.264909

In the staging, restaging, and assessment of the treatment response of lung cancer, ¹⁸F-FDG PET/CT is useful (1,2). Evaluation of lung lesions can be influenced by respiration effects, which extend to blurred images, SUV, and metabolic tumor volume (MTV) (3–6). It has been reported that the respiratory motion of the lungs is greater in the lower lobe than in the upper lobe by a maximum of 6–12 cm (7,8). As an imaging biomarker, SUV is highly reproducible and ideal for monitoring tumor response to treatment in individual patients (9). But the reliability of ¹⁸F-FDG PET as a way to assess treatment response is compromised if these indices, which monitor tumor responsiveness in areas affected by respiratory motion and areas not affected by respiratory motion, cannot be evaluated equivalently.

To solve these problems, a scan method with respiration gating has been developed to detect breathing motion using a device that captures respiration as a waveform and detects the expiratory phase to get a low-motion image (10,11). However, as only the expiration phase is used from the collected data, the scan time is extended. A mechanism was proposed that combines amplitude-based PET gating with elastic motion correction for comprehensive respiratory management (12). Based on the spectral analysis method developed for single-bed-position PET imaging, respiration-gated imaging can be performed with deviceless waveforms that are derived directly from PET list-mode raw data (13,14). Several different approaches toward deviceless waveform generation for PET have been robustly demonstrated on single-bed-position PET (14–16). The deviceless waveform in the multibed position was first realized by step-and-shoot collection (17).

OncoFreeze (Siemens) is a type of respiration gating software that combines continuous bed motion (CBM) and device- and amplitude-based PET gating with elastic motion compensation (12). OncoFreeze provides a new respiration gating function based on HD-Chest (Siemens) technology that does not require an increase in imaging time. OncoFreeze uses a mass-preserving optical flow to generalize respiratory motion and reconstructs the image using all breath-count data from the HD-Chest image as a reference.

Received Sep. 13, 2022; revision accepted Jan. 4, 2023.
For correspondence or reprints, contact Takeshi Nii (nii21@koto.kpu-m.ac.jp).
Published online Feb. 7, 2023.
COPYRIGHT © 2023 by the Society of Nuclear Medicine and Molecular Imaging.

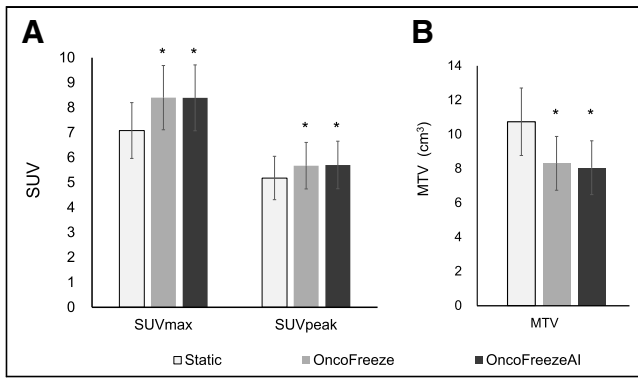


FIGURE 1. SUV_{max} and SUV_{peak} (A) and MTV (B) for static reconstruction, OncoFreeze, and OncoFreeze AI. * $P < 0.001$ for static reconstruction.

OncoFreeze AI (Siemens), a data-driven deviceless respiration gating system (DDG), was later created (18,19). OncoFreeze AI extracts respiratory waveforms for each patient from continuous PET data using FlowMotion technology (Siemens) and reconstructs respiration-gated images based on those respiratory waveforms. OncoFreeze AI estimates the respiratory waveform on the basis of the features of DDG and FlowMotion.

Both OncoFreeze AI and OncoFreeze are equipped on the Biograph Horizon 4R PET/CT system (Siemens) (19). The purpose of this study was to verify their usefulness in lung lesions.

MATERIALS AND METHODS

The Institutional Review Board and Ethics Committee of Kyoto Prefectural University of Medicine, Japan, approved this retrospective study (approval ERB-C-2578), and the requirement to obtain informed consent was waived. Thirty-eight lesions in 32 lung cancer patients who underwent ^{18}F -FDG respiration-gated PET/CT between January 2022 and May 2022 were included. The lesions consisted of 18 in the upper lobe, 5 in the middle lobe, and 15 in the lower lobe. The mean age of the patients was 73.7 y (range, 50–93 y), 20 were men and 12 women, their mean (\pm SD) body mass index was 22.28 ± 3.62 , and the mean dose of ^{18}F -FDG was 202.28 ± 25.79 MBq (3.61 ± 0.65 MBq/kg).

The PET/CT examination was performed as follows. Before ^{18}F -FDG injection, the patients fasted for more than 4 h, and their blood glucose levels were confirmed to be below 200 mg/dL. Each patient received ^{18}F -FDG using an automatic injection system (Auto Dispensing Injector UG-05; Universal Giken Co. Ltd.). Imaging was performed 60 min after the ^{18}F -FDG injection using a Biograph Horizon 4R PET/CT system and using CBM at varying speeds (1.5 mm/s from the head to the pelvis and 3.5 mm/s for the lower limbs). During examination, the belt gating system (AZ-733VI; Anzai Medical, Co. Ltd.) recorded respiratory signals that were used for gating.

PET images were reconstructed using 3-dimensional ordered-subset expectation

maximization coupled with point-spread-function and time-of-flight algorithms. The following clinical parameters were set: 4 iterations, 10 subsets, a postreconstruction gaussian filter of 5 mm in full width at half maximum, and a matrix of 180×180 pixels (pixel size, 4 mm). A low-dose CT scan was acquired for PET attenuation correction, anatomic information, and image fusion with the following scanning parameters: tube voltage, 130 kV; quality reference mAs, 90; rotation time, 0.6 s; pitch, 1.5; slice thickness, 2.0 mm; transaxial field of view, 700 mm; and matrix size, 512×512 . At the chest, static reconstruction was performed, as well as respiration-gated reconstruction using OncoFreeze AI and OncoFreeze.

In the procedure for OncoFreeze AI, first the respiratory waveform was estimated using the change in the anterior–posterior direction from the PET data collected by FlowMotion (respiratory curve A). The PET data were then divided into 500-ms volumes and were Fourier-transformed with respect to time. Respiratory curve A was also Fourier-transformed to determine the conditions (frequency and range) to be used in the spectral analysis method. All PET data were then calculated using the spectral analysis method, and a mask was created for each voxel to compensate for the effect of respiration. The mask was applied to the temporally segmented volume data to generate a respiratory waveform (respiratory curve B), which was then normalized. Respiratory curves A and B were compared to create a deviceless respiratory waveform that matched the actual respiratory motion and allowed for respiration-gated image reconstruction (18,19).

For each reconstruction algorithm, SUV_{max} , SUV_{peak} , and MTV were measured; the threshold for MTV was set at 40% SUV_{max} , and the MTV unit was cm^3 . The SUVs were calculated using body weight.

The improvement rate (IR) over static reconstruction with respiration gating was calculated for SUV_{max} , SUV_{peak} , and MTV.

The IR of SUV_{max} (IRS_{max}) for OncoFreeze AI was calculated using the following formula:

$$IRS_{max} (\%) = \frac{(OncoFreeze\ AI - static)}{static} \times 100. \quad \text{Eq. 1}$$

The same formula was also used to calculate the IR of SUV_{peak} (IRS_{peak}) and the IR of MTV (IR_{MTV}), and OncoFreeze was calculated in the same way.

SUV SD (a surrogate for image noise) was measured using a 3-cm-diameter spheric region of interest in the lung that we

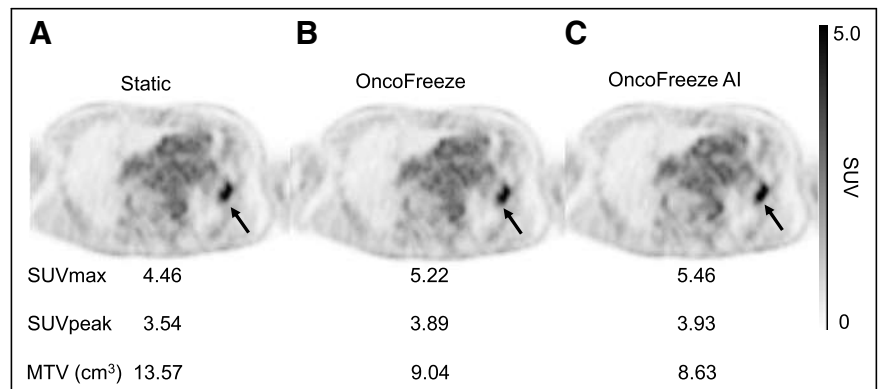


FIGURE 2. A 64-y-old man with lung cancer in left upper lobe (patient height, 175.8 cm; patient weight, 76.0 kg; ^{18}F -FDG dose, 2.99 MBq/kg). Transverse PET images are shown for static reconstruction (A), OncoFreeze (B), and OncoFreeze AI (C).

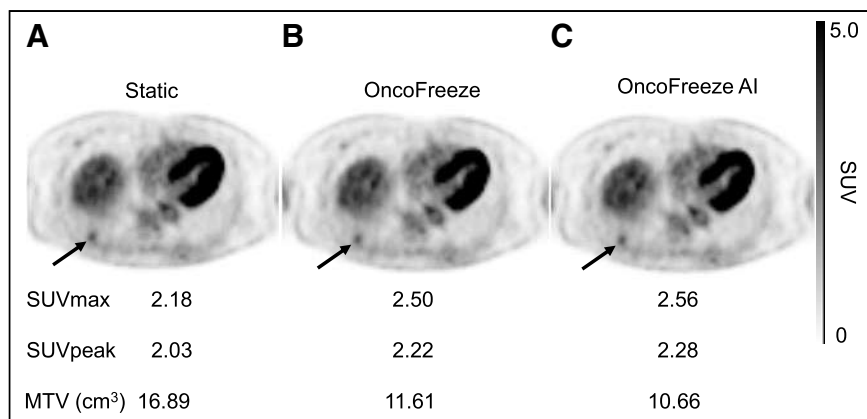


FIGURE 3. A 77-y-old woman with lung cancer in right lower lobe (patient height, 153.5 cm; patient weight, 56.7 kg; ¹⁸F-FDG dose, 3.26 MBq/kg). Transverse PET images are shown for static reconstruction (A), OncoFreeze (B), and OncoFreeze AI (C).

assessed to be free of disease. The contrast-to-noise ratio (CNR) for each sphere was calculated according to Equation 2 using the lesion SUV_{max}, background sphere SUV_{max}, and background sphere SUV SD:

$$\text{CNR} = \frac{(\text{lesion SUV}_{\text{max}} - \text{background sphere SUV}_{\text{max}})}{\text{background sphere SUV SD}}. \quad \text{Eq. 2}$$

The respiratory rate of the DDG-generated waveform was compared with the respiratory rate accepted by the waveform device. The accepted respiratory rate was recorded on the PET device.

⁶⁸Ge cylinder phantom CS-27 (Siemens), with a volume of 8,407 mL, radius of 10 cm, and radioactivity of 73.01 MBq (8.68 kBq/mL), was used to examine the quantitative accuracy in those areas where OncoFreeze AI was applied that were largely unaffected by respiratory motion. PET data were acquired at bed speeds of 0.6–3.0 mm/s (0.3 mm/s increments). A large volume of interest was constructed in the center to avoid partial-volume and edge effects, and SUV_{mean}, SUV_{max}, SUV SD, and radioactivity (Bq/mL) were calculated. These indices were determined using syngo.via (Siemens).

All statistical analyses were performed with EZR (Saitama Medical Center, Jichi Medical University), which is a graphical user interface for R (The R Foundation for Statistical Computing) designed to add statistical functions frequently used in biostatistics (20). The significance of SUV_{max}, SUV_{peak}, MTV, and CNR were determined by the Wilcoxon signed-rank test with Bonferroni adjustment. IRS_{max}, IRS_{peak}, and IRMTV were determined by the

Mann–Whitney *U* test, and the waveform respiration rate was determined by the paired *t* test.

RESULTS

SUV_{max}, SUV_{peak}, and MTV calculated by OncoFreeze AI were almost the same as those calculated by OncoFreeze. Compared with static reconstruction, SUV_{max} and SUV_{peak} showed an increase and MTV a decrease (Figs. 1–3). The mean (±SE) SUV_{max} for static reconstruction, OncoFreeze, and OncoFreeze AI was 7.08 ± 1.11, 8.40 ± 1.28, and 8.39 ± 1.31, respectively; SUV_{peak} was 5.18 ± 0.86, 5.67 ± 0.93, and 5.70 ± 0.95, respectively; and MTV was 10.73 ± 1.96, 8.31 ± 1.56, and 8.05 ± 1.51, respectively. The SUV_{max}, SUV_{peak}, and MTV of OncoFreeze AI and OncoFreeze correlated well (Fig. 4).

IRS_{max}, which represents the improvement in SUV_{max}, was 18.3% ± 2.6% for OncoFreeze and 17.9% ± 2.2% for OncoFreeze AI. IRS_{peak} was 9.7% ± 1.3% for OncoFreeze and 9.6% ± 1.3% for OncoFreeze AI. IRMTV was −24.2% ± 3.2% for OncoFreeze and −25.5% ± 2.9% for OncoFreeze AI. IRS_{max} in the upper and lower lobes was 12.0% ± 2.2% and 26.7% ± 5.2%, respectively, for OncoFreeze and 13.9% ± 2.2% and 23.8% ± 4.3%, respectively, for OncoFreeze AI. IRS_{peak} in the upper and lower lobes was 7.5% ± 1.0% and 13.3% ± 2.9%, respectively, for OncoFreeze and 7.4% ± 1.1% and 12.9% ± 2.7%, respectively, for OncoFreeze AI. IRMTV in the upper and lower lobes was −17.2% ± 3.9% and −33.7% ± 5.7%, respectively, for OncoFreeze and −22.1% ± 3.8% and −32.1% ± 5.2%, respectively, for OncoFreeze AI (Figs. 5 and 6). Only the IRS_{max} of OncoFreeze differed significantly between the upper and lower lobes (*P* = 0.0273); otherwise, there were no significant differences between the upper and lower lobes for either OncoFreeze or OncoFreeze AI.

CNR was significantly higher for OncoFreeze and OncoFreeze AI than for static reconstruction (Fig. 7). The percentage increases for CNR in comparison to static reconstruction for OncoFreeze and OncoFreeze AI were 17.9% and 18.0%, respectively. In OncoFreeze AI and OncoFreeze, the number of breaths in the generated waveform was expressed as counts. The respiratory rate of the DDG-generated waveform (OncoFreeze AI) was 223.7 ± 31.2 counts, and the respiratory rate accepted by the waveform device (OncoFreeze) was 218.0 ± 52.5 counts; this difference was not significant (*P* = 0.602). Statistical significance was set as *P* < 0.05. The

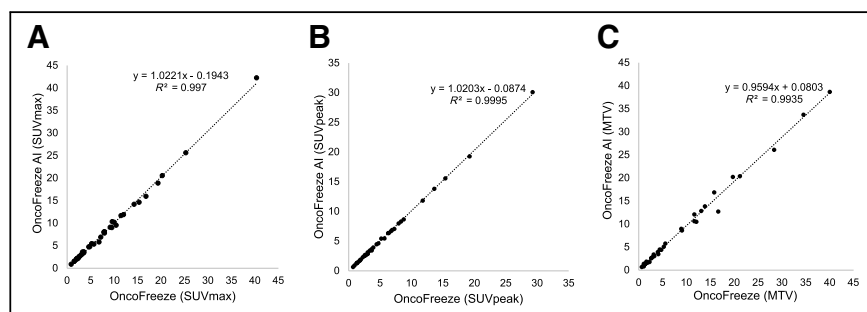


FIGURE 4. Correlation of OncoFreeze and OncoFreeze AI for SUV_{max} (A), SUV_{peak} (B), and MTV (C).

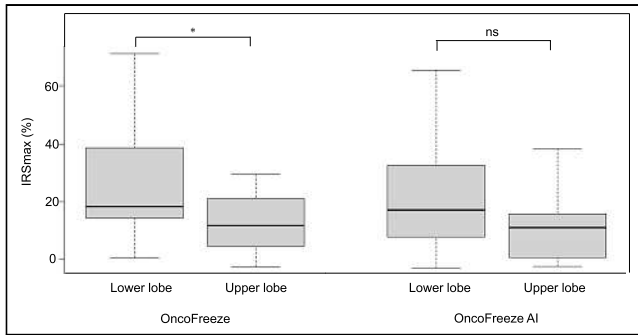


FIGURE 5. IRS_{max} from static reconstruction to OncoFreeze and OncoFreeze AI for 18 upper-lobe and 15 lower-lobe lesions. ns = not statistically significant. * $P = 0.0273$.

correlation of the accepted respiratory rate was $y = 1.31x - 76.57$, with $R^2 = 0.61$ (x , OncoFreeze AI; y , OncoFreeze).

The effect of OncoFreeze AI on quantitative accuracy was examined using a ^{68}Ge cylinder phantom, assuming a region of unchanged counts, and the SUV_{mean} of the volume of interest was 1.04 for both static reconstruction and OncoFreeze AI, regardless of bed speed. On the other hand, SUV_{max} for both static reconstruction and OncoFreeze AI increased slightly with increasing bed speed. SUV_{max} was slightly higher for OncoFreeze AI than for static reconstruction. The SUV_{max} of OncoFreeze AI, when the SUV_{max} of static reconstruction was set to 1, averaged 1.05 ± 0.02 , showing little deviation from the increase in the SUV_{max} of static reconstruction with increasing bed speed. The radioactivity at the acquisition date, calculated from the radioactivity at the assay date, was 8.68 kBq/mL, and the mean radioactivity of static reconstruction and OncoFreeze AI was 9.06 ± 0.01 and 9.02 ± 0.02 kBq/mL, respectively (Table 1).

DISCUSSION

We compared OncoFreeze AI, a deviceless respiration gating system for CBM imaging, with OncoFreeze, a device-based system, on the Biograph Horizon, a popular commercially available general-purpose PET/CT machine. Reports so far have not investigated use on popular PET/CT systems and

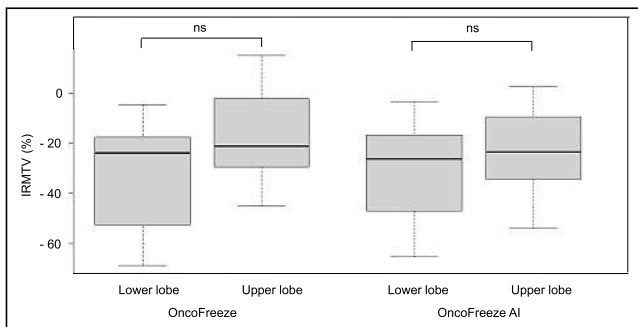


FIGURE 6. IRMTV from static reconstruction to OncoFreeze and OncoFreeze AI for 18 upper-lobe and 15 lower-lobe lesions. ns = not statistically significant.

instead have focused on the high-end Biograph mCT (Siemens) and a semiconductor PET machine, Biograph Vision (Siemens) (18,21). In this study, we found that on the Biograph Horizon, OncoFreeze AI and OncoFreeze had the same SUV_{max}, SUV_{peak}, and MTV in lung lesions (Fig. 4).

Respiratory motion is greater in the lower lobe than in the upper lobe (4). IRS_{max}, IRS_{peak}, and IRMTV showed a trend toward a greater correction effect on respiratory motion in the lower lobe than in the upper lobe. However, there was no significant difference in correction effect between the upper and lower lobes, except for IRS_{max} in OncoFreeze ($P = 0.0273$) (Figs. 5 and 6). Robin et al. reported a greater increase in SUV and decrease in MTV in the lower lobe than in the upper lobe because of the correction effect of respiratory motion on amplitude-based respiration-gated HD-Chest imaging (6). In the present study, the same trend was observed for both OncoFreeze and OncoFreeze AI.

Meier et al. used CNR as a metric to capture both SUV_{max} and noise. Their study reported a decrease in CNR with correction methodologies that use decreasing amounts of PET data; however, in lung lesions, the elastic motion deblurring algorithm improved the CNR of the lesion by 17.8%, with the least increase in image noise (22). In the present study, OncoFreeze and OncoFreeze AI, which did not involve a decrease in PET data, showed a significant increase in CNR (17.9% and 18.0%, respectively). The fact that the respiratory rate generated by OncoFreeze AI, which generates respiratory waveforms without a device, was not significantly different from the respiratory rate measured by the device also indicates the usefulness of OncoFreeze AI.

Since OncoFreeze AI is a deviceless method, the waveforms generated are completely dependent on the acquired PET data. To extract respiratory signals, respiratory motion must be present in the PET data (19). Therefore, using a ^{68}Ge cylinder phantom, we verified the accuracy of quantification in a region where no respiratory motion was assumed, and we found that SUV_{mean} and quantification accuracy were

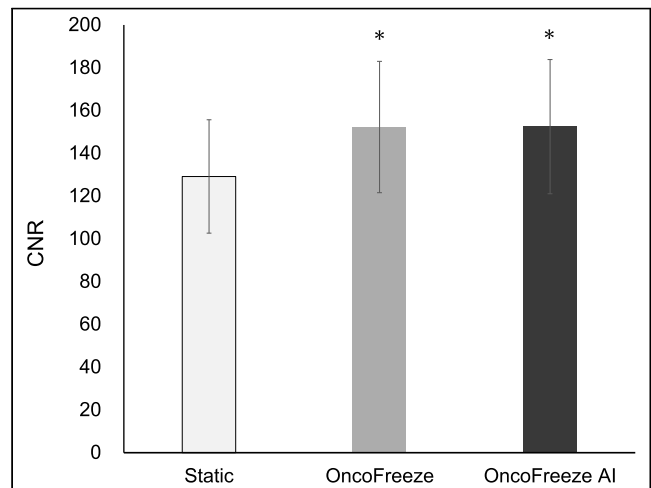


FIGURE 7. Static reconstruction, OncoFreeze, and OncoFreeze AI in CNR. * $P < 0.001$ for static reconstruction.

TABLE 1
Relationship Between Bed Motion Speed, Radioactivity Concentration, and SUV in ^{68}Ge Cylinder Phantom

Bed speed (mm/s)	Activity (kBq/mL)		SUV _{mean}		SUV SD		SUV _{max}	
	Static	OncoFreeze AI	Static	OncoFreeze AI	Static	OncoFreeze AI	Static	OncoFreeze AI
0.6	9.05	9.03	1.04	1.04	0.04	0.04	1.22	1.28
0.9	9.06	9.02	1.04	1.04	0.05	0.06	1.25	1.33
1.2	9.05	9.02	1.04	1.04	0.05	0.06	1.31	1.39
1.5	9.07	9.04	1.04	1.04	0.06	0.07	1.34	1.38
1.8	9.06	9.02	1.04	1.04	0.07	0.08	1.44	1.50
2.1	9.08	9.04	1.05	1.04	0.07	0.09	1.44	1.50
2.4	9.06	9.00	1.04	1.04	0.08	0.10	1.42	1.55
2.7	9.07	9.01	1.04	1.04	0.08	0.10	1.47	1.52
3.0	9.07	8.99	1.04	1.04	0.09	0.10	1.43	1.59

comparable to those of static reconstruction. SUV_{max} was slightly higher for OncoFreeze AI than for static reconstruction, but the change in SUV_{max} with increasing bed speed was the same for static reconstruction and OncoFreeze AI (Table 1). These results indicate that OncoFreeze AI reduced the effect of respiratory motion without compromising quantitative accuracy in the absence of respiratory motion.

There were some limitations to our study. Though the image quality and other semiquantitative parameters improved, clinical impact on patient management needs further evaluation. The present technique not only improved detection of lung lesions but also may improve detection of subdiaphragmatic hepatic lesions, which is a potential additional advantage but not examined in the present study.

One of the features of PET/CT with the CBM mechanism, such as on the Biograph Horizon, is the whole-body dynamic imaging function. At present, dynamic images from whole-body dynamic imaging cannot be combined with OncoFreeze AI; however, when this capability is realized, it will be useful (23–27). OncoFreeze AI eliminates the need to attach the device to the patient, leading to shorter examination times for the patient and reduced radiation exposure for the operator. Respiration-gated reconstruction that takes into account the effects of respiratory motion is expected to significantly contribute to SUV and harmonization, which are widely used in clinical studies of lung cancer (28,29).

CONCLUSION

OncoFreeze AI, which does not require a device, can calculate SUVs and metabolic volumes comparable to those of OncoFreeze, which uses a device to measure respiratory motion. Compared with static reconstruction, OncoFreeze AI provides more accurate lung lesion images with significantly larger SUVs and smaller metabolic volumes.

DISCLOSURE

No potential conflict of interest relevant to this article was reported.

ACKNOWLEDGMENTS

We thank Nagara Tamaki, Shigenori Matsushima, and Maki Kiba (Department of Radiology, Graduate School of Medical Science, Kyoto Prefectural University of Medicine), as well as Koki Shirako and Azusa Tahata (Department of Radiological Technology, University Hospital, Kyoto Prefectural University of Medicine), for their contributions to this report.

KEY POINTS

QUESTION: Is a commercialized DDG application useful for evaluating lung lesion uptake in CBM ^{18}F -FDG PET?

PERTINENT FINDINGS: Data-driven respiration gating was performed on 38 lung lesions in a CBM ^{18}F -FDG PET study and significantly increased SUV and decreased MTV compared with no gating. Although data-driven deviceless respiration-gated reconstruction assumes the presence of respiratory motion, the phantom test results did not impair quantification in regions where respiratory motion was absent.

IMPLICATIONS FOR PATIENT CARE: DDG reconstruction for evaluation of lung lesions in CBM FDG PET can properly evaluate ^{18}F -FDG uptake.

REFERENCES

- Brinkl I, Schumacher T, Mixl M, et al. Impact of ^{18}F -FDG-PET on the primary staging of small cell lung cancer. *Eur J Nucl Med Mol Imaging*. 2004; 31:1614–20.
- Verhagen AF, Bootsma GP, Tjan-Heijnc VCG, et al. FDG-PET in staging lung cancer: how does it change the algorithm? *Lung Cancer*. 2004;44:175–181.
- García Vicente AM, Soriano Castrejón AM, Talavera Rubio MP, et al. ^{18}F -FDG PET-CT respiratory gating in characterization of pulmonary lesions: approximation towards clinical indications. *Ann Nucl Med*. 2010;24:207–214.
- Lupi A, Zaroccolo M, Salgarello M, Malfatti V, Zanco P. The effect of ^{18}F -FDG-PET/CT respiratory gating on detected metabolic activity in lung lesions. *Ann Nucl Med*. 2009;23:191–196.
- Callahan J, Binns D, Dunn L, Kron T. Motion effects on SUV and lesion volume in 3D and 4D PET scanning. *Australas Phys Eng Sci Med*. 2011;34:489–495.

6. Robin P, Bourhis D, Bernard B, et al. Feasibility of systematic respiratory-gated acquisition in unselected patients referred for ^{18}F -fluorodeoxyglucose positron emission tomography/computed tomography. *Front Med (Lausanne)*. 2018;5:36.
7. Seppenwoolde Y, Shirato H, Kitamura K, et al. Precise and real-time measurement of 3D tumor motion in lung due to breathing and heartbeat, measured during radiotherapy. *Int J Radiat Oncol Biol Phys*. 2002;53:822–834.
8. Knybel L, Cvek J, Molenda L, Stieberova N, Feltl D. Analysis of lung tumor motion in a large sample: patterns and factors influencing precise delineation of internal target volume. *Int J Radiat Oncol Biol Phys*. 2016;96:751–758.
9. Lodge MA. Repeatability of SUV in oncologic ^{18}F -FDG PET. *J Nucl Med*. 2017;58:523–532.
10. Nehmeh SA, Erdi YE, Ling CC, Rosenzweig KE, Schoder H, Larson SM. Effect of respiratory gating on quantifying PET images of lung cancer. *J Nucl Med*. 2002;43:876–881.
11. Werner MK, Parker JA, Kolodny GM, English JR, Palmer MR. Respiratory gating enhances imaging of pulmonary nodules and measurement of tracer uptake in FDG PET/CT. *AJR*. 2009;193:1640–1645.
12. Pösse S, Büther F, Mannweiler D, et al. Comparison of two elastic motion correction approaches for whole-body PET/CT: motion deblurring vs gate-to-gate motion correction. *EJNMMI Phys*. 2020;7:19.
13. Walker MD, Morgan AJ, Bradley KM, McGowan DR. Data-driven respiratory gating outperforms device-based gating for clinical ^{18}F -FDG PET/CT. *J Nucl Med*. 2020;61:1678–1683.
14. Schleyer PJ, O'Doherty MJ, Barrington SF, Marsden PK. Retrospective data-driven respiratory gating for PET/CT. *Phys Med Biol*. 2009;54:1935–1950.
15. Kesner AL, Bundschuh RA, Detorie NC, et al. Respiratory gated PET derived in a fully automated manner from raw PET data. *IEEE Trans Nucl Sci*. 2009;56:677–686.
16. Büther F, Dawood M, Stegger L, et al. List mode-driven cardiac and respiratory gating in PET. *J Nucl Med*. 2009;50:674–681.
17. Walker MD, Morgan AJ, Bradley KM, McGowan DR. Evaluation of data-driven respiratory gating waveforms for clinical PET imaging. *EJNMMI Res*. 2019;9:1.
18. Büther F, Jones J, Seifert R, Stegger L, Schleyer P, Schäfers M. Clinical evaluation of a data-driven respiratory gating algorithm for whole-body PET with continuous bed motion. *J Nucl Med*. 2020;61:1520–1527.
19. Jones J, Hamill J, Fuerst S, Schleyer P, Hong I. *White Paper: OncoFreeze AI Deviceless Motion Management for PET Imaging*. Siemens Healthcare GmbH; 2020.
20. Kanda Y. Investigation of the freely available easy-to-use software 'EZR' for medical statistics. *Bone Marrow Transplant*. 2013;48:452–458.
21. Dias AH, Schleyer P, Vendelbo MH, Hjorthaug K, Gormsen LC, Munk OL. Clinical feasibility and impact of data-driven respiratory motion compensation studied in 200 whole-body ^{18}F -FDG PET/CT scans. *EJNMMI Res*. 2022;12:16.
22. Meierl JG, Wu CC, Cuellar SLB, et al. Evaluation of a novel elastic respiratory motion correction algorithm on quantification and image quality in abdominothoracic PET/CT. *J Nucl Med*. 2019;60:279–284.
23. Nishimura M, Tamaki N, Matsushima S, et al. Dynamic whole-body ^{18}F -FDG PET for differentiating abnormal lesions from physiological uptake. *Eur J Nucl Med Mol Imaging*. 2020;47:2293–2300.
24. Kotani T, Nishimura M, Tamaki N, et al. Comparison between dynamic whole-body FDG-PET and early-delayed imaging for the assessment of motion in focal uptake in colorectal area. *Ann Nucl Med*. 2021;35:1305–1311.
25. Nii T, Hosokawa S, Shirako K, et al. Achievements of true whole-body imaging using a faster acquisition of the lower extremities in variable-speed continuous bed motion. *Radiol Phys Technol*. 2021;14:373–380.
26. Naganawa M, Gallezot JD, Shah V, et al. Assessment of population-based input functions for Patlak imaging of whole body dynamic ^{18}F -FDG PET. *EJNMMI Phys*. 2020;7:67.
27. Osborne DR, Acuff S. Whole-body dynamic imaging with continuous bed motion PET/CT. *Nucl Med Commun*. 2016;37:428–431.
28. Berghmans T, Dusart M, Paesmans M, et al. Primary tumor standardized uptake value (SUVmax) measured on fluorodeoxyglucose positron emission tomography (FDG-PET) is of prognostic value for survival in non-small cell lung cancer (NSCLC): a systematic review and meta-analysis (MA) by the European lung cancer working party for the IASLC lung cancer staging project. *J Thorac Oncol*. 2008;3:6–12.
29. Houdu B, Lasnon C, Licaj I, et al. Why harmonization is needed when using FDG PET/CT as a prognosticator: demonstration with EARL-compliant SUV as an independent prognostic factor in lung cancer. *Eur J Nucl Med Mol Imaging*. 2019;46:421–428.

Abnormal Biologic Distribution Related to Normal Saline Among ^{99m}Tc -Dimercaptosuccinic Acid Scans

Turkiya Mahmood Al Bulushi¹, Khalsa Zahran Al-Nabhani¹, Deeksha Shetty¹, Marwa Hamed Al Sabahi¹, and Abdulhakeem Al-Rawahi²

¹Nuclear Medicine Department and Molecular Imaging Center, Royal Hospital, Ministry of Health, Muscat, Oman; and

²Oman Medical Specialty Board, Muscat, Oman

The primary aim was to describe the incidence and causes of abnormal distribution of ^{99m}Tc -dimercaptosuccinic acid (^{99m}Tc -DMSA) among patients who underwent renal scans in Royal Hospital (Oman) in 2020. The secondary aim was to assess the effect of a specific batch of normal saline A (batch 132129) compared with another normal saline, B (batches 132589 and 133325), used in the preparation of ^{99m}Tc -DMSA on the abnormal biodistribution of ^{99m}Tc -DMSA. **Methods:** This was an ambidirectional cohort study that included all patients who underwent ^{99m}Tc -DMSA renal scanning between January and December 2020. Both prospective and retrospective data collection was used. The collected data included possible causes of abnormal biodistribution, quality of ^{99m}Tc -DMSA and normal saline, and time of ^{99m}Tc -DMSA injection. **Results:** The total incidence of abnormal biodistribution was 26.5%, with the most common cause being a high creatinine level (29%). Normal saline batch A was significantly associated with abnormal biodistribution (49.7%), compared with batch B (6.6%) ($P < 0.001$). This association was more prominent among patients injected with the ^{99m}Tc -DMSA preparation after 2 h (83.0%) compared with before 2 h (13.3%). **Conclusion:** A high incidence of abnormal biodistribution of ^{99m}Tc -DMSA was detected and—for what is the first time, to our knowledge, in the literature—a specific preservative-free, normal saline that is up to standard has been identified as a significant cause of abnormal biodistribution. Nuclear medicine professionals and pharmaceutical companies should take note of this possible cause of abnormal ^{99m}Tc -DMSA biodistribution.

Key Words: renal scintigraphy; ^{99m}Tc -DMSA; normal saline; biodistribution; liver uptake

J Nucl Med Technol 2023; 51:38–43

DOI: 10.2967/jnmt.122.264241

The kidneys, one of the most vital organs in the human body, can develop a wide range of diseases that can affect bodily functions and homeostasis. Therefore, a well-timed renal disease diagnosis and an efficient treatment plan play an important role in promoting patient health and reducing side effects from prolonged treatment (1). To visualize any abnormalities in the kidneys, various noninvasive techniques are used, such

as radiologic examinations through ultrasound and CT and nuclear medicine examinations through γ -camera scanning (2).

Nuclear medicine imaging is worthwhile in clinical practice, and its analysis and correct interpretation aid professionals in making correct decisions and taking subsequent therapeutic measures. Renal scintigraphy is a nuclear medicine technique that uses medical radioisotopes to evaluate renal function (3). ^{99m}Tc -dimercaptosuccinic acid (^{99m}Tc -DMSA) is the most routinely used radiopharmaceutical for renal cortex imaging because of its nuclear properties, ready availability, low cost (4), accumulation in the renal cortex, and guidance in detecting any morphologic parenchymal abnormality (5). Uptake of ^{99m}Tc -DMSA in the kidneys, as normal biodistribution, provides an index to evaluate functional tubular mass, which depends on the proximal tubular cell membrane transport function and renal blood flow (3). Biodistribution of ^{99m}Tc -DMSA depends on its physical and chemical characteristics and, to a high degree, on the binding of proteins in the plasma (6).

Knowledge about the causes of, and factors involved in, interference with normal biodistribution of radiopharmaceuticals is worthwhile to achieve accurate diagnoses (7). It is well known that human physiology, as well as physicochemical alterations of radiopharmaceuticals, can cause disturbances in ^{99m}Tc -DMSA biologic distribution (8,9). The literature describes many reasons for altered ^{99m}Tc -DMSA biodistribution; these can be categorized mainly as related to ^{99m}Tc -DMSA preparation and formulation, such as product concentration, labeling efficiency, and pH; patients' medical conditions, such as renal tubular acidosis and renal failure; or patients' medications, such as urinary alkalinizer drugs, which contain sodium bicarbonate.

Studying the factors affecting biodistribution is important to discover unexpected trends that may significantly affect the accuracy of nuclear medicine procedures and reporting. Hence, when uptake occurs in an uncommon location, such as the liver or gallbladder, it is important to avoid attributing it to pathologic reasons, potentially reducing the procedure's diagnostic yield (10).

Between January and December 2020, we observed a difference in physiologic uptake in our renal ^{99m}Tc -DMSA patients that did not appear to stem from any of these known reasons. Furthermore, in the same period we observed abnormal biodistribution in our patients that could not be explained by any of the

Received Apr. 11, 2022; revision accepted Sep. 14, 2022.
For correspondence, contact Turkiya Al Bulushi (umyumna@hotmail.com).
Published online Oct. 4, 2022.
COPYRIGHT © 2023 by the Society of Nuclear Medicine and Molecular Imaging.

causes mentioned in the literature. Most of these patients had been injected 2 h after the ^{99m}Tc -DMSA had been prepared. It was assumed that a specific new batch of normal saline A used in the ^{99m}Tc -DMSA preparation was responsible for the abnormal biodistribution in general and at the 2-h interval specifically.

This study had 2 main objectives. The first was to estimate the incidence of abnormal ^{99m}Tc -DMSA distribution and the prevalence of its well-known causes among patients who underwent renal scans at the Royal Hospital, Oman, from January to December 2020. The second objective was to assess the effect of using a new batch of normal saline A (batch 132129) on the abnormal biodistribution of ^{99m}Tc -DMSA, compared with using saline B (batches 132589 and 133325). All of these are routinely used in the preparation of ^{99m}Tc -DMSA; however, B batches had been routinely used before A batches were recently introduced into the service.

MATERIALS AND METHODS

All patients ($n = 339$) who underwent a renal scan during the study period were included. Those who presented in January or February were retrospectively assessed using their medical records in the hospital information system (Al-Shifa +3), picture archiving and communication system (PACS). Those who presented from March to December were prospectively assessed. The assessors of biodistribution outcome were unaware of the ^{99m}Tc -DMSA preparation procedures and the patients' medical histories.

Evaluation of Health Condition and Medications

Patient data such as age, sex, scan indication, renal function test results, underlying health conditions, and medications were gathered. For assessing the incidence and possible causes of abnormal biodistribution, all ^{99m}Tc -DMSA scans during the study period were independently reviewed by an experienced nuclear medicine physician who was asked to report any abnormal biodistribution. In addition, a senior expert was consulted to resolve any issues, and an interobserver agreement assessment was done. Possible causes for any abnormality were assessed by a senior technologist and radiopharmacist by reviewing the clinical notes from the medical records.

^{99m}Tc -DMSA Injection and Scanning

The administered radioactivity for adults ranged from 150 to 200 MBq, and for children, radioactivity was calculated using the European Association of Nuclear Medicine dosage card (2016) with a minimum dose of 40 MBq. The volume of each dose was maintained at around 0.5–1 mL. Children were injected through an intravenous cannula, whereas adults were injected directly into a vein in the antecubital or dorsal metacarpal region. The patients were asked to stay well hydrated after injection. In addition, they were instructed to empty their bladders just before undergoing scanning. The patients were positioned supine for scanning, and static anterior, posterior, and bilateral oblique images of the abdomen were acquired 2 h after radiotracer injection using a low-energy high-resolution parallel-hole collimator. Each image was developed for 300 kilocounts and a 256×256 matrix. Images were processed to acquire split function for both kidneys and analyzed for the presence of any scars. Three different calibrated γ -cameras were used on a random basis for imaging: a Siemens Intevo (SPECT/CT), a Siemens Evo (SPECT), and a GE Healthcare Discovery (SPECT). A Symbia.net (Siemens) processing station (Symbiote) was used for the Intevo and the Evo, and a

Xeleris (GE Healthcare) processing station was used for the Discovery. All acquired data were stored on a computer, including counts and measurement times. For all images of kidneys, count rates were determined by choosing suitable regions of interest, and a region surrounding each region of interest was used for background correction.

The central research and ethics committee at the Royal Hospital approved this study, and the requirement to obtain informed consent was waived.

^{99m}Tc -DMSA Preparation and Formulation Evaluation

The DMSA lyophilized reagent (Technescan DMSA; Mallinckrodt) and the sodium pertechnetate (^{99m}Tc) solutions eluted from the Mallinckrodt Ultra-TechneKow generator were used in this study. All kits were prepared on the day of the procedure. Storage temperature, air bubbles, and syringe type were controlled. The Technescan DMSA was stored according to its commercial leaflet instructions at a controlled temperature (2°C – 8°C). The radiopharmaceuticals were prepared strictly following manufacturer criteria and stored at room temperature (21°C – 24°C). Air bubbles were physically removed during preparation. In addition, the time between preparation and injection was recorded. Other parameters that may have influenced the ^{99m}Tc -DMSA preparation and formulation, such as product concentration and product quality control measures, were gathered and evaluated. The DMSA vials were checked for expiration date, which was documented along with batch number.

Quality Control. The quality of the eluted solution was routinely tested for ^{99}Mo breakthrough, aluminum breakthrough, and pH. The DMSA reagent was prepared with 5 mL of ^{99m}Tc -sodium pertechnetate solution using varied tracer activities of 1,200–3,700 MBq. It was then incubated at room temperature for 15 min. The radiochemical purity was determined using Biodex chromatography strips and acetone as a mobile phase. The pH of the final product was checked using validated Merck pH indicator strips.

Normal Saline Batches. Patients for whom different batches of normal saline were routinely used in the preparation of ^{99m}Tc -DMSA during the study period were compared for abnormal biodistribution.

The normal saline brand used, along with the different batch numbers and their expiration dates, were checked. Three different routinely used normal saline batches were assessed in this study: a newly introduced batch A (batch 132129, used for 17 wk during the study) and 2 batches of B (batches 133325 and 132589, used for 15 wk during the study). The pH meter SI Analytics Lab 850 was used to check the pH of normal saline and to compare with validated pH strips. The limulus amoebocyte lysate test was performed to check for bacterial endotoxins in normal saline using a calibrated Charles River Endosafe PTS. Blood platelets, chocolate agar plate, and brain heart infusion broth were used to test normal saline sterility in an institutional microbiology lab.

Data Analysis

Data were analyzed by SPSS, version 24 (IBM). Categorized variables and incidence were presented as frequencies and percentages. The difference in the incidence of abnormal biodistribution in the 2 compared groups (batches A and B) was assessed using the χ^2 test with relative risk and its 95% CI. A P value of less than 0.05 was considered significant.

RESULTS

In total, 339 patients who underwent a ^{99m}Tc -DMSA renal scan were included in this study, 54% of whom were male.

TABLE 1
Medical Conditions and Medication Affect ^{99m}Tc -DMSA Biodistribution

Cause	Patients (n)
High creatinine	26
Medication/urinary alkalinizer	3
Fatty liver	1
Liver and spleen enlargement	1
Poor quality control measures for ^{99m}Tc -DMSA	0

TABLE 2
Quality Control Test Results for Eluted Solutions and Final Products

Test	Accepted limit	Average result
^{99}Mo breakthrough	<0.1%	0.02%
Al^{+3} breakthrough	Eluted spot less intensely colored than standard solution	All passed
^{99m}Tc pH	4.0–8.0	5.0
^{99m}Tc -DMSA pH	2.5–3.5	3.1
Labeling efficiency	≥95%	98.2%

The sample included 48% children, 35% infants, and 17% adults. Indications for the ^{99m}Tc -DMSA renal scan included vesicoureteral reflux (19%), urinary tract infection (12%), renal scars (11%), posterior urethral valves (9%), and neuro-pathic bladder (7%), as well as evaluation for potential kidney donation (3%).

The incidence of abnormal biodistribution among the studied sample was 26.5% (90 patients); 31 of these patients were found to have obvious causes for abnormal biodistribution. Table 1 summarizes the data on patients with known causes of abnormal biodistribution. High creatinine in patients with chronic kidney disease was responsible for 26 (29%) of the abnormal cases. Urinary alkalinizer treatment was responsible for 3 cases. Fatty liver and enlargement of the liver and spleen were responsible for 2 cases, respectively.

Regarding the quality control measures, none of the abnormal biodistribution cases were attributed to poor quality control measurement for ^{99m}Tc -DMSA. The quality

control tests of prepared ^{99m}Tc -DMSA were performed for all eluted solutions and final products before clinical use. The labeling efficiency and pH were within the acceptance level at 15 min and 2 h after preparation. Quality control results are shown in Table 2.

In relation to normal saline quality control, all 3 normal saline batches used were preservative-free. All institutional investigation results for the 3 normal saline batches complied with manufacturer specifications in the certificate of analysis. Table 3 shows the quality control results for normal saline batches compared with manufacturer standards.

Of the total number of patients, 157 (46%) were injected with ^{99m}Tc -DMSA prepared using batch A normal saline, and 182 (54%) were injected using batch B. Among the batch A group, 78 scans (49.7%) showed abnormal biodistribution, compared with 12 (6.6%) among the batch B group. The relative risk was 7.5 (95% CI, 4.3–13.3). This difference was statistically significant ($P < 0.001$).

Regression analysis revealed that the use of normal saline A, the presence of a cause, and injection of ^{99m}Tc -DMSA after 2 h from preparation were all independent factors for abnormal biodistribution ($P < 0.001$).

Subanalysis showed that the association of normal saline A and abnormal biodistribution existed mainly among those who were injected after 2 h. In this regard, among this group (injected after 2 h), 83.0% of the normal saline A group developed abnormal biodistribution, compared with 8.1% in the normal saline B group ($P < 0.001$). However, in those who were injected before 2 h, 13.3% of the normal saline A group developed abnormal biodistribution, compared with 4.8% of the normal saline B group ($P = 0.6$).

With regard to the association between different factors and abnormal biodistribution, 88.2% of those who reported obvious causes for abnormal biodistribution developed abnormal biodistribution, compared with 19.7% among those who did not report any obvious cause ($P < 0.001$). With regard to time of injection, 42.0% of those who were injected after 2 h from ^{99m}Tc -DMSA preparation developed abnormal biodistribution, compared with 8.9% among those who were injected before 2 h ($P < 0.001$).

DISCUSSION

Initiation of this study was based on clinical observation of an increased number of abnormal ^{99m}Tc -DMSA biodistribution

TABLE 3
Institutional Investigation Results Compared with Manufacturer Specifications for Normal Saline Quality Control

Test	Accepted limit	Normal saline		
		Batch A (132129)	Batch B (132589)	Batch B (133325)
Visual inspection	Clear, colorless	Clear, colorless	Clear, colorless	Clear, colorless
pH	4.5–7.0	5.5	5.6	5.8
Osmolarity (mmol/L)	308	287	282	280
Endotoxin/pyrogen (IU/mL)	<2.5	<2.5	<2.5	<2.5
Sterility	No growth or turbidity	Sterile	Sterile	Sterile

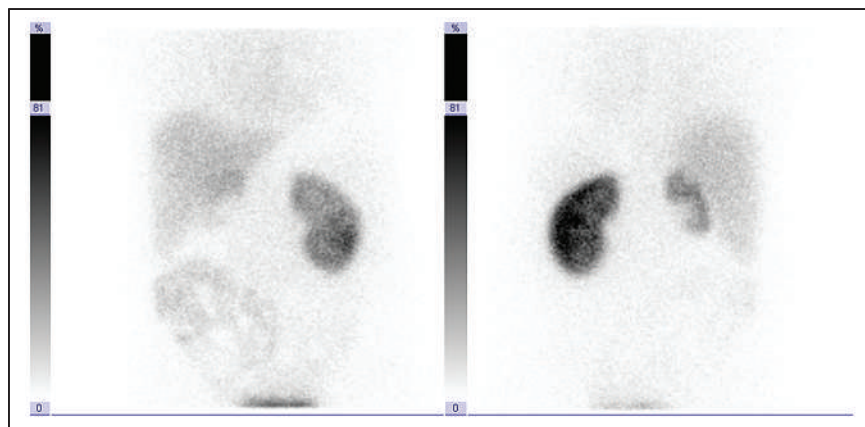


FIGURE 1. Anterior and posterior images of adult with abnormal ^{99m}Tc -DMSA distribution pattern in liver, colon, and background.

cases among patients who underwent ^{99m}Tc -DMSA scanning over a specific period. Unexpectedly, this study found a high incidence of abnormal ^{99m}Tc -DMSA biodistribution among the scanned patients. The radiotracer uptake was seen as a high background level with accumulation in the liver and, to a lesser extent, in the gallbladder and bowel loops. These are commonly reported sites for abnormal ^{99m}Tc -DMSA biodistribution, as shown in Figure 1 for adults and Figure 2 for children. The common reported causes for abnormal biodistribution in this study were high creatinine level, medications, and liver diseases. In addition, we found that a certain batch of normal saline used in the preparation of ^{99m}Tc -DMSA was associated with abnormal biodistribution of ^{99m}Tc -DMSA.

of altered ^{99m}Tc -DMSA biologic behavior. In this study, 26 patients with abnormal biodistribution had renal problems with high creatinine levels; therefore, this was the explanation for high background and liver uptake among these patients. In addition, liver and spleen diseases may also influence the biodistribution of ^{99m}Tc -DMSA (5). Two of the evaluated patients in our study who demonstrated abnormal biodistribution had liver and spleen diseases.

Besides disease status, recent medication history was assessed for all patients to evaluate for possible interference and impact on the bioavailability of the radiopharmaceutical at abnormal sites and, therefore, on image quality. Gomes et al. (12) and Bernardo et al. (7) found evidence that the biodistribution of radiopharmaceuticals may be altered

Although we found no study in the literature addressing the incidence of abnormal biodistribution of ^{99m}Tc -DMSA, in a normal situation and according to clinical observation, the incidence of abnormal biodistribution is expected to be lower than the reported 26%. This can be extrapolated from the incidence of abnormal biodistribution among patients who received normal saline batch B (6.6%), which had been routinely used before normal saline A batch was introduced into the service for preparation of ^{99m}Tc -DMSA.

According to Rajić et al. (11), impairment of tubular function is considered the most important cause

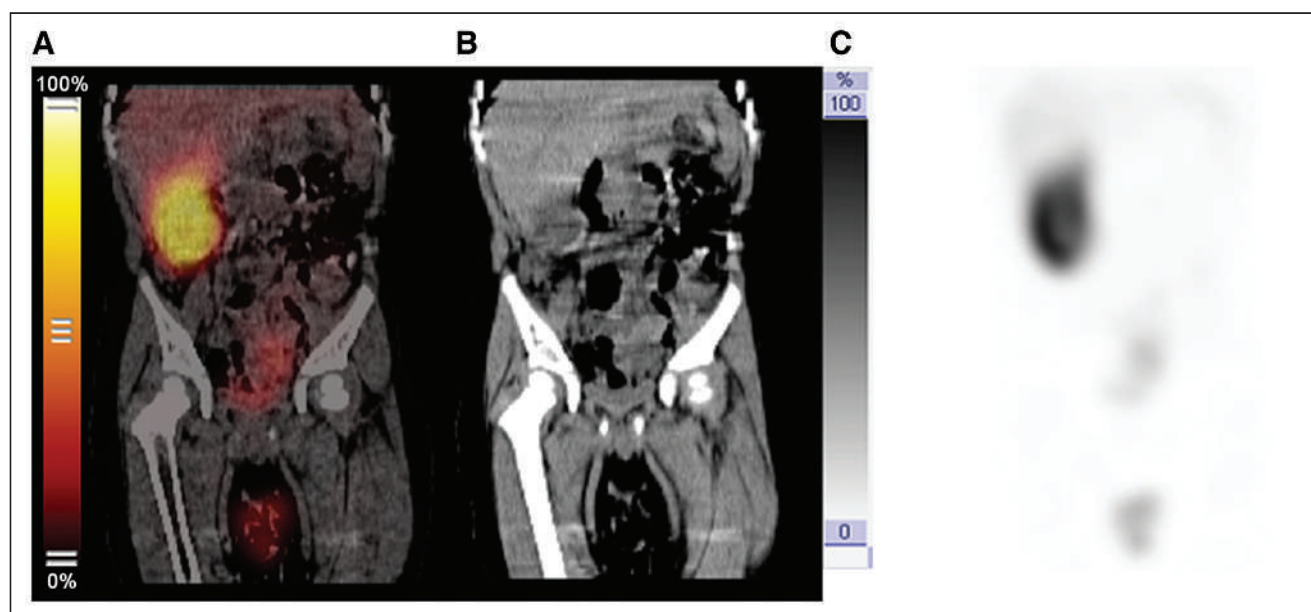


FIGURE 2. (A) Fused sagittal image of ^{99m}Tc -DMSA study of child with history of cross-fused ectopic kidney, showing high background, liver, and colon uptake. (B) Corresponding CT image. (C) Corresponding SPECT image.

by patient medications. Medications such as ammonium chloride and sodium bicarbonate can reduce renal uptake and increase liver uptake (10). Three of the patients in this study were receiving urinary alkalinizer drugs, which contain sodium bicarbonate. Furthermore, contamination during dispensing or administering of antiseptics can lead to abnormal biologic distribution of ^{99m}Tc -DMSA. One example is chlorhexidine antiseptic, which can interfere with ^{99m}Tc -DMSA and lead to the formation of a colloidal complex and, subsequently, to unfavorable liver and spleen uptake (13). In this study, the antiseptic used contained isopropyl alcohol.

On the other hand, Fakhari et al. (5) reported that dehydrated patients have less kidney uptake of ^{99m}Tc -DMSA because of decreasing kidney capacity, leading to abnormal biodistribution of ^{99m}Tc -DMSA. Hydration significantly alters the biologic distribution of ^{99m}Tc -DMSA; thus, maintaining adequate hydration is an important factor to decrease background levels of ^{99m}Tc -DMSA (9). As part of our local departmental procedural protocol, all patients in this study were instructed to stay well hydrated after injection.

Moreover, small changes in preparation procedures can cause differences in the formation of different types of products and lead to differences in their biodistribution (14). Therefore, procedures for kit preparation and injection were studied and standardized in this study, with the kits prepared in the same manner and following the manufacturer's instructions. Temperature can also affect biodistribution, as product stability decreases when temperature is raised (2). The ^{99m}Tc -DMSA cold kits used in our department are stored in a calibrated, controlled-temperature refrigerator (2°C – 8°C), and labeled vials are stored at a temperature below 25°C . Furthermore, it is known that liver uptake can increase when 1 mL of air is bubbled into the ^{99m}Tc -DMSA solution 20 min before injection (15). During preparation in this study, the solutions were not exposed to oxygen and the product was used within 4 h after preparation. In addition, it has been documented by Vallabhajosula et al. (10) that in the preparation of ^{99m}Tc -DMSA, radiochemical impurities increase with decreased product concentration. In our study, ^{99m}Tc -DMSA products were prepared with an appropriate concentration of 1,200–3,700 (MBq/5mL) to achieve an acceptable labeling efficiency according to the manufacturer's instructions. The radiochemical purity test, used just before administration of the radiotracer, revealed acceptable results with less than 2% radiochemical impurity.

It has been proven that ^{99m}Tc -DMSA stability is sensitive to pH and reactants (16). In our study, the eluted solution of ^{99m}Tc had an average pH of 5.0, and 3.1 was the average pH of the ^{99m}Tc -DMSA. The quality, safety, and efficacy of all products were confirmed by quality control tests

performed for all products before clinical use. In particular, the labeling efficiency and pH were tested at 15 min and 2 h after ^{99m}Tc -DMSA preparation. However, there was still a profoundly abnormal biodistribution.

The effect of normal saline used in the preparation of ^{99m}Tc -DMSA on the abnormal biodistribution of ^{99m}Tc -DMSA was checked by comparing different batches. These batches were tested and compared with the manufacturer's certificate of analysis to investigate any problem. All institutional investigation results complied with the manufacturer specifications and showed laboratory results similar to other tested batches.

Our study showed that normal saline batch A was responsible for the unexpected increase in abnormal ^{99m}Tc -DMSA biodistribution and that the abnormality was present mainly in patients injected 2 h after preparation of the ^{99m}Tc -DMSA. To our knowledge, this was the first study to discover that a specific preservative-free normal saline that is up to standard is a significant cause of abnormal biodistribution. Other studies have attributed a similar finding to the preservatives that may be added to the saline. Most of these effects were linked to reactions with benzyl alcohol, the most common preservative used in sterile normal saline (17,18). Another finding is that bacteriostatic normal saline, used in the preparation and dilution of many ^{99m}Tc -radiochemicals, can adversely affect radiochemical purity, stability, and biodistribution compared with preparation with preservative-free normal saline (19). Furthermore, it has been reported that dilution of ^{99m}Tc -pertechnetate with bacteriostatic normal saline increases the percentage of insoluble and colloidal impurities (19).

CONCLUSION

In this study, the abnormal biodistribution of ^{99m}Tc -DMSA among scanned patients was high. We clearly observed that a certain preservative-free batch of normal saline, which was up to standard, was a parameter in abnormal biodistribution for ^{99m}Tc -DMSA procedures. Although the effect of normal saline on ^{99m}Tc -DMSA kit preparation is yet to be revealed, the literature does not, to our knowledge, include studies evaluating such a factor. This should alert nuclear medicine professionals to question the validity of any unexpected abnormal biodistribution among scanned patients. It seems that quality control measures are not enough to judge the use of any new batch of normal saline in ^{99m}Tc -DMSA preparation. Pharmaceutical companies should consider testing new manufactured normal saline batches on a sample of patients before marketing the batches.

DISCLOSURE

No potential conflict of interest relevant to this article was reported.

KEY POINTS

QUESTION: Can a preservative-free normal saline be a significant cause of abnormal biodistribution of ^{99m}Tc -DMSA among patients undergoing a renal scan?

PERTINENT FINDINGS: The incidence of abnormal biodistribution among patients who underwent a ^{99m}Tc -DMSA renal scan was high when a specific batch of normal saline was used to prepare the ^{99m}Tc -DMSA, especially in patients injected 2 h after preparation.

IMPLICATIONS FOR PATIENT CARE: Awareness by nuclear medicine professionals that a specific preservative-free normal saline can cause abnormal ^{99m}Tc -DMSA biodistribution will benefit patient care.

REFERENCES

- Matovinović MS. Pathophysiology and classification of kidney diseases. *EJIFCC*. 2009;20:2–11.
- Jan SU, Abbass HG. Preparation and evaluation of ^{99m}Tc -DMSA lyophilized kit for renal imaging. *Pak J Pharm Sci*. 2013;26:547–551.
- Çaglar M, Topaloğlu R. Reduced Tc-99m DMSA uptake in a patient with renal tubular acidosis: effect of acid-base imbalance. *Ann Nucl Med*. 2002;16:499–501.
- Hernández-Valdés D, Blanco-González A, García-Fleitas A, et al. Insight into the structure and stability of Tc and Re DMSA complexes: a computational study. *J Mol Graph Model*. 2017;71:167–175.
- Fakhari A, Mamaghani FF, Gharepapagh E, Dabiri S. Dos and don'ts that are issued through radiolabeling process of DMSA (dimercaptosuccinic acid) by $^{99m}\text{TcO}_4$ -as ^{99m}Tc -DMSA (III), the gold standard radiopharmaceutical for renal cortical scintigraphy. *J Nucl Med Radiat Ther*. 2018;9:2.
- Vanlić-Razumenić N, Joksimović J, Ristić B, et al. Interaction of ^{99m}Tc -radiopharmaceuticals with transport proteins in human blood. *Nucl Med Biol*. 1993;20:363–365.
- Bernardo-Filho M, Santos-Filho SD, Moura EG, et al. Drug interaction with radiopharmaceuticals: a review. *Braz Arch Biol Technol*. 2005;48:13–27.
- Ghione S, Fommei E, Palla L, et al. Changes in renal function during physical and mental effort. *Clin Exp Hypertens A*. 1987;9(suppl 1):89–96.
- Yee CA, Lee HB, Blaufox MD. Tc-99m DMSA renal uptake: influence of biochemical and physiologic factors. *J Nucl Med*. 1981;22:1054–1058.
- Vallabhajosula S, Killeen RP, Osborne JR. Altered biodistribution of radiopharmaceuticals: role of radiochemical/pharmaceutical purity, physiological, and pharmacologic factors. *Semin Nucl Med*. 2010;40:220–241.
- Rajić M, Bogicevic M, Antic S, et al. Alteration of ^{99m}Tc -DMSA biodistribution in glomerulonephritis. *Nucl Med Rev Cent East Eur*. 2002;5:15–19.
- Gomes ML, Braga AC, Mattos DM, et al. Effect of the mitomycin-C on the biodistribution of the radiopharmaceutical ^{99m}Tc -phytic acid in mice: a model to evaluate the toxic effect of a chemical drug. *J Appl Toxicol*. 2002;22:85–87.
- Firuzyar T, Ghaedian T. The effect of antiseptic on ^{99m}Tc -DMSA scans. *Clin Nucl Med*. 2017;42:237–238.
- Staník R, Světlík J, Benkovský I. DMSA and its complexes with radioisotopes. *J Radioanal Nucl Chem*. 2012;293:545–554.
- de Castro TOM, da Silva NG, Colturato MT, et al. Study of ^{99m}Tc -DMSA biodistribution in experimental animals. International Atomic Energy Agency website. https://inis.iaea.org/collection/NCLCollectionStore/_Public/48/094/48094690.pdf?r=1. Published 2017. Accessed November 2, 2022.
- Zolle I, ed. *Technetium-99m Pharmaceuticals*. Springer; 2007:291–292.
- Luo J, Yu H, Wang H, Wang H, Peng F. Aerobic oxidation of benzyl alcohol to benzaldehyde catalyzed by carbon nanotubes without any promoter. *Chem Eng J*. 2014;240:434–442.
- Li J, Li M, Sun H, Ao Z, Wang S, Liu S. Understanding of the oxidation behavior of benzyl alcohol by peroxymonosulfate via carbon nanotubes activation. *ACS Catal*. 2020;10:3516–3525.
- Ponto JA. Volume 11, lesson 1: preparation and dispensing problems associated with technetium Tc-99m radiopharmaceuticals. University of New Mexico website. https://pharmacyce.unm.edu/program_information/freesessionfiles/vol11lesson1.pdf. Published 2002. Accessed November 2, 2022.

A Headrest Made of Extruded Polystyrene Reduces the Influence of Attenuation Correction on Human Brain SPECT Images

Makoto Ohba¹, Yasuaki Kokubo², Koji Suzuki¹, Masafumi Kanoto³, and Yukihiro Sonoda²

¹Department of Radiology, Yamagata University Hospital, Yamagata, Japan; ²Department of Neurosurgery, Faculty of Medicine, Yamagata University, Yamagata, Japan; and ³Department of Radiology, Division of Diagnostic Radiology, Yamagata University Graduate School of Medical Science, Yamagata, Japan

Previous reports suggest that a headrest made of carbon significantly influences cerebral blood flow in the anterior and posterior regions by image reconstruction and attenuation correction (AC). The present study aimed to develop a headrest that reduces the influence of the AC process on human brain SPECT. **Methods:** To validate the performance of a headrest made of extruded polystyrene (XPS), 10 healthy controls and 43 patients with cerebrovascular disease underwent ^{99m}Tc-ethyl cysteinate dimer SPECT using a carbon headrest and an XPS headrest. We evaluated the anterior-to-posterior and middle-to-posterior ratio of the brain regions in filtered backprojection (FBP) Chang AC, ordered-subset expectation maximization (OSEM) Chang AC, and OSEM CT-based AC. **Results:** The anterior-to-posterior ratio was significantly higher with the carbon headrest than with the XPS headrest in FBP Chang AC and OSEM Chang AC ($P < 0.001$). There was no significant difference between the materials in OSEM CT-based AC. The middle-to-posterior ratio did not differ to a statistically significant extent in any correction process. **Conclusion:** Acquisition of brain SPECT images with an XPS headrest and processing by the FBP or OSEM Chang AC method enables the influence of the headrest to be reduced, especially in anterior and posterior brain regions.

Key Words: SPECT; headrest; image reconstruction; attenuation correction; XPS; extruded polystyrene

J Nucl Med Technol 2023; 51:44–48
DOI: 10.2967/jnmt.122.264729

In the acquisition of brain SPECT images, various interactions (e.g., image reconstruction, attenuation correction [AC], and scatter correction [SC]) should be considered. The influence of these interactions results in decreased image contrast and errors for which AC and SC compensate. There are 2 representative methods for AC in SPECT: Chang AC and CT-based AC (CTAC). Chang AC is based on the assumption of uniform attenuation of γ -rays by intracranial tissues. However, since there are complex structures

in the cranium (e.g., air, soft tissues, the paranasal sinus, and various degrees of skull thickness), attenuation is difficult to accurately correct (1). On the other hand, the recent widespread use of SPECT/CT has led to correction using CT data, such as CTAC. Attenuation of intracranial tissue that is nonuniform with the attenuation coefficient distribution derived from CT data can also be corrected. Thus, CTAC is expected to become more accurate than Chang AC (2).

A headrest is indispensable for brain SPECT. At present, carbon and polyethylene are the materials commonly used to construct standard headrests. Since the CT value of carbon is 300 Hounsfield units (HU), which affects the degree of γ -ray attenuation, γ -ray attenuation can affect image reconstruction processes, including AC and SC. Previous reports that compared SPECT images constructed using 2 types of AC methods have shown that CTAC is more accurate than the Chang method based on experimental data obtained with a phantom simulating the brain (3). Furthermore, in the Chang method, the anterior region of the brain shows relatively high blood flow because uniform correction is performed without considering the attenuation of γ -rays in part of the headrest. Thus, CTAC may contribute to reducing the influence of the headrest in comparison to Chang AC. However, Chang AC is still used in the reconstruction process for SPECT because SPECT/CT is not widespread enough. Therefore, headrest materials with a low CT value are needed because of the rareness of SPECT/CT systems.

We previously investigated the influence of headrests on brain SPECT using various SC and AC methods (4). We acquired a SPECT image with and without a carbon headrest to compare SPECT images. The blood flow value in the anterior region of the brain was higher than that evaluated by methods other than ordered-subset expectation maximization (OSEM) and CTAC image reconstruction. Thus, SPECT images are affected by the headrest unless both OSEM and CTAC are used to process the image. To solve this problem, we thought it necessary to use a headrest with a low CT value, almost equivalent to air, rather than carbon. Finally, we found a material, extruded polystyrene (XPS), that has a low CT value (practically equivalent to air), and

Received Jul. 28, 2022; revision accepted Nov. 3, 2022.
For correspondence or reprints, contact Yasuaki Kokubo (ykokubo@med.id.yamagata-u.ac.jp).
Published online Nov. 9, 2022.
COPYRIGHT © 2023 by the Society of Nuclear Medicine and Molecular Imaging.

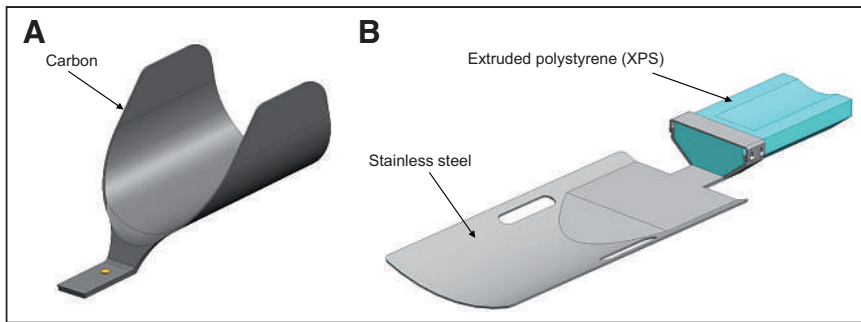


FIGURE 1. (A) Carbon headrest covering temporal to occipital regions of head, with CT value of 300 HU. (B) Hybrid headrest constructed from XPS and stainless steel, covering occipital region of head (which is in contact with XPS), with CT value of –980 HU.

we developed a new headrest made of this material. The purpose of this study was to compare the XPS headrest with a carbon headrest in healthy controls and patients with cerebrovascular disease.

MATERIALS AND METHODS

This study was approved by the Ethical Review Committee of Yamagata University Faculty of Medicine for epidemiologic research (approval 2018-199). The participants gave written informed consent to inclusion in the study and publication of their data.

Subjects

Healthy Controls. We enrolled 10 healthy controls (male, $n = 10$; mean age, 50.20 ± 7.97 y; range, 32–59 y) who had no organic lesions on MRI and no stenosis or occlusion of the intracranial artery on MR angiography. The fact that the healthy control group comprised only men was coincidental; no selection bias was made. They were assessed by brain ^{99m}Tc -ethyl cysteinate dimer (ECD) SPECT with headrests made of carbon and XPS from July 2018 to April 2019.

Patients with Cerebrovascular Disease. We enrolled 43 patients (male, $n = 30$; female, $n = 13$; mean age, 59.46 ± 16.46 y; range, 22–85 y). Seventeen patients had cervical internal carotid artery stenosis, 16 had moyamoya disease, and 4 had intracranial artery stenosis. They were assessed by brain ^{99m}Tc -ECD SPECT with carbon and XPS headrests from October 2018 to August 2020.

SPECT Acquisition

Images were acquired by ^{99m}Tc -ECD SPECT/CT using a Symbia T2 (Siemens Healthineers) with a rotating, dual-detector γ -camera; a low-energy high-resolution collimator; and 360° continuous rotation (2.5 min/rotation \times 6 rotations). Magnification was 1.45, the matrix was 128×128 (3.3 mm/pixel), the main window was 141 ± 10.5 keV, and the subwindow was 7%. The subjects were intravenously injected with 600 MBq of ^{99m}Tc -ECD while supine with their eyes closed and their head placed on the headrest. The SPECT acquisition with the carbon headrest took 20 min, starting 5 min after injection. The SPECT acquisition with the XPS headrest then took 20 min, starting 30 min after injection. CT imaging was also performed for both.

Headrests

The existing headrest (Fig. 1A) was of carbon, covered the occipital to the temporal regions, and had a CT value of 300 HU.

The new headrest (Fig. 1B) was a hybrid of XPS and stainless steel (SUS304). XPS was chosen because it is easy to process, high in strength, low in cost, not metal, and as low as –980 HU in CT value. It was structured without temporal parts to reduce the attenuation of γ -rays. To increase stability of the head, we formed a dent in the headrest where it touches the back of the patient's head. Testing of whether the headrest is strong enough for an actual clinical SPECT examination found that it could withstand a force of up to 200 N ($\text{kg}\cdot\text{m}/\text{s}^2$) and was as durable as the carbon headrest, which could withstand a force of up to 180 N. Furthermore, if the occipital region is close

to stainless steel, the cerebral blood flow cannot be evaluated correctly because of metal artifacts. Therefore, the patient's neck was positioned at the joint between the XPS and the stainless steel so that the stainless steel did not enter the cerebral blood flow evaluation site.

Image Analysis

Images were reconstructed by filtered backprojection (FBP) and ordered-subset expectation maximization (OSEM) with the combination of AC and SC. Chang AC, which is used in FBP and OSEM, creates an attenuation coefficient distribution that does not consider the headrest, as correction applies only to intracranial tissue. The CTAC used in OSEM creates an attenuation coefficient distribution of CT data and corrects both the intracranial tissue and the headrest. SC in SPECT was performed with a multienergy window.

^{99m}Tc -ECD SPECT was analyzed using a 3-dimensional (3D) stereotactic region-of-interest template (PDRadiopharma Inc.) to verify the influence of the headrest materials. The regions of interest were grouped into 12 segments in each hemisphere (A, callosomarginal; B, precentral; C, central; D, parietal; E, angular; F, temporal; G, posterior; H, pericallosal; I, lenticular nucleus; J, thalamus; K, hippocampus; and L, cerebellar) (5). We evaluated the count ratios for the anterior region (A+B) to the posterior region (G) and for the middle region (D+F) to the posterior region (G) to investigate the influence in the anterior and middle areas of the brain defined by the 3D stereotactic region-of-interest template (Fig. 2). We divided the images into the following 3 groups based on the methods of image reconstruction

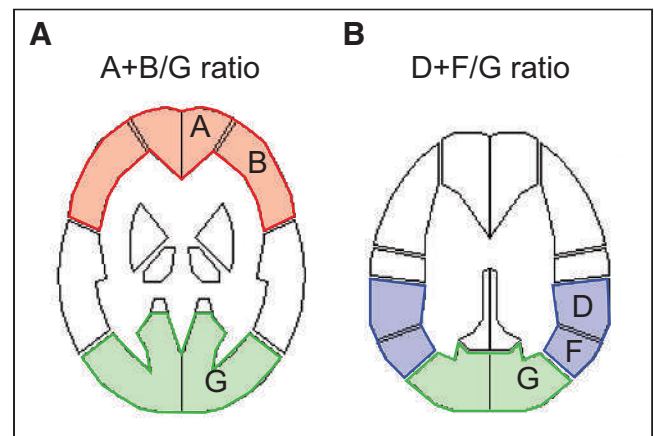


FIGURE 2. 3D stereotactic region-of-interest template for A+B/G ratio (A) and D+F/G ratio (B).

TABLE 1
Comparison of A+B/G and D+F/G Ratios Between Carbon and XPS Headrests in Healthy Controls ($n = 10$)

Parameter	A+B/G			D+F/G		
	Carbon	XPS	<i>P</i>	Carbon	XPS	<i>P</i>
FBP Chang AC	0.97 ± 0.02	0.93 ± 0.02	<0.001*	0.89 ± 0.02	0.89 ± 0.02	0.173
OSEM Chang AC	0.98 ± 0.04	0.94 ± 0.02	<0.001*	0.90 ± 0.02	0.90 ± 0.02	0.423
OSEM CTAC	0.91 ± 0.02	0.91 ± 0.02	0.322	0.88 ± 0.01	0.88 ± 0.01	0.037

*Statistically significant.

and AC: FBP Chang AC, OSEM Chang AC, and OSEM CTAC. The results for the 4 groups were compared between the carbon and XPS headrests.

All statistical analyses were performed using the SPSS software program (version 26; SPSS Inc.). Differences in the A+B/G and D+F/G ratios among the different image reconstruction and correction methods with and without a headrest were analyzed using a paired *t* test. *P* values of less than 0.01 were considered to indicate statistical significance.

RESULTS

Healthy Controls

Table 1 compares the average A+B/G ratio and D+F/G ratio for each group using the carbon and XPS headrests. In FBP Chang AC and OSEM Chang AC, there were significant differences in the A+B/G ratio between the carbon and XPS headrests ($P < 0.001$). On the other hand, in OSEM CTAC, there were no significant differences in the A+B/G ratio between the carbon and XPS headrests. There were no significant differences in the D+F/G ratio between the carbon and XPS headrests in any group.

Figure 3 shows representative images. For the anterior brain region, images constructed using FBP Chang AC and OSEM Chang AC with a carbon headrest showed a higher blood flow than those with an XPS headrest. On the other hand, images constructed using OSEM CTAC with a carbon headrest did not differ from images constructed using the same methods with an XPS headrest.

Table 2 compares the average A+B/G ratio and D+F/G ratio for each group between the carbon and XPS headrests. In FBP Chang AC and OSEM Chang AC, significant differences in the A+B/G ratio were observed between the carbon and XPS headrests ($P < 0.001$). On the other hand, in OSEM CTAC, the A+B/G ratio did not differ between the carbon and XPS headrests. The D+F/G ratio

did not differ to a statistically significant extent between the carbon and XPS headrests in any group.

Figure 4 shows representative images. A 45-y-old man with atherothrombotic infarction due to left middle cerebral artery stenosis underwent MRI, 3D CT angiography, and ^{99m}Tc -ECD SPECT. MRI fluid-attenuated inversion-recovery sequences showed high-intensity lesions due to cerebral infarction in the left frontal and temporal lobes, including the insular cortex. 3D CT angiography showed severe stenosis of the left middle cerebral artery. For the anterior brain region, images constructed using FBP Chang AC and OSEM Chang AC with a carbon headrest showed a higher blood flow than those obtained using an XPS headrest. On the other hand, images using OSEM CTAC with a carbon headrest did not differ from those obtained using an XPS headrest. The ratio of the ischemic side to the nonischemic side for the counts in region-of-interest B, which

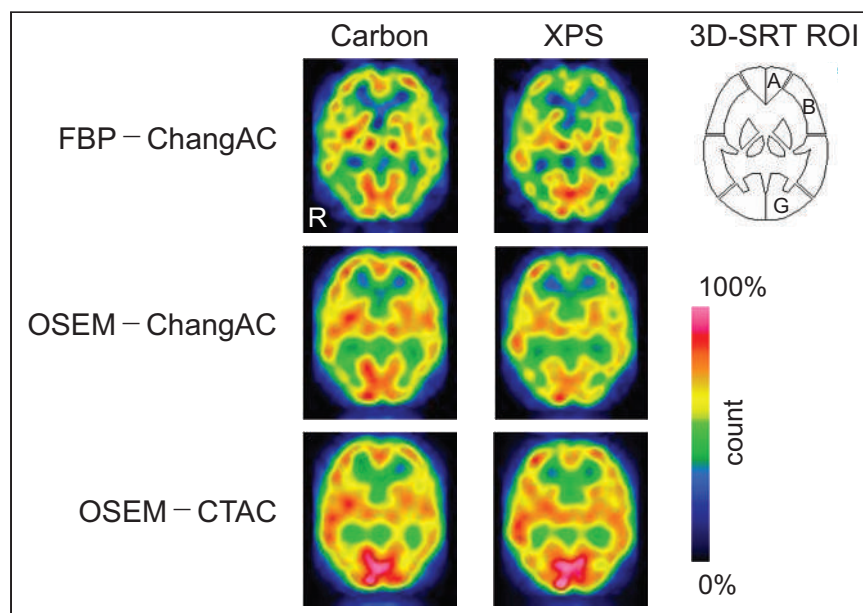


FIGURE 3. Comparison of ^{99m}Tc -ECD SPECT images obtained using carbon and XPS headrests in healthy controls. Images constructed with FBP Chang AC and OSEM Chang AC using carbon headrest show higher cerebral blood flow in anterior part of brain than do images constructed with same methods using XPS headrest. In images constructed with OSEM CTAC, anterior and posterior parts of brain do not differ between images obtained using carbon and XPS headrests. SRT = stereotaxic region-of-interest template; ROI = region of interest.

TABLE 2
Comparison of A+B/G and D+F/G Ratios Between Carbon and XPS Headrests in Patients with Cerebrovascular Disease ($n = 43$)

Parameter	A+B/G			D+F/G		
	Carbon	XPS	<i>P</i>	Carbon	XPS	<i>P</i>
FBP Chang AC	0.96 ± 0.05	0.91 ± 0.05	$<0.001^*$	0.87 ± 0.04	0.87 ± 0.04	0.343
OSEM Chang AC	0.96 ± 0.05	0.92 ± 0.06	$<0.001^*$	0.88 ± 0.04	0.88 ± 0.04	0.938
OSEM CTAC	0.89 ± 0.04	0.89 ± 0.05	0.893	0.86 ± 0.03	0.86 ± 0.03	0.099

*Statistically significant.

includes the middle cerebral artery territory, was 0.97 for carbon and 0.95 for XPS when viewed with FBP Chang AC.

DISCUSSION

XPS as a Headrest Material

Previous studies reported that the headrest affected SPECT images when the Chang method was used for AC (2,3). The cause is considered to be the effect of the carbon from which the headrest is constructed on image reconstruction processes, especially AC. Since carbon has a high CT value of 300 HU, a carbon headrest can attenuate γ -rays generated from brain parenchyma adjacent to the headrest (e.g., the occipital region in Chang AC). Thus, the posterior region is relatively low, and the anterior region is considered to have a high cerebral blood flow distribution. Our previous report (4)

showed that with FBP Chang AC and OSEM Chang AC, significant differences in A+B/G ratio were observed between images obtained with and without a headrest. As a result, the anterior region appeared to have a higher cerebral blood flow than the posterior region, except when the OSEM CTAC method was used. Therefore, we need to create a headrest made of materials with low CT values and a low degree of γ -ray attenuation. Among such materials, the CT value of XPS is -980 HU, which is extremely low. Since XPS comprises innumerable bubbles, attenuation of γ -rays is considered to be small and the CT value low. Furthermore, the structure of XPS differs from that of expanded polystyrene beads, a well-known material with a structure consisting of continuous large bubbles. Since the bubbles are not continuous and are partitioned by a thin film of polystyrene resin in XPS, XPS has high strength and is suitable for headrest construction.

Additionally, since XPS is in a completely sealed state, it suppresses water attenuation and heat conduction, is unlikely to change, and has high durability. Thus, we finally selected XPS as the headrest material.

Comparison Between Carbon and XPS for the Acquisition of ^{99m}Tc -ECD SPECT Images

For the anterior brain region, images obtained using FBP Chang AC and OSEM Chang AC with a carbon headrest showed a higher blood flow than those with XPS in all participants. This is because the γ -rays generated from the brain parenchyma around the headrest, especially in the occipital region, are absorbed by the carbon headrest because of the γ -ray attenuation. Thus, the cerebral blood flow distribution is low in the occipital region and relatively high in the anterior region (3).

Our results show that use of an XPS headrest reduces the difference between the anterior and posterior regions of the

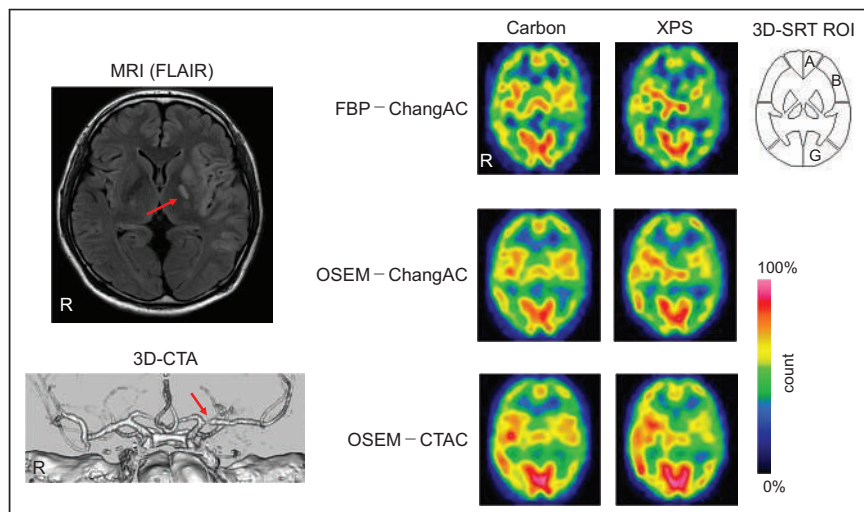


FIGURE 4. Comparison of ^{99m}Tc -ECD SPECT images obtained using carbon and XPS headrests in patients with cerebrovascular disease. Fluid-attenuated inversion-recovery MR images show high-intensity lesions due to cerebral infarction in left frontal and temporal lobes, including insular cortex. 3D CT angiography shows severe stenosis of left middle cerebral artery. For anterior brain region, images constructed using FBP Chang AC and OSEM Chang AC with carbon headrest show higher cerebral blood flow than do images constructed using same methods with XPS headrest. Images constructed using OSEM CTAC with carbon headrest show no difference from images constructed using same methods with XPS headrest. CTA = CT angiography; FLAIR = fluid-attenuated inversion-recovery; ROI = region of interest; SRT = stereotaxic region-of-interest template.

brain. Thus, AC using XPS is less likely to affect image acquisition, even with the Chang method. In OSEM CTAC, there was no significant difference between carbon and XPS because correction from the CT data is based on both the intracranial tissue and the headrest, considering the nonuniformity of the brain in the CTAC method (6). Therefore, OSEM CTAC can be considered a reference standard. The A+B/G ratio by Chang AC using XPS and OSEM CTAC was similar. The skull has different degrees of thickness depending on the site. Since occipital bone is thicker than frontal bone, attenuation of γ -rays is considered to be more significant in the occipital region. Thus, the Chang method, which assumes that the head is a uniform absorber, is considered to be more significantly affected by the carbon headrest (7).

Regarding the clinical meaning of the difference between carbon and XPS, a representative case demonstrated in Figure 4 suggests the possibility that decreased blood flow will be underestimated in ischemic lesions when carbon is used for the headrest.

On the other hand, regarding the D+F/G ratio, no significant difference was observed between carbon and XPS in any combination of image reconstruction and AC methods. Regions D, F, and G were covered by the carbon headrest. Thus, like the posterior region, these regions were considered to be affected by the headrest.

A limitation of the present study is that, to minimize interactions such as attenuation and scattering of γ -rays emitted from brain tissue, the XPS headrest does not cover the side of the head, unlike the carbon headrest. Consequently, fixation during examination may have been a little unstable. Thus, further improvement is needed. In AC using the Chang method, the effect on images is considered to be less with the XPS headrest than with the conventional carbon headrest. Therefore, in the future, consideration may be given to use of XPS as a headrest material for SPECT image acquisitions.

CONCLUSION

We developed a new headrest constructed from XPS instead of carbon for brain SPECT. XPS has a low CT value of -980 HU, with excellent versatility, workability, and strength. The A+B/G ratio in FBP Chang AC and OSEM Chang AC significantly differed between the carbon and XPS headrests in healthy controls and patients with cerebrovascular disease. On the other hand, the A+B/G

ratios in OSEM CTAC were not affected by the headrest material. There was no significant difference in the D+F/G ratio in FBP Chang AC or OSEM Chang AC. Thus, a headrest made of XPS reduces the influence of AC on brain SPECT images, especially in anterior and posterior brain regions when processed using the FBP or OSEM Chang AC method.

DISCLOSURE

No potential conflict of interest relevant to this article was reported.

KEY POINTS

QUESTION: Can a headrest be developed that reduces the influence of AC on SPECT images of the human brain?

PERTINENT FINDINGS: In healthy volunteers and cerebrovascular patients, a headrest made of XPS reduced the influence of AC on brain SPECT images, especially in anterior and posterior brain regions, when processed by the FBP or OSEM Chang AC method.

IMPLICATIONS FOR PATIENT CARE: The headrest made of XPS might allow acquisition of more precise human brain SPECT images.

REFERENCES

1. Farid K, Habert MO, Martineau A, Vigneron NC, Sibon I. CT nonuniform attenuation and TEW scatter corrections in brain Tc-99m ECD SPECT. *Clin Nucl Med*. 2011;36:665–668.
2. Gillen R, Firbank MJ, Lloyd J, O'Brien JT. CT-based attenuation and scatter correction compared with uniform attenuation correction in brain perfusion SPECT imaging for dementia. *Phys Med Biol*. 2015;60:6775–6787.
3. Ishii K, Hanaoka K, Okada M, et al. Impact of CT attenuation correction by SPECT/CT in brain perfusion images. *Ann Nucl Med*. 2012;26:241–247.
4. Ohba M, Kokubo Y, Suzuki K, Kanoto M, Sonoda Y. Influence of a headrest on reconstruction and attenuation correction of human brain SPECT images. *J Nucl Med Technol*. 2021;49:54–57.
5. Takeuchi R, Yonekura Y, Matsuda H, Konishi J. Usefulness of a three-dimensional stereotaxic ROI template on anatomically standardised ^{99m}Tc -ECD SPECT. *Eur J Nucl Med Mol Imaging*. 2002;29:331–341.
6. Patton JA, Turkington TG. SPECT/CT physical principles and attenuation correction. *J Nucl Med Technol*. 2008;36:1–10.
7. Hayashi M, Deguchi J, Utsunomiya K, et al. Comparison of methods of attenuation and scatter correction in brain perfusion SPECT. *J Nucl Med Technol*. 2005;33: 224–229.

Optimization of the Attenuation Coefficient for Chang Attenuation Correction in ^{123}I Brain Perfusion SPECT

Taisuke Murata^{1,2}, Yuri Hayashi¹, Masahisa Onoguchi², Takayuki Shibutani², Takashi Iimori¹, Koichi Sawada¹, Tetsuro Umezawa¹, Yoshitada Masuda¹, and Takashi Uno³

¹Department of Radiology, Chiba University Hospital, Chiba, Japan; ²Department of Quantum Medical Technology, Graduate School of Medical Sciences, Kanazawa University, Kanazawa, Japan; and ³Department of Diagnostic Radiology and Radiation Oncology, Graduate School of Medicine, Chiba University, Chiba, Japan

N-isopropyl-*p*- ^{123}I -iodoamphetamine brain perfusion SPECT has been used with various attenuation coefficients (μ -values); however, optimization is required. This study aimed to determine the optimal μ -value (μ_{opt} -value) for Chang attenuation correction (AC) using clinical data by comparing the Chang method and CT-based AC. **Methods:** We used 100 patients (reference group, 60; disease group, 40) who underwent *N*-isopropyl-*p*- ^{123}I -iodoamphetamine SPECT. SPECT images of the reference group were obtained to calculate the AC using the Chang method (μ -values, 0.07–0.20; 0.005 interval) and the CT-based method, both without scatter correction (SC) and with SC. The μ_{opt} -value with the smallest mean percentage error for the brain regions of the reference group was calculated. Agreement between the Chang and CT-based methods applying the μ_{opt} -value was evaluated using Bland–Altman analysis. Additionally, the percentage error in the region of hypoperfusion in the diseased group was compared with the percentage error in the same region in the reference group when the μ_{opt} -value was applied. **Results:** The μ_{opt} -values were 0.140 for Chang without SC and 0.160 for Chang with SC. In the Chang method, with the μ_{opt} -value applied, fixed and proportional biases were observed in the Bland–Altman analysis (both $P < 0.05$), and there was a tendency for the percentage error to be underestimated in the limbic regions and overestimated in the central brain regions. There was no significant difference between the disease group and the reference group in the region of hypoperfusion in either Chang without SC or Chang with SC. **Conclusion:** The present study revealed that the μ_{opt} -values of the Chang method are 0.140 without SC and 0.160 with SC.

Key Words: SPECT; brain perfusion; Chang attenuation correction

J Nucl Med Technol 2023; 51:49–56

DOI: 10.2967/jnmt.122.264990

Brain perfusion SPECT is required to be qualitatively and quantitatively accurate. SPECT projection data are subject to scattering and attenuation of γ -rays caused by the subject. Particularly, attenuation causes a depth-dependent decrease in counts within the subject, leading to significant accuracy errors

in quantitative evaluation (1). Therefore, attenuation correction (AC) is vital to obtain accurate brain perfusion SPECT images.

CT-based AC (a nonuniform AC) and Chang AC (a uniform AC) are used mainly in brain perfusion SPECT. The CT-based method is considered the gold standard for AC because of its high correction accuracy. Contrastingly, the Chang method is widely used in routine clinical practice primarily because of its simplicity in AC processing. It does not require a CT scan, thereby eliminating radiation exposure. The attenuation map of the Chang method is given by a constant attenuation coefficient (μ -value) for each radionuclide energy. Various μ -values have been used for *N*-isopropyl-*p*- ^{123}I -iodoamphetamine brain perfusion SPECT, with variations (broad-beam: 0.07 (2), 0.08 (3), 0.09 (4), and 0.10 (5); narrow-beam: 0.11 (3), 0.12 (6), 0.146 (2,5,7), 0.160 (8), 0.166 (9), and 0.167 (10)). Optimization of μ -values is required for the Chang method in *N*-isopropyl-*p*- ^{123}I -iodoamphetamine brain perfusion SPECT.

It is necessary to consider the effect of skull attenuation (11–13) and the difference in μ -value depending on the slice position (9,12,14) to optimize the μ -value of the Chang method. The skull is relatively thicker in the occipital region than in other regions (15), making it difficult to reproduce the actual skull thickness in the phantom accurately. Additionally, when μ -values are determined using a pooled phantom, the basal ganglia level is the evaluation target (16), resulting in inadequate evaluation of the parietal and cerebellar levels. Van Laere et al. (13,17) noted that μ -values determined experimentally using phantoms cannot be directly extrapolated for application to clinical data.

This study aimed to determine the optimal μ -value (μ_{opt} -value) using clinical data. The μ -value that most closely approximates the AC effect of the CT-based method, the gold standard, was determined as the μ_{opt} -value of the Chang method. We further validated the μ_{opt} -value by evaluating agreement between the Chang and CT-based methods when μ_{opt} -values were applied and by evaluating the error of the μ_{opt} -values in hypoperfusion regions.

MATERIALS AND METHODS

This retrospective study was approved by our institution's ethics review committee. All data used for analysis were obtained from

Received Oct. 4, 2022; revision accepted Jan. 17, 2023.
For correspondence or reprints, contact Masahisa Onoguchi (onoguchi@staff.kanazawa-u.ac.jp).
COPYRIGHT © 2023 by the Society of Nuclear Medicine and Molecular Imaging.

routine clinical diagnostic investigations; no other examinations were performed for the study. The requirement for written consent was waived by the ethics review committee.

Patients

This study included 100 patients (male, 47; female, 53; median age, 66.0 y [range, 23.1–90.3 y]) who underwent *N*-isopropyl-*p*-¹²³I-iodoamphetamine brain perfusion SPECT between January and December 2021. Patients diagnosed with generally preserved perfusion or mild nonspecific hypoperfusion were defined as the reference group. Patients diagnosed with specific hypoperfusion were defined as the disease group. The reference group included 60 patients (male, 28; female, 32; median age, 63.5 y [23.1–90.3 y]), and the disease group included 40 patients (male, 19; female, 21; median age, 72.5 y [48.4–88.2 y]). Disease groups included Alzheimer disease, dementia with Lewy bodies, frontotemporal lobar degeneration, and multiple-system atrophy of the cerebellar type, with 10 patients each. Patients with diseases other than the above and equivocal hypoperfusion were excluded from being selected for the disease groups.

Data Acquisition and Reconstruction

All patients were administered 111 MBq of *N*-isopropyl-*p*-¹²³I-iodoamphetamine, and the SPECT scan was obtained using a dual-head γ -camera (NM/CT 870 DR hybrid SPECT/CT scanner; GE Healthcare) equipped with an extended low-energy general-purpose collimator. The energy peak was set at 159 keV with a 20% energy window. The subwindow for scatter correction (SC) was set at 20% centered at 130 keV. SPECT scans were obtained with the following parameters: continuous-acquisition mode, 360° circular orbit, 90 projections of a 4° step angle, an 180-s acquisition per cycle for 8 cycles, a radius rotation of 150 mm, and 64 × 64 matrices with a zoom magnification of ×2.0. CT scans for AC were obtained with the following acquisition and reconstruction parameters: helical scan mode, tube voltage of 120 kVp, tube current of 40 mA, 0.5 s of rotation time, and slice thickness of 3.75 mm (matrix, 512 × 512; pixel size, 0.97 mm). The CT data were converted with bilinear scaling to attenuation maps corresponding to 159 keV using the scanner software.

All patient SPECT projection data were reconstructed using ordered-subset expectation maximization (OSEM; 5 iterations and 10 subsets). The reconstructions for each patient included OSEM plus the Chang method (ChangAC), OSEM plus the Chang method plus SC (ChangACSC), OSEM plus the CT-based method (CTAC), and OSEM plus the CT-based method + SC (CTACSC). For ChangAC and ChangACSC, AC was performed by varying the μ -values from 0.07 to 0.20 (0.05 intervals). A threshold process for each patient determined the contour of the attenuation map when performing the Chang method. The threshold value whose contour was nearest the outer edge of the skull was adopted by referring to the CT images (12). The dual-energy window method was used for SC (18). The pixel size of the reconstructed SPECT image was 4.42 mm, and the slice thickness was also 4.42 mm. A Butterworth filter (cutoff, 0.5 cycles/cm; order, 8) was used for smoothing.

Data Analysis

All SPECT images were analyzed using AZE Virtual Place HAYABUSA software (Canon Medical Systems), and 3-dimensional stereotactic surface projection analysis was performed. To avoid anatomic standardization errors, the head tilt was adjusted to the anterior commissure–posterior commissure line (19,20). Counts of 37 brain regions were measured using volume-of-interest templates

incorporated into the 3-dimensional stereotactic surface projection on anatomically standardized SPECT images. The 37 brain regions included were the left and right parietal lobes, temporal lobe, frontal lobe, occipital lobe, posterior cingulate gyrus, anterior cingulate gyrus, medial frontal lobe, medial parietal lobe, medial temporal lobe, sensorimotor cortex, visual cortex, caudate nucleus, cerebellum, cerebellar vermis, putamen, parahippocampal gyrus, amygdala, thalamus, and pons (not divided into left and right).

Determination of μ_{opt} -Value

The percentage error of each brain region for ChangAC/CTAC pairs and ChangACSC/CTACSC pairs was calculated for the reference group:

$$\text{Percentage error} = \frac{\text{count}_{\text{ChangAC, ChangACSC}} - \text{count}_{\text{CTAC, CTACSC}}}{\text{count}_{\text{CTAC, CTACSC}}}.$$

First, the mean percentage error for all brain regions (37 volumes of interest) was calculated for each patient. The μ -value with the smallest mean percentage error was the μ_{opt} -value for each patient. The number distribution of the μ_{opt} -values for each patient was determined to identify the range of individual differences.

Next, the mean percentage error of all brain regions (2,220 volumes of interest) in the 60 reference patients was calculated. The absolute value of the percentage error in each brain region was also calculated to identify the magnitude of the error. Additionally, unsuitable μ -values with significant differences from those of the CT-based method were identified by comparing the counts of all brain regions in ChangAC/CTAC pairs and ChangACSC/CTACSC pairs.

Bland–Altman analysis was performed on each pair of counts to evaluate agreement between ChangAC (with μ_{opt} -value)/CTAC pairs and between ChangACSC (with μ_{opt} -value)/CTACSC pairs. The percentage error of each pair was also identified for each brain region.

Validation of μ_{opt} -Values

SPECT images of the disease group with ChangAC and ChangACSC with μ_{opt} -values were used. The percentage error in the hypoperfusion region for the ChangAC/CTAC and ChangACSC/CTACSC pairs was calculated and compared with the percentage error in the same region in the reference group. The hypoperfusion regions were defined as the posterior cingulate gyrus and medial temporal lobe for Alzheimer disease, the occipital lobe for dementia with Lewy bodies, the frontal and temporal lobes for frontotemporal lobar degeneration, and the cerebellum for multiple-system atrophy of the cerebellar type.

Statistical Analysis

Statistical analyses were performed using JMP Pro (version 16.1.0; SAS Institute). The difference in counts between ChangAC/CTAC pairs and ChangACSC/CTACSC pairs with varying μ -values for the Chang method was evaluated using the Wilcoxon signed-rank test. Fixed and proportional biases for ChangAC/CTAC pairs and ChangACSC/CTACSC pairs were evaluated using Bland–Altman analysis. A paired *t* test and linear regression analysis were used to analyze the fixed and proportional biases, respectively, on the Bland–Altman plots. The percentage error of the disease and reference groups for ChangAC/CTAC pairs and ChangACSC/CTACSC pairs in the hypoperfusion region was evaluated using the Wilcoxon signed-rank test. For all statistical analyses, a *P* value of less than 0.05 was considered statistically significant.

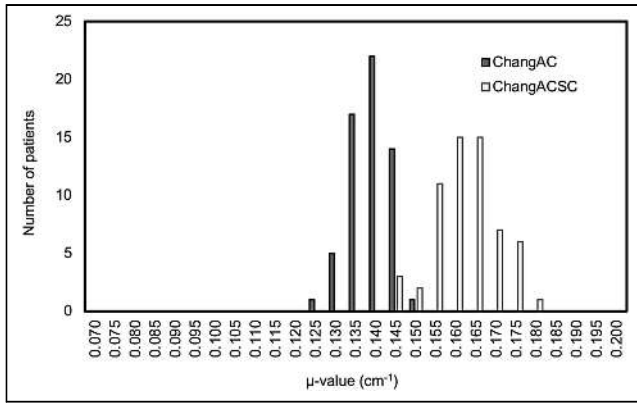


FIGURE 1. Distribution of number of μ_{opt} -values per patient in reference group.

RESULTS

The distribution of the number of μ_{opt} -values per patient in the reference group is shown in Figure 1. The μ_{opt} -values differed among patients. In ChangAC, the μ_{opt} -values ranged from 0.125 to 0.150, with 0.140 being the most common value. In ChangACSC, the μ_{opt} -values ranged from 0.145 to 0.180, with 0.160 and 0.165 being the most common values.

The percentage error of ChangAC in the reference group is listed in Table 1, and Table 2 shows the percentage error of ChangACSC. ChangAC exhibited the smallest percentage error with CTAC with a μ -value of 0.140, whereas ChangACSC displayed the smallest percentage error with CTACSC with a μ -value of 0.160. For both ChangAC and ChangACSC, smaller μ -values tended to underestimate counts, and larger μ -values resulted in overestimated counts. The maximum absolute percentage error was 22.81% for ChangAC with a μ -value of 0.140 and 31.63% for ChangACSC with a μ -value of 0.160. Comparison of counts between the Chang and CT-based methods revealed significant differences in all μ -values except 0.140 for ChangAC and 0.160 and 0.165 for ChangACSC.

Agreement between ChangAC applying a μ_{opt} -value of 0.140 and CTAC and between ChangACSC applying a μ_{opt} -value of 0.160 and CTACSC in the reference group are shown in Figures 2A and 2B. We identified a positive fixed bias between ChangAC and CTAC and a negative fixed bias between ChangACSC and CTACSC (both $P < 0.05$). Therefore, there was an overall overestimation trend for ChangAC and an underestimation trend for ChangACSC. Linear regression analysis revealed a proportional bias for ChangAC and ChangACSC (both $P < 0.05$).

TABLE 1
Percentage Error and Absolute Percentage Error Between ChangAC Applying Each μ -Value and CTAC

μ -value	Percentage error	Absolute percentage error	<i>P</i>
0.070	-38.22 ± 4.02 ($-46.17, -29.28$)	38.22 ± 4.02 (29.28, 46.17)	<0.05
0.075	-36.13 ± 3.90 ($-46.51, -28.14$)	36.13 ± 3.90 (28.14, 46.51)	<0.05
0.080	-33.78 ± 3.85 ($-42.76, -25.84$)	33.78 ± 3.85 (25.84, 42.76)	<0.05
0.085	-31.40 ± 3.64 ($-41.03, -22.94$)	31.40 ± 3.64 (22.94, 41.03)	<0.05
0.090	-28.75 ± 3.66 ($-39.59, -19.08$)	28.75 ± 3.66 (19.08, 39.59)	<0.05
0.095	-26.24 ± 3.34 ($-36.81, -19.01$)	26.24 ± 3.34 (19.01, 36.81)	<0.05
0.100	-23.78 ± 3.10 ($-35.49, -16.19$)	23.78 ± 3.10 (16.19, 35.49)	<0.05
0.105	-21.01 ± 3.03 ($-32.43, -12.95$)	21.01 ± 3.03 (12.95, 32.43)	<0.05
0.110	-18.24 ± 2.79 ($-32.14, -9.23$)	18.24 ± 2.79 (9.23, 32.14)	<0.05
0.115	-15.40 ± 2.50 ($-25.94, -6.05$)	15.40 ± 2.50 (6.05, 25.94)	<0.05
0.120	-12.12 ± 3.59 ($-25.31, 1.84$)	12.12 ± 3.59 (0.16, 25.31)	<0.05
0.125	-9.00 ± 3.94 ($-22.25, 7.01$)	9.07 ± 3.78 (0.06, 22.25)	<0.05
0.130	-5.85 ± 4.40 ($-19.93, 14.24$)	6.38 ± 3.58 (0.00, 19.93)	<0.05
0.135	-2.45 ± 4.95 ($-17.42, 18.89$)	4.54 ± 3.13 (0.00, 18.89)	<0.05
0.140	0.96 ± 5.62 ($-13.92, 22.81$)*	4.45 ± 3.57 (0.00, 22.81)*	0.58
0.145	4.18 ± 6.78 ($-10.06, 28.65$)	6.14 ± 5.07 (0.00, 28.65)	<0.05
0.150	8.13 ± 6.93 ($-8.82, 35.49$)	8.58 ± 6.37 (0.00, 35.49)	<0.05
0.155	11.95 ± 7.74 ($-6.43, 38.81$)	12.06 ± 7.57 (0.00, 38.81)	<0.05
0.160	15.86 ± 8.57 ($-3.87, 49.12$)	15.87 ± 8.54 (0.13, 49.12)	<0.05
0.165	19.92 ± 8.88 ($-1.74, 52.43$)	19.92 ± 8.87 (0.01, 52.43)	<0.05
0.170	23.93 ± 9.61 (1.83, 56.66)	23.93 ± 9.61 (1.83, 56.66)	<0.05
0.175	28.23 ± 10.50 (4.85, 64.57)	28.23 ± 10.50 (4.85, 64.57)	<0.05
0.180	32.72 ± 11.41 (8.26, 70.96)	32.72 ± 11.41 (8.26, 70.96)	<0.05
0.185	37.16 ± 12.69 (6.29, 82.40)	37.16 ± 12.69 (6.29, 82.40)	<0.05
0.190	42.19 ± 13.82 (13.63, 91.62)	42.19 ± 13.82 (13.63, 91.62)	<0.05
0.195	46.63 ± 14.82 (13.69, 99.40)	46.63 ± 14.82 (13.69, 99.40)	<0.05
0.200	52.23 ± 16.26 (20.34, 107.87)	52.23 ± 16.26 (20.34, 107.87)	<0.05

*Smallest mean percentage error and absolute percentage error.
Data are mean \pm SD, followed by range in parentheses.

TABLE 2
Percentage Error and Absolute Percentage Error Between ChangACSC Applying Each μ -Value and CTACSC

μ -value	Percentage error	Absolute percentage error	P
0.070	-45.25 \pm 5.28 (-60.55, -23.14)	45.25 \pm 5.28 (23.14, 60.55)	<0.05
0.075	-43.35 \pm 5.31 (-61.10, -21.36)	43.35 \pm 5.31 (21.36, 61.10)	<0.05
0.080	-41.39 \pm 5.34 (-56.87, -18.13)	41.39 \pm 5.34 (18.13, 56.87)	<0.05
0.085	-39.25 \pm 5.31 (-53.72, -15.78)	39.25 \pm 5.31 (15.78, 53.72)	<0.05
0.090	-37.34 \pm 5.35 (-55.51, -14.08)	37.34 \pm 5.35 (14.08, 55.51)	<0.05
0.095	-35.15 \pm 5.34 (-49.77, -11.23)	35.15 \pm 5.34 (11.23, 49.77)	<0.05
0.100	-32.88 \pm 5.33 (-50.07, -9.59)	32.88 \pm 5.33 (9.59, 50.07)	<0.05
0.105	-32.92 \pm 7.79 (-56.93, -6.89)	32.92 \pm 7.79 (6.89, 56.93)	<0.05
0.110	-28.30 \pm 5.44 (-48.50, -5.35)	28.30 \pm 5.44 (5.35, 48.50)	<0.05
0.115	-26.04 \pm 5.60 (-45.59, -2.26)	26.04 \pm 5.60 (2.26, 45.59)	<0.05
0.120	-23.26 \pm 5.71 (-43.11, -0.11)	23.26 \pm 5.71 (0.11, 43.11)	<0.05
0.125	-20.84 \pm 6.01 (-41.59, 3.75)	20.86 \pm 5.96 (0.02, 41.59)	<0.05
0.130	-18.40 \pm 5.69 (-39.99, 4.84)	18.42 \pm 5.61 (0.03, 39.99)	<0.05
0.135	-15.66 \pm 5.92 (-36.30, 8.17)	15.74 \pm 5.70 (0.02, 36.30)	<0.05
0.140	-13.43 \pm 5.85 (-35.95, 10.34)	13.56 \pm 5.54 (0.01, 35.95)	<0.05
0.145	-10.56 \pm 6.29 (-29.52, 13.57)	10.99 \pm 5.51 (0.05, 29.52)	<0.05
0.150	-7.58 \pm 6.67 (-29.75, 19.25)	8.65 \pm 5.21 (0.01, 29.75)	<0.05
0.155	-4.40 \pm 7.33 (-26.91, 26.51)	7.04 \pm 4.85 (0.01, 26.91)	<0.05
0.160	-1.11 \pm 7.94 (-27.83, 31.63)*	6.37 \pm 4.88 (0.01, 31.63)*	0.06
0.165	2.26 \pm 8.76 (-20.46, 39.34)	6.97 \pm 5.76 (0.01, 39.34)	0.05
0.170	5.63 \pm 9.40 (-19.51, 42.13)	8.37 \pm 7.07 (0.02, 42.13)	<0.05
0.175	9.39 \pm 10.45 (-16.02, 50.41)	10.88 \pm 8.88 (0.04, 50.41)	<0.05
0.180	12.99 \pm 11.28 (-19.97, 62.12)	13.76 \pm 10.32 (0.00, 62.12)	<0.05
0.185	17.09 \pm 11.83 (-11.97, 64.69)	17.33 \pm 11.46 (0.02, 64.69)	<0.05
0.190	20.98 \pm 12.77 (-10.09, 69.26)	21.10 \pm 12.57 (0.00, 69.26)	<0.05
0.195	24.45 \pm 13.11 (-16.22, 72.17)	24.51 \pm 12.98 (0.08, 72.17)	<0.05
0.200	28.34 \pm 14.13 (-11.36, 86.37)	28.37 \pm 14.07 (0.05, 86.37)	<0.05

*Smallest mean percentage error and absolute percentage error.
Data are mean \pm SD, followed by range in parentheses.

The percentage error in each brain region for ChangAC applying a μ_{opt} -value of 0.140 and CTAC and for ChangACSC applying a μ_{opt} -value of 0.160 and CTACSC in the reference group is shown in Figure 3. In both ChangAC and ChangACSC, some brain regions in the limbic region were underestimated (the right temporal lobe, right frontal lobe, and right sensorimotor cortex and, bilaterally, the parietal lobes, occipital lobes, and visual cortex), and some brain regions in the central region tended to be overestimated (pons and, bilaterally, the medial temporal lobes, caudate nucleus, pons, putamen, parahippocampal gyrus, and thalamus).

Examples of SPECT images of reference patients with ChangAC/CTAC and ChangACSC/CTACSC are shown in Figures 4A and 4B. ChangAC and ChangACSC tended to slightly overestimate the central brain regions and underestimate the limbic cortex in the μ_{opt} -value in series normalization. In CT-based method normalization, the μ_{opt} -value produced SPECT images more similar to the CT-based method than did the conventionally used μ -values.

Table 3 summarizes the percentage error results in the hypoperfusion region for ChangAC applying a μ_{opt} -value of 0.140 and ChangACSC applying a μ_{opt} -value of 0.160. The percentage error in the hypoperfusion region for each disease group did not significantly differ from that of the

same region in the reference group for either ChangAC or ChangACSC.

DISCUSSION

We determined μ_{opt} -values in ChangAC and ChangACSC retrospectively using clinical data. The μ_{opt} -values were 0.140 for ChangAC and 0.160 for ChangACSC. However, some brain regions were under- or overestimated in the SPECT images when the μ_{opt} -values were applied. Limitations of the Chang method, as a uniform AC, were also revealed.

The distribution of μ_{opt} -values per patient displayed some variation, with 0.140 being the most common value for ChangAC and 0.160 and 0.165 being most common for ChangACSC. However, it is not practical to apply individual μ -values for each patient. Therefore, we determined μ_{opt} -values by averaging out the variation in patients by analyzing all brain regions together in 60 reference patients. By comparing the counts of the Chang method with those of the CT-based method, we identified significant differences for all μ -values except 0.140 in ChangAC and 0.160 and 0.165 in ChangACSC, thereby providing statistical support for the μ_{opt} -value. Stodilka et al. (12) reported a relative

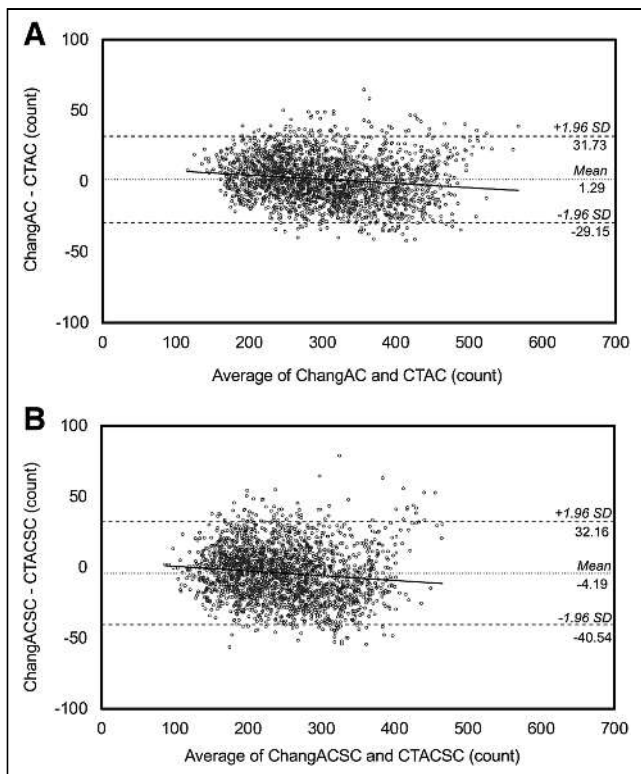


FIGURE 2. Results of Bland–Altman analysis comparing ChangAC applying μ_{opt} -value of 0.140 and CTAC (A) and comparing ChangACSC applying μ_{opt} -value of 0.160 and CTACSC in reference group (B). Solid lines show regressions; 95% limits of agreement are represented by dashed lines. 95% CIs were 0.66 to 1.92 (A) and -4.95 to -3.44 (B).

quantification error of 20% by applying a μ -value of 0.120 to ChangAC in a phantom study. In the present patient-based study, the absolute percentage error for ChangAC applying the μ_{opt} -value was 22.81%. Although the degree of error was comparable, the μ_{opt} -values for phantoms and patients were different. For quantitation using ^{123}I , Iida et al. reported a maximum percentage error of 30% for ChangAC with a μ -value of 0.090 and for ChangACSC with a μ -value of 0.166 (9). For ChangAC, a smaller percentage error was achieved by applying the μ_{opt} -value in this study. For ChangACSC, there was no noticeable difference from this study because the μ -values were close to our μ_{opt} -values. Interindividual variability of anatomic standardization in brain perfusion SPECT is 3%–9% (21–23). The absolute percentage error between the CT-based and Chang methods in the present study averaged 4.45% for

ChangAC and 6.37% for ChangACSC. Application of the μ_{opt} -values achieved an AC error comparable to the interindividual variation of anatomic standardization that can occur in routine clinical practice.

Bland–Altman analysis revealed systematic bias in ChangAC and ChangACSC when applying the μ_{opt} -value, and agreement with the CT-based method was not perfect. The percentage error for ChangAC and ChangACSC tended to be underestimated in the limbic brain regions and overestimated in the central brain regions. This trend was visually confirmed in an example of the SPECT image of a reference patient shown in Figure 4. Ito et al. (4) reported an overestimation of central brain regions in ChangACSC applying a μ -value of 0.166, relatively close to our μ_{opt} -value. These facts highlight the limitations of the Chang method even when using μ_{opt} -values and reiterate the superiority of the CT-based method.

The skull possesses a higher μ -value than brain tissue because of greater photon loss. Further, the thickness of the skull varies slightly with age and sex (24). The different μ_{opt} -values per patient in the present study appear to be due to skull thickness variations among patients. Nicholson et al. (11) reported that the skull paradoxically affects broad-beam μ -values, and other studies (12,13) also reported lower μ -values than those of uniform soft tissue. Stodilka et al. (12) observed that μ_{opt} -values at the cerebellar level, surrounded by thick bony structures, are smaller than those at the basal ganglia level. Iida et al. (9) reported smaller μ -values at the cerebellar level, where the airway is included in the slice position, and higher μ -values at the parietal level, where the skull is relatively thick. These reports indicate a complex

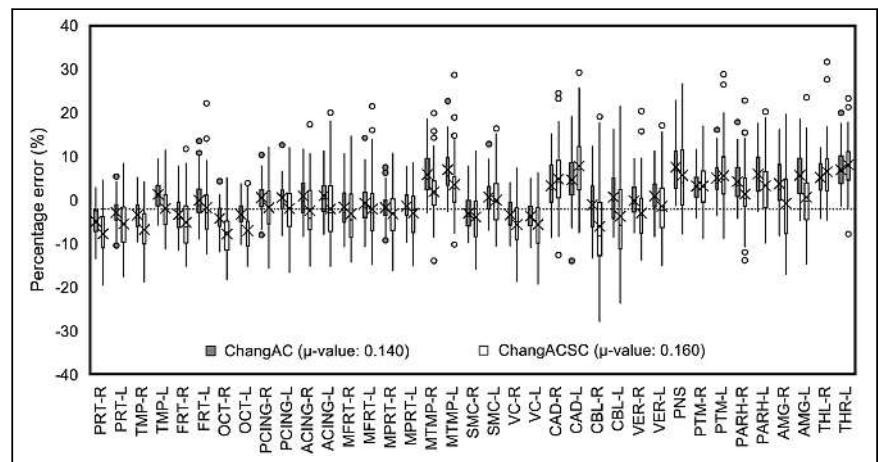


FIGURE 3. Percentage error in each brain region for ChangAC applying μ_{opt} -value of 0.140 and CTAC and for ChangACSC applying μ_{opt} -value of 0.160 and CTACSC in reference group. Dotted line indicates zero. For ChangAC and ChangACSC, limbic brain regions tended to be underestimated and central brain regions overestimated. PRT = parietal lobe; TMP = temporal lobe; FRT = frontal lobe; OCT = occipital lobe; PCING = posterior cingulate gyrus; ACING = anterior cingulate gyrus; MFRT = medial frontal lobe; MPRT = medial parietal lobe; MTMP = medial temporal lobe; SMC = sensorimotor cortex; VC = visual cortex; CAD = caudate nucleus; CBL = cerebellum; VER = cerebellar vermis; PNS = pons; PTM = putamen; PARH = parahippocampal gyrus; AMG = amygdala; THL = thalamus.

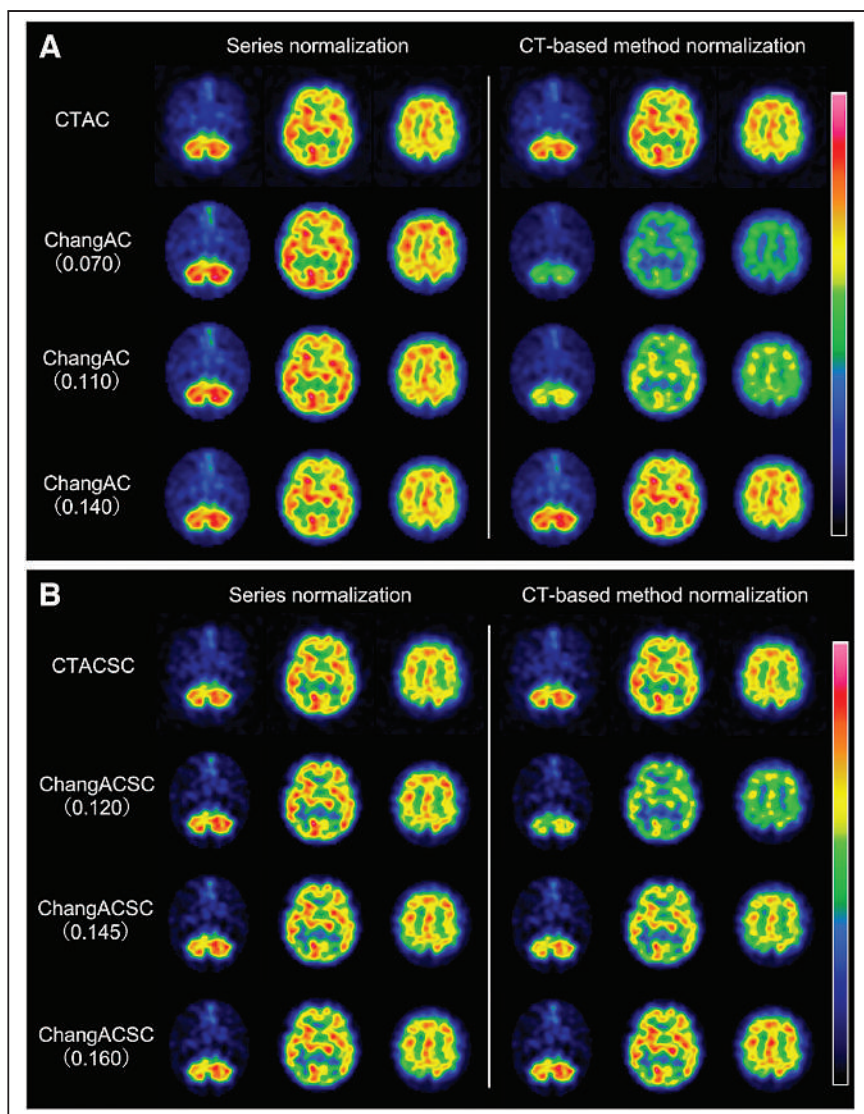


FIGURE 4. Comparison of SPECT images of CTAC and ChangAC (A) and CTACSC and ChangACSC (B) in 1 reference patient. For ChangAC, μ -values of 0.07, 0.110, and 0.140 were applied; for ChangACSC, μ -values of 0.12, 0.145, and 0.160 were applied. On left are SPECT images normalized by maximum counts in series; on right are SPECT images normalized by maximum counts of CT-based method. From left to right, axial slices are at cerebellar, basal ganglia, and parietal levels.

interplay of several factors involved in optimizing μ -values. In this study, we averaged the differing μ_{opt} -values in patients by a combined analysis of 60 reference patients and accounted for differences in correction error among brain regions by analyzing all brain regions together using anatomic standardization. Our method provides a generalizable μ_{opt} -value that considers differences in skull thickness (an error factor for interpatient variation) and differences in attenuation structure for each imaging slice position (an error factor for inpatient variation). Consequently, the μ_{opt} -value determined in the present study is relatively high compared with the various μ -values conventionally used.

The theoretic narrow-beam μ -value for water for the 159-keV γ rays emitted by ^{123}I is 0.148 (25). Using the theoretic

narrow-beam μ -value for ChangAC overcorrects for attenuation and overestimates the brain center region (26). Harris et al. (27) reported that a slightly lower μ -value should be applied than the theoretic μ -value. Here, the μ_{opt} -value of ChangAC was also lower than the theoretic narrow-beam μ -value.

The μ_{opt} -value of ChangACSC in our study was higher than the theoretic narrow-beam μ -value, whereas previous studies proposed lower values than the theoretic narrow-beam μ -value (12,13,16). Some previous studies using phantoms focused on assessing the uniformity of AC (12,16) because brain perfusion SPECT images are commonly normalized by the maximum count in the series. The uniformity of AC contributes to qualitative improvement. In this study using clinical data, the SD of the percentage error at low μ -values was small, and uniformity within the series was preserved. Contrarily, the absolute percentage error applying μ_{opt} -values was comparable to that reported by Stodilka et al. (12), indicating that quantification was assured. Iida et al. (9) reported no apparent difference in regional CBF images obtained with the measured attenuation map and ChangACSC applying a high μ -value of 0.166. Therefore, it is difficult for the Chang method to achieve both qualitative and quantitative performance because low μ -values contribute to qualitative improvement whereas high μ -values contribute to quantitative improvement. Since the degree of contribution of high μ -values to the quantitation improvement was greater than the degree of contribution of low

μ -values to the qualitative improvement, using high μ -values is recommended.

We validated the μ_{opt} -value determined using the reference group in hypoperfusion regions to confirm their adaptability to the disease group. The choice of target diseases was considered so that the entire brain region (anterior, posterior, lateral, parietal, and basal regions) could be included as hypoperfusion regions. We observed no significant difference in the percentage error in the hypoperfusion regions in the reference and disease groups when the μ_{opt} -value was applied, indicating adaptability of the μ_{opt} -value for the disease group.

The reference group used in the present study included patients who underwent routine clinical examinations and not healthy volunteers. However, conducting studies on healthy

TABLE 3

Comparison of Percentage Error Between Hypoperfusion Region in Each Disease Group and Same Region in Reference Group for ChangAC Applying μ_{opt} -Value of 0.140 and ChangACSC Applying μ_{opt} -Value of 0.160

Disease	Brain region	Side	ChangAC			ChangACSC		
			Disease	Reference	P	Disease	Reference	P
AD	Posterior cingulate gyrus	R	0.55 ± 3.49	-0.71 ± 3.04	0.34	-3.71 ± 2.78	-1.76 ± 5.72	0.14
		L	0.52 ± 3.44	0.17 ± 2.48	0.83	-4.85 ± 4.19	-1.97 ± 5.75	0.13
	Medial temporal lobe	R	3.00 ± 3.32	5.82 ± 4.76	0.08	-0.55 ± 4.36	1.89 ± 6.26	0.23
		L	4.83 ± 3.38	6.95 ± 5.03	0.18	2.38 ± 3.64	3.51 ± 6.57	0.83
DLB	Occipital lobe	R	-4.24 ± 3.38	-4.33 ± 2.57	0.89	-7.82 ± 5.09	-7.47 ± 4.97	0.69
		L	-3.33 ± 2.96	-2.89 ± 3.10	0.64	-7.03 ± 4.64	-6.33 ± 3.66	0.44
FTLD	Frontal lobe	R	-3.29 ± 4.34	-3.79 ± 1.41	0.85	-5.15 ± 6.02	-5.26 ± 0.86	0.80
		L	-0.09 ± 4.45	-1.39 ± 2.05	0.56	-1.76 ± 6.75	-2.89 ± 4.25	0.84
	Temporal lobe	R	-2.70 ± 3.48	-3.43 ± 3.16	0.59	-5.98 ± 4.51	-1.45 ± 4.66	0.88
		L	1.64 ± 3.30	1.27 ± 3.26	0.70	-1.45 ± 4.66	-1.88 ± 4.89	0.88
MSA-C	Cerebellum	R	-1.11 ± 5.51	-0.13 ± 3.40	0.69	-6.05 ± 9.54	-8.79 ± 4.63	0.45
		L	0.66 ± 5.83	2.32 ± 3.71	0.36	-3.70 ± 9.93	-6.62 ± 4.76	0.72

AD = Alzheimer disease; DLB = dementia with Lewy bodies; FTLD = frontotemporal lobar degeneration; MSA-C = multiple system atrophy of cerebellar type.

Data are mean ± SD.

volunteers is not practical to determine μ_{opt} -values. Licho et al. (28) also evaluated patients who underwent routine clinical examinations to validate the effects of various AC methods. In clinical routine, there are few patients in whom brain perfusion is generally preserved. We included patients diagnosed with a mild degree of nonspecific hypoperfusion in the reference group to obtain a larger cohort of patients for inclusion in the present study. Additionally, including more patients enables more generalizable μ_{opt} -values to be determined.

This study had some limitations. First, it was difficult for all patients to achieve an ideal head tilt because of patient-specific limitations in body position during SPECT imaging. These factors may have influenced the variation of μ_{opt} -values depending on the slice position. Second, the specifications for SC of the SPECT/CT system used in this study were limited to the dual-energy window method only. Since ^{123}I also emits photons with energies of as high as 529 keV, it is best to use a multiple-window method, including the triple-energy-window method, to improve the effects of down scatter. Third, we investigated using one type of γ -camera for ^{123}I with constant parameters for image reconstruction and SC. A preliminary validation using several patients confirmed that the μ_{opt} -values for each patient did not change when the number of iterations for image reconstruction and the weighting factor for SC was changed; however, this was not sufficient. The possibility that μ_{opt} -values may change when other radionuclides, γ -cameras, or other SC are used cannot be extrapolated to other clinical applications. These should be investigated in further studies.

CONCLUSION

We evaluated the μ_{opt} -value for the Chang method using clinical data by comparing it with the CT-based method.

The μ_{opt} -values of the Chang method were 0.140 for ChangAC and 0.160 for ChangACSC. It was possible to achieve mean AC accuracies of 4.45% for ChangAC and 6.37% for ChangACSC using μ_{opt} -values.

DISCLOSURE

No potential conflict of interest relevant to this article was reported.

ACKNOWLEDGMENT

We thank Editage (www.editage.com) for English language editing.

KEY POINTS

QUESTION: Can we optimize the μ -value of the Chang method using clinical data?

PERTINENT FINDINGS: In this retrospective study, we determined the μ_{opt} -value for the Chang method by comparing this method with the CT-based method, the gold standard for AC. We found that the μ_{opt} -values were 0.140 for the Chang method without SC and 0.160 for the Chang method with SC, although various μ -values have been used in previous studies.

IMPLICATIONS FOR PATIENT CARE: The Chang method can achieve more accurate AC using our determined μ -values.

REFERENCES

1. Zaidi H, Hasegawa B. Determination of the attenuation map in emission tomography. *J Nucl Med.* 2003;44:291–315.

2. Hayashi M, Deguchi J, Utsunomiya K, et al. Comparison of methods of attenuation and scatter correction in brain perfusion SPECT. *J Nucl Med Technol.* 2005;33:224–229.
3. Inoue Y, Hara T, Ikari T, Takahashi K, Miyatake H, Abe Y. Super-early images of brain perfusion SPECT using ^{123}I -IMP for the assessment of hyperperfusion in stroke patients. *Ann Nucl Med.* 2018;32:695–701.
4. Ito H, Iida H, Kinoshita T, Hatazawa J, Okudera T, Uemura K. Effects of scatter correction on regional distribution of cerebral blood flow using I-123-IMP and SPECT. *Ann Nucl Med.* 1999;13:331–336.
5. Shiga T, Kubo N, Takano A, et al. The effect of scatter correction on ^{123}I -IMP brain perfusion SPET with the triple energy window method in normal subjects using SPM analysis. *Eur J Nucl Med Mol Imaging.* 2002;29:342–345.
6. Yamashita K, Uchiyama Y, Ofuji A, et al. Fully automatic input function determination program for simple noninvasive ^{123}I -IMP microsphere cerebral blood flow quantification method. *Phys Med.* 2016;32:1180–1185.
7. Ishii K, Hanaoka K, Okada M, et al. Impact of CT attenuation correction by SPECT/CT in brain perfusion images. *Ann Nucl Med.* 2012;26:241–247.
8. Iida H, Nakagawara J, Hayashida K, et al. Multicenter evaluation of a standardized protocol for rest and acetazolamide cerebral blood flow assessment using a quantitative SPECT reconstruction program and split-dose ^{123}I -iodoamphetamine. *J Nucl Med.* 2010;51:1624–1631.
9. Iida H, Narita Y, Kado H, et al. Effects of scatter and attenuation correction on quantitative assessment of regional cerebral blood flow with SPECT. *J Nucl Med.* 1998;39:181–189.
10. Kim KM, Watabe H, Hayashi T, et al. Quantitative mapping of basal and vasoreactive cerebral blood flow using split-dose ^{123}I -iodoamphetamine and single photon emission computed tomography. *Neuroimage.* 2006;33:1126–1135.
11. Nicholson R, Doherty M, Wilkins K, Prato F. Paradoxical effects of the skull on attenuation correction requirements for brain SPECT. *J Nucl Med.* 1988;29:1316.
12. Stodilka RZ, Kemp BJ, Prato FS, Nicholson RL. Importance of bone attenuation in brain SPECT quantification [abstract]. *J Nucl Med.* 1998;39:190–197.
13. Van Laere K, Koole M, Versijpt J, Dierckx R. Non-uniform versus uniform attenuation correction in brain perfusion SPET of healthy volunteers. *Eur J Nucl Med.* 2001;28:90–98.
14. Arlig A, Gustafsson A, Jacobsson L, Ljungberg M, Wikkelsö C. Attenuation correction in quantitative SPECT of cerebral blood flow: a Monte Carlo study. *Phys Med Biol.* 2000;45:3847–3859.
15. Law SK. Thickness and resistivity variations over the upper surface of the human skull. *Brain Topogr.* 1993;6:99–109.
16. Kemp BJ, Prato FS, Dean GW, Nicholson RL, Reese L. Correction for attenuation in technetium-99m-HMPAO SPECT brain imaging. *J Nucl Med.* 1992;33:1875–1880.
17. Van Laere K, Koole M, Kauppinen T, Monsieurs M, Bouwens L, Dierck R. Nonuniform transmission in brain SPECT using ^{201}Tl , ^{153}Gd , and $^{99\text{m}}\text{Tc}$ static line sources: anthropomorphic dosimetry studies and influence on brain quantification. *J Nucl Med.* 2000;41:2051–2062.
18. Jaszcak RJ, Greer KL, Floyd CE Jr, Harris CC, Coleman RE. Improved SPECT quantification using compensation for scattered photons. *J Nucl Med.* 1984;25:893–900.
19. Onishi H, Matsutake Y, Kawashima H, Matsutomo N, Amijima H. Comparative study of anatomical normalization errors in SPM and 3D-SSP using digital brain phantom. *Ann Nucl Med.* 2011;25:59–67.
20. Minoshima S, Koeppe RA, Mintun MA, et al. Automated detection of the intercommissural line for stereotactic localization of functional brain images. *J Nucl Med.* 1993;34:322–329.
21. Imran MB, Kawashima R, Sato K, et al. Mean regional cerebral blood flow images of normal subjects using technetium-99m-HMPAO by automated image registration. *J Nucl Med.* 1998;39:203–207.
22. Jonsson C, Pagani M, Johansson L, Thurfjell L, Jacobsson H, Larsson SA. Reproducibility and repeatability of $^{99\text{m}}\text{Tc}$ -HMPAO rCBF SPET in normal subjects at rest using brain atlas matching. *Nucl Med Commun.* 2000;21:9–18.
23. Catafau AM, Lomeña FJ, Pavia J, et al. Regional cerebral blood flow pattern in normal young and aged volunteers: a $^{99\text{m}}\text{Tc}$ -HMPAO SPET study. *Eur J Nucl Med.* 1996;23:1329–1337.
24. Lillie EM, Urban JE, Lynch SK, Weaver AA, Stitzel JD. Evaluation of skull cortical thickness changes with age and sex from computed tomography scans. *J Bone Miner Res.* 2016;31:299–307.
25. Berger MJ, Hubbell JH. *XCOM: Photon Cross Sections on a Personal Computer.* National Bureau of Standards; 1987. Report NBSIR 87-3597.
26. Zaidi H, Montandon ML. Which attenuation coefficient to use in combined attenuation and scatter corrections for quantitative brain SPET? *Eur J Nucl Med Mol Imaging.* 2002;29:967–969, author reply 969–970.
27. Harris CC, Greer KL, Jaszcak RJ, Floyd CE Jr, Fearnow EC, Coleman RE. Tc-99m attenuation coefficients in water-filled phantoms determined with gamma cameras. *Med Phys.* 1984;11:681–685.
28. Licho R, Glick SJ, Xia W, Pan TS, Penney BC, King MA. Attenuation compensation in $^{99\text{m}}\text{Tc}$ SPECT brain imaging: a comparison of the use of attenuation maps derived from transmission versus emission data in normal scans. *J Nucl Med.* 1999;40:456–463.

Technologist-Based Implementation of Total Metabolic Tumor Volume into Clinical Practice

Erina Quinn¹, Claire Olson, CNMT², Manoj K. Jain², Jaiden Sullivan, CNMT³, Matthew P. Thorpe³, Geoffrey B. Johnson^{3,4}, and Jason R. Young²

¹Lake Erie College of Osteopathic Medicine, Bradenton, Florida; ²Department of Radiology, Mayo Clinic, Jacksonville, Florida; ³Department of Radiology, Mayo Clinic, Rochester, Minnesota; and ⁴Department of Immunology, Mayo Clinic, Rochester, Minnesota

Metabolic tumor volume (MTV) is defined as the total metabolically active tumor volume seen on ¹⁸F-FDG PET/CT examinations. Calculating MTV is often time-consuming, requiring a high degree of manual input. In this study, the MTV calculations of a board-certified nuclear radiologist were compared with those of 2 nuclear medicine technologists. As part of the technologists' educational program, after their classroom time they were trained by the radiologist for 30 min. The technologists calculated MTV within 7.5% of the radiologist's calculations in a set of patients who had diffuse large B-cell lymphoma and were undergoing initial staging ¹⁸F-FDG PET/CT. These findings suggest that nuclear medicine technologists may help accelerate implementation of MTV into clinical practice with favorable accuracy, possibly as an initial step followed by validation by the interpreting physician. The aim of this study was to explore whether efficiency is improved by integrating nuclear medicine technologists into a semiautomated workflow to calculate total MTV.

Key Words: oncology; PET/CT; quality assurance; MTV; PET/CT; tumor segmentation

J Nucl Med Technol 2023; 51:57–59

DOI: 10.2967/jnmt.122.264714

Metabolic tumor volume (MTV) can be calculated from ¹⁸F-FDG PET/CT by many methods and may help predict patient outcomes, especially for those with diffuse large B-cell lymphoma (DLBCL) (1–5). MTV is a volume defined either by quantitatively or manually selected segments representing the metabolically active tumor on ¹⁸F-FDG PET/CT (1). Total MTV is calculated by adding the MTV of all malignant lesions and is a method for measuring total tumor burden. Total MTV has shown promise in the initial staging of DLBCL and in determining its treatment response (2,4,6,7). However, tumor segmentation of ¹⁸F-FDG-avid lesions on PET/CT is often time-consuming. Advancements in threshold-based segmentation methods for filtering out background activity or signal-to-background ratios have been proposed to increase the efficacy of results (3).

Therefore, the optimal tumor segmentation method varies with the purpose of the study.

DLBCL is the most common type of non-Hodgkin lymphoma (8). The current standard for staging DLBCL is the Lugano classification, which includes a 5-point Deauville score when staging with ¹⁸F-FDG PET/CT (9), yet many studies support the significant prognostic value of total MTV in DLBCL (2–7,9). This study explored the use of nuclear medicine technologists for clinical implementation of total MTV.

MATERIALS AND METHODS

Two nuclear medicine technologists at Mayo Clinic in Rochester underwent a 30-min training session by a board-certified nuclear radiologist on distinguishing physiologic from pathologic lymphomatous ¹⁸F-FDG uptake. The technologists previously completed 4 mo of technologist classroom time and 8–12 h of experience observing the technologist side of clinical PET practice (~85 examinations per day). The technologists had no other PET education or image interpretation experience. The patient cohort comprised 10 random patients with DLBCL who were treated at a large tertiary referral center between June 22, 2016, and September 24, 2018. The technologists independently evaluated the examinations from these patients before and after systemic therapy. The technologists and the radiologist separately reviewed the images using the LesionID workflow (MIM Software Inc.). The workflow automatically segments PET lesions on the basis of an absolute SUV_{max} threshold. The threshold was set using the SUV_{max} within a 3-cm spheric region of interest within normal liver. The workflow then segmented everything with an SUV_{max} greater than the liver threshold. The technologists and the radiologist separately evaluated each segmentation to distinguish lymphoma from nonlymphomatous or physiologic segmentation. The nonlymphomatous segments were deleted after noting the anatomic location, and the total MTV was then calculated. If the student was uncertain whether a segment included lymphoma, the segment was included in the MTV calculation.

RESULTS

The mean (±SD) MTVs of the 10 patients were 446.0 cm³ (±555.6 cm³) and 38.5 cm³ (±77.6 cm³) for the radiologists and 414.8 cm³ (±597.6 cm³) and 27.7 cm³ (±57.3 cm³) for the technologists in the pre- and posttherapy examinations, respectively (Fig. 1). The mean MTVs were 7.5% and 28.0% higher for the radiologists than for the technologists in the

Received Jul. 26, 2022; revision accepted Oct. 27, 2022.
For correspondence or reprints, contact Erina Quinn (efq@case.edu).
Published online Nov. 9, 2022.
COPYRIGHT © 2023 by the Society of Nuclear Medicine and Molecular Imaging.

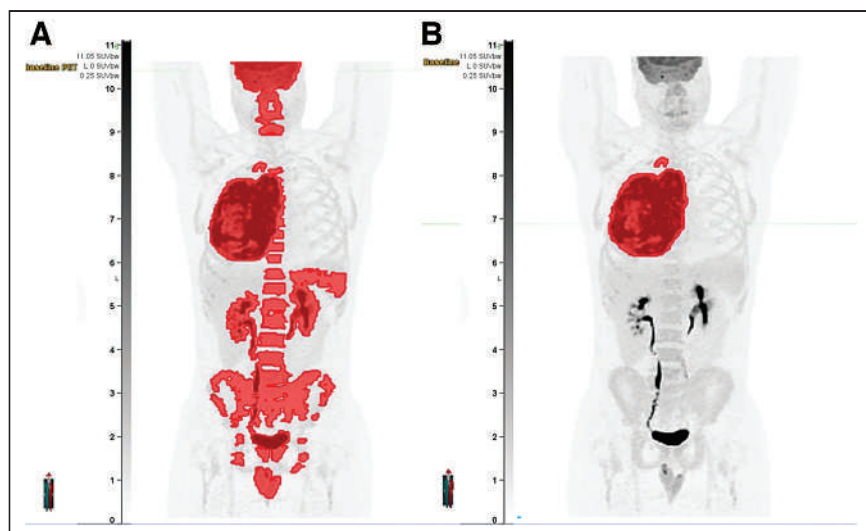


FIGURE 1. (A) Maximum-intensity projection from ^{18}F -FDG PET in patient with DLBCL demonstrating automated segmentation using normal-liver SUV as threshold, with volumetric regions of interest produced throughout body. (B) After manual input from technologists, segments around physiologic uptake are removed and only lymphomatous lesions are segmented.

pre- and posttherapy examinations, respectively. In 2 of the 10 patients, the technologists missed critical segments: a mediastinal mass that was perceived as physiologic heart uptake and a scalp lesion mistaken for physiologic brain activity. The mean number of nonlymphomatous segments removed was 20.6 (range, 8–28) and 18.3 (range, 9–41) for the radiologist and 19.2 (range, 7–33) and 17.8 (range, 7–49) for the

the final segmentation for continuous feedback and quality improvement, especially around areas with high physiologic uptake, which were the regions of discordant reporting between the technologists and the radiologist. There was a minor difference in calculation of the total MTV between the technologists and the radiologist, with the technologists missing 2 major lymphomatous lesions.

TABLE 1
Comparison of Technologists' and Radiologists' Pretherapy and Posttherapy MTVs ($P = 0.893$) and Number of Lesions ($P = 0.771$)

Patient no.	Timing	MTV (cm^3)		Student and radiologist absolute difference in MTV	Total lesions (n)	
		Technologist	Radiologist		Technologist	Radiologist
1	Posttherapy	0	0	0	10	15
1	Pretherapy	60	428	368	31	27
2	Posttherapy	0	0	0	7	12
2	Pretherapy	4	11	7	9	20
3	Posttherapy	0	0	0	14	14
3	Pretherapy	102	102	0	10	10
4	Posttherapy	106	214	108	27	41
4	Pretherapy	1,059	1,041	18	28	28
5	Posttherapy	0	0	0	12	12
5	Pretherapy	48	47	1	33	27
6	Posttherapy	171	171	0	24	15
6	Pretherapy	1,573	1,581	8	17	23
7	Posttherapy	0	0	0	49	39
7	Pretherapy	4	4	0	22	22
8	Posttherapy	0	0	0	11	11
8	Pretherapy	1,296	1,130	166	11	17
9	Posttherapy	0	0	0	10	9
9	Pretherapy	0	0	0	24	24
10	Posttherapy	0	0	0	14	15
10	Pretherapy	2	102	100	7	8

technologists in the pre- and posttherapy examinations, respectively. Common sites of removed physiologic segmentation included the urinary bladder (5%), brain (5%), lung (7%), mouth (8%), bowel (8%), kidney (22%) and musculoskeletal system (25%). Statistical analysis revealed no significant difference in total MTV or number of lesions between technologists and radiologist (Table 1).

DISCUSSION

Our study demonstrates a potential role for technologists in calculating total MTV for patients with DLBCL. We developed an effective 2-step MTV calculation workflow: in the first step, the technologist sets a threshold, removes obvious erroneous segments, and flags uncertain segments; in the second step, the radiologist reviews and finalizes the segmentation for MTV calculation. The technologist might then review

Our results demonstrate that technologists with minimal training can aid radiologists in tumor segmentation using a fixed absolute threshold of normal-liver SUV_{max} . This threshold method has proven favorable in calculating MTV to aid in predicting prognosis and outcomes (1,10–12).

Segmenting tumors on ^{18}F -FDG PET remains challenging because of the relatively low resolution of PET images, the partial-volume effect, the high variability of biodistribution, and the high intensity of physiologic uptake (12). To increase the efficiency of tumor segmentation, an alternative to the use of technologists is the use of artificial intelligence and machine learning (13–15). Early studies have shown promise in using a deep learning method to generate total MTVs prognostic of outcome in a large group of patients with DLBCL (13).

CONCLUSION

Our results on a group of patients with DLBCL suggest that the use of technologists as a preliminary step in calculating total MTV has favorable accuracy. However, more data are needed to support this approach.

DISCLOSURE

No potential conflict of interest relevant to this article was reported.

REFERENCES

1. Im HJ, Bradshaw T, Solaiyappan M, Cho SY. Current methods to define metabolic tumor volume in positron emission tomography: which one is better? *Nucl Med Mol Imaging*. 2018;52:5–15.
2. Vercellino L, Cottreau AS, Casanovas O, et al. High total metabolic tumor volume at baseline predicts survival independent of response to therapy. *Blood*. 2020;135:1396–1405.
3. Cottreau AS, Buvat I, Kanoun S, et al. Is there an optimal method for measuring baseline metabolic tumor volume in diffuse large B cell lymphoma? *Eur J Nucl Med Mol Imaging*. 2018;45:1463–1464.
4. Song MK, Chung JS, Shin HJ, et al. Clinical significance of metabolic tumor volume by FDG PET/CT in stages II and III of diffuse large B cell lymphoma without extranodal site involvement. *Ann Hematol*. 2012;91:697–703.
5. Martín-Saladich Q, Reynés-Llompart G, Sabaté-Llobera A, et al. Comparison of different automatic methods for the delineation of the total metabolic tumor volume in I-II stage Hodgkin lymphoma. *Sci Rep*. 2020;10:12590.
6. Guzmán Ortiz S, Mucientes Rasilla J, Vargas Núñez JA, Royuela A, Navarro Matilla B, Mitjavila Casanovas M. Evaluation of the prognostic value of different methods of calculating the tumour metabolic volume with ^{18}F -FDG PET/CT, in patients with diffuse large cell B-cell lymphoma. *Rev Esp Med Nucl Imagen Mol (Engl Ed)*. 2020;39:340–346.
7. Cheson BD, Fisher RI, Barrington SF, et al. Recommendations for initial evaluation, staging, and response assessment of Hodgkin and non-Hodgkin lymphoma: the Lugano classification. *J Clin Oncol*. 2014;32:3059–3068.
8. Cronin KA, Lake AJ, Scott S, et al. Annual report to the nation on the status of cancer, part i: national cancer statistics. *Cancer*. 2018;124:2785–2800.
9. Kostakoglu L, Mattiello F, Martelli M, et al. Total metabolic tumor volume as a survival predictor for patients with diffuse large B-cell lymphoma in the GOYA study. *Haematologica*. 2022;107:1633–1642.
10. Byun BH, Kong C-B, Park J, et al. Initial metabolic tumor volume measured by ^{18}F -FDG PET/CT can predict the outcome of osteosarcoma of the extremities. *J Nucl Med*. 2013;54:1725–1732.
11. Im HJ, Pak K, Cheon GJ, et al. Prognostic value of volumetric parameters of ^{18}F -FDG PET in non-small-cell lung cancer: a meta-analysis. *Eur J Nucl Med Mol Imaging*. 2015;42:241–251.
12. Pak K, Cheon GJ, Nam HY, et al. Prognostic value of metabolic tumor volume and total lesion glycolysis in head and neck cancer: a systematic review and meta-analysis. *J Nucl Med*. 2014;55:884–890.
13. Capobianco N, Meignan M, Cottreau AS, et al. Deep-learning ^{18}F -FDG uptake classification enables total metabolic tumor volume estimation in diffuse large B-cell lymphoma. *J Nucl Med*. 2021;62:30–36.
14. Barrington SF, Zwezerijnen BGJC, de Vet HCW, et al. Automated segmentation of baseline metabolic total tumor burden in diffuse large B-cell lymphoma: which method is most successful? A study on behalf of the PETRA consortium. *J Nucl Med*. 2021;62:332–337.
15. Blanc-Durand P, Jégou S, Kanoun S, et al. Fully automatic segmentation of diffuse large B cell lymphoma lesions on 3D FDG PET/CT for total metabolic tumour volume prediction using a convolutional neural network. *Eur J Nucl Med Mol Imaging*. 2021;48:1362–1370.

Posttreatment Exposure Rates for ^{90}Y -Microsphere Patients: A Comparison of Products

Steven Blum¹, Eugenio Silvestrini^{2,3}, Jonathan Weinstein⁴, and Craig Greben⁴

¹Hofstra University, Hempstead, New York; ²Radiation Safety, Department of Radiology, Northwell Health, Manhasset, New York;

³Department of Physics and Astronomy, Hofstra University, Hempstead, New York; and ⁴Donald and Barbara Zucker School of Medicine, Northwell Health, Hofstra University, Hempstead, New York

There has been a significant increase in the use of ^{90}Y -microspheres in treating liver malignancies. This increase could be seen over the last 30 y, and Food and Drug Administration approval of 2 products—Sirtex SIR-Spheres and Boston Scientific TheraSphere—has helped in the proliferation of these treatments. As the increase in use of both products rose at our institution, there was a need to determine whether there should be special considerations for patients who receive one product compared with patients who receive the other product. This determination was made by measuring exposure rates for several regions of the patient before and after implantation. An independent-samples *t* test analysis ($\alpha = 0.05$) was performed for 50 patients (25 TheraSphere and 25 SIR-Spheres) to determine whether the products behaved similarly to the extent that exposure to others was minimized and that as-low-as-reasonably-achievable principles were kept. The results showed that the products exhibited no significant differences in exposure rates, suggesting that no special considerations are needed for the procedure for one product compared with the other.

Key Words: yttrium-90; ^{90}Y ; ^{90}Y -microspheres; TheraSphere; SIR-Spheres

J Nucl Med Technol 2023; 51:60–62

DOI: 10.2967/jnmt.122.264335

In the treatment of liver tumors, especially hepatocellular carcinoma, ^{90}Y -microspheres have found a useful role. The procedure can be classified as radioembolization, a process that uses both radiation and embolization to block the tumor vascularization, thereby helping to destroy the cancer cells. ^{90}Y radioembolization has been used and studied since the 1960s and has seen improvements in both technique and efficacy since that time (1). Today, 2 products are commonly used: SiRTeX SIR Spheres and Boston Scientific TheraSphere.

Although the treatment site is in the liver, some spheres will end up in the lungs because of lung shunting. The percentage of lung shunting is determined by a pretreatment $^{99\text{m}}\text{Tc}$ -macroaggregated albumin (2,3). This is a critical step, since the cumulative dose cannot exceed 50 Gy or, for a single administration,

30 Gy. To help minimize exposure of others, a patient release criterion is needed. The criterion at our institution is an exposure rate of less than 2 mR h^{-1} at 1 m from the torso.

The program in ^{90}Y -microsphere therapy at our institution began in late 2019. As of December 2021, there had been more than 60 patients who received ^{90}Y -microsphere therapy with either SIR-Spheres or TheraSphere. These products have physical differences, such as in diameter, the material of the sphere, and where the ^{90}Y is located (SIR-Spheres coat the sphere in ^{90}Y ; TheraSphere embeds the ^{90}Y into the sphere). The differences have been well documented (2). Typical doses prescribed for a ^{90}Y -microsphere treatment are on the order of 50–150 Gy, but some studies have investigated the use of higher doses, reaching 3,000 Gy (4,5). The goal of this investigation was to determine whether the physical differences between these 2 products were significant enough to require a new end-to-end procedure for one product compared with the other. Another goal was to ascertain whether a higher prescribed dose would also require a new protocol for this treatment.

MATERIALS AND METHODS

Fifty patients ($n = 25$ for TheraSphere and $n = 25$ for SIR-Spheres) were surveyed before and after the implantation using a calibrated Fluke 451B survey meter, with the window opened (calibration date, September 20, 2021). The regions measured were the liver and lungs at the surface of the patient, and the reading at 1 m from the torso was also measured. Once the data were collected, an independent-samples *t* test analysis was performed ($\alpha = 0.05$) for the average readings for each region.

RESULTS

Figures 1, 2, and 3 show how the exposure rates changed over time and between the 2 products for the liver surface readings, the lung surface readings, and the readings at 1 m from the torso, respectively. Figure 4 shows the exposure rates for both liver and lungs at the surface for both SIR-Spheres and for TheraSphere. Table 1 displays the average and maximum exposure rates for these regions.

DISCUSSION

The measured exposure rates between the 2 products were consistent regardless of region measured. There was a

Received May 6, 2022; revision accepted Aug. 19, 2022.

For correspondence or reprints, contact Eugenio Silvestrini (esilvestr1@northwell.edu).

Published online Aug. 30, 2022.

COPYRIGHT © 2023 by the Society of Nuclear Medicine and Molecular Imaging.

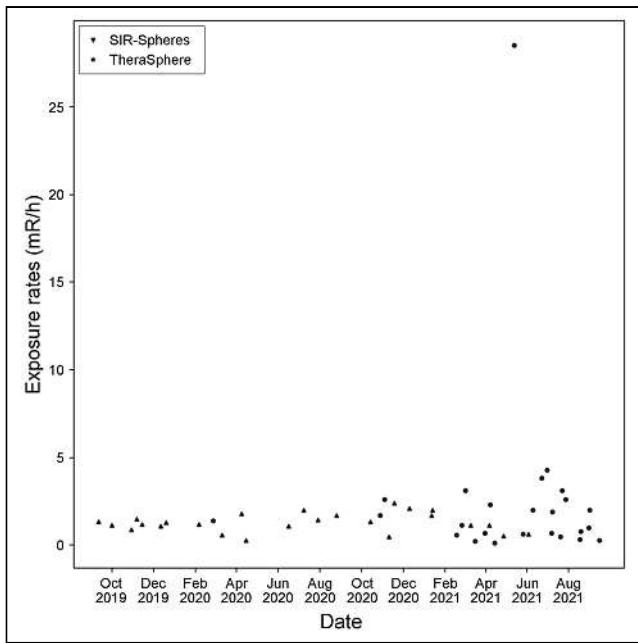


FIGURE 1. Liver exposure rates at surface of patient's body between SIR-Spheres and TheraSphere over time.

discrepancy between the liver readings for TheraSphere and for SIR-Spheres. With TheraSphere, the assumed activity per sphere was higher than with SIR-Spheres, and the dose was delivered in single-compartment dosing (6,7). This means that a higher tumor dose can be delivered via TheraSphere than SIR-Spheres using the same number of spheres. As a result, there should be a higher maximum exposure rate, and the average exposure rate would also increase. In addition, a higher dose administered will also increase the maximum

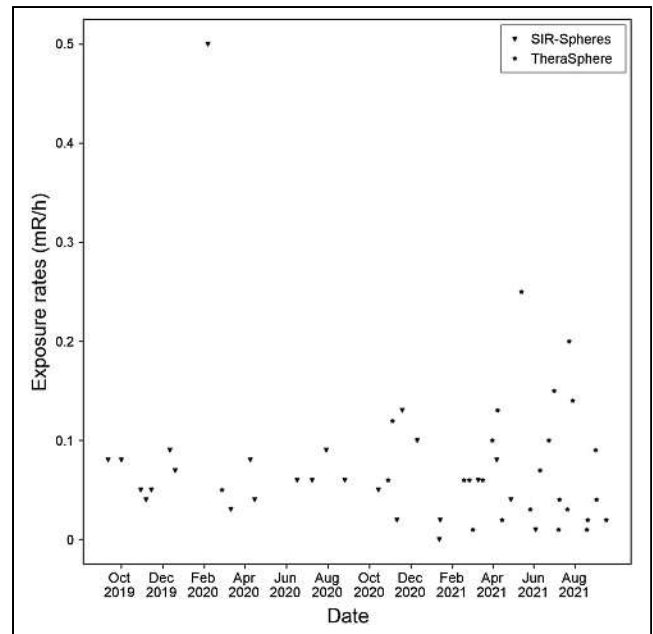


FIGURE 3. Exposure rates at 1 m from torso between SIR-Spheres and TheraSphere over time.

exposure rate and average exposure rate. At our institution, these higher doses are typically delivered via TheraSphere. For 1 patient, the administered activity was a 11.5-GBq TheraSphere vial (first-week calibration), which is the highest activity to date. In addition, it is likely that the perfusion volume was more anterior, which can explain why the maximum exposure rate was much higher than that for SIR-Spheres.

The regions reported in Table 1 were chosen for their importance in the procedure. The liver and lungs were

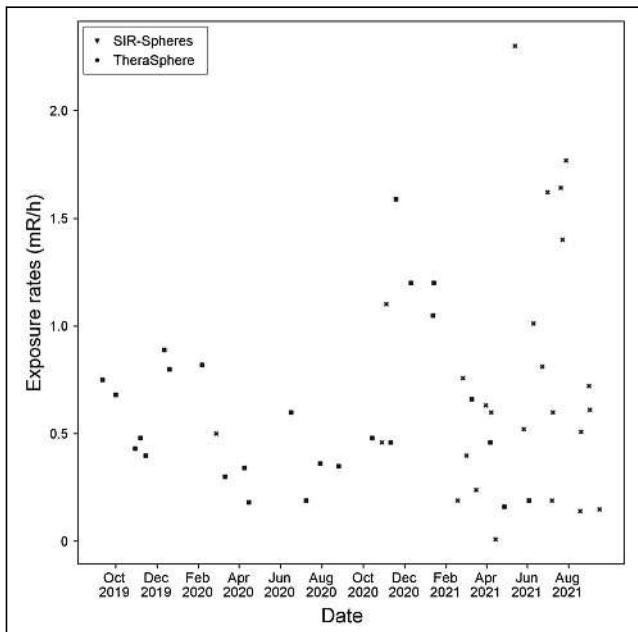


FIGURE 2. Lung exposure rates at surface of patient's body between SIR-Spheres and TheraSphere over time.

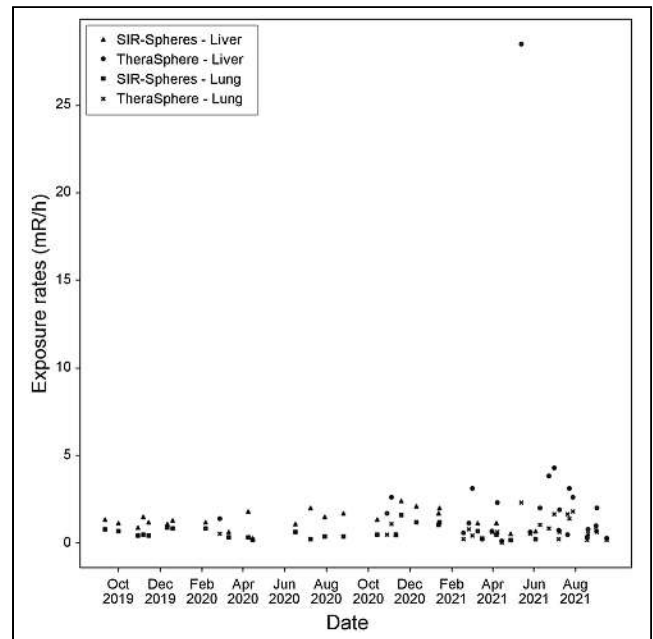


FIGURE 4. Exposure rates at surface for lungs and liver differentiated by either SIR-Spheres or TheraSphere over time.

TABLE 1
Exposure Rates for Regions of Interest for 50 Patients Split by Product Received

Site*	TheraSphere (n = 25)		SIR-Spheres (n = 25)	
	Average reading	Maximum reading	Average reading	Maximum reading
Liver	2.65	28.50	1.23	2.39
Lungs	0.76	2.30	0.56	1.59
1 m from torso	0.07	0.20	0.07	0.50

*For organs, surface readings were recorded.
Data are mR/h.

chosen since these are critical structures in this process, and the liver is also the organ containing our target volume. These regions were read at the surface to get the highest possible reading, which would be as close to the true value (if the survey meter were in direct contact with the structure) as possible. The reading at 1 m from the torso was used as the release criterion. There are no specified values for ^{90}Y therapy according to U.S. Nuclear Regulatory Commission Regulatory Guide 8.39 (8). At our institution, the release criterion is 2 mR/h at 1 m. This value corresponds to the release criterion for iodine therapy at our institution, which itself is related to Table 2 of Regulatory Guide 8.39 from the U.S. Nuclear Regulatory Commission (8) and was chosen to keep the release criterion consistent among therapies at our institution. To date, no patient has reached this maximum.

A qualitative analysis was performed by visual inspection of the graphs in Figures 1–4. This gave the impression that the exposure rates between the products were very similar by trending the readings over time. However, a more concrete analysis was conducted by an independent-samples *t* test. The results confirmed that the 2 products are not significantly different ($P < 0.05$).

CONCLUSION

A quantitative analysis was performed between 2 ^{90}Y -microsphere products at 1 institution for patients with hepatocellular carcinoma. The results showed that these products were not significantly different in terms of the exposure rates measured at the surface of the patient's body for the liver and for the lungs or at 1 m from the torso. From a radiation safety point of view, there is no need to use special considerations for one product compared with the other for factors such as release criteria, posttreatment shielding, or even steps in the implantation procedures.

DISCLOSURE

No potential conflict of interest relevant to this article was reported.

ACKNOWLEDGMENTS

We thank Timothy Ogden (Bethpage, NY) for generating the figures via Python programming.

KEY POINTS

QUESTION: Are SIR-Spheres and TheraSphere different enough to require special considerations when one product is used as opposed to the other?

PERTINENT FINDINGS: SIR-Spheres and TheraSphere resulted in non-significantly different posttreatment patient exposure rates for surface readings at the liver and the lungs, as well as at 1 m from the torso.

IMPLICATIONS FOR PATIENT CARE: Since the 2 ^{90}Y products are similar, there is no need to amend a current protocol when using one product or the other.

REFERENCES

1. Saini A, Wallace A, Alzubaidi S, et al. History and evolution of yttrium-90 radioembolization for hepatocellular carcinoma. *J Clin Med*. 2019;8:55.
2. Dezarn WA, Cessna JT, DeWerd LA, et al. Recommendations of the American Association of Physicists in Medicine on dosimetry, imaging, and quality assurance procedures for ^{90}Y microsphere brachytherapy in the treatment of hepatic malignancies. *Med Phys*. 2011;38:4824–4845.
3. Kim YC, Kim YH, Uhm SH, et al. Radiation safety issues in ^{90}Y microsphere selective hepatic radioembolization therapy: possible radiation exposure from the patients. *Nucl Med Mol Imaging*. 2010;44:252–260.
4. Kennedy AS, Nutting C, Coldwell D, Gaiser J, Drachenberg C. Pathologic response and microdosimetry of ^{90}Y microspheres in man: review of four explanted whole livers. *Int J Radiat Oncol Biol Phys*. 2004;60:1552–1563.
5. Lewandowski RJ, Salem R. Yttrium-90 radioembolization of hepatocellular carcinoma and metastatic disease to the liver. *Semin Intervent Radiol*. 2006;23:64–72.
6. Lewandowski RJ, Ryu RK, Mulcahy MF, et al. Optimization of radioembolic effect with extended-shelf-life yttrium-90 microspheres: results from a pilot study. *J Vasc Interv Radiol*. 2009;20:1557–1563.
7. Srinivas SM, Nasr EC, Kunam VK, et al. Administered activity and outcomes of glass versus resin ^{90}Y microsphere radioembolization in patients with colorectal liver metastases. *J Gastrointest Oncol*. 2016;7:530–539.
8. Regulatory guide 8.39: release of patients administered radioactive materials. U.S. Nuclear Regulatory Commission website. <https://www.nrc.gov/docs/ML0833/ML083300045.pdf>. Published April 1997. Accessed November 8, 2022.

National Diagnostic Reference Levels for Nuclear Medicine in Qatar

Hadi Fayad^{1,2}, Sultan Ahmed¹, Alaa El khatib¹, Amer Ghujeh¹, Antar Aly^{1,2}, Mohammad Hassan Kharita¹, and Huda Al-Naemi^{1,2}

¹Occupational Health and Safety Department, Hamad Medical Corporation, Doha, Qatar; and ²Weill Cornell Medicine–Qatar (WCM-Q), Doha, Qatar

Nuclear medicine (NM) started in Qatar in the mid-1980s with a 1-head γ -camera in Hamad General Hospital. However, Qatar is expanding, and now Hamad Medical Corp. has 2 NM departments and 1 PET/CT Center for Diagnosis and Research, with several hybrid SPECT/CT and PET/CT cameras. Furthermore, 2 new NM departments will be established in Qatar in the coming 3 y. Therefore, there is a need to optimize radiation protection in NM imaging and establish diagnostic reference levels (DRLs) for the first time in Qatar. This need is not only for the NM part of the examination but also for the CT part, especially in hybrid SPECT/CT and PET/CT.

Methods: Data for adult patients were collected from the 3 SPECT/CT machines in the 2 NM facilities and from the 2 PET/CT machines in the PET/CT center. The 75th percentile values (also known as the third quartile) were considered preliminary DRLs and were consistent with the most commonly administered activities. The results for various general NM protocols were described, especially ^{99m}Tc-based radiopharmaceuticals and PET/CT protocols including mainly oncologic applications. **Results:** The first DRLs for NM imaging in Qatar adults were established. The values agreed with other published DRLs, as was the case, for example, for PET oncology using ¹⁸F-FDG, with DRLs of 258, 230, 370, 400, and 461–710 MBq for Qatar, Kuwait, Korea, the United Kingdom, and the United States, respectively. Similarly, for cardiac stress or rest myocardial perfusion imaging using ^{99m}Tc-methoxyisobutylisonitrile, the DRLs were 926, 976, 1,110, 800, and 945–1,402 MBq for Qatar, Kuwait, Korea, the United Kingdom, and the United States, respectively. **Conclusion:** The optimization of administered activity that this study will enable for NM procedures in Qatar will be of great value, especially for new departments that adhere to these DRLs.

Key Words: DRLs; nuclear medicine; Qatar; PET/CT; SPECT/CT

J Nucl Med Technol 2023; 51:63–67

DOI: 10.2967/jnmt.122.264415

There is no doubt that the use of ionizing radiation and radioactive substances in diagnostic and therapeutic procedures is beneficial. According to the World Nuclear Association, today around 50 million nuclear medicine (NM) procedures are done worldwide every year. As such, medical radiation exposure has been continuously increasing during the past

decade, reaching levels that are comparable to or even greater than exposure of the population to natural sources of radiation (1). One of the main constraints of nuclear medicine procedures is that the capacity of ionizing radiation to penetrate and then transform or kill tissue cells can make it potentially dangerous to health. General principles of radiation protection from the hazard of ionizing radiation are summarized as 3 key words: justification, optimization, and dose limits (2). The main idea is therefore to make the radiation as low as reasonably achievable by balancing the benefits to the risks and therefore optimizing clinical protocols and minimizing their potentially harmful effects.

Three general categories of medical practice involve such ionizing radiation: diagnostic radiology, NM, and radiation therapy. This paper will focus on diagnostic NM imaging.

Medical exposure differs from occupational and public exposure in that patients are directly, and in a known way, exposed to radiation for their diagnostic or therapeutic benefit. It is therefore not appropriate to apply administered activity limits or administered activity constraints, the remaining rule being that the given activity should cause more benefit than harm. As a result, medical radiation systems use diagnostic reference levels (DRLs) as reference values and do not have administered activity limits (3).

DRLs are an important tool that helps to reduce patient exposure while optimizing NM clinical protocols. This optimization is especially important in multimodality imaging, such as imaging that includes an NM component (for which exposure is caused by the injected radiopharmaceutical) along with a CT component in a hybrid PET/CT or SPECT/CT imaging system.

Given that Qatar is expanding and that at least 2 new NM departments will be inaugurated in the upcoming 3 y, creating specific DRLs for Qatar NM is a must. The results presented in this paper will be the first national DRLs for NM procedures in Qatar and can serve as a starting point for future updates.

MATERIALS AND METHODS

Data Collection and DRL Calculation

Hamad Medical Corp. is the only institute in Qatar offering NM diagnostic services for adults. The services are distributed into 3 main sites: Hamad General Hospital, the National Center for Cancer Care and Research, and the PET/CT Center for Diagnosis and

Received May 15, 2022; revision accepted Aug. 24, 2022.
For correspondence or reprints, contact Hadi Fayad (hfayad1@hamad.qa).
Published online Aug. 30, 2022.
COPYRIGHT © 2023 by the Society of Nuclear Medicine and Molecular Imaging.

Research. Data were collected from the 3 SPECT/CT machines in the 2 NM facilities and from the 2 PET/CT machines in the PET/CT center. The institutional review board at Hamad Medical Corp. approved this retrospective study; all patients were adults.

The DRLs were determined using 5 steps. In the first step, protocols for each type of NM examination performed at each site were identified. The second step was creation of a radiopharmaceutical database of the administered activity for each NM examination performed from the beginning of 2020 till the end of 2021. Third, the median (50 percentile) and the third quartile (75th percentile) of the administered activity were calculated. The DRLs were established on the basis of the third quartile (4) as recommended by the International Commission on Radiological Protection. The results were then compared with those of other countries, including Kuwait, Korea, Japan, Australia, the United Kingdom, the United States, and Europe.

In the fourth step, a second database was created containing the volume CT dose index ($CTDI_{vol}$) and the dose-length product (DLP) for each NM examination that had an associated CT scan obtained through SPECT/CT or PET/CT. The median and 75th percentile were calculated for each $CTDI_{vol}$ and DLP. The DRLs for the CT portion of PET/CT and SPECT/CT were based on the scanned region. For PET/CT, these regions were whole-body 1 (WB1, base of skull to mid-thigh), whole-body 2 (WB2, vertex to knees), and total body (TB, vertex to toes); for SPECT/CT, these regions were heart (corresponding to a myocardial perfusion study) or whole body (WB).

Finally, to assess the radiation dose from the CT component of the examination, the effective dose (ED) was calculated using the DLP and a conversion factor k (where $ED [mSv] \approx k \times DLP$).

A factor of 0.0096 was used for PET/CT WB1 and WB2 and SPECT/CT WB; 0.0093 was used for PET/CT TB and 0.015 was used for SPECT/CT cardiac studies (5,6).

Statistical Analysis

The median, mean \pm SD, and 75th percentile were estimated using Microsoft Excel.

RESULTS

Figure 1 presents 2 examples of distribution histograms showing the number of patients compared with the administered activity for an ^{18}F -FDG PET scan (Fig. 1A) and a ^{99m}Tc -diphosphonate NM bone scan (Fig. 1B). The respective mean administered activities were 231.12 ± 44.82 MBq and 721.97 ± 78.67 MBq.

Table 1 shows the results for different procedures and radiopharmaceuticals for both PET and SPECT and including the median injected administered activities and the DRLs. For ^{18}F -based tracers, DRLs were between 187 MBq for NaF and 260 MBq for prostate-specific membrane antigen. For ^{99m}Tc , DRLs were between 19 MBq for nanocolloid and phytate and 926 MBq for methoxyisobutylisonitrile NM cardiac stress or rest studies.

Table 2 compares the obtained DRLs with those of other countries for protocols for which an associated DRL exists. Oncologic PET studies using ^{18}F -FDG had DRLs of 258, 230, 370, 400, and 461–710 MBq for Qatar, Kuwait, Korea, the United Kingdom, and the United States, respectively. Similarly, for cardiac stress or rest NM studies using ^{99m}Tc -methoxyisobutylisonitrile, the DRLs were 926, 976, 1,110, 800, and 945–1,402 MBq, respectively. Regarding ^{99m}Tc -diphosphonate, the DRLs were 740, 944, 925, 600, and 848–1,185 MBq, respectively.

Moreover, achievable CT doses and DRLs (from both PET/CT and SPECT/CT) in Qatar for both $CTDI_{vol}$ and DLP are shown in Table 3. Regarding CT from PET/CT, the DRLs for $CTDI_{vol}$ ranged from 4.42 to 5.3 mGy for PET/CT TB and PET/CT WB1, respectively. The DRLs for DLP ranged from 521.75 to 831.5 mGy·cm for PET/CT WB2 and PET/CT TB, respectively. For CT from SPECT/CT, the DRLs for DLP ranged from 103.58 mGy·cm for SPECT/CT myocardial perfusion to 211.48 mGy·cm for SPECT/CT WB.

Finally, the obtained EDs are shown in Table 4. For CT from PET/CT, EDs ranged from 5.01 mSv for PET/CT WB2 to 7.73 mSv for PET/CT TB. For CT from SPECT/CT, EDs ranged from 1.59 mSv for SPECT/CT myocardial perfusion to 3.17 mSv for SPECT/CT WB.

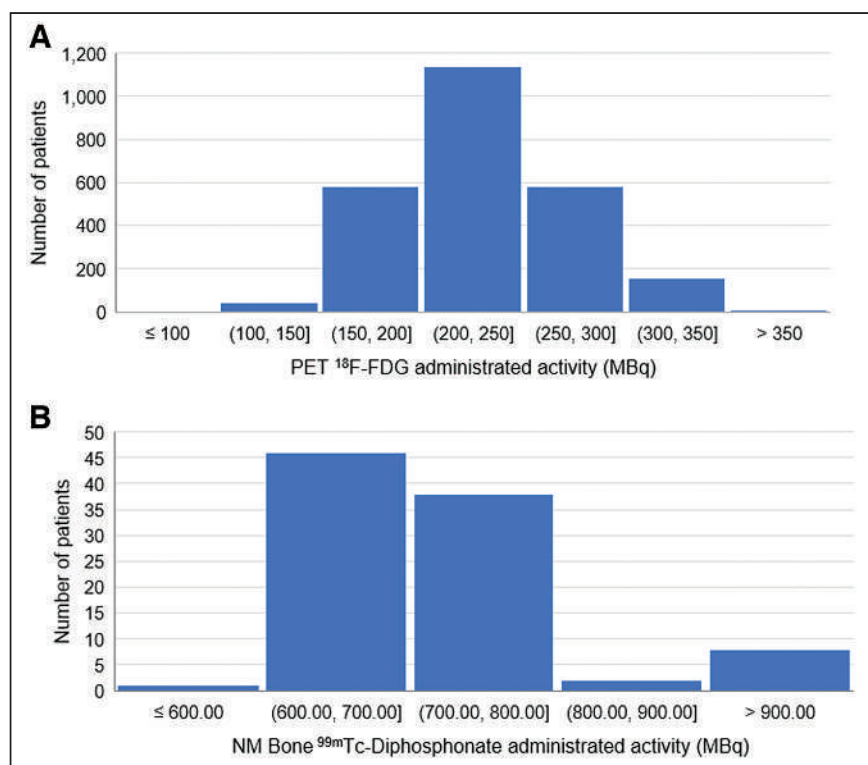


FIGURE 1. Distribution histogram showing number of patients compared with administered activities for PET ^{18}F -FDG patients (A) and NM bone ^{99m}Tc -diphosphonate patients (B). NM = nuclear medicine.

TABLE 1
PET/CT and General NM Procedures: Number of Included Studies, Median Activities (50th Percentile),
and DRLs (75th Percentile)

Procedure	Agent	Studies (n)	Median activity, 50th percentile (MBq)	DRL, 75th percentile (MBq)
PET oncology	¹⁸ F-FDG	2,523	228	258
PET brain	¹⁸ F-FDG	10	200	202
PET oncology	¹⁸ F- or ⁶⁸ Ga-PSMA	94	234	260
PET oncology	¹⁸ F-NaF	449	158	187
PET oncology	⁶⁸ Ga-DOTATATE	107	135	140
NM bone	^{99m} Tc-diphosphonate	95	703	740
NM thyroid uptake	^{99m} Tc-pertechnetate	457	189	195
NM WB	¹³¹ I-Nal	32	185	190
NM parathyroid	^{99m} Tc-MIBI	118	374	384
NM cardiac stress or rest	^{99m} Tc-MIBI	2,556	925	926
NM lung	^{99m} Tc-MAA	82	74	103
NM lymphoscintigraphy	^{99m} Tc-phytate	8	19	19
NM hepatobiliary	^{99m} Tc-HIDA	19	185	188
NM gastric emptying	^{99m} Tc-phyton	52	19	36
NM renogram	^{99m} Tc-DTPA	13	186	189
NM renogram	^{99m} Tc-MAG3	356	185	189
NM renal scintigraphy	^{99m} Tc-DMSA	71	75	101
NM sentinel node localization in breast	^{99m} Tc-nanocolloid	211	19	19
NM cardiac	^{99m} Tc-pyrophosphate	22	722	740
NM lung ventilation	^{99m} Tc-Technegas*	23	74	99

*Cyclomedica.

PSMA = prostate-specific membrane antigen; MAA = macroaggregated albumin; HIDA = hepatobiliary iminodiacetic acid;
DTPA = diethylenetriaminepentaacetate; MAG3 = mercaptoacetyltriglycine; DMSA = dimercaptosuccinic acid.

DISCUSSION

The first NM DRLs for adults in Qatar were established on the basis of local data assessment. Application of the third quartile, which is the same standard as in other studies to establish the DRLs of NM imaging, was confirmed as appropriate for domestic NM imaging studies. When any

DRL is consistently exceeded at a facility (i.e., the median value of the DRL for a representative sample of patients within a certain weight range is greater than the DRL in International Commission on Radiological Protection publication 135), possible reasons should be investigated and a plan should be implemented and documented without delay if corrective action is required (7).

TABLE 2
Qatar DRLs for PET/CT and General NM Procedures in Comparison to Other Countries

Procedure	Agent	Qatar (this study)	Kuwait (10)	Korea (11)	Japan (12)	Australia (13)	U.K. (14)	U.S. (15)	European Union (16)
PET oncology	¹⁸ F-FDG	258	230	370	240	310	400	461–710	200–400
PET brain	¹⁸ F-FDG	202	231	370	240	250	250		
NM bone	^{99m} Tc-diphosphonate	740	944	925	950	920	600	848–1,185	500–1,110
NM thyroid uptake	^{99m} Tc-pertechnetate	195	185	217	300	215	80		75–222
NM WB	¹³¹ I-Nal	190	200	185		185	400		90–400
NM parathyroid	^{99m} Tc-MIBI	384	900	740	800	900	900		400–900
NM cardiac stress or rest	^{99m} Tc-MIBI	926	976	1,110	1,200	1,520	800	945–1,402	
NM lung	^{99m} Tc-MAA	103	217.5	222	260	240	100	147–226	100–296
NM lymphoscintigraphy	^{99m} Tc-phytate	19	40	148		52	40		74–150
NM gastric emptying	^{99m} Tc-phyton	36	37	111		44	12	31–50	150–540
NM renogram	^{99m} Tc-DTPA	189	90	555	400	500	300	407–587	
NM renogram	^{99m} Tc-MAG3	189	370	500	400	305	100	283–379	100–370
NM renal scintigraphy	^{99m} Tc-DMSA	101	200	185	210	200	80	189–289	70–183

MIBI = methoxyisobutylisonitrile; MAA = macroaggregated albumin; DTPA = diethylenetriaminepentaacetate; MAG3 = mercaptoacetyltriglycine.

TABLE 3

Achievable Dose (50th Percentile) and DRLs (75th Percentile) for Both CTDI_{vol} and DLP for Different Scan Regions Including CT Imaging in PET/CT- and SPECT/CT-Based Scans

Protocol	Scan region	CTDI _{vol} (mGy)		DLP (mGy-cm)	
		Achievable dose, 50th percentile	DRL, 75th percentile	Achievable dose, 50th percentile	DRL, 75th percentile
PET/CT WB1	Base of skull to mid-thigh	4.08	5.3	378.1	547.93
PET/CT WB2	Vertex to knees	3.68	4.49	453.6	521.75
PET/CT TB	Vertex to toes	3.08	4.42	540.4	831.5
SPECT/CT myocardial perfusion	Mid chest to lower neck	3.72	4.26	89.62	103.58
SPECT/CT WB*	Thorax and abdomen	4.86	4.86	211.48	211.48

*Fixed region size.

DRLs can be used to optimize radiation protection by setting the appropriate level of administered activity and its associated CT parameters (affecting CT dose) in hybrid systems for adults undergoing NM imaging. The calculated CT ED, although based on k factors, helped to obtain a clear idea of the radiation impact of including CT in different PET/CT- and SPECT/CT-based scans having different fields of views.

DRLs are not a method of patient-by-patient radiation dose monitoring and are not an indicator of good or bad practice but, rather, provide additional data to verify that the department is operating optimally. When DRLs are exceeded, the reason should be verified. In some cases, such as when certain old machines are used, some higher DRLs can be acceptable. The highest priority for any diagnostic examination is to achieve sufficient image quality (8).

The DRLs for Qatar agreed well with those for other countries and regions and therefore are adequate with the required optimization. Comparing our study results with those of other countries in the Gulf region, the DRLs for Qatar were lower than those for Kuwait by 20% for NM thyroid uptake studies, 57% for NM parathyroid studies, 50% for NM lung studies, 49% for NM renography, and 50% for NM renal scintigraphy. The PET oncology and PET brain DRLs were in line with that for Kuwait and lower

by 20%–30% than those for other countries, such as Korea, Australia, the United Kingdom, and the European Union, as presented in Table 2. In only 3 protocols were Qatar DRLs lower than in any other country—a finding that may be advantageous, given that physicians agreed that the obtained images were of sufficient quality. These protocols were NM parathyroid studies using ^{99m}Tc-methoxyisobutylisonitrile, NM lymphoscintigraphy using ^{99m}Tc-phytate, and NM renography using ^{99m}Tc-diethylenetriaminepentaacetate.

Regarding the CT in hybrid PET/CT WB1 studies, the Qatar DRLs were lower than French and Japanese DRLs (5.3 vs. 6.6 and 5.5 for CTDI_{vol} and 547.93 vs. 628 and 550 for DLP, respectively). Similarly, for CT in hybrid SPECT/CT WB studies, the Qatar DRLs were lower than Japanese DRLs (4.86 vs. 5.03 for CTDI_{vol} and 211.48 vs. 384.1 for DLP, respectively).

The present study had some limitations. One is specific to our study, and the others exist for equivalent studies. First, for adults in Qatar, only 2 NM facilities and 1 PET/CT facility are available. As a result, the obtained values should be updated whenever new facilities are established. Second, although clinicians demand images of diagnostic quality, including image quality as a factor during DRL calculation (regarding radiopharmaceutical administered activity or CT dose) is not achievable in either our study or other published DRL studies, given

TABLE 4

Median Activity (50th Percentile) and DRLs (75th Percentile) for ED Calculated Using k Factor for Different Scan Regions Including CT Imaging in PET/CT- and SPECT/CT-Based Scans

Protocol	Scan region	k factor (mSv-mGy ⁻¹ .cm ⁻¹)	Effective dose (mSv)	
			Median, 50th percentile	DRL, 75th percentile
PET/CT WB1	Base of skull to mid-thigh	0.0096	3.63	5.26
PET/CT WB2	Vertex to knees	0.0096	4.35	5.01
PET/CT TB	Vertex to toes	0.0093	5.03	7.73
SPECT/CT myocardial perfusion	Mid chest to lower neck	0.015	1.34	1.59
SPECT/CT WB*	Thorax and abdomen	0.015	3.17	3.17

*Fixed region size.

that it is not easy to assess NM or CT images objectively. Third, because the study was of adults only, pediatric DRLs were not established. However, Qatar uses the European Association of Nuclear Medicine pediatric dosage card (9), and dose for pediatric patients is therefore fixed and based on their weight.

CONCLUSION

Radiation protection is an essential part of NM, especially in growing countries such as Qatar. DRLs can help to optimize such radiation protection to establish the safest NM practice. DRLs for Qatar should be reviewed 5 y after this study.

DISCLOSURE

This study was supported by the Qatar National Research Fund (a member of the Qatar Foundation) under grant NPRP10-0126-170263. No other potential conflict of interest relevant to this article was reported.

KEY POINTS

QUESTION: Can DRLs be established for the first time in Qatar to optimize radiation protection in NM imaging?

PERTINENT FINDINGS: DRLs for administered activity in Qatar, as well as the associated CT dose in hybrid systems, were successfully established and were consistent with published DRLs for Europe, Japan, Korea, Australia, and the United States.

IMPLICATIONS FOR PATIENT CARE: Optimization of administered activity for NM procedures in Qatar, especially when new departments are opened, may spare patients and staff from exposure to ionizing radiation.

REFERENCES

1. *Radiation Protection and Safety in Medical Uses of Ionizing Radiation*. International Atomic Energy Agency; 2018:1.
2. Do K-H. General principles of radiation protection in fields of diagnostic medical exposure. *J Korean Med Sci*. 2016;31(suppl 1):S6–S9.
3. ICRP publication 105: radiation protection in medicine. *Ann ICRP*. 2007;37:1–63.
4. Vassileva J, Rehani M. Diagnostic reference levels. *AJR*. 2015;204:W1–W3.
5. Diagnostic reference levels in medical imaging: review and additional advice. *Ann ICRP*. 2001;31:33–52.
6. Shrimpton PC, Jansen JTM, Harrison JD. Updated estimates of typical effective doses for common CT examinations in the UK following the 2011 national review. *Br J Radiol*. 2016;89:20150346.
7. Vañó E, Miller DL, Martin CJ, et al. ICRP publication 135: diagnostic reference levels in medical imaging. *Ann ICRP*. 2017;46:1–144.
8. Cho S-G, Kim J, Song H-C. Radiation safety in nuclear medicine procedures. *Nucl Med Mol Imaging*. 2017;51:11–16.
9. Lassmann M, Treves ST. Paediatric radiopharmaceutical administration: harmonization of the 2007 EANM paediatric dosage card (version 1.5.2008) and the 2010 North American consensus guidelines. *Eur J Nucl Med Mol Imaging*. 2014;41:1036–1041.
10. Alnaaimi MA, Alduaij MA, Shenawy FA, et al. National diagnostic reference levels for nuclear medicine in Kuwait. *J Nucl Med Technol*. 2022;50:54–59.
11. Song H-C, Na MH, Kim J, Cho S-G, Park JK, Kang K-W. Diagnostic reference levels for adult nuclear medicine imaging established from the national survey in Korea. *Nucl Med Mol Imaging*. 2019;53:64–70.
12. Abe K, Hosono M, Igarashi T, et al. The 2020 national diagnostic reference levels for nuclear medicine in Japan. *Ann Nucl Med*. 2020;34:799–806.
13. Current Australian diagnostic reference levels for nuclear medicine. Australian Radiation Protection and Nuclear Safety Agency website. <https://www.arpsa.gov.au/research-and-expertise/surveys/national-diagnostic-reference-level-service/current-australian-drls/nm>. Accessed November 8, 2022.
14. Hart D, Wall B. UK nuclear medicine survey 2003–2004. *Nucl Med Commun*. 2005;26:937–946.
15. NCRP report no. 172: reference levels and achievable doses in medical and dental imaging—recommendations for the United States. National Council of Radiation Protection and Measurements website. <https://ncrponline.org/shop/reports/report-no-172-reference-levels-and-achievable-doses-in-medical-and-dental-imaging-recommendations-for-the-united-states-2012/>. Published 2012. Accessed November 8, 2022.
16. Article citations: European Commission (EC) (2014) diagnostic reference levels in thirty-six European countries part 2/2—radiation protection n°180. Scientific Research Publishing website. [https://www.scirp.org/\(S\(lz5mqp453ed%20snp55rrgjt55\)\)/reference/referencespapers.aspx?referenceid=3023821](https://www.scirp.org/(S(lz5mqp453ed%20snp55rrgjt55))/reference/referencespapers.aspx?referenceid=3023821). Accessed November 8, 2022.

Radioactive Iodine Uptake in Postoperative Seroma: A Cause for False Positivity

Piyush Aggarwal¹, Rajkumar K. Seenivasagam², Ashwani Sood¹, Sarika Prashar¹, Piyush Pathak³, Naresh Sachdeva⁴, and Pariksha Gupta⁵

¹Department of Nuclear Medicine, PGIMER, Chandigarh, India; ²Department of Surgical Oncology, AIIMS, Rishikesh, India;

³Department of Biochemistry, PGIMER, Chandigarh, India; ⁴Department of Endocrinology, PGIMER, Chandigarh, India; and

⁵Department of Cytopathology and Gynecologic Pathology, PGIMER, Chandigarh, India

Besides the known physiologic uptake of ¹³¹I, the literature describes various false-positive findings on ¹³¹I scans in benign lesions, inflammation, traumatic sites, and postsurgical sites, to name a few. However, to the best of our knowledge, no study has shown false-positive uptake of ¹³¹I in a postoperative seroma at the postsurgical site. We describe such a case here.

Key Words: ¹³¹I; seroma; papillary thyroid carcinoma

J Nucl Med Technol 2023; 51:68–69

DOI: 10.2967/jnmt.122.264569

Radioactive iodine (¹³¹I) uptake at the inflammatory or postoperative site is an uncommon finding, with few reports showing false-positive ¹³¹I uptake at the site of surgical sutures, subcutaneous injections, postoperative inflammation, or trauma (1–4). Here, we report the case of an elderly man with papillary thyroid cancer who showed postoperative false-positive ¹³¹I localization in a seroma. The patient gave informed consent for the study as a part of the institutional protocol.

CASE REPORT

A 61-y-old man presented with insidious, neglected right-sided swelling in the thyroid of 20-y duration, rapidly increasing for the previous 2 y. Contrast-enhanced CT of the neck revealed hypodense lesions in the thyroid gland with enlarged supraclavicular and infraclavicular lymph nodes. He was incidentally diagnosed with multiple myeloma on detailed evaluation and was started on steroids

and combination chemotherapy. Cytopathology from the thyroid lesion and right supraclavicular lymph node revealed papillary thyroid cancer. He underwent total thyroidectomy with central and bilateral modified radical neck dissection. Histopathology revealed multifocal classic-variant papillary thyroid cancer, with gross extrathyroidal extension into the strap muscles, angioinvasion, and perineural invasion but free surgical margins. Thirty of 82 resected lymph nodes were involved (largest, ~1.5 cm) along with the extranodal extension, resulting in a stage of pT3bN1Mx. After surgery, he developed gradually progressive, well-defined, nonpulsatile, and fluctuant bilateral supraclavicular swelling and had undergone multiple therapeutic aspirations from the recurrent right-sided supraclavicular swelling. His stimulated

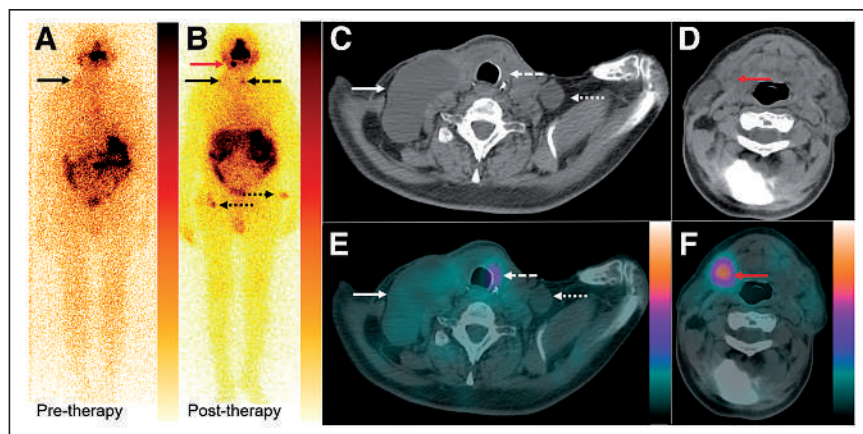


FIGURE 1. (A and B) Whole-body diagnostic (A) and posttherapy planar (B) anterior scans showing faint uptake in right supraclavicular region (solid black arrows) and increased uptake at midline of neck (dashed black arrow), in right submandibular region (red arrow), and bilaterally in thigh regions (dotted black arrows). (C–F) CT and SPECT/CT of the head and neck region are shown. Posttherapy CT (C [CT of the neck region] and D [CT of the head region]) and SPECT/CT (E [SPECT/CT of the neck region] and F [SPECT/CT of the head region]) images showing faint tracer avidity in right supraclavicular hypodense collection (solid white arrows), non-tracer-avid left supraclavicular hypodense collection (dotted white arrows), tracer-avid thyroid bed remnant (dashed white arrows), and tracer-avid right level IB cervical lymph node (red arrows).

Received Jun. 24, 2022; revision accepted Oct. 5, 2022.

For correspondence or reprints, contact Ashwani Sood (sood99@yahoo.com).

Published online Nov. 9, 2022.

COPYRIGHT © 2023 by the Society of Nuclear Medicine and Molecular Imaging.

serum thyroglobulin, antithyroglobulin, and thyroid-stimulating hormone levels after thyroid hormone withdrawal were 47.6 ng/mL (reference range, 0–9), 1.9 IU/mL (<10), and

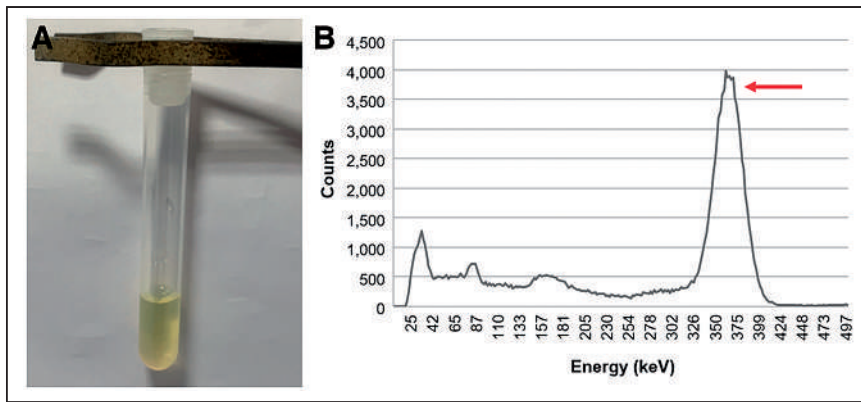


FIGURE 2. (A) Test tube containing clear yellow fluid aspirated from right-sided swelling. (B) γ -ray emission spectrum of aspirated fluid, with peak (arrow) corresponding to γ -energy of ^{131}I (364 keV).

217.5 $\mu\text{IU/mL}$ (reference range, 0.27–4.2), respectively. Whole-body diagnostic and posttherapy (5 d after adjuvant therapy with $\sim 100 \text{ mCi}/3,700 \text{ MBq}$) ^{131}I planar and SPECT/CT scans of the neck (Fig. 1) revealed a faintly tracer-avid right supraclavicular hypodense cystic neck swelling ($\sim 9.0 \times 4.3 \times 6.7 \text{ cm}$) and a non-tracer-avid left supraclavicular hypodense cystic neck swelling ($\sim 2.8 \times 2.3 \times 2.5 \text{ cm}$). The posttherapy SPECT/CT showed a tracer-avid thyroid bed remnant and a right level IB lymph node, with tracer contamination bilaterally over the thigh regions. Lymphoscintigraphy ruled out lymphocele as the etiology of the bilateral cystic neck swelling. The right-sided swelling yielded clear yellow serous fluid on aspiration, having protein, triglyceride, and thyroglobulin levels of 3.77 g/dL, 10.9 mg/dL, and 4.75 ng/mL, respectively (Fig. 2). Fluid cytology showed sparse inflammatory cells without any malignant thyroid cells. The aspirated fluid counted in a well counter showed a γ -ray emission spectrum with a peak corresponding to ^{131}I γ -energy (364 keV), confirming the presence of radioiodine in the aspirated fluid (Fig. 2).

DISCUSSION

Only a few reports have shown false-positive ^{131}I uptake in the postoperative and inflammatory sites (1–4), but to the best of our knowledge, no previous study has shown false-positive uptake in a postoperative seroma after thyroidectomy and neck node dissection. The localized inflammatory hyperemia and exudation of radioiodine-containing serous fluid into the

postsurgical site may explain the radioiodine localization in this index case. Serous cystic lesions can retain radioiodine by passive diffusion from the blood pool or, as a possible alternate mechanism, a slow exchange of water and chemical elements (5). Though postthyroidectomy seroma formation may be multifactorial, recurrent seroma in this index case despite multiple aspirations might be due to steroid treatment for multiple myeloma (6,7). Moreover, multiple aspirations from the right-sided cystic swelling resulted in frequent microhemorrhages and radioiodine leakage into that cavity but not in the contralateral cystic swelling.

CONCLUSION

Radioiodine localization at the postoperative site on planar scintigraphy may be misleading, but the combination of clinical history, cross-sectional imaging (SPECT/CT), and biochemical and cytopathologic examination proved crucial in guiding the correct diagnosis and management in this index case.

DISCLOSURE

No potential conflict of interest relevant to this article was reported.

REFERENCES

- Oh JR, Ahn BC. False-positive uptake on radioiodine whole-body scintigraphy: physiologic and pathologic variants unrelated to thyroid cancer. *Am J Nucl Med Mol Imaging*. 2012;2:362–385.
- Chudgar AV, Shah JC. Pictorial review of false-positive results on radioiodine scintigrams of patients with differentiated thyroid cancer. *Radiographics*. 2017;37:298–315.
- Chowdhary AW, Kavanal AJ, Sood A, et al. Posttraumatic scab on ^{131}I whole-body scan: a false-positive finding. *Clin Nucl Med*. 2021;46:512–514.
- Albano D, Motta F, Baronchelli C, et al. ^{131}I whole-body scan incidental uptake due to spermatocele. *Clin Nucl Med*. 2017;42:901–904.
- Okuyama C, Ushijima Y, Kikkawa M, et al. False-positive I-131 accumulation in a liver cyst in a patient with thyroid carcinoma. *Clin Nucl Med*. 2001;26:198–201.
- Sheahan P, O'Connor A, Murphy MS. Comparison of incidence of postoperative seroma between flapless and conventional techniques for thyroidectomy: a case-control study. *Clin Otolaryngol*. 2012;37:130–135.
- Ramouz A, Rashiashemi SZ, Daghigh F, et al. Predisposing factors for seroma formation in patients undergoing thyroidectomy: cross-sectional study. *Ann Med Surg (Lond)*. 2017;23:8–12.

Confirmation of Intracranial Neuroendocrine Metastasis Using ^{68}Ga -DOTATATE PET/CT

Rahim Ismail, Mark Manganaro, and James Bai

Department of Imaging Science, University of Rochester Medical Center, Rochester, New York

Neuroendocrine tumors (NETs) are rare neoplasms with an exceedingly low incidence of intracranial metastasis. We present a 79-y-old woman with a biopsy-proven pulmonary neuroendocrine tumor who presented with an intracranial mass in the posterior fossa that was avid on ^{68}Ga -DOTATATE PET/CT, facilitating the rare diagnosis of intracranial NET metastasis. The case highlights the utility of advanced imaging techniques in differentiating intracranial NET metastasis from other etiologies.

Key Words: oncology; PET/CT; DOTATATE; intracranial; metastasis; neuroendocrine

J Nucl Med Technol 2023; 51:70–72

DOI: 10.2967/jnmt.122.264834

Neuroendocrine tumors (NETs) typically present in an indolent clinical course, with an incidence of 6.98 per 100,000 (1). These lesions primarily, but not exclusively, originate from the gastrointestinal and bronchopulmonary systems (2). Intracranial metastases of NETs are rare, with an estimated incidence of 1.5%–5% (2,3). The sites of spread in intracranial metastasis are relatively uncharacteristic, with reported metastatic disease in the parenchyma, pineal gland, posterior fossa, dura, and even within an existing meningioma in the skull base (4,5).

Prognosis can vary depending on the NET stage and site of origin. Registry data on 10-y specific survival rates in 6,792 patients with small-intestine NETs found ranges of 77%–95% for locally advanced disease, 68%–77% for nodal disease, and 42% for distant metastatic disease. The median survival time after diagnosis of brain metastasis was 10.0 mo; however, this increased to 3.2 y in patients who underwent resection and whole-brain radiation therapy (3). Therefore, accurate diagnosis of intracranial metastases of NETs plays an important role in providing a reliable prognosis and clinical management.

A rare clinical scenario is a patient with multiple potential primary oncologic processes, making accurate diagnosis more critical for guiding clinical management. We present the case

of a 79-y-old woman with biopsy-proven pulmonary NET and additional incidental renal and thyroid lesions who presented with a symptomatic posterior fossa mass with avidity on ^{68}Ga -DOTATATE PET/CT, leading to a diagnosis of intracranial NET metastasis.

CASE PRESENTATION

The patient was a 79-y-old woman who presented because of progressive gait instability over the previous 5 mo. MRI demonstrated a 2.9-cm avidly enhancing mass in the cerebellum containing intralesional hemorrhage (Fig. 1). CT of the chest, abdomen, and pelvis showed a dominant 4.1-cm mass in the left upper lobe of the lung (Fig. 2C) and several lung nodules bilaterally throughout the lungs. CT-guided lung biopsy found an epithelial neoplasm with neuroendocrine differentiation, favoring carcinoid tumor.

^{18}F -FDG PET CT demonstrated hypermetabolism of the left lung mass (Fig. 3A). The intracranial lesion had ^{18}F -FDG uptake similar to that of the surrounding hypermetabolic brain (Fig. 3B). Additional metastatic workup revealed 2 more lesions: a small 1-cm enhancing right renal lesion and a heterogeneous hypodense left thyroid nodule, both of which have a known propensity for intracranial hemorrhagic metastasis. ^{68}Ga -DOTATATE PET/CT demonstrated corresponding uptake within the focal lesion in the right cerebellum (Fig. 2A) and left lung mass, confirming somatostatin receptor expression in these lesions.

In this case, intracranial metastasis from the thyroid gland and the kidney was essentially excluded as a feasible diagnosis given the ^{68}Ga -DOTATATE uptake. Other intracranial lesions that exhibit ^{68}Ga -DOTATATE uptake include meningiomas and hemangioblastomas. However, intratumoral hemorrhage in meningioma is rare, and hemangioblastomas demonstrate mural enhancing nodules with cystic components on structural brain MRI. Given the presumed recent onset, the ^{68}Ga -DOTATATE avidity, and the hemorrhage, the lesion in this clinical context would likely be a neuroendocrine metastasis.

The patient received 4 d of stereotactic volumetric modulated arc therapy for a total of 3,000 cGy in 5 fractions. On follow-up MRI 3 mo after treatment, the lesion had decreased in size and enhancement. Only monitoring was used for the pulmonary lesions, because of lack of associated symptoms.

Received Aug. 26, 2022; revision accepted Nov. 7, 2022.

For correspondence or reprints, contact Mark Manganaro (mark_manganaro@urmc.rochester.edu).

Published online Jan. 4, 2023.

COPYRIGHT © 2023 by the Society of Nuclear Medicine and Molecular Imaging.

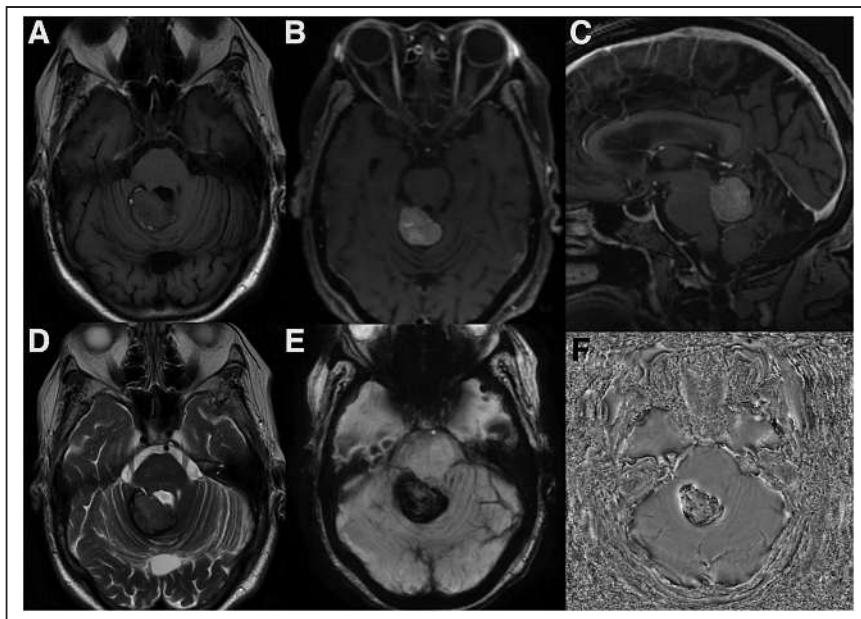


FIGURE 1. (A) Axial T1 unenhanced image demonstrates an extra-axial posterior fossa lesion in the right superior cerebellar region with predominantly intermediate T1 signal. (B) Axial and (C) sagittal T1 contrast-enhanced images show avid enhancement within this lesion. (D) Corresponding axial T2 image demonstrates intermediate signal intensity. (E) Susceptibility-weighted image and (F) phase image demonstrate signal loss within the lesion, suggesting intralesional hemorrhage.

DISCUSSION

NETs are a rare and diverse group of neoplasms that generally follow an indolent course and have a high propensity

to metastasize. Intracranial NET metastasis is extremely rare, with variable imaging characteristics and distributions on imaging when described in the literature. Functional data from ^{68}Ga -DOTATATE PET/CT provide additional valuable information for lesion characterization, increasing the diagnostic accuracy for NET intracranial metastasis. ^{68}Ga -radiopharmaceuticals have been used for the diagnosis and staging of NETs for multiple reasons. The somatostatin receptor type 2 expression of NETs allows for somatostatin analog radiopharmaceuticals to be used to identify tumors. The gold standard for detection and staging of most NETs is ^{111}In -diethylenetriaminepentaacetic acid-octreotide, with a sensitivity of between 50% and 95%, depending on the subtype of NET (6). However, ^{68}Ga , when linked to a DOTA peptide, demonstrates an increased affinity for somatostatin receptor subtype 2, with the highest affinity being seen for ^{68}Ga -DOTATATE (7). ^{68}Ga -DOTATATE has been shown to be useful in identifying

primary and metastatic NETs that express the somatostatin receptor (6). Recent European guidelines on imaging in search of a primary NET include cross-sectional imaging with CT or

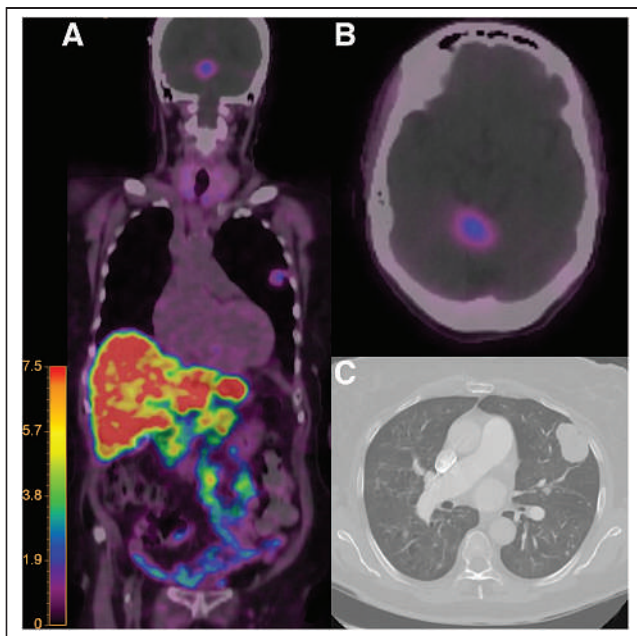


FIGURE 2. (A) Whole body coronal color fusion map and (B) axial color fusion map ^{68}Ga -DOTATATE PET/CT demonstrate corresponding uptake within the posterior fossa lesion and left lung mass. (C) Chest CT demonstrates the mass in the left upper lobe of the lung. Intensity scale bar in units of SUV.

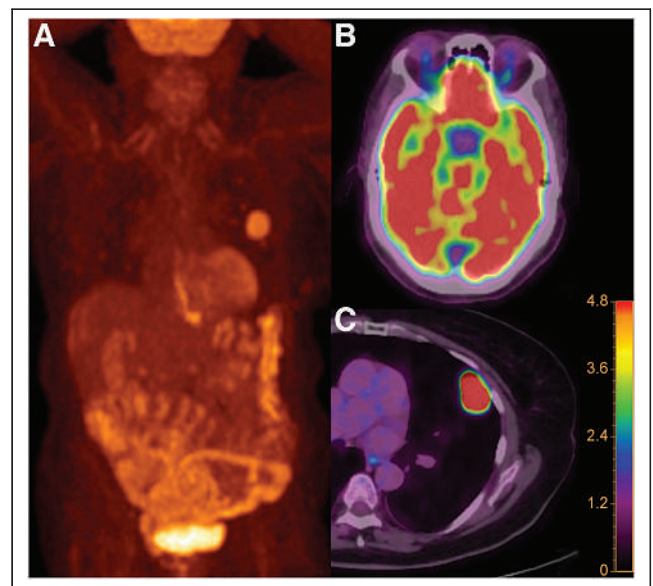


FIGURE 3. ^{18}F -FDG PET/CT. (A) Whole-body coronal fusion map maximal-intensity-projection and (C) axial image of the chest color fusion map demonstrate increased uptake in the left upper lobe lung mass. (B) Axial image of the brain demonstrates uptake in the posterior fossa lesion similarly to that in the hypermetabolic brain parenchyma.

MRI, followed by ^{68}Ga -DOTATATE PET in combination with native or triple-phase enhanced CT (8).

Although ^{68}Ga -DOTATATE PET/CT helps to distinguish intracranial metastases from NETs versus other primary neoplasms, other intracranial lesions expressing somatostatin receptors, particularly meningiomas and hemangioblastomas, can also demonstrate ^{68}Ga -DOTATATE uptake. Oh et al. reported the case of a 36-y-old woman with von Hippel–Lindau disease in which ^{68}Ga -DOTATATE PET/CT for pancreatic tumor restaging found new avid cerebellar and spinal hemangioblastomas (9). In cases for which distinguishing between meningioma/hemangioblastoma and NET is necessary, structural brain MRI and the clinical context remain crucial to reaching an accurate diagnosis.

CONCLUSION

Intracranial metastases from NETs are extremely rare and can have an uncharacteristic and variable imaging appearance on conventional imaging. Accurate diagnosis of these lesions is important to provide a reliable prognosis and to guide appropriate treatment. This case report demonstrates the utility of ^{68}Ga -DOTATATE PET CT in combination with conventional imaging, providing more robust lesion characterization and an accurate diagnosis in this patient with NET intracranial metastasis.

DISCLOSURE

No potential conflict of interest relevant to this article was reported.

REFERENCES

1. Dasari A, Shen C, Halperin D, et al. Trends in incidence, prevalence, and survival outcomes in patients with neuroendocrine tumors in the United States. *JAMA Oncol*. 2017;3:1335–1342.
2. Mallory GW, Fang S, Giannini C, Van Gompel JJ, Parney IF. Brain carcinoid metastases: outcomes and prognostic factors. *J Neurosurg*. 2013;118:889–895.
3. Krug S, Teupe F, Michl P, Gress TM, Rinke A. Brain metastases in patients with neuroendocrine neoplasms: risk factors and outcome. *BMC Cancer*. 2019;19:362.
4. Bhojwani N, Huang J, Gupta A, Badve C, Cohen ML, Wolansky LJ. Rectal carcinoid tumor metastasis to a skull base meningioma. *Neuroradiol J*. 2016;29:49–51.
5. Cuoco JA, Kortz MW, McCray E, et al. Case report: metastatic bronchopulmonary carcinoid tumor to the pineal region. *Front Endocrinol (Lausanne)*. 2021;12:623756.
6. Krenning EP, Kwekkeboom DJ, Bakker WH, et al. Somatostatin receptor scintigraphy with [^{111}In -DTPA-D-Phe 1]- and [^{123}I -Tyr 3]-octreotide: the Rotterdam experience with more than 1000 patients. *Eur J Nucl Med*. 1993;20:716–731.
7. Hofman MS, Lau WF, Hicks RJ. Somatostatin receptor imaging with ^{68}Ga DOTATATE PET/CT: clinical utility, normal patterns, pearls, and pitfalls in interpretation. *Radiographics*. 2015;35:500–516.
8. Niederle B, Pape UF, Costa F, et al. ENETS consensus guidelines update for neuroendocrine neoplasms of the jejunum and ileum. *Neuroendocrinology*. 2016;103:125–138.
9. Oh JR, Kulkarni H, Carreras C, et al. Ga-68 somatostatin receptor PET/CT in von Hippel–Lindau disease. *Nucl Med Mol Imaging*. 2012;46:129–133.

False-Positive ^{68}Ga -DOTATATE PET/CT Findings in Hereditary Hypophosphatemia–Osteomalacia Mimicking Culprit Lesions of Tumor-Induced Osteomalacia

Rahul V. Parghane and Sandip Basu

Radiation Medicine Centre, Bhabha Atomic Research Centre, Tata Memorial Hospital Annexe, and Homi Bhabha National Institute, Mumbai, India

^{68}Ga -DOTATATE PET/CT is an important imaging modality for detection of culprit lesions of tumor-induced osteomalacia in clinically symptomatic patients with hypophosphatemia–osteomalacia. Somatostatin receptor expression may at times be observed in inflammatory or granulomatous conditions and in fractures or degenerative bone disease, leading to false-positive scan findings. We present a rare case of hereditary hypophosphatemia–osteomalacia that showed increased false-positive uptake (for possible tumor-induced osteomalacia lesions) in an inflammatory condition of the maxillary sinus and a fracture of the tibia on somatostatin receptor–based ^{68}Ga -DOTATATE PET/CT.

Key Words: ^{68}Ga -DOTATATE PET/CT; hypophosphatemia–osteomalacia; tumor-induced osteomalacia; TIO; MRI

J Nucl Med Technol 2023; 51:73–74

DOI: 10.2967/jnmt.121.263776

In tumor-induced osteomalacia (TIO), the culprit lesions are usually mesenchymal tumors with somatostatin receptor (SSTR) expression, and ^{68}Ga -DOTATATE PET/CT plays an important role in tumor localization and management. We present a rare case of hereditary hypophosphatemia–osteomalacia that showed false-positive foci on ^{68}Ga -DOTATATE PET/CT mimicking possible TIO lesions.

CASE REPORT

In a 45-y-old man with bony pain in the chest wall, back, and lower limbs of 1.5-y duration, multiple old healed rib fractures were found, and blood work revealed a low level of serum phosphorus (2.1 mg/dL), a raised level of serum alkaline phosphatase (208 IU/L), and a markedly raised level of fibroblast growth factor 23 (FGF-23) (1,561.5 relative units/mL). The clinical features, low level of serum phosphorus, and raised level of FGF-23 were highly suggestive of TIO. The patient underwent ^{68}Ga -DOTATATE PET/CT for detection of the culprit lesion of TIO. Whole-body PET/CT was performed on

a Philips Gemini TF time-of-flight 16 PET/CT scanner 60 min after intravenous injection of 74 MBq (2 mCi) of ^{68}Ga -DOTATATE. Images were acquired using a 3-dimensional PET protocol at 3 min per bed position. Data were reconstructed using an iterative algorithm (row-action maximum likelihood: 2 iterations and 21 subsets). Non-contrast-enhanced, low-dose CT (voltage, 120 kVp; slice thickness, 5 mm; pitch, 0.83; field of view, 600 mm; rotation time, 0.5 s; 50 mA) was used for anatomic localization and attenuation correction of PET data. Maximum-intensity-projection PET (Fig. 1A) showed abnormal SSTR uptake in the maxillary sinus and knee region. Transaxial PET/CT (Fig. 1B) showed mildly increased SSTR uptake (SUV_{max} , 5.42) in the left maxillary sinus, with mucosal thickening. Coronal PET/CT (Fig. 1D) showed mild SSTR uptake (SUV_{max} , 3.84 on right) and faint SSTR uptake (SUV_{max} , 2.3 on left) in a sclerotic lesion in the medial part of the upper condyle of tibia, bilaterally (right > left side). These findings were suggestive of culprit lesions of TIO. In view of the doubtful findings on ^{68}Ga -DOTATATE PET/CT, multiplanar MRI of the paranasal sinus and knee was performed using spin-echo T1-weighted, fast spin-echo T2-weighted, turbo inversion-recovery magnitude, and short-tau inversion-recovery sequences. MRI of the maxillary sinus (Fig. 1C) showed moderate T2 hyperintense mucosal thickening in the left maxillary sinus, with central T2 hypointense areas due to retained secretion. MRI of the knee (Fig. 1E) showed a fracture along the proximal inner medial part of the left and right tibiae on a T1-weighted coronal view, with mild periosteal edema. The MRI findings were suggestive of benign disease in both regions. Subsequently, the patient was evaluated for hereditary hypophosphatemia. The *SLC2A2* (–) phenotype was identified, which is pathogenic for the autosomal recessive disorder Fanconi–Bickel syndrome.

DISCUSSION

^{68}Ga -DOTATATE PET/CT is an important noninvasive imaging modality for detection and localization of the culprit lesion of TIO. Other than in tumors, SSTR expression is observed in inflammatory or granulomatous conditions and in fractures or degenerative bone disease, leading to false-positive scan findings in various oncologic cases (1–4). A raised level of FGF-23 is not specific to TIO and can also be found

Received Dec. 30, 2021; revision accepted Jan. 28, 2022.
For correspondence or reprints, contact Sandip Basu (drsab@yahoo.com).
Published online Feb. 23, 2022.
COPYRIGHT © 2023 by the Society of Nuclear Medicine and Molecular Imaging.

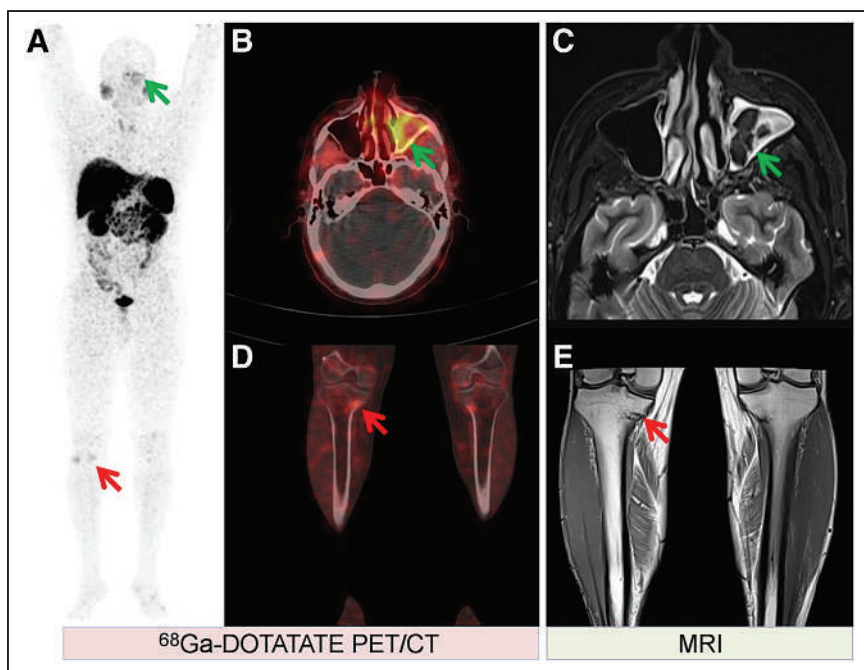


FIGURE 1. (A) Maximum-intensity-projection ^{68}Ga -DOTATATE PET image showing abnormal SSTR uptake in maxillary sinus (green arrow) and knee (red arrow) regions. (B and D) Transaxial ^{68}Ga -DOTATATE PET/CT image showing mildly increased uptake (arrow, SUV_{max} of 5.42) in left maxillary sinus, with mucosal thickening (B), and coronal ^{68}Ga -DOTATATE PET/CT image showing mildly SSTR-avid sclerotic lesion (arrow, SUV_{max} of 3.84) in medial part of upper condyle of right tibia and faint SSTR uptake in medial part of upper condyle of left tibia (D). (C and E) MRI of maxillary sinus showing moderate T2 hyperintense mucosal thickening in left maxillary sinus, with central T2 hypointense areas due to retained secretion (C, arrow), and MRI with T1-weighted coronal view of knee showing fracture along proximal inner medial part of left and right tibiae (E, arrow), both of which were suggestive of benign etiologies.

in hereditary hypophosphatemia- and osteomalacia-inducing musculoskeletal disorders, such as X-linked hypophosphatemic rickets and autosomal dominant and recessive hypophosphatemic rickets (5). Our patient presented with long-standing systemic symptoms of hypophosphatemia, with a raised level of FGF-23. ^{68}Ga -DOTATATE PET/CT was considered to localize the culprit lesion of TIO in view of the clinically symptomatic and biochemically proven case of hypophosphatemia with an increased FGF-23 level. Increased SSTR uptake was seen in the maxillary sinus and bilaterally in the

tibial regions, which on MRI were illustrative of benign etiopathologies. Finally, the patient was diagnosed with hereditary hypophosphatemia caused by the autosomal recessive disorder Fanconi–Bickel syndrome.

CONCLUSION

^{68}Ga -DOTATATE PET/CT is used as the first-line imaging modality in suspected cases of TIO. In addition to being found in TIO, a raised FGF-23 level can also be found in other hypophosphatemia- and osteomalacia-inducing musculoskeletal disorders. However, SSTR uptake is also seen in inflammatory or granulomatous conditions and in fractures or degenerative bone disease. This should be kept in mind when one is interpreting ^{68}Ga -DOTATATE PET/CT images with equivocal or doubtful findings in hypophosphatemia–osteomalacia cases.

DISCLOSURE

No potential conflict of interest relevant to this article was reported.

REFERENCES

1. Tertychnyi AS, Akhrieva KM, Zayratyants OV, Selivanova LS, Birg TM. Somatostatin receptor expression in the ileal mucosa of patients with inflammatory bowel disease [in Russian]. *Arkh Patol.* 2016;78:19–24.
2. Vanhagen PM, Markusse HM, Lamberts SW, Kwekkeboom DJ, Reubi JC, Krenning EP. Somatostatin receptor imaging: the presence of somatostatin receptors in rheumatoid arthritis. *Arthritis Rheum.* 1994;37:1521–1527.
3. Klinaki I, Al-Nahhas A, Soneji N, Win Z. ^{68}Ga DOTATATE PET/CT uptake in spinal lesions and MRI correlation on a patient with neuroendocrine tumor: potential pitfalls. *Clin Nucl Med.* 2013;38:e449–e453.
4. Demirci E, Akyel R, Kilic F, Kantarci F, Halac M, Sonmezoglu K. Dual false positive of ^{68}Ga -DOTA-TATE PET/CT scan in a patient with a history of pancreatic neuroendocrine tumor: a case report. *Rev Esp Med Nucl Imagen Mol.* 2015;34:133–135.
5. Ramon I, Kleynen P, Body JJ, Karmali R. Fibroblast growth factor 23 and its role in phosphate homeostasis. *Eur J Endocrinol.* 2010;162:1–10.

Metachronous Adenocarcinoma of the Lung in the Setting of Metastatic Gastric Neuroendocrine Tumor: Value of Elucidating Discordance on Dual-Tracer PET/CT with Ki-67 Index

Sarvesh Loharkar and Sandip Basu

Radiation Medicine Centre, Bhabha Atomic Research Centre, Tata Memorial Hospital Annexe, and Homi Bhabha National Institute, Mumbai, India

Dual-tracer PET/CT (^{18}F -FDG and ^{68}Ga -DOTATATE) has become established practice in the management of metastatic neuroendocrine neoplasms (NENs) and has demonstrated the advantages to patient management of deciphering the molecular PET characteristics of the tumor. Judicious elucidation of the findings is important, especially in scenarios of discordance with reported histopathology, potentially leading to an unsuspected diagnosis such as second primary malignancies. Such a diagnosis established early in the disease course, and mostly at an asymptomatic stage, provides lead time for timely, appropriate management. This concept was elaborated in a case of incidentally detected ^{18}F -FDG-avid metachronous lung adenocarcinoma in a patient with metastatic, well-differentiated gastric NEN, wherein dual-tracer PET/CT showed ^{18}F -FDG-avid but not ^{68}Ga -DOTATATE-avid lung opacity.

Key Words: ^{18}F -FDG; ^{68}Ga -DOTATATE; dual-tracer PET/CT; neuroendocrine neoplasm; somatostatin receptor; SSTR

J Nucl Med Technol 2023; 51:75–77

DOI: 10.2967/jnmt.121.263415

Neuroendocrine neoplasms (NENs) comprise a heterogeneous group of tumors originating from neuroendocrine cells at different sites and organs. Few reports have highlighted the link between NENs and associated second primary malignancies (1,2), with the prevalence of second primary malignancy ranging from 4% to 25% in different cohorts and an observed preponderance of gastrointestinal, genitourinary, and breast malignancies, primarily in settings of gastrointestinal and pancreatic NENs. The utility of dual-tracer PET/CT (^{18}F -FDG and ^{68}Ga -DOTATATE) in NENs is now evident (3), providing multiple added merits such as an understanding of tumor biology and intra- and intertumoral heterogeneity, help with treatment decision making, and (rarely) detection of multifocal primary NENs and second primary malignancies. Discordant ^{18}F -FDG-positive/SSTR-negative lesions, especially in low-grade NENs, might correspond to a second primary or NEN tumor heterogeneity. We present a case of metastatic gastric

NEN in which a metachronous primary lung malignancy was diagnosed primarily through suspicion when discordance on dual-tracer PET/CT was seen in an asymptomatic patient.

CASE STUDY

A 60-y-old-man who had a giant excavating ulcer with an elevated margin at the greater curvature of the stomach was diagnosed on endoscopic biopsy to have metastatic grade II well-differentiated gastric NEN (Ki-67, 5%). He had received 2 cycles of ^{177}Lu -DOTATATE peptide-receptor radionuclide therapy (cumulative dose: 13.87 GBq) in view of progressive disease, and uptake with a Krenning score of 4 was seen in multiple hypodense liver lesions on ^{68}Ga -DOTATATE PET/CT (Fig. 1).

Recent follow-up PET/CT with ^{68}Ga -DOTATATE showed somatostatin receptor (SSTR)-expressing stable hepatic disease, but there was a minimally SSTR-expressing centimeter-sized ill-defined opacity at the upper lobe of the right lung, initially

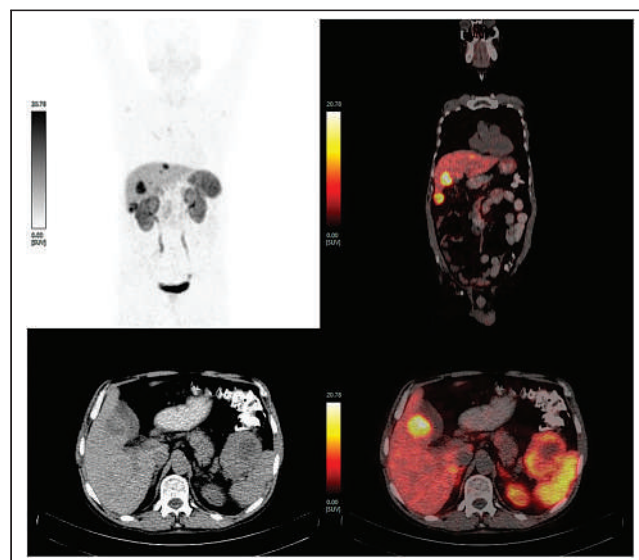


FIGURE 1. Baseline ^{68}Ga -DOTATATE PET/CT (upper left: maximum-intensity projection image; upper right: fused coronal; lower left: transaxial CT only; and lower right: fused transaxial) showing multiple SSTR-expressing hepatic metastases (liver segment V lesion).

Received Oct. 21, 2021; revision accepted Mar. 2, 2022.

For correspondence or reprints, contact Sandip Basu (drsanb@yahoo.com).

Published online Apr. 19, 2022.

COPYRIGHT © 2023 by the Society of Nuclear Medicine and Molecular Imaging.

suspected of being metastatic disease. The lesion was ^{18}F -FDG-avid (Fig. 2) (SUV_{max} , 9.6). Considering that this new lesion was not consistent with other hepatic metastatic lesions, a CT-guided biopsy was considered. Subsequently, the patient defaulted for more than 6 months and missed his appointments because of the coronavirus disease 2019 lockdown.

At the next visit, he was reevaluated with dual-tracer PET/CT (Figs. 3 and 4), which showed SSTR-expressing multiple (at least 4) hypodense lesions in both lobes of the liver and a soft-tissue mass at the splenic hilum. In the upper lobe of the right lung, an ^{18}F -FDG-avid lesion of soft-tissue density and with irregular margins was noted, along with a similar new, smaller lesion in the apical segment of the same lobe. Although the hypodense liver lesions and the soft-tissue lesion at the splenic hilum were weakly ^{18}F -FDG-concentrating, both the SSTR-avid hepatic lesions and the ^{18}F -FDG-avid lung lesions showed an increase in size and tracer uptake suggestive of disease progression (Fig. 3). Considering the discordance in the lung lesions (^{18}F -FDG-avid but not SSTR-expressing), the possibility of a metachronous primary lung malignancy arose. The larger lung lesion was targeted with CT-guided biopsy and, on histopathology, was found to harbor primary pulmonary adenocarcinoma. On immunohistochemistry, the tumor cells were positive for thyroid transcription factor-1 but negative for synaptophysin. The patient underwent a further peptide-receptor radionuclide therapy cycle, with a referral to a thoracic oncologist, who performed mutational analysis. The patient's disease course has since remained symptomless for both malignancies.

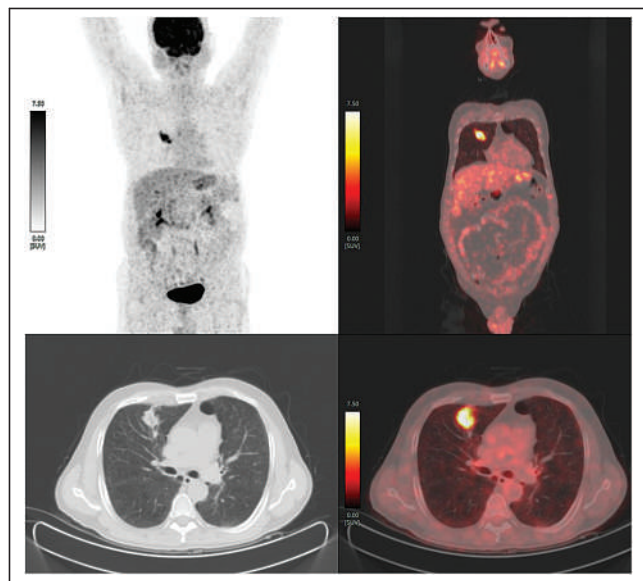


FIGURE 2. ^{18}F -FDG PET/CT after 2 cycles of peptide-receptor radionuclide therapy (upper left: maximum-intensity projection image; upper right: fused coronal; lower left: transaxial CT; and lower right: fused transaxial) showing ^{18}F -FDG-concentrating (SUV_{max} , 9.6) ill-defined opacity in upper lobe of right lung.

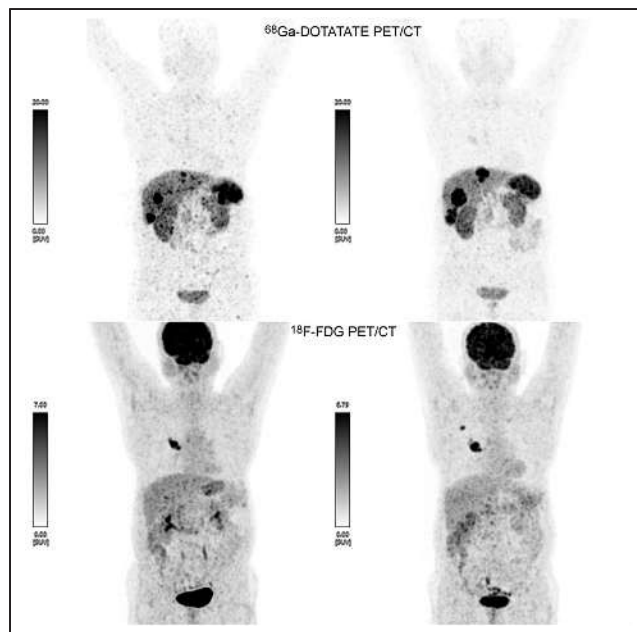


FIGURE 3. Follow-up dual-tracer PET/CT maximum-intensity projections obtained 6 mo apart (right panel later than left panel) and showing disease progression in terms of increase in size and number of SSTR-expressing hepatic lesions on ^{68}Ga -DOTATATE PET/CT and increase in size and number of ^{18}F -FDG-avid lung lesions on ^{18}F -FDG PET/CT.

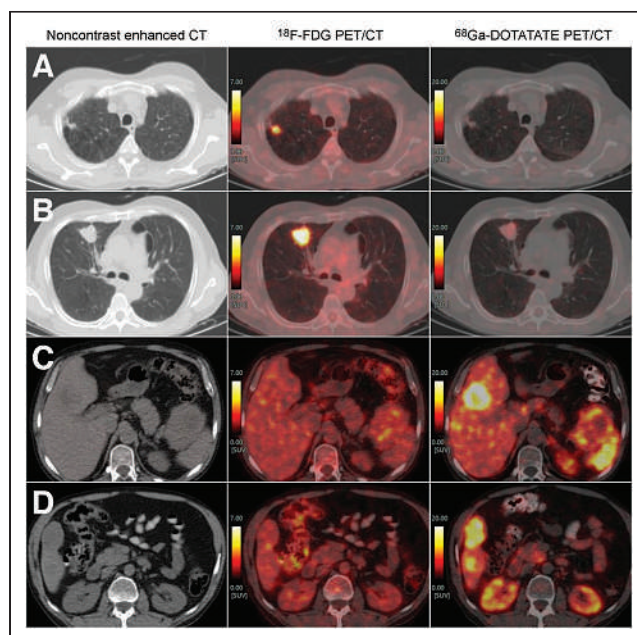


FIGURE 4. Follow-up dual-tracer transaxial PET/CT images showing ^{18}F -FDG-avid (SUV_{max} , 10.9), non-SSTR-expressing (SUV_{max} , 4.7) lung lesions in right upper lobe (A and B); non- ^{18}F -FDG-concentrating (SUV_{max} , 2.8), highly SSTR-expressing (SUV_{max} , 29.4) hypodense segment V lesion in liver and nodal mass at splenic hilum (C); and similar non- ^{18}F -FDG-concentrating (SUV_{max} , 2.4), highly SSTR-expressing hypodense segment VI lesion in liver (SUV_{max} , 26.5) (D).

DISCUSSION

The present report emphasizes the importance of performing dual-tracer PET/CT examinations and analyzing them adequately to decode the disease pathology. There is one report that discordance on dual-tracer PET/CT had utility in the diagnosis of triple-negative breast carcinoma in a patient with NEN (4). Dual-tracer PET/CT has also enabled a diagnosis of primary lung NEN in the scenario of metastasis with unknown primary (5). This molecular PET imaging technique enables us to understand the biology of tumor lesions noninvasively and can provide added benefits as demonstrated in this case.

In the presented case, dual-tracer PET/CT findings raised suspicion regarding the lung lesion noted early in the disease course. Such findings have potential to provide enough lead time to make treatment with curative intent feasible.

CONCLUSION

This case underscored the value of correlation of discordant findings on dual-tracer PET/CT in NEN patients, including use of biopsy when indicated. Attending physicians should be

familiar with NEN variants and differentials when interpreting such studies.

DISCLOSURE

No potential conflict of interest relevant to this article was reported.

REFERENCES

1. Parra-Medina R, Moreno-Lucero P, Jimenez-Moreno J, et al. Neuroendocrine neoplasms of gastrointestinal tract and secondary primary synchronous tumors: a systematic review of case reports. Casualty or causality? *PLoS One*. 2019;14:e0216647.
2. Kauffmann RM, Wang L, Phillips S, et al. Incidence of additional primary malignancies in patients with pancreatic and gastrointestinal neuroendocrine tumors. *Ann Surg Oncol*. 2014;21:3422–3428.
3. Basu S, Sirohi B, Shrikhande SV. Dual tracer imaging approach in assessing tumor biology and heterogeneity in neuroendocrine tumors: its correlation with tumor proliferation index and possible multifaceted implications for personalized clinical management decisions, with focus on PRRT. *Eur J Nucl Med Mol Imaging*. 2014;41:1492–1496.
4. Kalshetty A, Basu S. Interpreting discordance on dual-tracer positron emission tomography-computed tomography in the setting of metastatic neuroendocrine tumor: detection of metachronous triple-negative breast carcinoma. *World J Nucl Med*. 2020;19:414–416.
5. Polish A, Vergo MT, Agulnik M. Management of neuroendocrine tumors of unknown origin. *J Natl Compr Canc Netw*. 2011;9:1397–1402.

Femoral Neck Fracture with Avascular Necrosis

Elissa R. Ballas¹, Vincent T. Nguyen¹, and Ely A. Wolin^{1,2}

¹David Grant USAF Medical Center, Travis Air Force Base, California; and ²Uniformed Services University, Bethesda, Maryland

Hip fractures are common in the aging population, with complications such as avascular necrosis. We describe a case of an 85-y-old woman with early avascular necrosis as a complication from femoral neck fracture discovered on routine bone densitometry screening.

Key Words: avascular necrosis; femoral neck fracture; DEXA

J Nucl Med Technol 2023; 51:78–79
DOI: 10.2967/jnmt.122.264354

Avascular necrosis of the femoral head is a known complication of femoral neck fractures. Various imaging modalities, including MRI and bone scintigraphy, can be used to evaluate avascular necrosis.

CASE REPORT

An 85-y-old woman underwent routine screening bone densitometry. On the images, the femoral neck appeared foreshortened (Fig. 1), and radiography was recommended. Hip radiographs then showed a displaced subcapital left femoral neck fracture (Fig. 2), and chart review revealed that the patient had sustained a ground-level fall 3 wk beforehand. Whole-body bone scanning and MRI of the hip were performed to evaluate for avascular necrosis and osseous metastases. The bone scan showed photopenia over the left femoral head on blood pool and delayed images, raising concern about early avascular necrosis (Fig. 3). MRI showed a hypointense femoral head on T1-weighted sequences, confirming the diagnosis of avascular necrosis (Fig. 4). The patient subsequently underwent hemiarthroplasty of the left hip.

DISCUSSION

Dual-energy x-ray absorptiometry is recommended for women aged 65 y or older to screen for osteopenia and osteoporosis (1). The goal of screening is to identify those

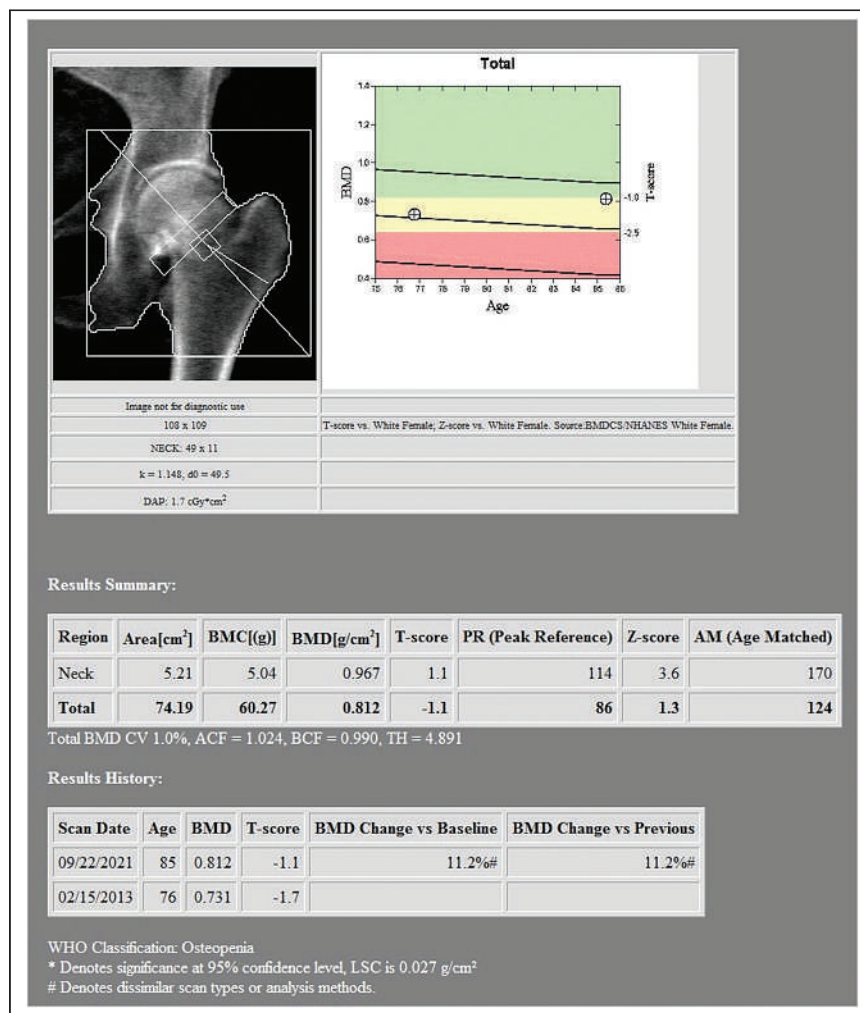


FIGURE 1. Dual-energy x-ray absorptiometry image suggesting foreshortened femoral neck. AM = age matched; BMC = bone mineral content; BMD = bone mineral density; DAP = dose area product; BMDCS/NHANES = Bone Mineral Density in Childhood Study/National Health and Nutrition Examination Surveys; LSC = least significant change; PR = peak reference; WHO = World Health Organization.

Received May 4, 2022; revision accepted Jul. 29, 2022.
For correspondence, contact Elissa Ballas (erballas@hotmail.com).
Published online Aug. 30, 2022.
COPYRIGHT © 2023 by the Society of Nuclear Medicine and Molecular Imaging.

at increased risk of an insufficiency fracture due to a low bone mass. Screening typically evaluates the hip and lumbar spine and, occasionally, the forearm. The World Health



FIGURE 2. Anterior-posterior pelvic radiograph showing displaced subcapital femoral neck fracture.

Organization has devised the Fracture Risk Assessment Tool to estimate the risk that a patient will sustain a major osteoporotic fracture or hip fracture, based, in part, on bone mineral density (2).

Hip fractures are problematic, particularly in the elderly, with complications such as avascular necrosis of the femoral head. In one study, the incidence of avascular necrosis in patients with femoral neck fractures was 14.3% (3). MRI is the gold standard for evaluating avascular necrosis (4). However,

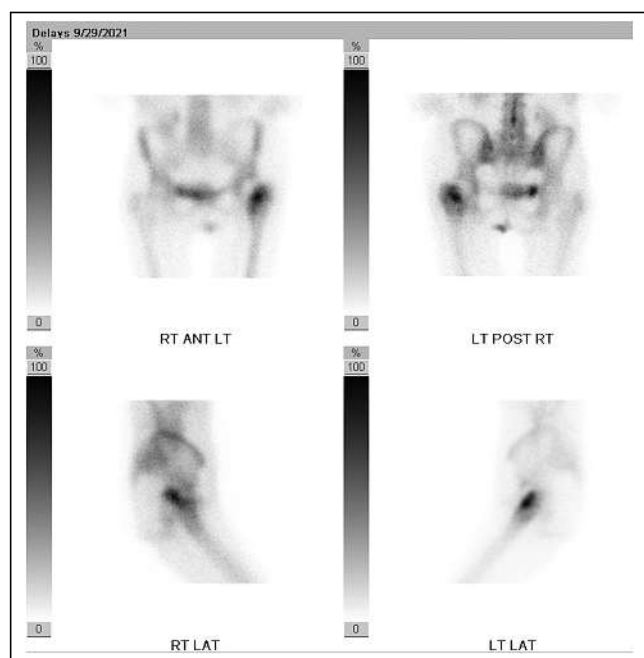


FIGURE 3. Delayed-phase bone scintigraphy images showing photopenia over left femoral head, with expected uptake in femoral neck fracture. ANT = anterior; LAT = lateral; LT = left; POST = posterior; RT = right.

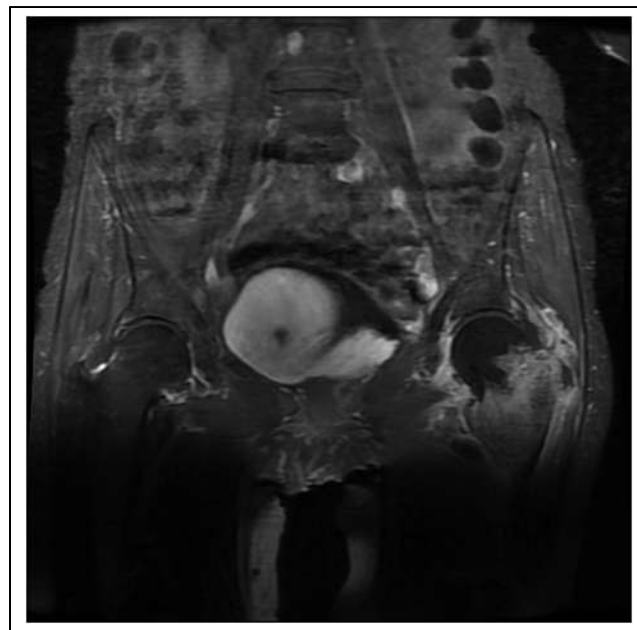


FIGURE 4. Coronal T1-weighted MR image through pelvis showing hypointense left femoral head.

bone scintigraphy is an option. Expected findings on MRI are hypointensity on T1-weighted images, sometimes bordered by a hyperintense line. T2-weighted images may show the double-line sign, consisting of a hyperintense inner line between normal marrow and ischemic marrow. On bone scintigraphy, early avascular necrosis shows photopenia on all phases because of absence of blood flow. Late avascular necrosis shows increased bone tracer activity due to reparative uptake.

CONCLUSION

Bone densitometry is a useful screening tool for osteopenia and osteoporosis. The limited images may yield unexpected findings, as demonstrated in this case, during which a displaced femoral neck fracture was discovered. Avascular necrosis is a common complication of femoral neck fractures and can be evaluated with MRI or bone scintigraphy.

DISCLOSURE

The views expressed are solely those of the authors and do not reflect the official policy or position of the U.S. Air Force, the Department of Defense, or the U.S. Government. No potential conflict of interest relevant to this article was reported.

REFERENCES

1. Yu EW. Screening for osteoporosis in postmenopausal women and men. UpToDate website. <https://www.uptodate.com/contents/screening-for-osteoporosis-in-postmenopausal-women-and-men>. Updated August 4, 2022. Accessed August 15, 2022.
2. Kanis JA, Johansson H, Oden A, Dawson-Hughes B, Melton LJ III, McCloskey EV. The effects of a FRAX revision for the USA. *Osteoporos Int*. 2010;21:35–40.
3. Slobogean GP, Sprague SA, Scott T, Bhandari M. Complications following young femoral neck fractures. *Injury*. 2015;46:484–491.
4. Zalavras CG, Lieberman JR. Osteonecrosis of the femoral head: evaluation and treatment. *J Am Acad Orthop Surg*. 2014;22:455–464.

Radiation Treatments, Autoimmune Activation, and PET Imaging

TO THE EDITOR: PET imaging and radiation treatments (radiotherapy and radionuclide treatments) are commonly used for cancer. PET imaging is used to plan radiation treatments and assess the response to those treatments. In this letter, I want to emphasize the possibility that autoimmune inflammatory PET uptake after radiation treatments may mimic tumor or metastasis. Radiation kills cancer cells mainly via DNA damage, but radiation treatment-induced activation of the immune system (activation of T cells and other immune cells) via release of tumor antigens, proinflammatory cytokines, chemokines, and other signals may also contribute to death of cancer cells (1). Radiobiologic effects of radiotherapy can be seen in nearby nonirradiated cells (bystander effect), in nearby cancer cells receiving a lower dose (cohort effect), and in distant nonirradiated cancer cells (abscopal effect) because of activation of the immune system (2). In the abscopal effect, metastatic foci away from the radiotherapy field can shrink secondary to an activated immune system, and this effect may be visible on PET images. In systemic radionuclide treatments, activation of the immune system may contribute to cancer cell death and enhance the effect of immunotherapies (3,4). Activation of the immune system by radiation treatments may cause autoimmune inflammation in various local or remote tissues such as the lungs (immune-mediated pneumonitis), and this may be visible on PET images, particularly on ^{18}F -FDG PET

(similar to side effects of immune checkpoint inhibitor treatments seen on ^{18}F -FDG PET images), and require careful evaluation of the images so as not to mistake autoimmune inflammation for tumor (5,6).

REFERENCES

1. Carvalho HA, Villar RC. Radiotherapy and immune response: the systemic effects of a local treatment. *Clinics (São Paulo)*. 2018;73(suppl 1):e557s.
2. Daguene E, Louati S, Wozny AS, et al. Radiation-induced bystander and abscopal effects: important lessons from preclinical models. *Br J Cancer*. 2020;123:339–348.
3. Constanzo J, Galluzzi L, Pouget JP. Immunostimulatory effects of radioimmunotherapy. *J Immunother Cancer*. 2022;10:e004403.
4. Li M, Liu D, Lee D, et al. Targeted alpha-particle radiotherapy and immune checkpoint inhibitors induces cooperative inhibition on tumor growth of malignant melanoma. *Cancers (Basel)*. 2021;13:3676.
5. Morgan GW, Breit SN. Radiation and the lung: a reevaluation of the mechanisms mediating pulmonary injury. *Int J Radiat Oncol Biol Phys*. 1995;31:361–369.
6. Schierz JH, Sarikaya I, Wollina U, et al. Immune checkpoint inhibitor-related adverse effects and ^{18}F -FDG PET/CT findings. *J Nucl Med Technol*. 2021;49:324–329.

Ismet Sarikaya

Kirklareli University Faculty of Medicine

Kirklareli, Turkey

E-mail: isarikaya99@yahoo.com

Published online Nov. 9, 2022.
DOI: 10.2967/jnmt.122.265093

The 2022 Year in Review

The History Committee is charged with maintaining and compiling the history of the Technologist Section. With this charge, one of the items that the committee would like to begin and continue is this brief Year in Review.

Coming out of the pandemic, SNMMI hosted the Mid-Winter Meeting virtually, but the Annual Meeting was held using the first completely hybrid format in SNMMI's history (with the meeting being held both in-person in Vancouver, BC, and also virtually). The meeting was well attended, with many new sessions and topics being presented. Most importantly, colleagues came together for the first time since June 2019, the last in-person Annual Meeting. For those attending, it truly felt like a homecoming. In addition, SNMMI completed the year with the 2nd Theranostics Meeting, hosted at the Gaylord National Resort & Convention Center in Maryland. The introduction of this new hybrid-meeting format for SNMMI came with great interest and excitement for those unable to attend meetings every year.

The SNMMI Technologist Section was led by President Dusty M. York, CNMT, PET, RT(N)(CT), through the 2022 Annual Meeting with the new president, Krystle W. Glasgow, CNMT, NMTCB(CT), NMAA, assuming office at the end of the Annual Meeting in Vancouver. Dmitry D. Beyder, MPA, CNMT, was elected as President-elect.

The post-pandemic world had everyone moving and acting trepidatiously. In 2022, SNMMI continued to provide guidance regarding COVID-19 vaccines, and the Technologist Section supplemented the recommendations with articles on the benefits and experiences individuals had following vaccination, published in the *Journal of Nuclear Medicine Technology (JNMT)*.

SNMMI hosted the Artificial Intelligence and Barriers to Patient Access Summit in March—the first of its kind for the Society—designed to bring together thought leaders to discuss current obstacles in the field of nuclear medicine and provide solutions.

Mid-year, SNMMI announced the creation of the Mars Shot Fund, an initiative to raise \$100 million to help pay for nuclear medicine, molecular imaging, and therapy research. Applications for the first \$1 million were opened in December, producing an overwhelming amount of interest.

SNMMI approved the following statement: Safe and Equitable Healthcare for All: SNMMI's Position on the Doctor-Patient Relationship—"SNMMI believes that physicians must be able to provide safe, effective, and accessible evidence-based health care to patients without the threat of non-medical outside interference. We condemn any interference with the doctor-patient relationship outside of public health measures and acknowledge that such interference

can disproportionately impact historically and economically marginalized and disadvantaged populations. Physicians, legislators, regulators, and patients must work together to ensure safe and equitable health care for all."

The issue that hospitals are now facing is not the decreased number of hospital beds but the personnel shortages. This phenomenon is one that the entire world and almost all industries are grappling with as businesses fight to stay open and staffed. The workforce shortage poses a huge problem for healthcare—specifically, the nuclear medicine and molecular imaging community—creating the perfect storm. Nuclear medicine technologist programs and residencies are closing while more and more therapies are being approved. The field is booming and in desperate need of qualified individuals. The SNMMI and industry have partnered to tackle this issue through the Value Initiative Workforce Pipeline Domain and have identified several outreach strategies that will debut in 2023. The Technologist Section created a one-of-a-kind recruitment video showcasing the amazing careers, stability, and growth possibility as a Nuclear Medicine Technologist.

In March 2022, SNMMI named Stanford Health Care and the Dana-Farber Brigham Cancer Center as its first two designated Radiopharmaceutical Therapy Centers of Excellence. SNMMI created the Radiopharmaceutical Therapy Center of Excellence program to certify sites that meet strict regulatory, training, qualification, experience, and performance criteria for radiopharmaceutical therapy. With the Radiopharmaceutical Therapy Centers of Excellence designation, institutions can assure patients, their families, referring physicians, and payors that rigorous procedures are in place and followed, ultimately leading to appropriate patient selection and optimal outcomes from radiopharmaceutical therapy.

The Food and Drug Administration announced the approval of several new therapies and agents, including game-changing nuclear medicine treatment for metastatic prostate cancer, shown to reduce risk of death by 38% and risk of progression by 60% in metastatic castration-resistant prostate cancer patients. Technology and science in our field seemed to have exploded in 2022. The journals are jam-packed with new isotopes, instrumentation, techniques, and findings. The *JNMT* and its editor have expanded the journal, with so much information and new material, and to quote the editor, "Theranostics: The Future is NOW!" The Technologist Section also released a new book: *Artificial Intelligence in Nuclear Medicine*—the FIRST AI book from the SNMMI. The nuclear medicine and molecular imaging community also celebrated many new advances in science and technology over the past year, including (1):

- Novel PET Agent Effectively Detects Multiple Cancers, Identifies Patients for Targeted Therapies
- PET/MRI Machine Learning Model Can Eliminate Sentinel Lymph Node Biopsy in Majority of Breast Cancer Patients
- Novel PET Imaging Agent Detects Earliest Signs of Alzheimer's Disease
- Ultra-Low Dose Total Body PET/CT Effective for Evaluating Arthritis
- New PET Tracer Shows Promise for uPAR-Targeted Therapy of Neuroendocrine Neoplasms
- New Research Shows PSMA PET/CT Imaging Changes Management for Close to 50 Percent of Prostate Cancer Patients
- Revolutionary Technology Shortens Cardiac Scan Time, Provides High-Quality SPECT Images
- Novel Radiopharmaceutical Pair Detects and Treats Melanoma; Study Shows Potential for Broad Application in Solid Tumors
- Virtual CT Scans Cut Patient Radiation Exposure in Half During PET/CT Studies
- PET Imaging Confirms Link Between Obstructive Sleep Apnea and Heart Blood Flow Impairment
- Novel PET Agent Highly Effective for Imaging Meningiomas; Offers Logistical Advantages Over Standard Agents
- Novel Ultra-Low Dose PET Technique Significantly Reduces Radiation Exposure
- Novel Deep Learning Method Provides Early and Accurate Differential Diagnosis for Parkinsonian Diseases
- New Radionuclide Combination Therapy Safe and Effective in Metastatic Prostate Cancer Patients
- Molecular Imaging Uncovers Effects of COVID-19 on the Brain
- Novel Radioligand Therapy Proven Superior for Metastatic Prostate Cancer Patients
- PSMA PET Validates EAU Classification System to Determine Risk of Prostate Cancer Recurrence
- PET/CT Artificial Intelligence Model Ideal for Predicting Risk of Future Heart Attack

Both the SNMMI and the SNMMI-TS hosted Strategic Planning sessions in 2022, the first in more than 5 years due to the COVID-19 pandemic. For the first time in decades, it was agreed that there would be one mission and vision that directed the entire organization. The Technologist Section, who created their own mission and vision to focus on the technologist specifically, agreed that it was essential to have one cohesive mission and vision statement to ensure synergy moving forward.

The end of the year proved difficult as nuclear medicine reported a shortage of molybdenum-99 (Mo-99)/technetium-99m (Tc-99m) through and beyond the third week of November. More than 20 million Americans benefit each year from nuclear medicine procedures used to diagnose and treat a wide variety of diseases such as Alzheimer's, certain cancers, and heart disease. Any delay in the supply chain impacts patient care by preventing access to the most up-to-date treatments, imaging, and diagnostic tests. As we progress from 2022 into 2023, physicians are asking our technology if certain disease states may be seen and/or treated. The answer should be the title of Dr. Simon Cherry's 2022 Cassen Award presentation, "It's Just a Matter of Time."

The history of the SNMMI and SNMMI-TS is rich. The membership and leadership have contributed and continue to contribute greatly. But as one looks at history, one of its major contributing components is its technologists who propagate the technology on the front lines. Let us keep moving forward as we remember our past.

REFERENCE

1. SNMMI NEWS & PUBLICATIONS, NEWS AND MEDIA, SNMMI NEWS. <http://www.snmmi.org/NewsPublications/NewsList.aspx?metadadataid=34&navItemNumber=676>.



**We Are Here for Him
So He Is There for Her**



The Reliable, Responsive, Nuclear Pharmacy Provider

Jubilant Radiopharma pharmacies compound, prepare, and dispense radiopharmaceutical products in state-of-the-art cleanrooms engineered to meet the **ISO 14644** standards. Our primary buffer room meets **ISO 7** classification, ensuring high quality standards are met for all nuclear medicine products dispensed from our large and responsive distribution network. Our pharmacies are ready to dispense **PSMA-11 (gallium Ga68 gozetotide)** to your PET imaging center. We continuously evolve to overcome the ever-changing healthcare landscape. If your department needs flexibility, reliability and confidence, contact your local nuclear sales manager for more information by scanning the **QR code** or visiting www.jubilantradiopharma.com



Rapidly Delivering Both

Ilucix[®]

(kit for the preparation of gallium Ga68 gozetotide injection)

LOCAMETZ[®]

(kit for the preparation of gallium Ga68 gozetotide injection)



*Proud Leadership Circle Members
of the SNMMI Value Initiative*

Jubilant DraxImage Inc. dba Jubilant Radiopharma™
790 Township Line Road, Yardley, PA 19067
Phone: 215.550.2810
© Jubilant DraxImage Inc. 2022-US-PHARM-00014



www.JubilantRadiopharma.com

Improving Lives Through Nuclear Medicine™

Streamlined. Simple. Accurate.

CRC® Dose Calibrator Family

Combine the speed and accuracy you need to measure and prepare doses with the performance and reliability that you've come to expect in one of the industry's finest packages.



CRC® - PC Smart Chamber

Network Ready with Remote Connectivity
The Most Advanced in Dose Calibration.



CRC®-55tPET Dose Calibrator (Touch Screen)

Speed and accuracy to measure
and prepare doses.

Driving Innovation... Together

Two leading brands of nuclear medicine products and technology, the **Capintec™** and **Biodex™** teams have joined forces under Mirion Medical.



CAPINTEC
A MIRION MEDICAL COMPANY

Mirion, the Mirion logo, and other trade names of Mirion products listed herein are registered trademarks or trademarks of Mirion Technologies, Inc. or its affiliates in the United States and other countries.

OPS-4421 - 08/22

Visit capintec.com to learn
how we can support your
unique requirements.



